Characterization of Oxy-combustion Impacts in Existing Coal-fired Boilers

Topical Report

Reporting Period Start Date: October 1, 2008
Reporting Period End Date: June 30, 2009

Principal Authors: Dr. Bradley R. Adams, Dr. Andrew R. Fry, Dr. Constance L. Senior, Dr. Hong Shig Shim, Dr. Huafeng Wang, Prof. Jost Wendt (University of Utah), Dr. Christopher Shaddix (Sandia)

July 2009

DOE Cooperative Agreement No.: DE-NT0005288

Reaction Engineering International
77 West 200 South, Suite #210
Salt Lake City, UT 84101
(801) 364-6925

University of Utah (Subcontractor)
1471 East Federal Way, Salt Lake City, UT 84102-1821

Sandia National Laboratories Combustion Research Facility (Subcontractor)
P.O. Box 969, Livermore, California 94551

Disclaimer

Abstract

This report summarizes Year 1 results of a research program designed to use multi-scale experimental studies and fundamental theoretical models to characterize and predict the impacts of retrofit of existing coal-fired utility boilers for oxy-combustion. Through the course of Year 1 activities, great progress was made toward understanding the issues associated with oxy-combustion retrofit of coal-fired boilers. All four Year 1 milestones and objectives have been, or will be, completed on schedule and within budget. Progress in the four milestone areas may be summarized as follows:

- University of Utah has performed size segregated ash composition measurements in the Oxy-Fuel Combustor (OFC). These experiments indicate that oxy-combustion retrofit may impact ash aerosol mineral matter composition. Both flame temperature and flue gas composition have been observed to influence the concentration of calcium, magnesium and iron in the fine particulate. This could in turn impact boiler fouling and slagging.
- Sandia National Labs has shown that char oxidation rate is dependent on particle size (for sizes between 60 and 100 microns) by performing fundamental simulations of reacting char particles. These predictions will be verified by making time-resolved optical measurements of char particle temperature, velocity and size in bench-scale experiments before the end of Year 1.
- REI and Siemens have completed the design of an oxy-research burner that will be mounted on University of Utah's pilot-scale furnace, the L1500. This burner will accommodate a wide range of O_2, FGR and mixing strategies under conditions relevant for utility boiler operation. Through CFD modeling of the different burner designs, it was determined that the key factor influencing flame stabilization location is particle heat-up rate. The new oxy-research burner and associated equipment is scheduled for delivery before the end of Year 1.
- REI has completed a literature survey of slagging and fouling mechanisms in coal-fired power plants to understand key issues influencing these deposition regimes and infer their behavior under oxy-fired conditions. Based on the results of this survey, an algorithm for integrating slagging predictions into CFD models was outlined. This method accounts for ash formation, particle impaction and sticking, deposit growth and physical properties and impact of the deposit on system flow and heat transfer. A model for fouling in the back pass has also been identified which includes vaporization of sodium, deposition of sodium sulfate on fly ash particles and tube surfaces, and deposit growth rate on tubes.

In Year 1, REI has also performed a review of the literature describing corrosion in order to understand the behavior of oxidation, sulfidation, chloridation, and carburization mechanisms in air-fired and oxy-combustion systems. REI and Vattenfall have met and exchanged information concerning oxy-coal combustion mechanisms for CFD simulations currently used by Vattenfall. In preparation for Year 2 of this program, two coals (North Antelope PRB, Western bituminous) have been ordered, pulverized and delivered to the University of Utah and Sandia National Labs. Materials for the corrosion experiments have been identified, suppliers located, and a schedule for equipment fabrication and shakedown has been established. Finally, a flue gas recycle system has been designed and is being constructed for the OFC.

Table of Contents

1 EXECUTIVE SUMMARY

The primary objective of this program is to utilize experimental data and theoretical models to develop tools capable of characterizing and predicting impacts of CO_2 flue gas recycle and burner feed design on flame characteristics, slagging, fouling, and corrosion inherent in the retrofit of existing coal-fired boilers for oxy-coal combustion. Results from the four Year 1 milestones are summarized below, along with some additional activities completed.

Milestone 1 – *Complete ash characterization and deposition measurements under oxy-coal conditions with pure CO_2 in lieu of FGR.* Initial ash characterization testing has been conducted on the University of Utah Oxy-Fuel Combustor (OFC). As of June 30, 2009, preliminary experimental tests have been completed that allow comparison between the size segregated composition of the coal ash aerosol formed under air combustion and that formed under two different oxy-coal combustion conditions. These tests yielded the very first data currently available on size segregated composition, particle size distributions, soot content, and overall loss on ignition of ash from air and oxy-coal combustion. Additional tests to be performed from August 1 through September 30 of this year will complete the baseline data for ash particle size, composition, and characteristics, with once through CO_2 from an external supply (no recycle). These additional tests will employ a newly designed swirl burner to allow similarly stabilized pulverized coal flames under three previously specified inlet oxidant conditions, namely, air, 32% O_2 in CO_2 and 27% O_2 in CO_2. Culmination of the described work will complete this milestone.

OFC results to date show that the major effects of oxy-coal combustion on ash aerosol composition occur in the fine particle, or sub-micron particle size range. The larger super-micron particle size distributions appeared to be similar for air-fired and oxy-fired combustion alike. The volatilities of calcium and other elements are affected by flame temperature, with maximum concentrations of sub-micron particles being observed for the test conditions with the highest (theoretical) flame temperature. Changes in combustion environment may also be important for particles of sub-micron size. There, the elements calcium, magnesium, and iron were all found in higher relative concentrations in the oxy-fired cases compared to the air-fired cases at the same adiabatic flame temperatures, while potassium and sodium were in relatively higher abundance in air-fired cases. If confirmed in future experiments, these results may have profound implications on the effects of oxy-coal retrofit on fouling and slagging.

Milestone 2 – *Complete baseline char oxidation experiments.* Char oxidation studies have been carried out at Sandia National Laboratories. The reacting particle simulation code known as SKIPPY (Surface Kinetics in Porous Particles) was used to investigate the influence of particle size on boundary layer reactions of pulverized coal char during oxy-combustion. These effects are not accounted for in current CFD models of coal combustion. The results suggest that boundary layer effects begin to be important for particle sizes greater than 60 micrometers and are greatest for particles around 75 micrometers in size. Particles larger than 100 micrometers burn close to the diffusion limit, therefore thermal feedback from the boundary layer conversion of CO has a diminishing impact on the char combustion rate. These results show that particle size has a strong influence on the relative importance of boundary layer chemistry to char combustion under oxy-combustion conditions for relevant coal sizes.

During the remainder of FY09, optical measurements of char particle temperatures, velocities, and sizes will be collected for the three different size cuts of each coal (Utah Skyline high-volatile bituminous coal and North Antelope PRB subbituminous coal) for background oxygen levels varying from 12 – 36%. These experiments will provide the necessary data for detailed analysis by SKIPPY in FY10. Furthermore, collection of partially reacted char particles will be performed, to provide direct measurements of char burnout and available surface area.

Milestone 3 – *Complete pilot-scale oxy-burner design, construction and delivery.* REI and Siemens have completed the oxy-research burner design for use in the L1500 pilot-scale furnace. The final fabrication blueprints were completed and transmitted to the burner and burner plate manufacturers on July 15, 2009.

The delivery of these items to the University of Utah is scheduled for September 21, 2009. The initial design of the oxy-research burner was based on a patented commercial-scale design by Siemens Energy Inc. This burner design was reduced to a 1.03 MW (3.5 MBtu/hr) firing rate using a constant velocity scaling technique. The initial design was evaluated and compared to operation of the existing L1500 low-NOx burner through CFD modeling. The modeling results suggested that the constant velocity scaling method did not produce the desired flame behavior for the burner. To correct this behavior, primary gas velocity was reduced, the quarl was lengthened and the burner face setback relative to the quarl was lengthened. These modifications produced the desired flame stabilization location.

The modeling results suggest that the dominating parameter governing flame shape and stability is not solely velocity. The flame behavior is closely related to particle heating rate, i.e., in order to maintain similar burner behavior when scaling a burner, the particle temperature profile should be maintained. The particle temperature profile is influenced by many factors including: gas velocity, radiation intensity, particle size and hot flue gas recirculation characteristics inside of the quarl. CFD simulations provided an excellent approach to evaluate the combined impacts of all of these factors.

Milestone 4 - *Complete Slagging and Fouling mechanism parameter development and validation.* A complete literature survey on slagging and fouling mechanisms in coal-fired power plants was performed, with the objectives of understanding the state-of-the-art and applying this to the combustion conditions that are expected in an oxy-combustion environment. Key issues identified that a fundamentally-based deposition model must address include: 1) ash formation, 2) fluid dynamics and particle transport, 3) particle impaction and sticking, 4) deposit growth as a function of location in the combustion chamber, 5) deposit properties and strength development, 6) heat transfer through the deposit, 7) the effect of deposition on combustion conditions (e.g., temperatures and heat fluxes), and 8) deposit structure and its effect on flow patterns in the furnace.

Based on these issues, a slagging modeling approach has been selected which utilizes both a comprehensive CFD combustion code and a slagging submodel and should be able to predict the deposit build up and strength development in the furnace. Also, a model for fouling in the back pass has been outlined which includes: vaporization of sodium during the combustion process, deposition of sodium sulfate on fly ash particles and tube surfaces, deposit growth rate on convective pass tubes. Coal combustion experiments under oxy-combustion conditions will be used to provide necessary inputs and/or validation of slagging and fouling submodels. Key experimental data needed (and planned) are the size distribution of fly ash and the amount of vaporization of individual species.

Additional Activities – The following additional activities were completed or are in progress:

- Completed review of corrosion mechanism literature; identified descriptions for oxidation, sulfidation, chloridation, and carburization mechanisms;
- Conducted a mechanism exchange meeting with Vattenfall personnel;
- Selected, ordered, pulverized and shipped two test coals (North Antelope PRB, Utah Skyline bituminous) to University of Utah and Sandia;
- Developed a schedule for ordering, manufacturing, delivering and shaking down corrosion monitoring equipment to be used in Year 2 testing on the L1500;
- Designed and in process of ordering equipment for OFC flue gas recycle system (to be installed for Year 2 testing on the OFC).
- Prepared and delivered timely quarterly progress reports to DOE;
- Promoted technology transfer by presenting program results at five conferences.

2 RESULTS AND DISCUSSION

The following sections describe on a task-by-task basis the work completed and work remaining for the first program year (October 1, 2008 through September 30, 2009). Emphasis is placed on results from work completed to date, i.e., through the end of June 2009. Tasks scheduled for work in year one include:

- Task 1 - Project Management and Planning
- Task 2 - OFC Preparation and Baseline Ash Characterization and Deposition Tests
- Task 3 - Baseline Char Oxidation Experiments
- Task 4 - Pilot-scale Burner Development
- Task 5 - Mechanism Exchange
- Task 6 - Slagging and Fouling Mechanism Review and Development
- Task 7 - Corrosion Mechanism Review and Development

2.1 Task 1 – Project Management and Planning

REI has coordinated project kick-off and review meetings with all subcontractors. An initial kick-off meeting was held in November 2009 with team members from University of Utah, Siemens, Sandia, Brigham Young University, Praxair and the DOE program officer, Timothy Fout, to review project objectives, team member roles, and program technical tasks and proposed approaches, with specific focus on first-year tasks. In order to save costs, Vattenfall from Sweden and Corrosion-Management from the United Kingdom did not attend this meeting. REI personnel met with Vattenfall in a separate meeting previous to the kick-off meeting (see Section 2.5) and with Corrosion-Management in March 2009 (while they were traveling to the U.S. on other business).

In addition to coordinating kick-off and review meetings, key management tasks accomplished during the first year include:

- Signing contract agreements with all subcontractors;
- Preparing and delivering timely quarterly progress reports to DOE;
- Participating in NETL CO_2 Capture Technology for Existing Plants R&D Meeting;
- Promoting technology transfer by presenting program results at the International Flame Research Foundation (IFRF) Topically Oriented Technical Meeting (TOTeM) on oxy-combustion, Electric Power Conference, EUEC Energy and Environment Conference, Clearwater Clean Coal Conference, IEA Oxyfuel Combustion Conference (planned);
- Conducting a mechanism exchange meeting with Vattenfall personnel;
- Overseeing review and development of slagging, fouling and corrosion mechanisms;
- Preparing facilities at the University of Utah and Sandia to begin experiments;
- Selecting, ordering, pulverizing and shipping two coals (North Antelope PRB, Utah Skyline bituminous) to University of Utah and Sandia;
- Developing a pilot-scale oxy-research burner design;
- Selecting a fabrication facility (PCW in New Jersey) to build the pilot-scale oxy-research burner;
- Developing a schedule for ordering, manufacturing, delivering and shaking down the corrosion monitoring equipment to be used in year 2 testing on the L1500;
- Designing and ordering equipment for Oxy Fuel Combustor (OFC) flue gas recycle system (to be installed for year 2 testing on the OFC).

2.2 Task 2 – OFC Preparation and Baseline Ash Characterization and Deposition Tests

2.2.1 Experimental Equipment and Materials

Combustor. All experiments were conducted on the Oxy Fuel Combustor referred henceforth as the OFC (see Figure 2.2-1). The OFC is a 100 kW furnace that burned coal at a feed rate of 4.54 kg (10 lbs) per hour. The furnace itself is refractory lined with electric wall heaters in the flame zone that keep the walls a constant temperature. There are numerous sampling ports and thermocouples allowing for temperature readings throughout the furnace, and the opportunity to sample from a variety of locations (see Figure 2.2-2).

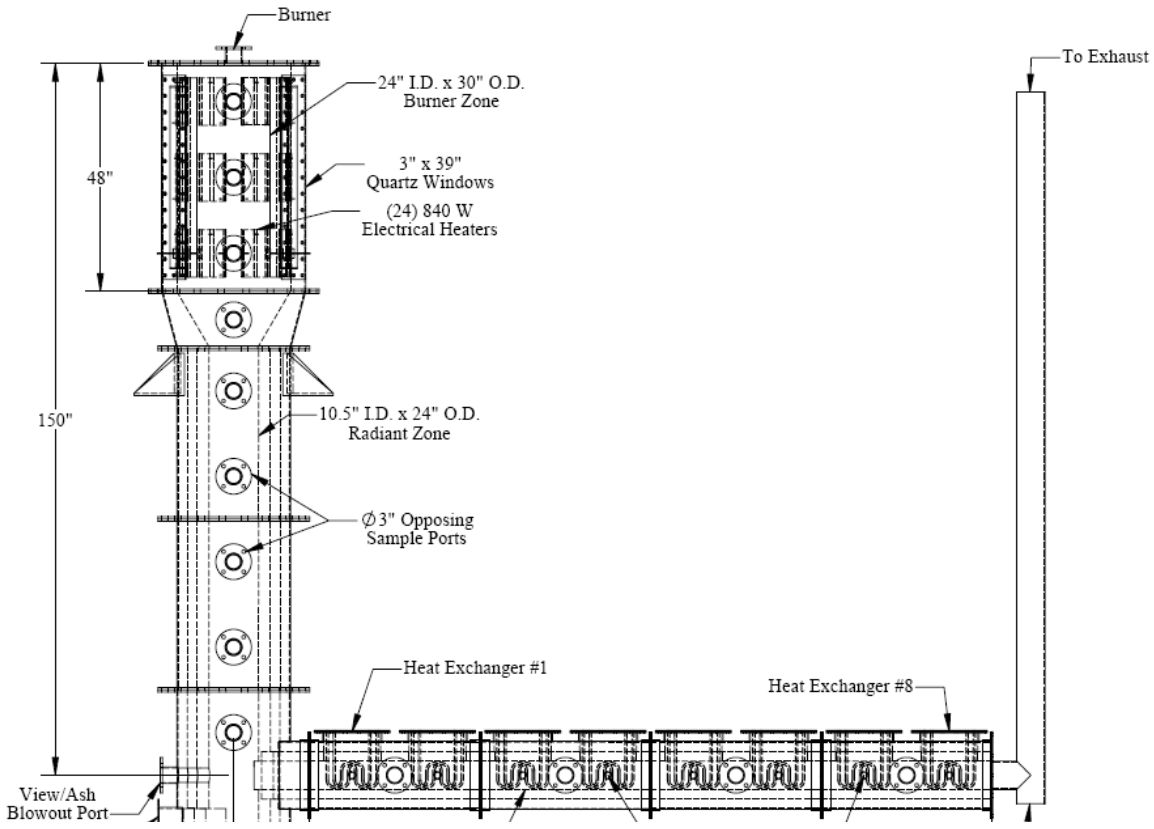

Figure 2.2-1. Schematic of overall OFC research facility (Zhang *et al*, 2009).

In these experiments, all sampling took place at the lowest sampling port before the flue gas was directed horizontally through the heat exchangers and then out the exhaust. This sampling location provided an easy work area with ample room to position equipment and was also at the same level as one of the thermocouples allowing for temperature readings of the flue gas as sampled.

Motive force for the flue gases is provided by an induced draft fan which provides the necessary suction to draw the flue gases out of the furnace. A damper can be opened to the proper using OPTO 22 controls to maintain the desired pressure within the furnace.

Coal Feeding System. The coal feeder is a K-Tron twin auger type feeder which has an operating range of 0-2,000 rpm and a feed rate of 0-9.08 kgs of coal per hour. In all tests, the coal was fed at a rate of 4.54 kg per hour corresponding to an indicated 1,000 rpm on the coal feeder motor. The coal was fed by the augers through a screen mesh to break up any large clumps of coal and facilitate steady feeding. The

coal is then fed into a plastic eductor where it is propelled by the primary air or a mixture of CO_2 and O_2 into the primary jet of the burner.

Figure 2.2-2. Top section of the OFC with wall heaters, refractory, and windows (Zhang *et al*, 2009).

The coal feeder is also on a set of rollers so that it may be adjusted to line the eductor up directly with the inlet of the coal burner. This proved to be critical for achieving a steady coal feed and stable flame without pulsing. It also allows the feeder to be rolled back away from the top of the furnace while running on natural gas in order to prevent heat damage to the feeder and the plastic eductor.

For combustion experiments, the wall heaters were set to a value of 1850 °F (982 °C, 1255K) to ensure consistent combustion conditions within the research furnace.

Air Delivery System. The air is delivered by a 25 horsepower Sullair compressor which provides compressed air through the workshop. The primary air and the secondary air are monitored and controlled by the use of calibrated mass flow controllers which are all controlled with OPTO 22 by a computer work station in the control room of the combustion laboratory. The primary air uses an HFC 202 S/N while the larger secondary flow requires an HFC 203 S/N. For air-fired combustion, primary air was fed at a rate of 4.59 kg or 10.1 lbs per hour and secondary air was fed at a rate of 43.5 kg or 95.8 lbs per hour.

O_2/CO_2 Delivery System. Both the O_2 and the CO_2 gases used in these experiments were generously provided by Praxair. Praxair also provided liquid storage tanks for both the CO_2 and the O_2. These tanks were both plumbed into the primary and secondary air lines for the burner and controlled through manual valves to select O_2 and CO_2 instead of air for combustion. The O_2 lines were cleaned and used materials specified by Praxair's safety recommendations in order to maintain a safe and consistent flow of O_2 for use in experiments.

The O_2 tank was specially constructed on a concrete drip pad for safety, and was surrounded by concrete pylons and a gated fence to prevent accidental damage or contact with the tank body, heat exchangers, valves, or regulators. All tank and valve adjustments were handled by Praxair service employees in order to ensure the safety of the students and staff members conducting research at the facility. Students do not make any adjustments with the tank, and should only operate the valve that allows oxygen to be fed to the

building. Any other adjustments and service were performed by Praxair technicians for safety reason. Any malfunction should immediately be reported to the laboratory manager and to Praxair.

The CO_2 tank provided the necessary dilution CO_2 for the combustion atmosphere under oxy-fuel conditions in the OFC. For all experiments contained in this body of work, the CO_2 in the combustion environment was once-through CO_2 from the liquid storage tank provided by Praxair. The CO_2 was not provided by recycled flue gas from the furnace itself as the intent of this research was to provide baseline data and insight into mechanisms of ash formation based on the difference of an O_2/N_2 air combustion environment, and an O_2/CO_2 combustion environment. Research involving recycled flue gas is currently being pursued.

The CO_2 is controlled by one master valve outside of the building adjacent to the tank. After it is opened, two valves must be switched in order for CO_2 to flow through the air lines. If this is not done, then air will continue to flow rather than CO_2.

It is very important that the O_2 flow be shut off from the furnace until the CO_2 flow through the furnace is established. Additionally, while changing from air delivery to O_2/CO_2 delivery, it is very important that flue gas oxygen analyzers are not sampling the flue gas as an oxygen free 100% CO_2 environment may damage the O_2 analyzer.

Burner Design. The preliminary ash aerosol experiments reported here were piggy-backed on other research in which flame stability was explored. These used an axial burner with no swirl, which had inherent flame stability limitations. All future ash aerosol work will use a new swirl burner that is inherently more stable. The burner was constructed from stainless steel. The burner consists of two concentric cylinders which comprise the primary jet, through which fuel and motive air or O_2/CO_2 and fed, and the secondary jet, through which the remaining air or O_2/CO_2 is fed to provide enough oxidant for combustion. The primary jet inner diameter measured I.D. = 18.57 mm, O.D. = 21.34 mm with a wall thickness of 2.769 mm. The secondary sleeve measured I.D. = 42.16 mm with a wall thickness of 3.556 mm. For more information see Zhang *et al*, 2009.

Coal. The coal used for these experiments was a Utah bituminous coal with the composition summarized in Table 2.2-1. The coal and ash analysis was performed by Huffman Laboratories, INC. 4630 Indiana Street Golden, CO. 80403.

Table 2.2-1. Utah coal and ash compositions.

Coal Analysis									
LOD	**Ash**						**Volatile**	**Fixed**	**HHV**
105 °C	**750°C**	**C**	**H**	**N**	**S**	**O (diff)**	**Matter**	**Carbon**	**BTU/lb**
%	%	%	%	%	%	%	%	%	
3.03	11.71	66.28	4.63	1.23	0.38	13.07	38.81	46.44	11731

Ash Analysis										
Al	**Ca**	**Fe**	**Mg**	**Mn**	**P**	**K**	**Si**	**Na**	**S**	**Ti**
as Al_2O_3	as CaO	as Fe_2O_3	as MgO	as MnO	as P_2O5	as K_2O	as SiO_2	as Na_2O	as SO_3	as TiO_2
%	%	%	%	%	%	%	%	%	%	%
13.3	11.75	5.06	2.88	0.05	0.3	1.49	52.37	1.44	2.44	0.65

Flue Gas Analysis. In order to verify correct combustion conditions, stoichiometric ratios, and flame consistency, several flue gas analyzers were used in order to provide the necessary information regarding the combustion environment and flame characteristics. Two analyzers were used for recording concentration of oxygen in the flue gas. One was a Yokogawa Zirconium Oxide instrument and the other was a Horiba O_2 MPA-510. Three analyzers were used for measuring CO_2 concentrations. The first analyzer, a ZRH infrared CO_2/CO by California Analytical Instruments, was used for air-fired combustion and measured concentrations of less than 20% by volume. It was also used to monitor CO in the 0-1,000 ppm range. The second analyzer, another a ZRH infrared CO_2/CO by California Analytical Instruments, was used for Oxy Fuel conditions and could measure CO_2 up to 100% concentration and CO in terms of percent volume. The third CO_2/CO analyzer, California Analytical Instruments ZRE CO_2 Gas Analyzer, was easily calibrated and set up for both air and oxy-conditions and was used as a second back up analyzer in either condition.

In addition to the O_2 and CO_2/CO analyzers, an NO/NO_2 and an NO analyzer were also utilized to monitor combustion conditions. The NO/NO_2 analyzer, Thermal Environmental 42 CHL, and the NO analyzer, Horiba NO CLA 51055, were both calibrated using an NO in N_2 standard for air-fired calibrations and an NO in CO_2 standard for oxy-fired calibrations.

Particle Probes and Sampling Systems. Two particle probes were used to draw samples for the experiments performed in this research. The first probe utilized was very simple and did not utilize dilution. It featured a 1" pipe which was measured to be 7/8" inner diameter. This was then sleeved by 1.5" tubing to form a water jacket to keep the probe cool. It was used in order to take a total ash sample for the loss of ignition measurements. The experimental set up is shown in Figure 2.2-3.

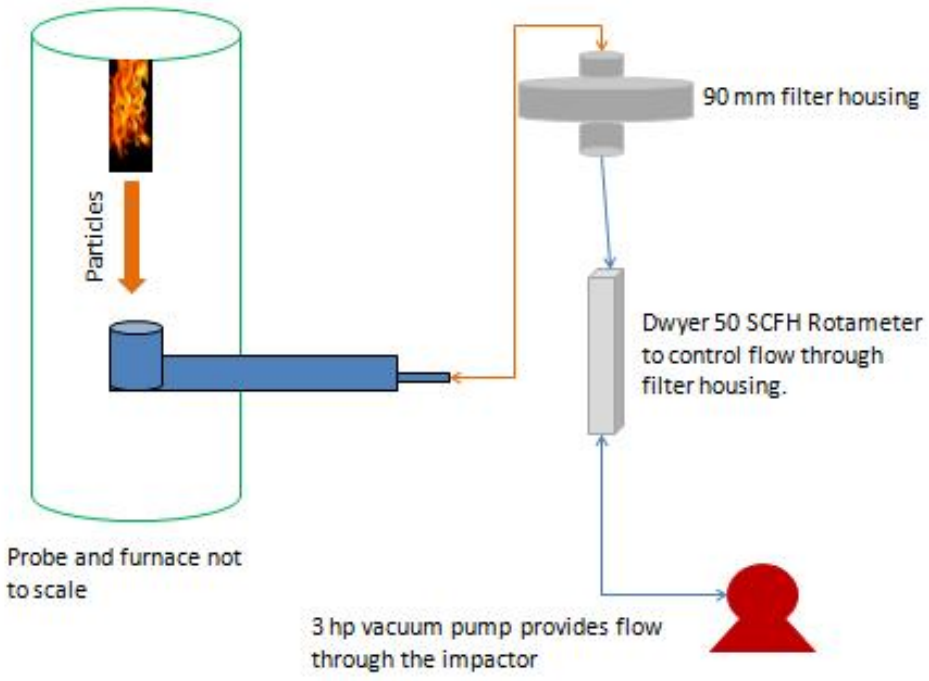

Figure 2.2-3. Schematic of sampling for LOI experiments.

In order to collect the samples, there had to be a filter housing which enclosed the filter, a vacuum pump to provide vacuum to draw the sample out of the furnace, and a rotameter to control the flow. The rotameter was a 50 SCFH unit from Dwyer. The amount of flow through the probe, which was to be as close to isokinetic as possible, was determined using the following equations from Hinds, 1999.

$$\frac{Q_s}{Q_0} = \left(\frac{D_s}{D_0}\right)^2 \qquad \textbf{(2.2-1)}$$

$$U_s = U_0 \qquad \textbf{(2.2-2)}$$

Where Q_s is the volumetric flow rate of the sample in the probe of diameter D_s and Q_0 is the volumetric flow through a circular duct with a diameter D_0. As a result, the velocity of the bulk gas in the duct is the same as the sample velocity in the probe.

The velocity given for air-fired conditions ranged between 2.30ft/s (0.701m/s) to 2.45ft/s (0.747m/s) as the temperature of the flue gas varied from 1100°F (593°C) to 1200°F (649°C). This velocity can be calculated knowing the known inner diameter of the furnace, the known temperature of the gas from a thermocouple reading, the known flue gas composition and coal firing rate, and the ideal gas law. The ideal gas law has been deemed sufficiently accurate for air pollution sampling (de Nevers, 2000). The air-fired cases required a flow rate through the probe of 34.5 to 36.5 cfh or about 16.3 to 17.3 lpm for air-fired conditions. These calculations can be repeated to show the flow needed for oxy-fired condition as well which turn out to be about 11.5 lpm for Case 3 and 9.2 lpm for Case 4. As particles deposited on the filter, the rotameter valve could be opened further to allow continuing sample flow through the probe and filter.

The second probe utilized in these experiments was brought from the University of Arizona and had been used in DOE sponsored research there (see Figure 2.2-4). This probe utilizes a stainless steel water jacket as well as a having a nitrogen jet at the tip of the probe allowing for dilution of the sample as well as quenching reactions and reducing the amount of coagulation of small particles (Hinds, 1999). This probe was used for all SMPS, PA, and BLPI data collection. The probe had a measured inner diameter of 0.265” or 6.73 mm.

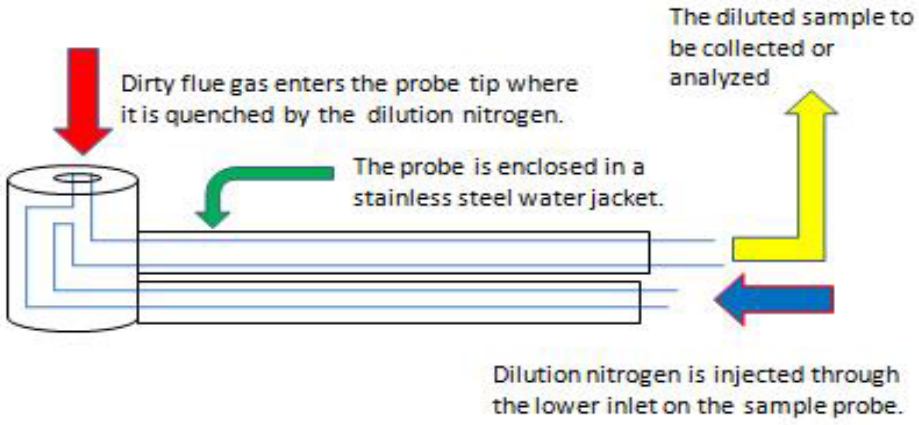

Figure 2.2-4. Schematic of dilution sampling probe illustrating concentric tubes for the water jacket with a nitrogen feed for dilution at the tip to dilute the outgoing sample.

When setting up the sampling system for photo acoustic and SMPS analysis or for sample collection with the impactor, the dilution probe was used in conjunction with a mass flow controller that metered the rate of dilution nitrogen into the sampling probe. It was found that at the controller manufacturer's recommended ideal operating feed pressure of nitrogen, the flow of nitrogen pulsed wildly through the probe due to the complicated bends of the nitrogen inlet near the probe tip. As a result, the inlet pressure of nitrogen to the mass flow controller was reduced from the recommended 85 psi to 45 psi to provide a steady flow.

The equipment set up for use with the SMPS and PA was rather involved (see Figure 2.2-5). The dilution probe was used with a mass flow controller to meter the amount of nitrogen from either a cylinder or a liquid nitrogen Dewar. The sample was withdrawn from the probe using an eductor which utilized clean dry motive air, which was then used for sample dilution. The motive air is supplied by compressed air which is filtered through progressively smaller particle filters and oil and water separators to protect the mass flow controller which regulates the amount of motive air to the eductor. The motive air is then finally sent through HEPA filters to ensure a clean dilution stream. The dilution at the probe tip and then at the eductor resulted in a compound dilution, which was important to remember when calculating data.

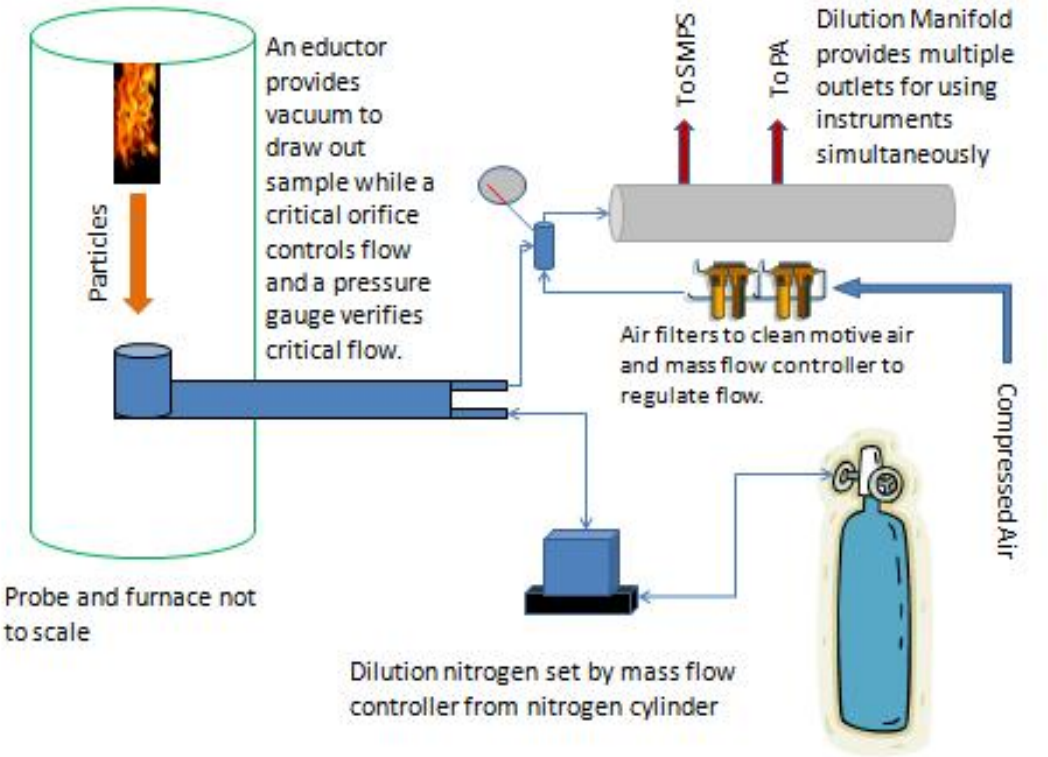

Figure 2.2-5. Diagram showing the sampling set up used for SMPS and PA analysis.

Flow through the probe is controlled by a critical orifice from O'Keefe controls that was measured to have a flow rate of 8.45 lpm using a Gillibrator bubble flow meter. A pressure gauge also verified the necessary 2:1 pressure drop across the orifice necessary to maintain constant choked flow.

After flowing through the critical orifice and eductor, the diluted sample stream was sent into the dilution manifold. The dilution manifold consists of a large tube with several sampling ports. As a result, it is possible to operate the SMPS and the PA simultaneously; however they will be operating at the same

dilution, which proved not to be ideal for this range of experiments. The following diagram illustrates the previously described instrumentation and sampling set up.

The setup used for sampling with the Berner Low Pressure Impactor (BLPI) was less complicated than the sampling system necessary for the PA and SMPS. It simply utilized the dilution probe with nitrogen from a cylinder or dewar controlled by the mass flow controller. The diluted sample was then sent through the BLPI while a 3 hp vacuum pump provided the necessary vacuum to create choked flow through the impactor where the last stage acts as a critical orifice. The flow through the impactor was measured with a Gillibrator bubble flow meter at 24.1 lpm. This was used in conjunction with the amount of dilution nitrogen to determine the dilution ratio of sample in flowing through the impactor.
A diagram of the BLPI sampling set up is shown in Figure 2.2-6.

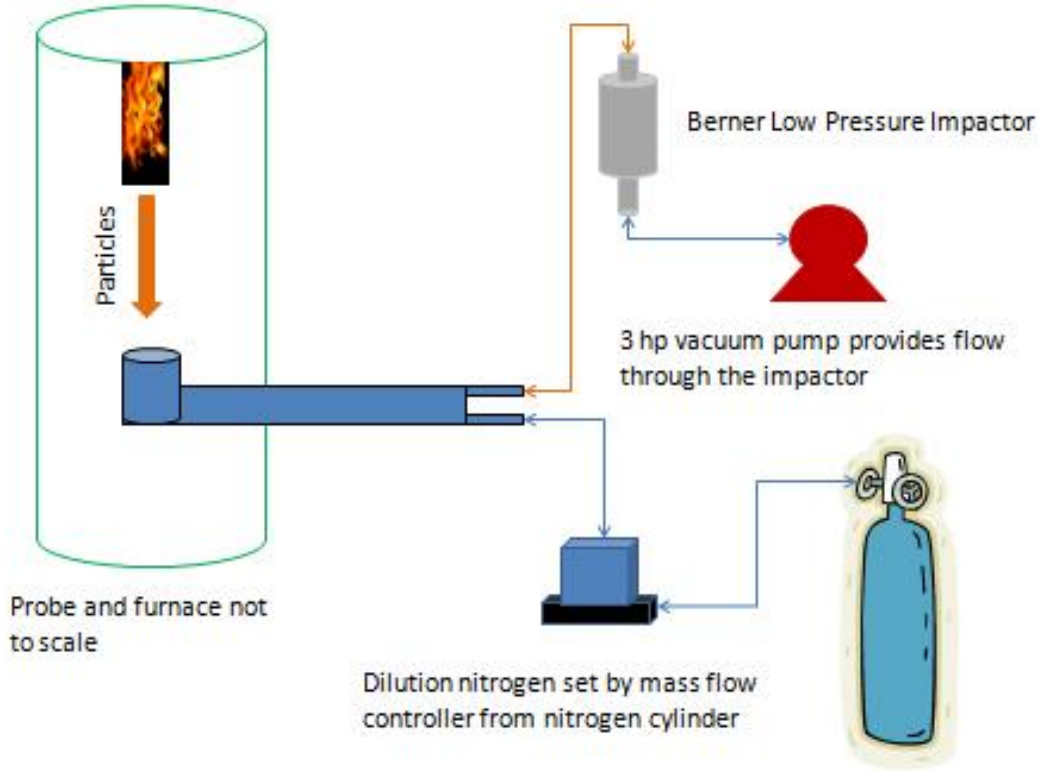

Figure 2.2-6. Sampling diagram for BLPI sample collection.

Particle Sizing and Analysis Instrumentation. A wide variety of equipment was used for particle analysis. A Scanning Mobility Particle Sizer, referred to as a SMPS, was used in order to determine the particle size and mass distribution for particles in the 15-660 nanometer (0.015-0.660 μm) range. The SMPS was a TSI 3080 classifier with a 3081DMA using a 3022A CPC model. The SMPS was used in conjunction with the dilution manifold and is controlled with a desktop PC work station using proprietary TSI Aerosol Instrument Manager (AIM) software. The data is saved as raw scans, and then must be exported as a tab delimited text file which can be opened in Excel for analysis.

Along with the SMPS, the particle stream was analyzed by a Photo-acoustic Analyzer referred to as the PA, which utilized as laser tuned to black carbon in order to measure the concentration of soot and pure black carbon particles found in the flue gas. For a detailed description of the instrument and its

verification, see Arnott *et al*, 2005. The PA, like the SMPS was controlled by a desktop PC. However, the PA is controlled through a Labview software interface. The PA continuously analyzed the particle stream and did not collect data as discrete scans. Instead, it collects a data point every 6 seconds. Using the Labview software, a selection switch exists that will allow for recording of the data as tab delimited text file that can be opened in Excel. Labview will only record data when this is selected.

Along with the SMPS and PA, a Fossil Energy Research HFLOI loss on ignition (LOI) instrument was used in order to gravimetrically determine the LOI of total ash samples that were collected during the experiments. LOI was measured for both oxy- and air-fired conditions at varying stoichiometric ratios. The instrument comes with a very easy to follow instruction manual and includes a feature for drying samples before they are analyzed. This proved to be valuable as with the water cooled sample probe, there was no way to maintain the sample temperature above the boiling point at the filter housing.

Samples that were collected to be analyzed for chemical composition were collected using a Berner Low Pressure Impactor (BLPI). The BLPI is a low pressure cascade impactor that size segregates particles to be collected for analysis. It has a much wider sub micron range than many other impactors, and suffers less from orifice clogging than does the Moody Impactor. Also, it contains midway a stage that acts as a critical orifice to maintain constant flow through the impactor, regardless of the downstream vacuum, provided the vacuum pump is large enough to maintain a pressure below that required from the critical pressure ratio. Figure 2.2-7 illustrates the eleven stages of the impactor including their aerodynamic cutoff particle diameters in microns. A three horsepower vacuum pump is used to provide the necessary vacuum to create critical flow through the impactor which remains constant. The BLPI consists of 11 different stages. Each stage has a different %50 aerodynamic cut off diameters. The cut off diameters are 0.030, 0.060, 0.090, 0.170, 0.340, 0.540, 0.980, 1.98, 3.77, 7.33, and 15.7 microns.

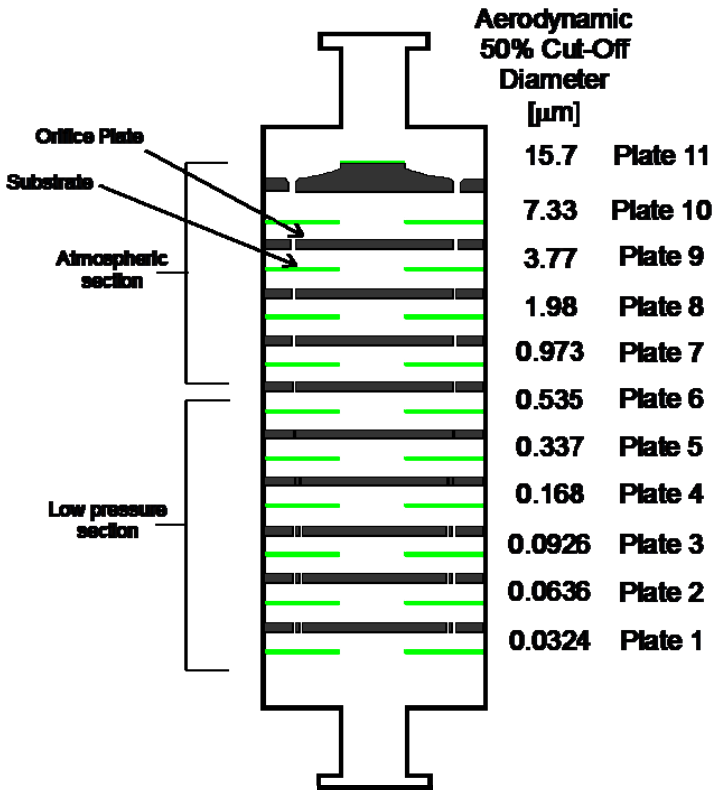

Figure 2.2-7. Berner Low Pressure Impactor cross-section illustrating the number of stages as well as the particle diameter range for each given stage.

Ash samples were taken to Enviropro Laboratories LLC in West Valley City, Utah. There, they were acid digested and analyzed with a Perkin Elmer ICP-OES to give elemental concentration. The samples were prepared using EPA method SW846 3050A and analyzed using EPA method 6010B. Samples were also collected using the BLPI for SEM/EDS analysis to be completed in-house. This was deemed especially necessary for Si analysis, which requires a special HF acid digestion and expensive consumable parts for an analytical instrument as a result.

2.2.2 Experimental Methods

Experimental Conditions. Three conditions were examined. For brevity, these are henceforth labeled Case 1, Case 3 and Case 4. These three cases represent air combustion, oxy-combustion with enough once-through CO_2 to maintain the same adiabatic flame temperature, and another hotter oxy-coal flame. In this work, the first two flames (Case 1 and Case 3) were both detached, the last (Case 4) was attached. Future work will employ only swirl based attached flames. Below are the conditions for each of the three cases.

Air-fired Condition:

- "Case 1"
- Conditions:
    - 10 lbs per hour of coal
    - 10.1 lbs per hour of primary air
    - 95.8 lbs per hour of secondary air
    - 20.9% O_2/79.1%N_2
    - Adiabatic flame temperature: 3853 °F (2123°C, 2396K)
    - Lifted air-fired axial diffusion flame

Oxygen-fired Conditions:

- "Case 3"
- Conditions:
    - Coal feed rate of 10 lbs per hour
    - 12.2 lbs per hour CO2 and 2.3 lbs per hour O_2 primary
    - 62.0 lbs per hour CO2 and 22.2 lbs per hour O_2 secondary
    - 31.2% O_2/68.8% CO_2 (average inlet oxidant, primary contained 21% O_2)
    - Adiabatic flame temperature of 3849 °F (2121°C, 2394K)
    - Lifted oxy-fired axial diffusion flame
- "Case 4"
- Conditions:
    - Coal feed of 10 lbs per hour
    - 12.2 lbs per hour CO2 and 2.3 lbs per hour O2 primary
    - 38 lbs per hour CO2 and 22.2 lbs per hour 02 secondary
    - 40.0% O_2/60% CO_2 (average inlet oxidant, primary contained 21% O_2)
    - Adiabatic flame temperature of 4576 °F (2524°C, 2797K)
    - Attached oxy-fired axial diffusion flame

Furnace temperature profiles for the three cases are shown on Figure 2.2-8 below. There are some accuracy problems with these measurements. The upper three are from Type K bare, thermocouples protruding into the gas near the wall, while the bottom three are Type B ceramic encased thermocouples, protruding well into the gas stream, but operating well below their optimum temperature range. Future research will ensure an accurate temperature profile.

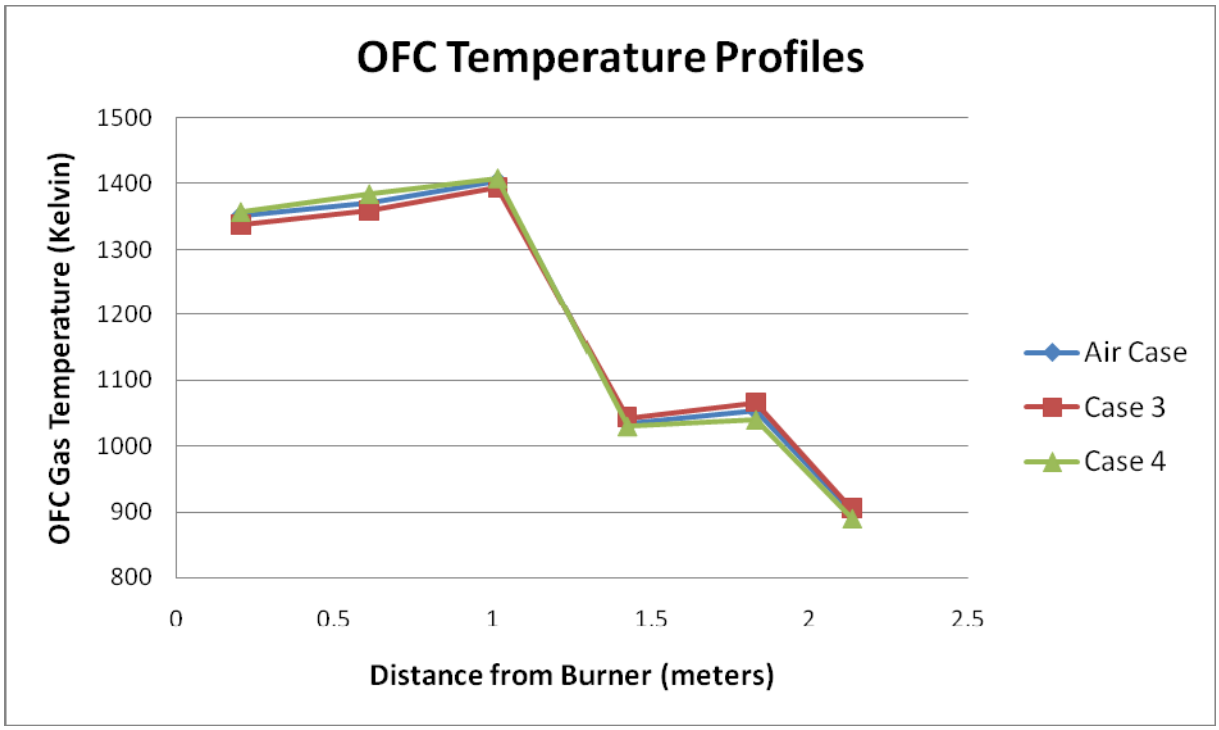

Figure 2.2-8. OFC temperature profiles for the three cases considered.

Experimental Methods – LOI The Loss on Ignition (LOI) tests were the first tests completed in this research. They allowed for insight into the performance and efficiency of the furnace as well as providing a relatively easily sampling procedure to practice sampling techniques for pending research. In each test, a vacuum pump was utilized to pull samples through the probe which was inserted in the lowest sampling port on the OFC. The vacuum pump pulled through a filter housing containing a cellulose acetate filter (Advantec grade: C045A090C 0.45 micron 90 mm diameter) which was contained in a 90 mm filter housing. Flow through the probe was controlled by a Dwyer rotameter in order to control the flow to maintain sampling as close to isokinetic as possible. Samples were collected on the filter paper for 30 minutes to ensure significant loading on the filter paper. A minimum of two pieces of filter paper were collected for each stoichiometric ratio to allow for four different samples to be analyzed for LOI for each specific case. The samples were collected on the filter paper and then transferred to glass sample vials. The ash was then analyzed in the Fossil Energy Research designated weigh boats using the Fossil Energy Research HFLOI. In the case of air, the stoichiometric ratios of 1.15, 1.1, 1.05, and 1 corresponded to 3.00%, 2.00%, 1.00% and 0.00% oxygen in the flue gas respectively. While this was obtainable down to 1.00% oxygen, it was not possible to accurately measure 0% oxygen in the flue gas as this condition would ruin the zirconium oxide element in the oxygen analyzer used to monitor flue gas oxygen concentration. As a result, considerable uncertainty surrounded the sampling of for LOI at the stoichiometric ratio of 1.00.

The stoichiometric ratios of the oxy-cases were also given as 1.15, 1.10, 1.05, and 1.00. However, the oxygen cases had higher concentrations of oxygen for a given stoichiometric ratio than the air-fired cases. As a result, the results are later presented based upon both stoichiometry and percent O_2 in the flue gas. Again, due to the limitations of the oxygen analyzer, it was not possible to precisely measure the oxygen down to a concentration of 0.00%, and thus a great deal of uncertainty resulted at that value.

Experimental Methods – SMPS. The SMPS required the use of significant dilution in order to bring the number or particle counts within operating range of the instrument. This was achieved with nitrogen dilution at the tip of the probe using an up to 50 liter per minute mass flow controller, which was calibrated using a Gillibrator bubble flow meter, to meter a specified flow from a compressed nitrogen gas cylinder or a liquid nitrogen Dewar. Of particular importance was that in order to use the mass flow controller with the dilution probe, the inlet pressure on the mass flow controller had to be reduced to 45 psi in order to provide steady flow. The flow was then validated using a Gillibrator bubble flow meter to ensure accurate recording of the amount of actual dilution nitrogen dilution in the probe. In order to provide enough data for averaging of scans to provide a smooth curve and mass distribution, up to twenty scans were taken of air-fired combustion on testing days. This ensured that there would be sufficient data even after erroneous scans were aborted or discarded due to unexpected or unintentional interruptions of the steady state combustion process. Also, the concentrations of flue gas O_2, CO_2, NO, and NO_2 were monitored to verify that scans were occurring during consistent combustion conditions. Tests were also performed on different days to address repeatability and consistency of data and combustion experimental conditions. Experiments were conducted on two separate occasions at least a week apart.

The dilution manifold uses an eductor to create the necessary suction to draw the samples through the probe and then the motive air from the eductor is used to dilute the sample as it is driven into the dilution manifold. The motive air is controlled by a calibrated mass flow controller, and the flow through the sampling probe is determined using a critical orifice available from a complete set from O'Keefe controls. This sampling set up was also utilized in all photo-acoustic experiments where the dilution manifold fed samples for both the SMPS and the photo-acoustic analyzer.

Using the sampling methods and probe equations described above, the sampling rate was kept as close to isokinetic as possible. However, due to small fluctuations in furnace operation as well as small errors in the calibration curves, the calculated ideal isokinetic sample flow rates of 0.8 to 1.5 lpm through the probe entrance were at times too small to be determined with great precision. As a result, the dilution was set such that the flow of the sample into the probe entered at 2 to 3 lpm in order to achieve consistent, uninterrupted flow as close to calculated isokinetic conditions as possible, with the result that some of the larger particles (> 5μm) may be lost.

For the oxy-coal combustion runs, the stoichiometric ratio of 1.15 was matched to that of the air case, rather than the O_2 concentration in the flue gas.

Experimental Methods – Photo-acoustic (PA) Black Carbon Measurements. PA experiments were conducted to measure the concentration of black carbon or soot particles found in the flue gas. These experiments were conducted to provide insight on soot formation differences between O_2/N_2 environments and O_2/CO_2 conditions. The PA experiments were conducted simultaneously with SMPS experiments using a dilution manifold which allowed up to three instruments to receive and analyze the sampling stream simultaneously.

The PA is controlled by the same PC work station as the SMPS, but is controlled through a different Lab View program specific to the PA. Instead of individual scans with the SMPS, the PA continuously takes data at a rate of one reading per six seconds. It was also run on different days and scans of several minutes were taken while collecting the SMPS data. PA scans are recorded by Lab View as a tab delimited text file which can then be imported into Microsoft Excel for analysis. The PA has been tested and validated during experiments involving diesel combustion and jet engine applications (Arnott *et al*, 2005).

The PA measurements are important because they determine what fraction of the ultrafine particles is composed of soot. Soot is not measured by any other technique other than LOI, which also includes char.

Experimental Methods – Berner Low Pressure Impactor (BLPI) Measurements. Samples deposited on BLPI plates were collected and analyzed in order to obtain size segregated ash aerosol composition under air and oxy-coal combustion conditions. This sampling and analysis technique is at the heart of this project, and required significant effort to be made to work smoothly and reliably.

The size segregated partitioning experiments were conducted utilizing the dilution probe, with nitrogen for the dilution, and a Berner Low Pressure Impactor referred to as a BLPI for particle size segregation. The flow through the impactor was measured using a Gillibrator bubble flow meter in order to determine the precise flow through the BLPI, 24.1 lpm, so that the dilution of the sample would be known.

Two BLPIs were required. One BLPI used a pre-separator cyclone to remove the large particles and allow for collection of ultrafine particle samples on Stages 1-5. Otherwise the upper plates would be overloaded, and particle bounce-off could not be avoided. These samples were collected over a time interval of 20 minutes. For the larger diameter particles, a BLPI was used without the cyclone and only sampled for five minutes to prevent particle overloading of the (upper) Stages 6-11.

Each stage was covered by a substrate on which the particles impacted. Two separate types of filters were used as substrates in the BLPIs. Each was tested for background contamination. Filter 1 was an expensive filter which was more difficult to digest, but much easier to handle. It is ideal for taking samples for SEM/EDS analysis. The specifications for Filter 1 are: Millipore Durapore Membrane filter Type 0.22 μm, catalog number: GVHP09050. Filter 2 was most economical and easier to acid digest and had specifications: Millipore Isopore membrane filter type 0.4 um catalog number: HTTP09030.

The filters are used on plates where samples were to be collected for analysis. On plates where samples were not be collected when sampling for short times, aluminum blanks were used. When using the cyclone, the upper stages 6-11 used aluminum blanks.

Substrates of 90 mm diameter to fit the BLPI impactor plates were made from the filter material and were cut out using a razor knife on a clean glass background. Those made of aluminum were cut out in the same fashion. The filters and blanks were then tacked into place on a piece of cardboard and then air brushed with a mixture of Fischer Scientific brand HPLC grade hexane and Apezion H grease. The grease mixture is approximately 15 grams of grease per liter of hexane. A light even coat should be applied to the substrates. The substrates should then be dried in an oven at no higher than 50°C for 12 hours and then placed in a desiccator overnight before use (Seames, 2000). The following day the substrates and blanks may be used to collect samples with the BLPI.

Collected samples were acid digested and analyzed using ICP-OES in order to provide elemental concentrations for the following elements, Si, Al, Fe, K, Mg, Ca, Na, Se, and As.

2.2.3 Results and Discussion

LOI Results. The averages of the loss of ignition results are presented Figure 2.2-9 below. The LOI results showed that the combustion furnace provided very complete burnout at SR>1.10, leaving behind a very limited amount of unburned char in the fly ash.

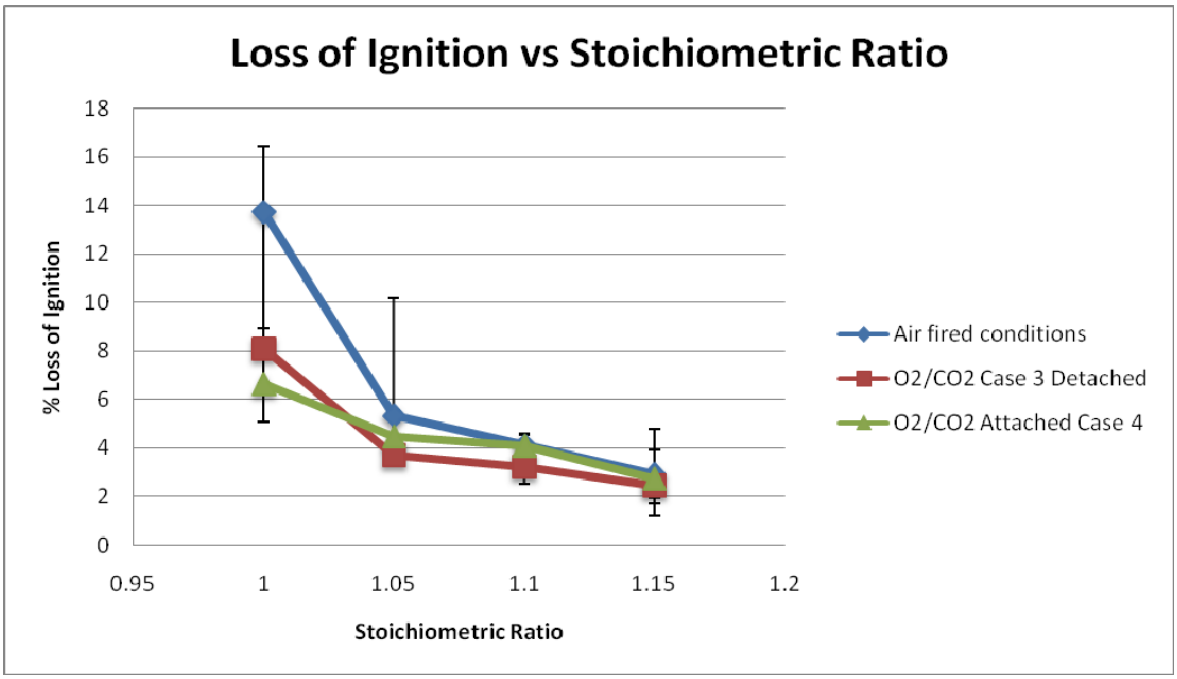

Figure 2.2-9. Averages of % LOI for all combustion scenarios.

Because of issues with the Zirconium Oxide oxygen analyzer, the results for a stoichiometric ratio of 1.00 are subject to substantial error, since the SR value had to be estimated from inlet flow rates, rather than flue gas O_2 concentrations.

While the oxy-cases have the lowest average ignition loss based upon stoichiometric ratio, they also have the highest concentrations of oxygen. The case 3 scenario is 31.2% oxygen while the Case 4 scenario is 40.2% oxygen. This is consistent with other drop tube experiments which found that in order to achieve the same burnout performance of an O_2/N_2 combustion environment, there must be a greater percentage of oxygen in the O_2/CO_2 environment (Borrego and Alvarez, 2007).

While the oxy-cases have lower average LOI, the most interesting result is that the Case 4 combustion scenario, which is a much higher percentage of oxygen, seems to have greater ignition loss than did the Case 3 combustion scenario, though the results are within the error limits. There are several possible mechanisms that may account for this, and they all have to do with enhanced mixing of the fuel and gas mixtures in Case 3.

It is useful to compare results at similar value of percent O_2 in the flue gas, since this does not necessarily translate to similar values of stoichiometric ratio. This comparison is shown on Figure 2.2-10 below. Note this is for once through CO_2 as the diluent, not recycled flue gas containing mainly CO_2.

For the two oxy-coal flames, at a constant O_2 value, any beneficial effect due to the higher temperature is overwritten by the slower mixing for the attached flame. At 3% O_2 in the exhaust, the air and matched oxy-coal flame have the same LOI. At lower flue oxygen values the oxy-coal flame may have lower LOI than the air flame, although any differences measured are within the error bars.

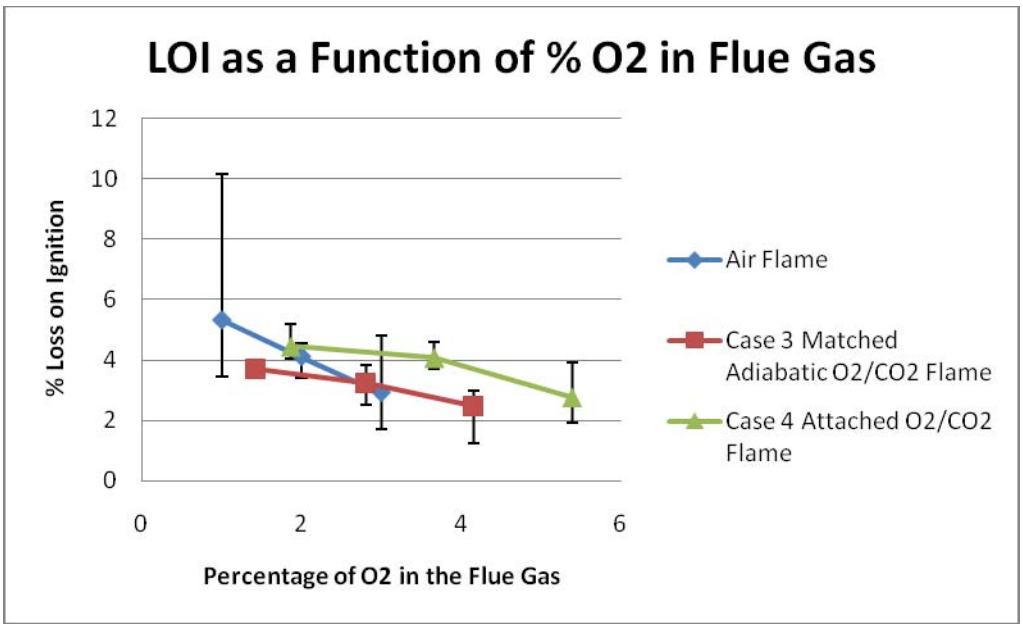

Figure 2.2-10. LOI as a function of $\%O_2$ in flue gas.

Scanning Mobility Particle Sizer (SMPS) Results. The SMPS counts particles in a dilute stream, one at a time, and places the number counts in closely and evenly spaced particle size bins based on electrical mobility, where each bin size corresponds to a range of particle sizes. It is assumed that each particle carries only a single charge. The SMPS measures particle size distributions in the 15nm (0.015μm) - 660nm (0.6μm) and thus focuses only on the ultra-fine, vaporization mode of the fly ash aerosol. Since the number particle size distribution is quite different from the mass particle size distribution (of interest to engineers), both are given here. Number size distributions are very much weighted towards the tiniest particles, which may be large in total number but tiny in aggregate mass.

Figure 2.2-11 shows a typical number distribution as delivered by the instrument, after accounting for sample dilution (number particles/cm^3 of flue gas) for ultrafine ash aerosols with a lower diameter cut-off at 15nm. The ordinate has been calculated in differential form, so that the area under the curve provides the number of particles between two particle sizes. The abscissa uses a log scale in order to accommodate a wide particle size range. This method of plotting aerosol particle size distributions is common in presenting aerosol PSD data. The ordinate has been scaled by a factor of 10^6 (the conversion from cm^3 to m^3), yielding ultrafine number concentrations in the flue gas of the order of ~1-10 particles/m^3, which is line with literature values.

The mass particle size distribution is given in Figure 2.2-12, together with error bars. The curve provides the average over all of the collected scans and shows how the ultra fine fume of condensed vapor particles occurs in the region of less than 30 nm particles and then tapers off until the mass increases again as the next mode becomes apparent. This proved to be a similar distribution to the matched adiabatic flame temperature oxy Case 3. However, there were some issues with the SMPS results. As one can see based upon the scan of the raw data, the number of counts is many orders of magnitude higher for the ultra fine particles than for the comparatively large sub micron particles in the half micron range. Consequently, there were a low number of counts for larger diameter particles. But, due to the higher percentage of mass of these particles, they have a very significant affect on the mass distribution. The result is that when the scans are averaged to give the mass distribution, there is irregularity in the larger particle size range because there are very few particles counted and thus the statistics are not as optimal. In the future

work, there will be many more scans which are averaged to find the mass distribution rather than the ten scans used here.

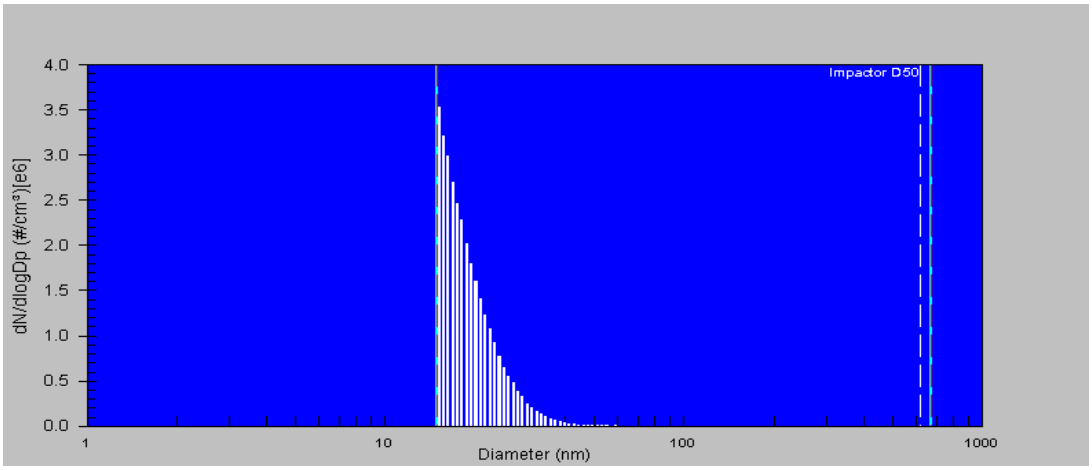

Figure 2.2-11. Sample SMPS scan for air-fired conditions.

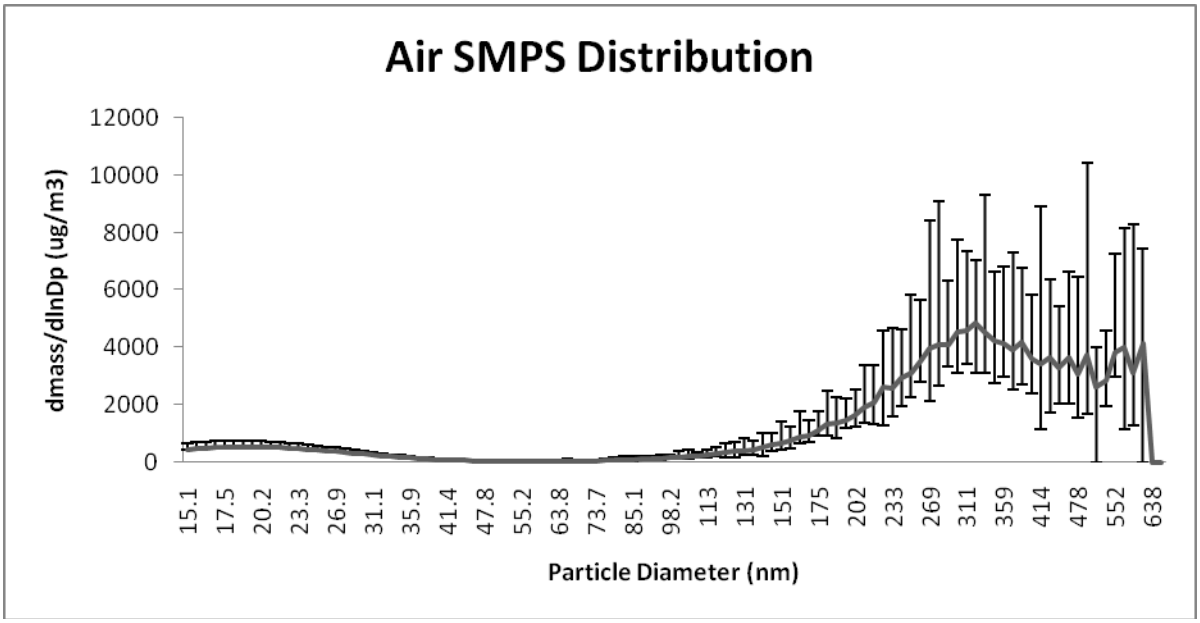

Figure 2.2-12. Average air-fired mass distribution for 15-660 nm particle diameter.

Figure 2.2-13 shows the analogous ultrafine particle number size distribution for Case 3, the oxy-coal case with the same adiabatic flame temperature. The particle number distribution appears to be similar to that of the air case (Figure 2.2-11).

While the distributions are similar, they are not identical, with the oxy-case showing a small shift in the mass PSD shape of the ultrafine flume to a particle diameter of a few nanometers larger. The oxygen-fired Case 3 data is shown on Figure 2.2-14.

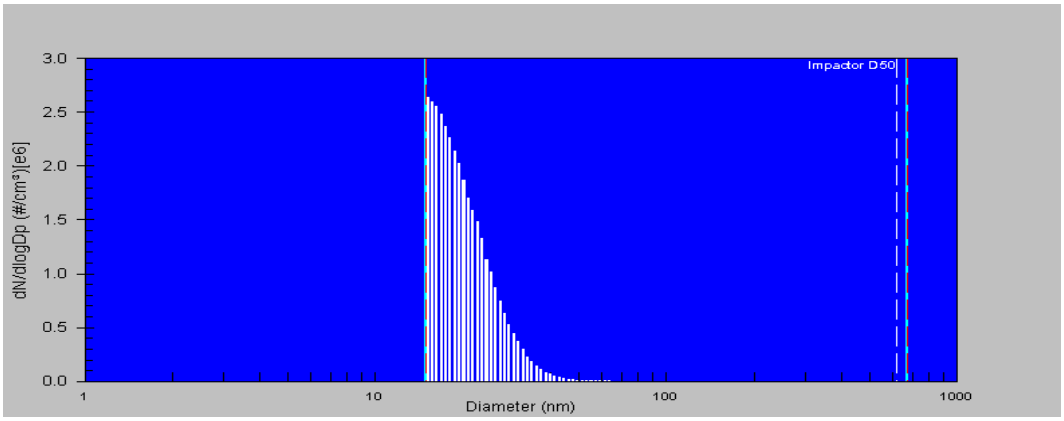

Figure 2.2-13. Sample of Case 3: O_2/CO_2 fired SMPS scan.

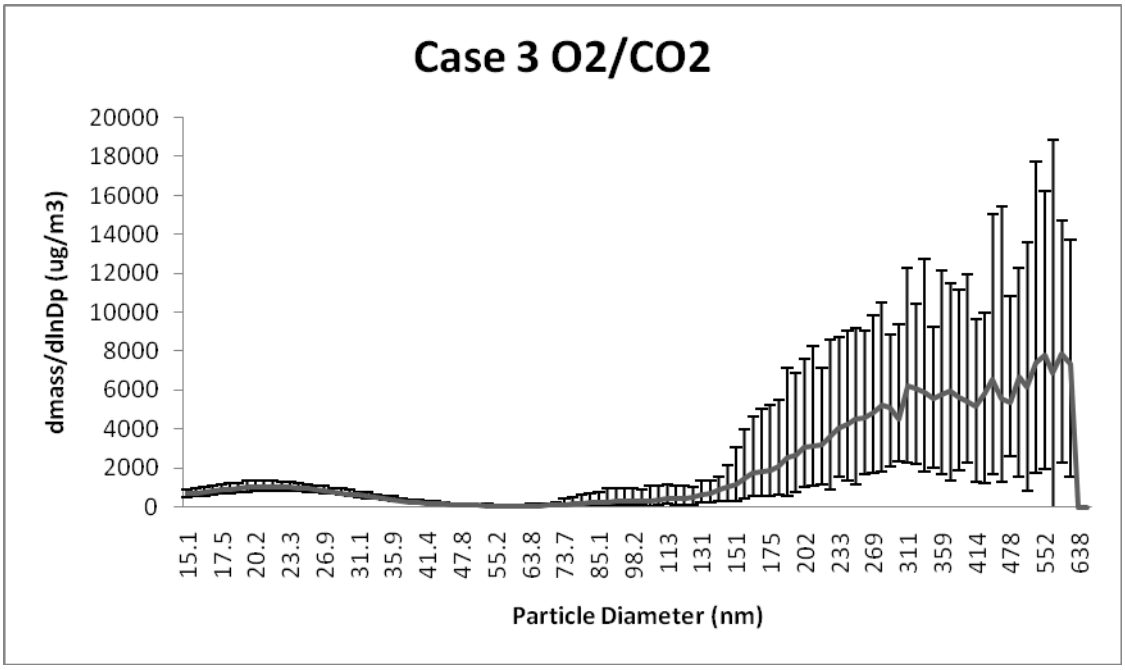

Figure 2.2-14. Averaged SMPS mass distribution of Case 3 oxy-fired conditions.

The discontinuous nature of PSD plot for the larger particle diameter region is due to the dilution required for the small diameter particles and the large differences between numbers of small particles and numbers of large particles. The dilution necessary to bring the number of small particles in range reduces the number of large particles that are counted. As a result, subtle differences in the number of larger particles that are counted, and which bin they are placed can result in a significant shift in mass. This is why collecting a larger number of data sets to be averaged is important to produce a continuous curve, and this will be done for subsequent experiments.

For Case 4, the high temperature, oxy-coal attached flame, there was a significant difference in the SMPS results. This was most likely due to the increased flame temperature and higher concentration of particles per m^3 of flue gas due to the lower volume of combustion flue gas. Both processes would facilitate greater coagulation among the smallest particles. This is clearly evident in the SMPS scans that were collected, summarized in Figure 2.2-15.

Increased amounts of sub-micron particle fume results from greater vaporization of metals at the very much higher (theoretical) flame (temperatures (2524°C versus 2121°C). This, together with a smaller volume of flue gas, and increased residence times, increases coagulation rates, as shown on Fig 2.16, leading to a coarser, but still ultrafine, fume at ~40nm (0.04μm).

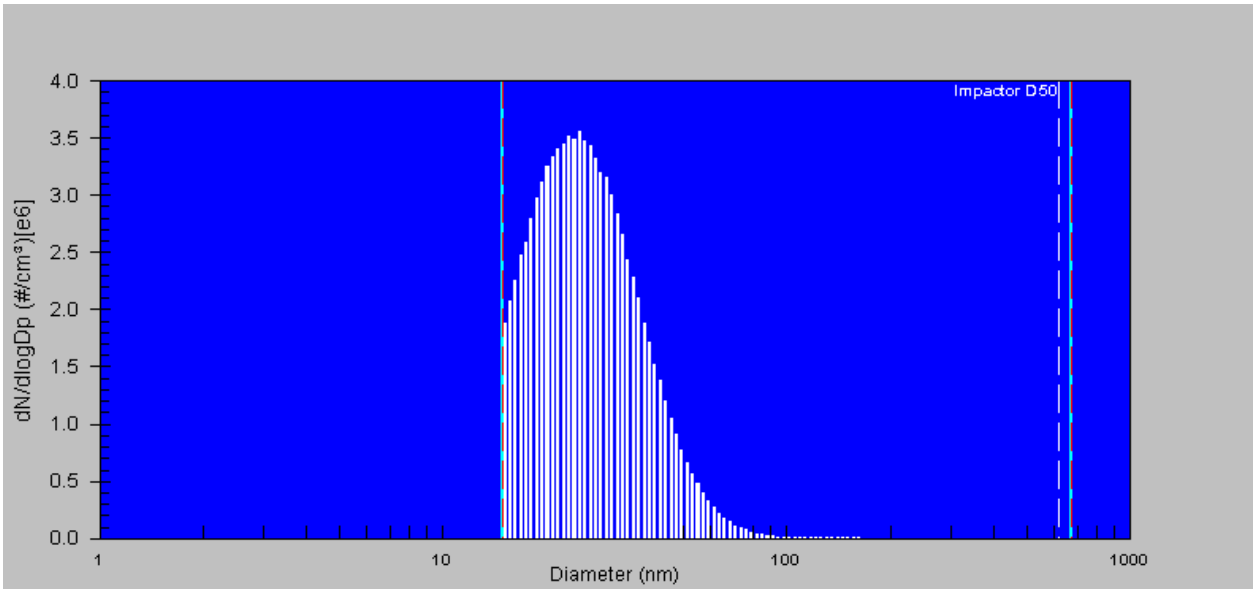

Figure 2.2-15. Sample SMPS scan of Case 4 conditions.

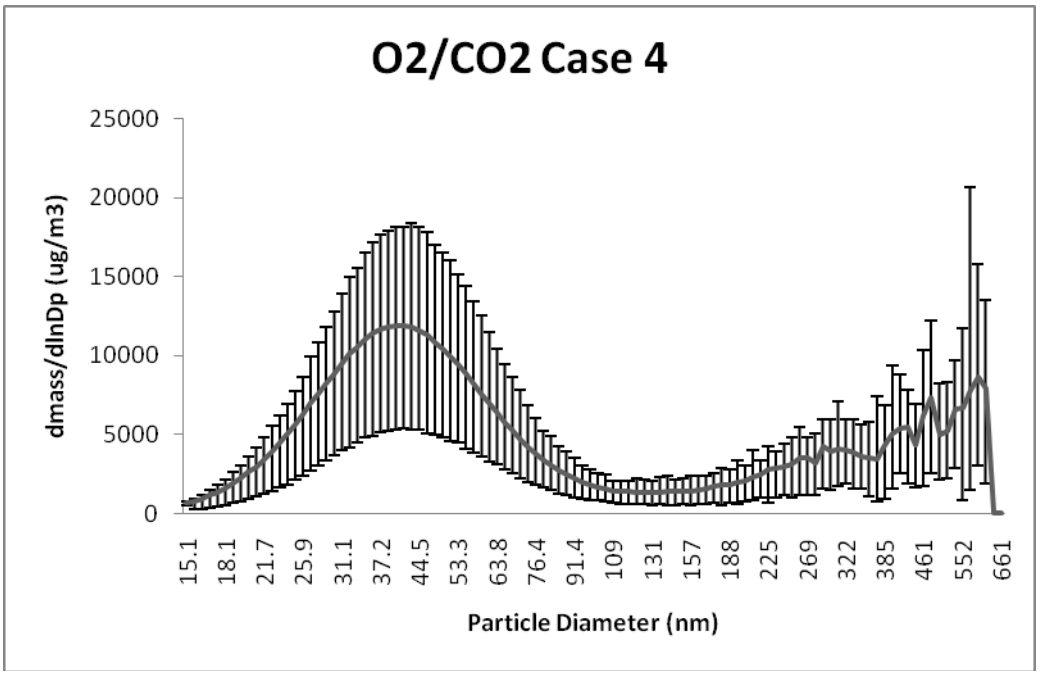

Figure 2.2-16. Averaged SMPS mass distribution for higher temperature Case 4 oxy-fired conditions.

Photoacoustic Black Carbon Results. The PA was utilized at the same time and the same dilution as the SMPS. Its value lies in its ability to detect the presence of soot among the ultrafine particles measured by the SMPS. Due to the very low LOI in all combustion cases at stoichiometric ratio 1.15, and the LOI would contain soot, if present. At the very high dilutions needed to operate the SMPS, the PA was reading at or near its detection limits during the duration of the experiments for air combustion and oxy-fired combustion cases. Although definitive conclusions could not be drawn, Figure 2.2-17 does show the same general trend found in the LOI experiments. The Case 3 scenario has the lowest average black carbon content for stoichiometric ratio of 1.15 while Case 4 and air are somewhat similar.

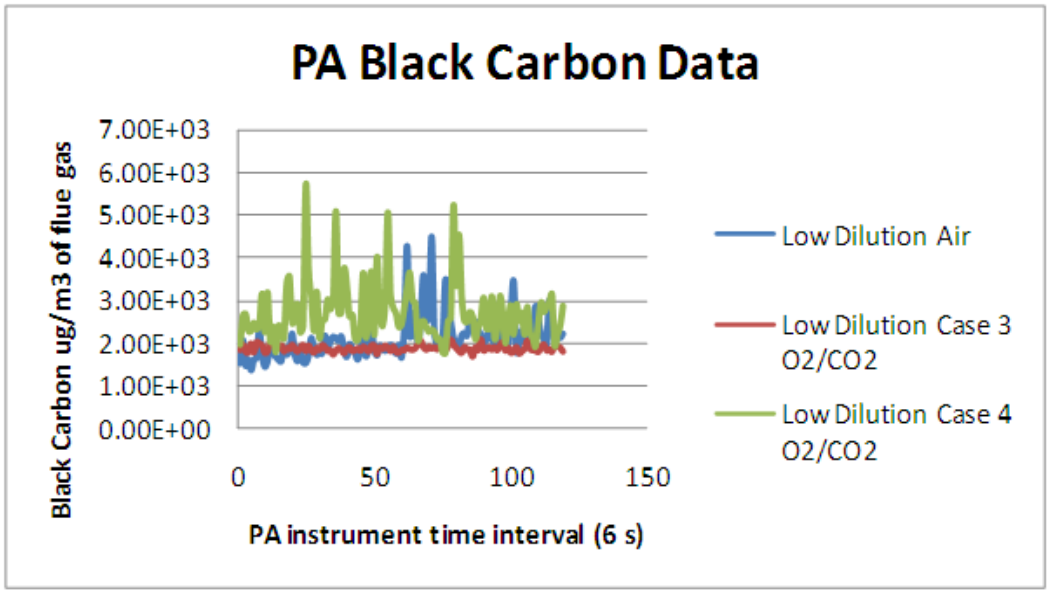

Figure 2.2-17. Sample of results from photo-acoustic experiments with air dilution ratio 88:1, Case 3 dilution ratio of 88:1, and a Case 4 dilution ratio of 124:1.

BLPI Results: Size Segregated Fly Ash Composition**.** The Berner Low Pressure Impactor (BLPI) collects the fly ash aerosol on eleven plates, distributed between 30nm (0.03µm) and 16000nm (16µm). The following elements were chosen for analysis: Si, Al, Fe, Mg, K, Ca, Na, Se, and Ar. Arsenic and Selenium, however, proved to be below detection limits in all cases due to the low sample mass available for digestion.

Particle composition was determined by two methods. The first method, using acid digestion and ICP-OES was completed off-campus. We believe the Si values for this to be in error for reasons described below. The second method employed University of Utah in-house SEM-EDS facilities. Comparison of results from both methods is currently in progress, and results of those comparisons will be reported later. At this point in time we believe that each method has strengths and weaknesses, and that ultimately a combination of both methods will be used. Each BLPI run consists of two replicates, with the average and the range reported. Runs that suggested inaccuracies due to contamination, particle bounce-off, or other causes have been discarded.

Silicon did not completely dissolve in the solution prescribed by EPA Method SW846 3050A indicating the need for the SEM-EDS data for accurate silicon concentration. As a result, it is not possible to discern definitive conclusions from the plot of silicon relative to the other elements as shown in the following figures. This is because the acid digestion may have been more effective on the particles of smaller

diameter rather than larger diameter, resulting in a somewhat skewed relative weight percentage. The relative weight percentage of silicon, shown on Figure 2.2-18, is the mass of Si (not the oxide) divided by the sum of the masses of all other elements (not their oxides) measured.

As expected the silicon concentration trails off at low particle diameters which would be part of the fume. Where the lack of digestion is more apparent is the larger particles on the upper stages where the silicon concentration falls off. This is most likely an error due to the poor digestion of silicon. The differential Si mass concentration plots are given on Figure 2.2-19. In Figure 2.2-19, it can be seen that the total silicon mass increases with particle diameter under all combustion scenarios before falling off towards the last stage of the impactor. This however matches the tri-modal distribution described as consisting of an ultrafine fume, fine fragmentation at 2 microns, and then a larger bulk fragmentation mode which is present at larger than recorded particle sizes (Seames, 2003).

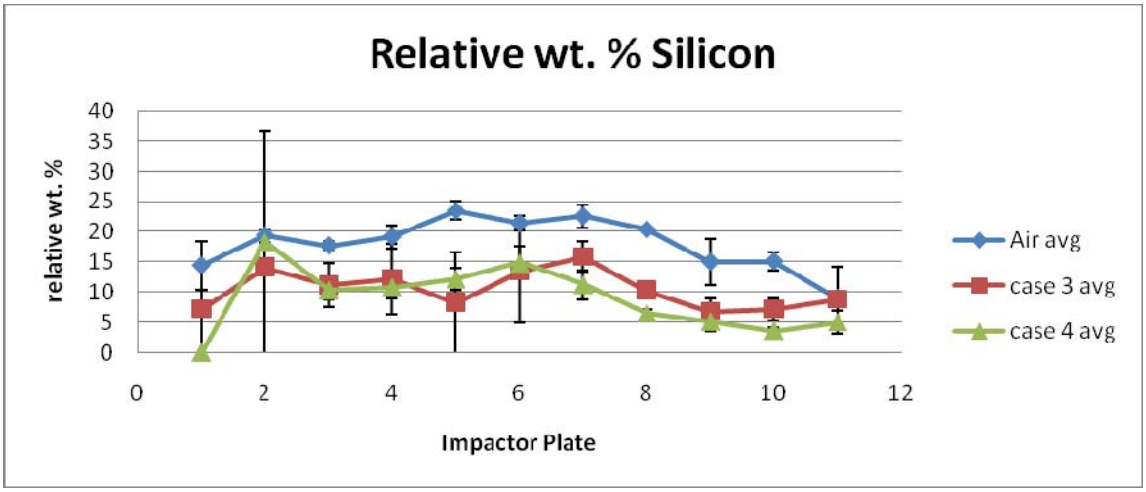

Figure 2.2-18. Averaged relative weight percentage of silicon.

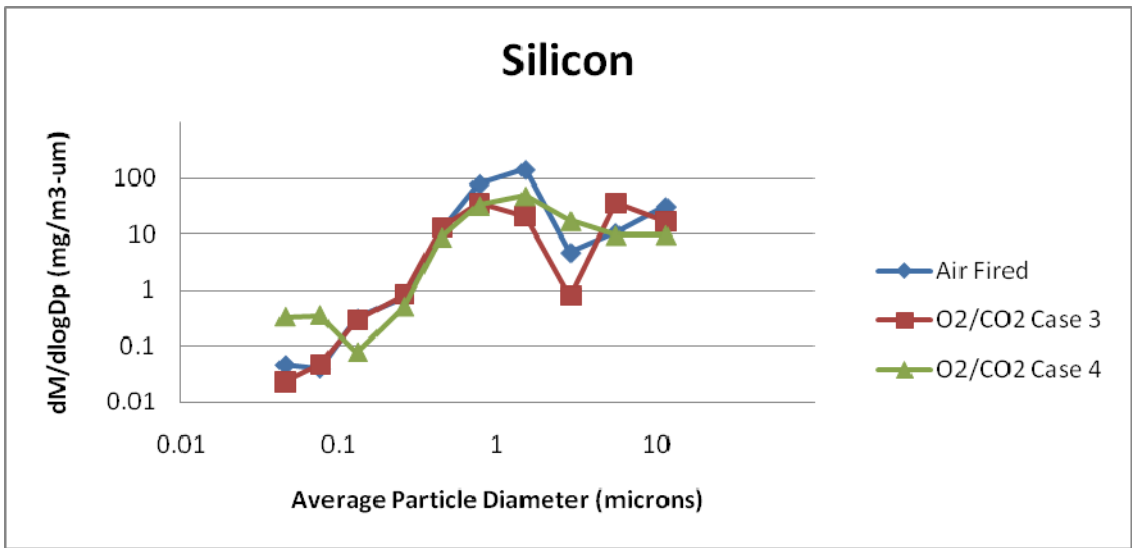

Figure 2.2-19. Differential mass of elemental silicon in terms of mg per standard cubic meter of flue gas.

The aluminum data (see Figure 2.2-20) show a similarly expected decrease in concentration at low particle diameters due to the high volatilization temperature of aluminum. The outlier point for the bottom impactor plate for Case 4 is suspected to be the result of contamination as it occurred in only one of the sample runs in the Case 4 results. The overall concentrations of aluminum seem to be consistent without discernable differences between oxy-fired conditions and air-fired conditions. This would indicate that using once through CO_2 instead of N_2 in the combustor does not significantly affect the distribution of aluminum in the particles of the size range of interest. Moreover the size segregated distribution of aluminum in the flue gas (Figure 2.2-21) is very similar for air fires and the two oxy-coal fired cases.

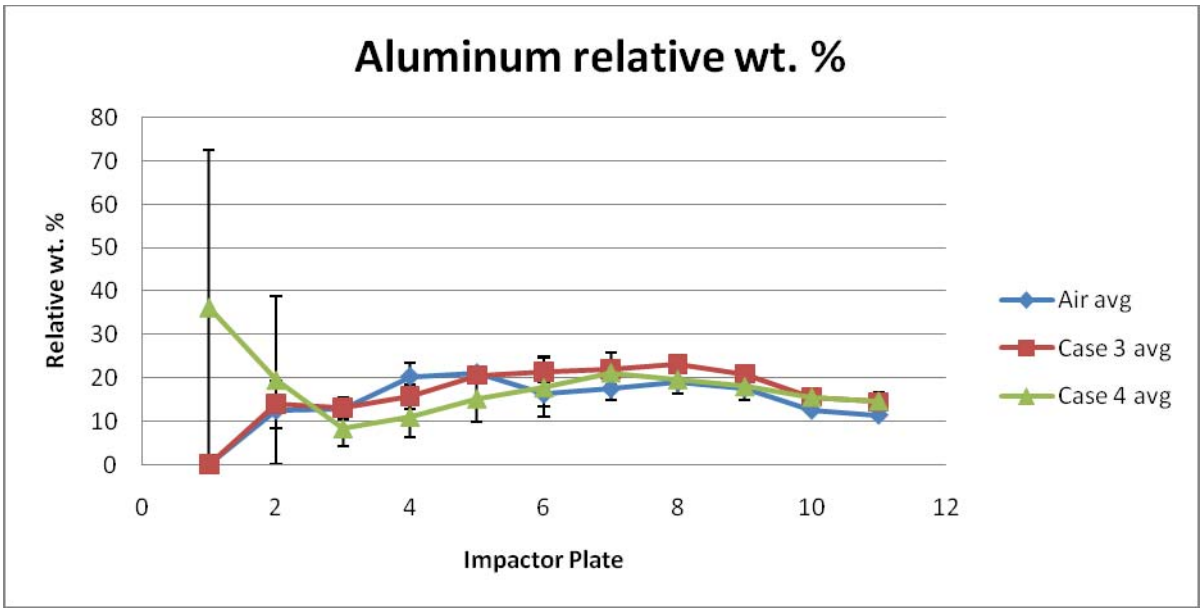

Figure 2.2-20. Average relative weight percentage of aluminum.

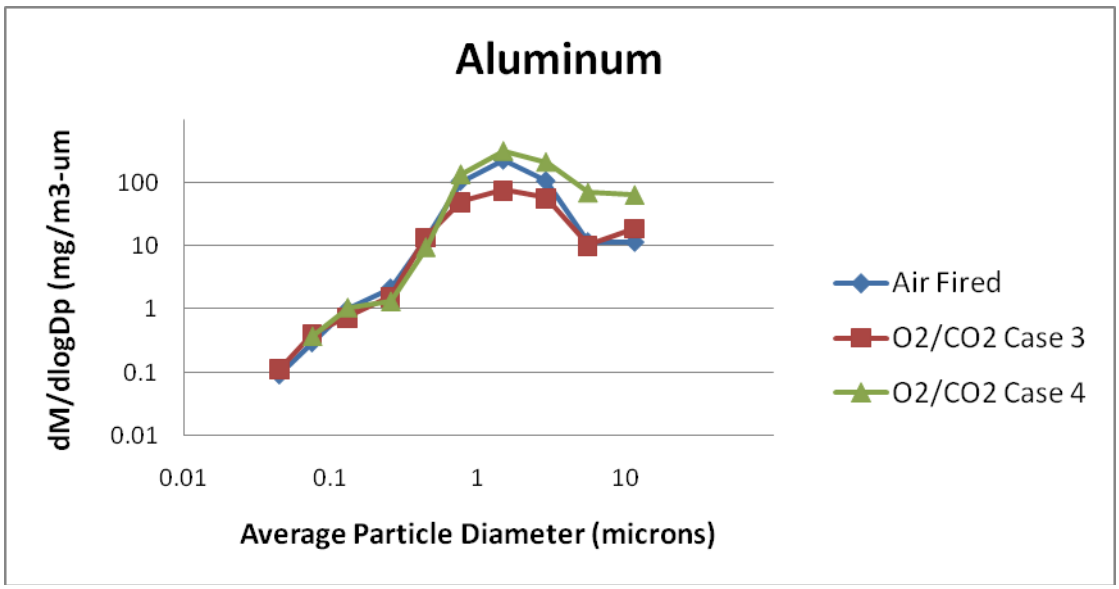

Figure 2.2-21. Differential mass of elemental aluminum per standard cubic meter of flue gas as a function of particle diameter.

Figure 2.2-22 shows that while the percentage of iron in the smallest particles is much higher for the high flame temperature oxy-fired Case 4, the relative weight percentage of iron appears to be higher across nearly all of the sub micron range for the oxy-fired cases than the air-fired cases. This indicates that the change in combustion environment may have an impact on the mechanisms which form particles containing iron. The finding is significant since particles containing iron are more likely to form slag deposits within the furnace.

Figure 2.2-23 also shows that the overall mass of iron in the fly ash increases in the middle mode of the particle size distribution. For the very large particles, where the bulk of the ash mass is concentrated, it again appears that the overall particle distribution is similar between the air-fired and the oxy-fired conditions. Figure 2.2-23 also shows that the Case 4 combustion scenario leads to a greater concentration of elemental iron per cubic meter of flue gas because there is a lower volume of flue gas due to the high oxygen concentration and reduced injection of CO_2.

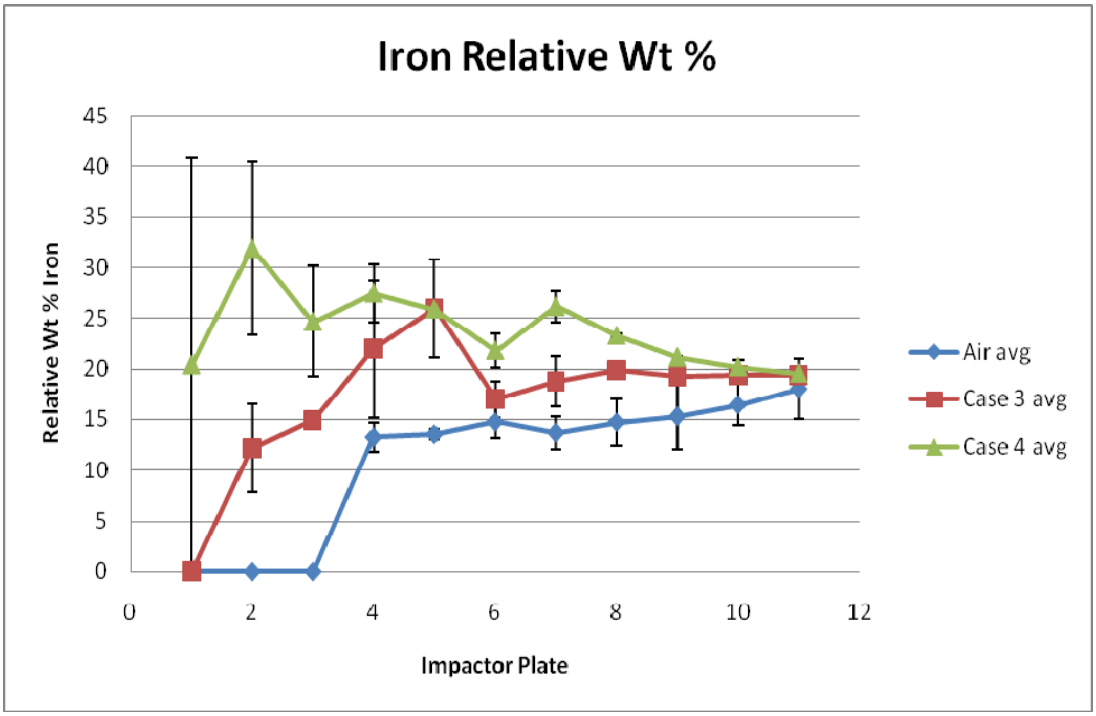

Figure 2.2-22. Averaged relative weight percentage of iron in fly ash.

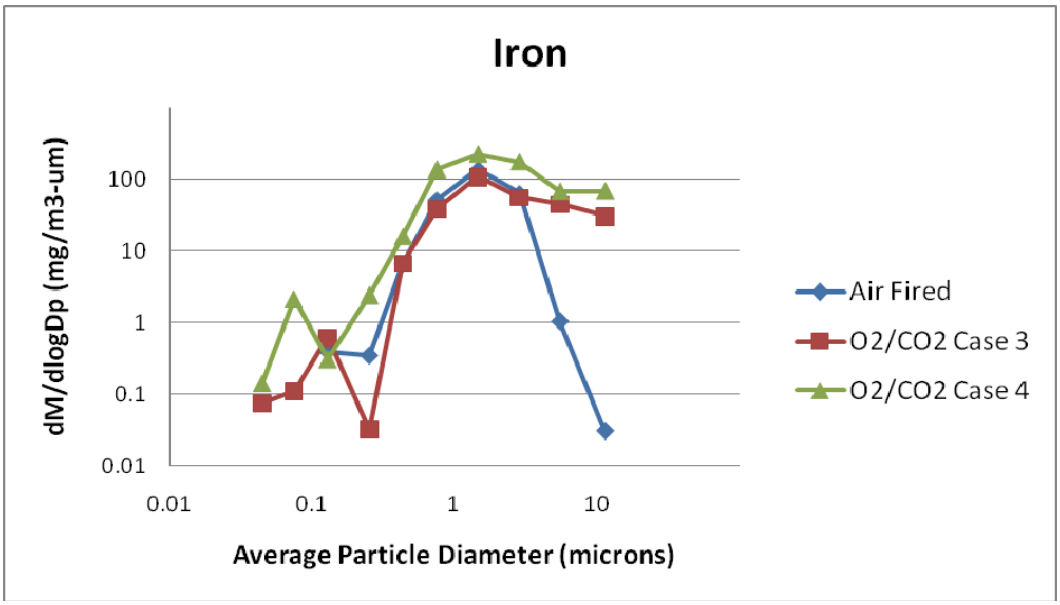

Figure 2.2-23. Differential mass of elemental iron per cubic meter of flue gas as a function of particle diameter. The first two points of air-fired combustion are omitted due to being below detectable limits and the issues with plotting zeros on a log scale.

Magnesium is another species which was not present in high enough amounts to be above detectable limits for all samples. Figure 2.2-24 suggests that the significantly higher flame temperature of the Case 4 oxy-fired scenario affects volatility of magnesium compounds in the combustion environment, as the relative percentage of magnesium is a factor of two higher than in the other combustion scenarios.

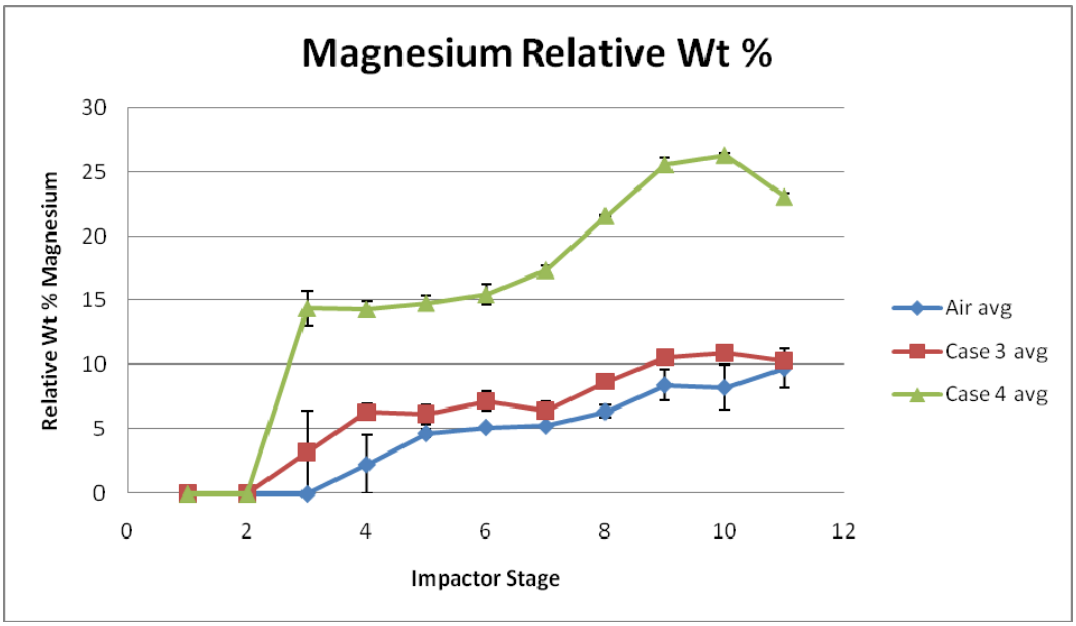

Figure 2.2-24. Relative percentage of magnesium in fly ash.

The magnesium proportions are also higher in the Case 3 flame than in the air-fired scenario. This indicates that there is a difference in the way magnesium affiliates with particles under oxy-fired conditions and under air-fired conditions even at the same adiabatic flame temperature. Therefore, it may be that the O_2/CO_2 combustion conditions also affect magnesium volatility and the mechanisms which drive the formation of magnesium compounds found in the fly ash.

The magnesium mass concentration distributions do not vary much between air and oxy-firing, as shown on Figure 2.2-25.

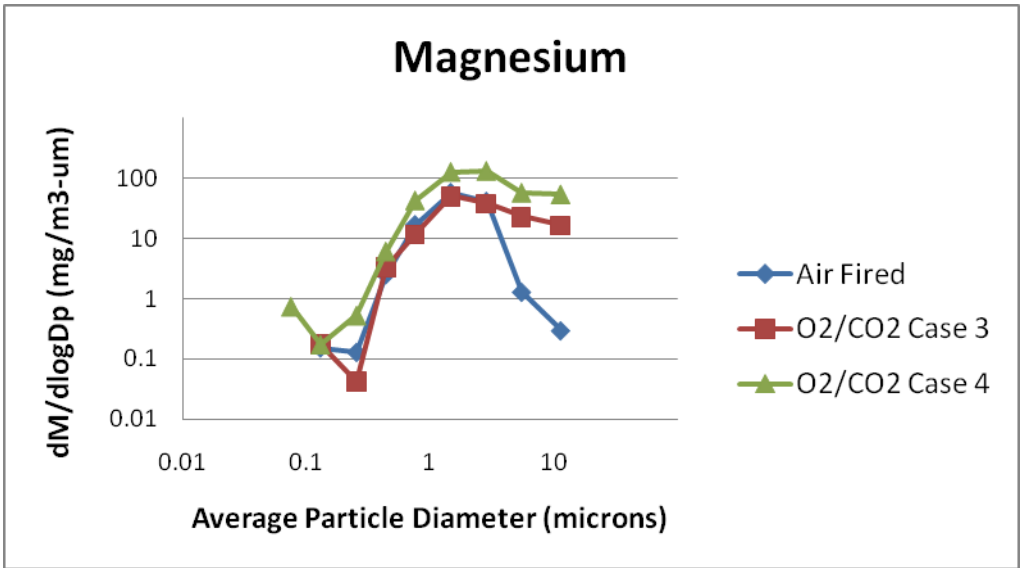

Figure 2.2-25. Differential mass of elemental magnesium in as a function of particle diameter. Data points for low particle diameters are omitted due to being below detectable limits and the issues with plotting zeros on a log scale.

Calcium is an important element from a fouling point of view. It is also reactive towards arsenic, selenium and phosphorus, and so those trace elements are likely to track the calcium PSDs. It is a more volatile element and is obviously a key element of the fume based upon the proportions of calcium found on the lower stages of the impactor in all combustion cases.

The calcium relative concentration, shown in Figure 2.2-26, is also very high on the third stage of Case 4, which corresponds with the larger amount of mass seen on the SMPS mass distributions in Figure 2.2-15 and Figure 2.2-16. There is not as great of a change in the average relative weight percent of calcium between Case 4 and Case 3 combustion scenarios indicating that calcium is sufficiently volatile to be vaporized even at the lower flame temperature of the Case 3 combustion scenarios. Also, the calcium proportions, like the concentrations of magnesium, tend to be higher in the oxy-fired cases rather than the air-fired case. This similarity is plausible due to the similar chemical structure and behavior of both elements being very similar. This indicates that there may be a correlation between metals that may form 2+ ions and their volatility and the mechanisms which affect their proportions in sub micron particles in the O_2/CO_2 combustion environment. Figure 2.2-27 shows the greatest variation in mass distribution at the lowest particle sizes.

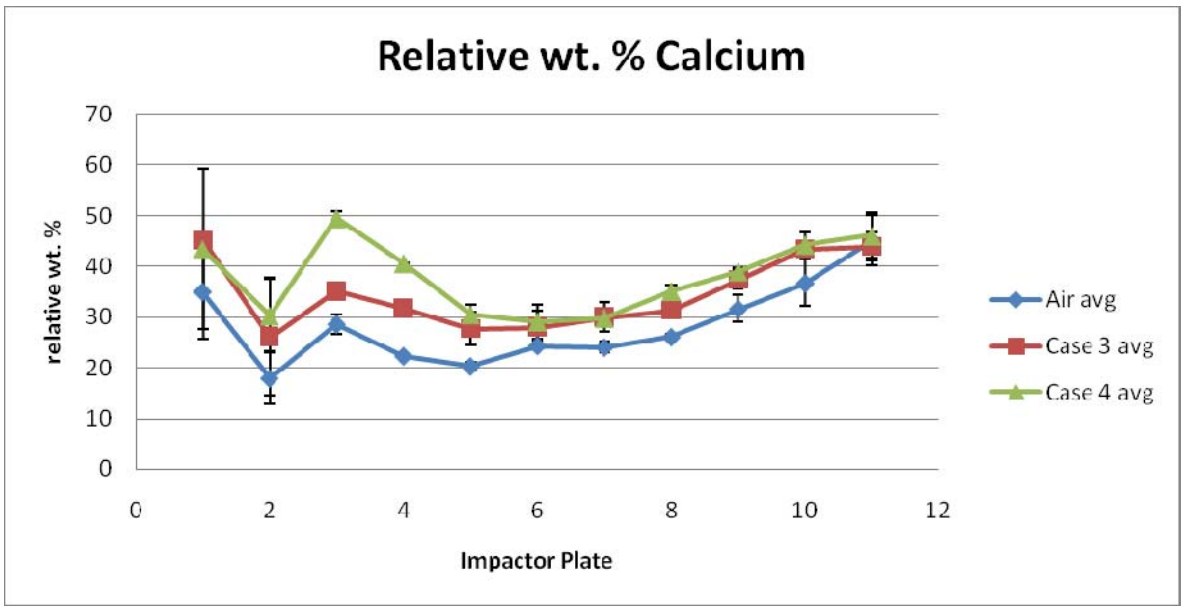

Figure 2.2-26. Average relative weight percent of calcium in fly ash.

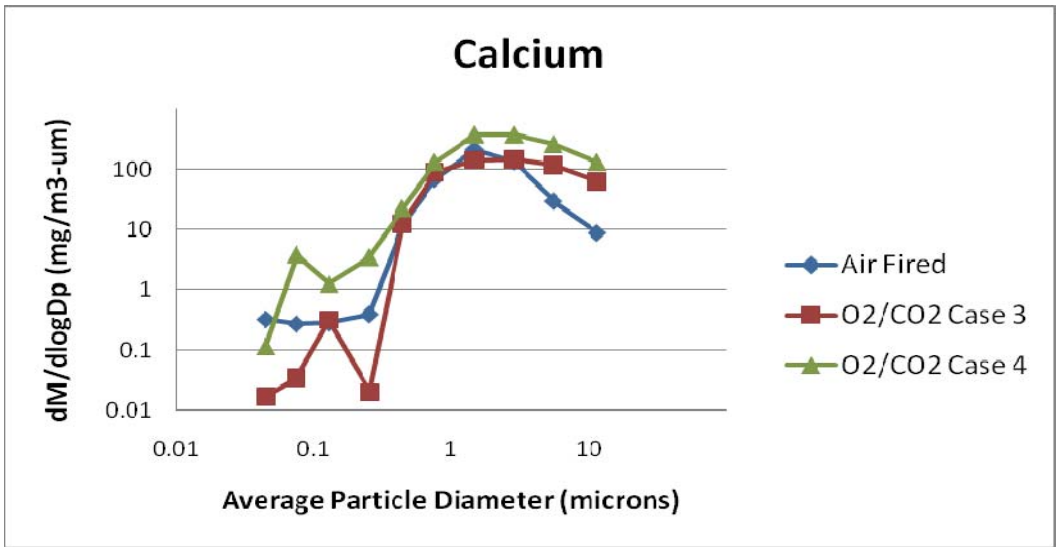

Figure 2.2-27. Differential mass of elemental calcium per cubic meter of standard flue gas as a function of particle diameter.

Sodium is likely the other main component of the fume, which is not surprising given that it is known to be a more volatile metal. This is clearly evident as it is present in very high proportions in the smallest size ranges in Figure 2.2-28. The sodium likely reacted on the surface of larger particles in the high temperature Case 4 flame, while it remained a high proportion of the small diameter flume particles and likely contributed to the very large flume region found in the SMPS mass distribution. It is also interesting to note that there was no sodium in the lower stages of the Case 4 scenario, but an increase in relative weight percent in the 340 nanometer range. This suggests that the sodium that is vaporized is being scavenged by larger particles.

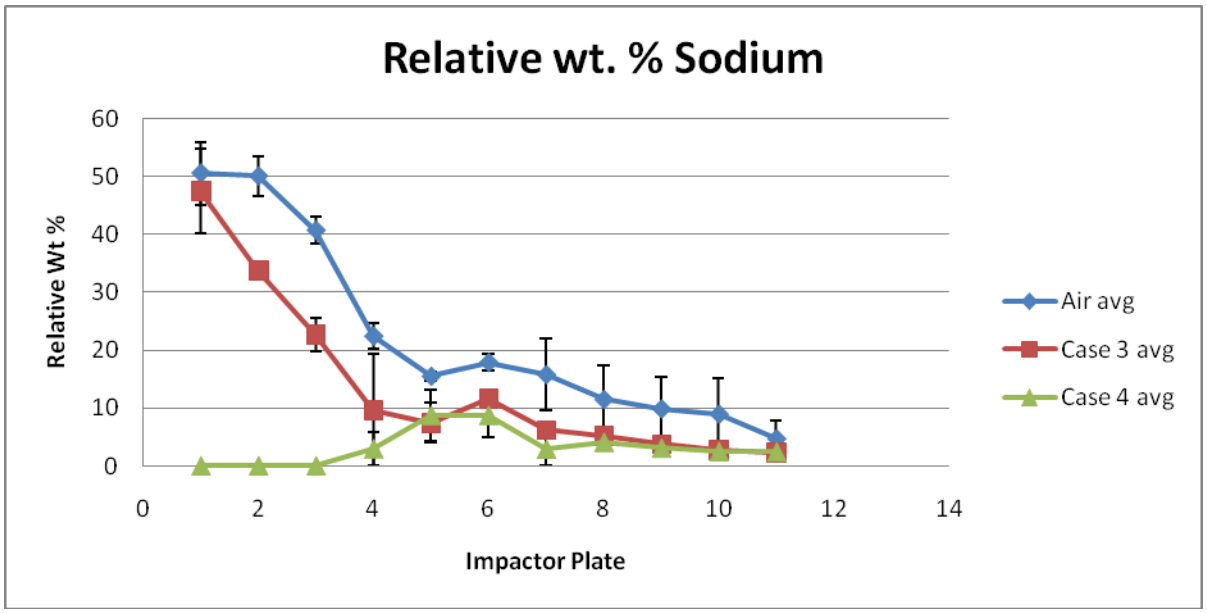

Figure 2.2-28. Relative weight percent sodium in fly ash.

Also of interest, is that unlike iron, calcium, and magnesium, there seems to be a higher weight percentage of sodium in the air-fired cases rather than the oxy-fired cases. This suggests that the behavior of sodium is different under oxy-fired conditions rather than air-fired conditions. It also suggests that the mechanisms which are affecting relative concentration of iron, calcium, and magnesium affect sodium differently, or are not the mechanisms which govern the formation of sodium compounds in the fly ash.

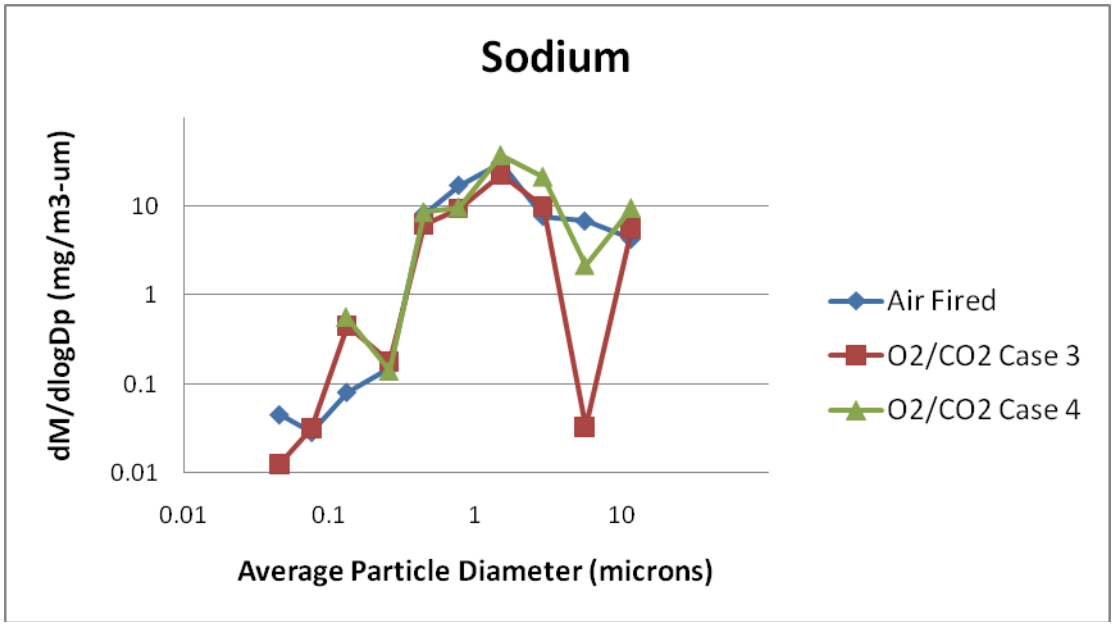

Figure 2.2-29. Differential mass of elemental sodium in mg per cubic meter of flue gas as a function of particle diameter.

Due to sodium's more volatile nature, its mass distribution varies from some of the other elements examined in the fly ash. It is possible to see the sub micron fume mode, and in the mass of sodium decreases earlier in the super micron mode indicating that the sodium in the ash is more likely to be vaporized to form ultrafine particles rather than be present in the larger super-micron particles as was the case with some of the other elements.

Potassium is chemically similar to sodium, but was not present in as high of concentrations as sodium in any of the ash. As a result, the potassium was below detectable limits in some cases. However, it is also chemically similar to sodium, and may have exhibited some similar behaviors.

Due to the low proportions of potassium in all of the samples, it is hard to make definitive conclusions about the behavior of potassium in the flue gas. In the upper stages, were there is more mass to digest yielding more dependable ICP results, it appears that the same trend of relatively higher weight percentages in the air-fired cases rather than the oxy-fired cases is similar to the behavior of sodium (see Figure 2.2-30 and Figure 2.2-31). It also appears as though there is a correlation between the behavior of the mass distribution of potassium in the flue gas and sodium in the flue gas. This is most certainly reasonable, as the two elements are very chemically similar. Thus it is reasonable to conclude that mechanisms which may influence which particles are enriched with sodium may also affect how potassium compounds are formed and distributed within the fly ash.

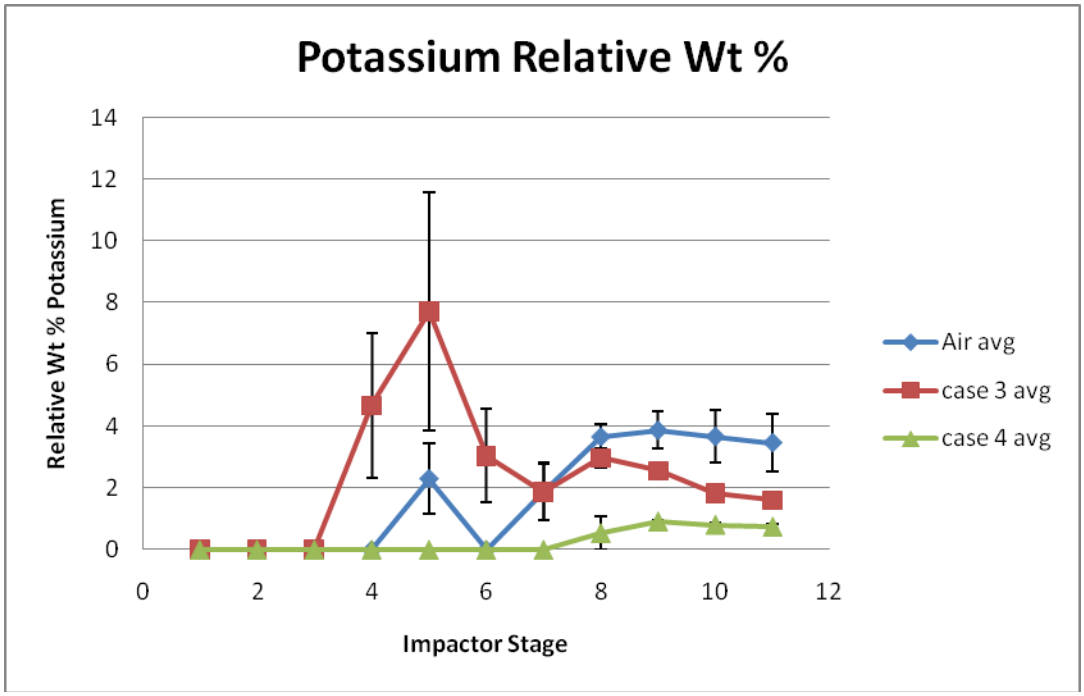

Figure 2.2-30. Averaged relative weight percentage of potassium in fly ash.

.

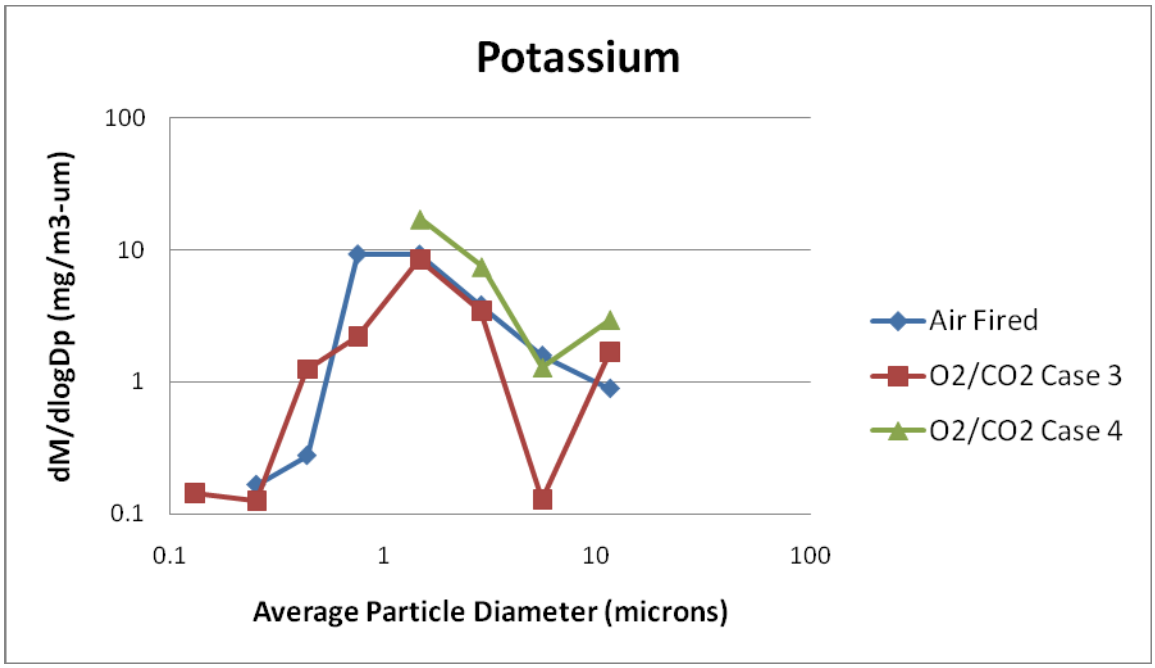

Figure 2.2-31. Differential ass of elemental potassium in mg per cubic meter of standard flue gas as a function of particle diameter. Data points that were below detection limits have been omitted rather than posted as zeros.

These data are still undergoing further analysis, involving comparisons to the bulk ash composition and comparison to the EDS results presented below. These data should be regarded as preliminary at this point in time.

Electron Dispersive Spectrometry (EDS) Results. The ICP-OES results shown above exhibited problems with silicon concentration measurements, because, among other things, the digestion procedure used off-campus in the commercial laboratory was inadequate. Furthermore, we had heard from an unnamed industrial organization very good results had been obtained with direct electron dispersive spectrometry (EDS) techniques of sampled particulates on the substrates. This type of analysis does not require digestion, and does not destroy the sample.

Using the in-house University of Utah scanning electron microscope, we were able to obtain the following data which is reported in the following order:

1) Comparisons of particle morphologies, for ash produced under air-fired (Case 1) versus that produced under oxy-coal conditions Case 3 and Case 4. Comparisons of both sub-micron and super-micron ash are presented.
2) Partial validation of EDS technique, using known XRF derived analysis of another bulk PRB ash, another bulk bituminous coal ash, and a bulk sorbent (denoted as "Arizona sorbent").
3) Comparative plots of EDS measured elemental oxide weight percents as a function of particle size, for Case 1 (air), Case 2 (oxy-coal – same adiabatic temperature) and Case 4 (oxy-coal high temperature). The data are interpreted although they appear to show some discrepancies with the ICP data, especially as regards the concentrations of sodium and iron in the very smallest particles. Reasons for this discrepancy are not clear, and will hopefully be elucidated in future work. The EDS results do provide additional data on phosphorus and on sulfur as a function of particle size. The results presented first are average values on each impactor plate. Future work will present differential plots in terms of concentrations in the flue gas.
4) Finally, ternary diagrams for *individual* larger single particles, collected on Plates 6 through 11 are presented. These data can be used to glean information on mineral speciation (rather than elemental composition) as a function of air-firing and oxy-coal firing. These data are still undergoing evaluation.

Particle morphologies. Figure 2.2-32, Figure 2.2-33 and Figure 2.2-34 show ash aerosol morphologies for Utah coal combusted in air (Case1), oxy-coal same adiabatic temperature (Case 3), and oxy-coal high adiabatic temperature respectively. Sub-micron particles are in the upper panel while super-micron particles are in the lower panel. These SEM micrographs show that ash particles formed under air case are similar to those formed under Case 3. However, particles from Case 4 are more spherical in shape than those from the other two cases. The results are related to combustion temperatures the three cases obtain. Since Case 3 maintained the same adiabatic flame temperature as the air case, ash particles formed under the two cases possess similar morphologies. On the other hand, the air case and Case 3 have a lower adiabatic flame temperature than Case 4, some unburned carbon-contained particles can be observed in the corresponding figures. Due to a higher temperature, coal particles burned more completely under Case 4 (lower LOI) and ash particles melt to a larger extent, which resulted in a larger number of spherical particles.

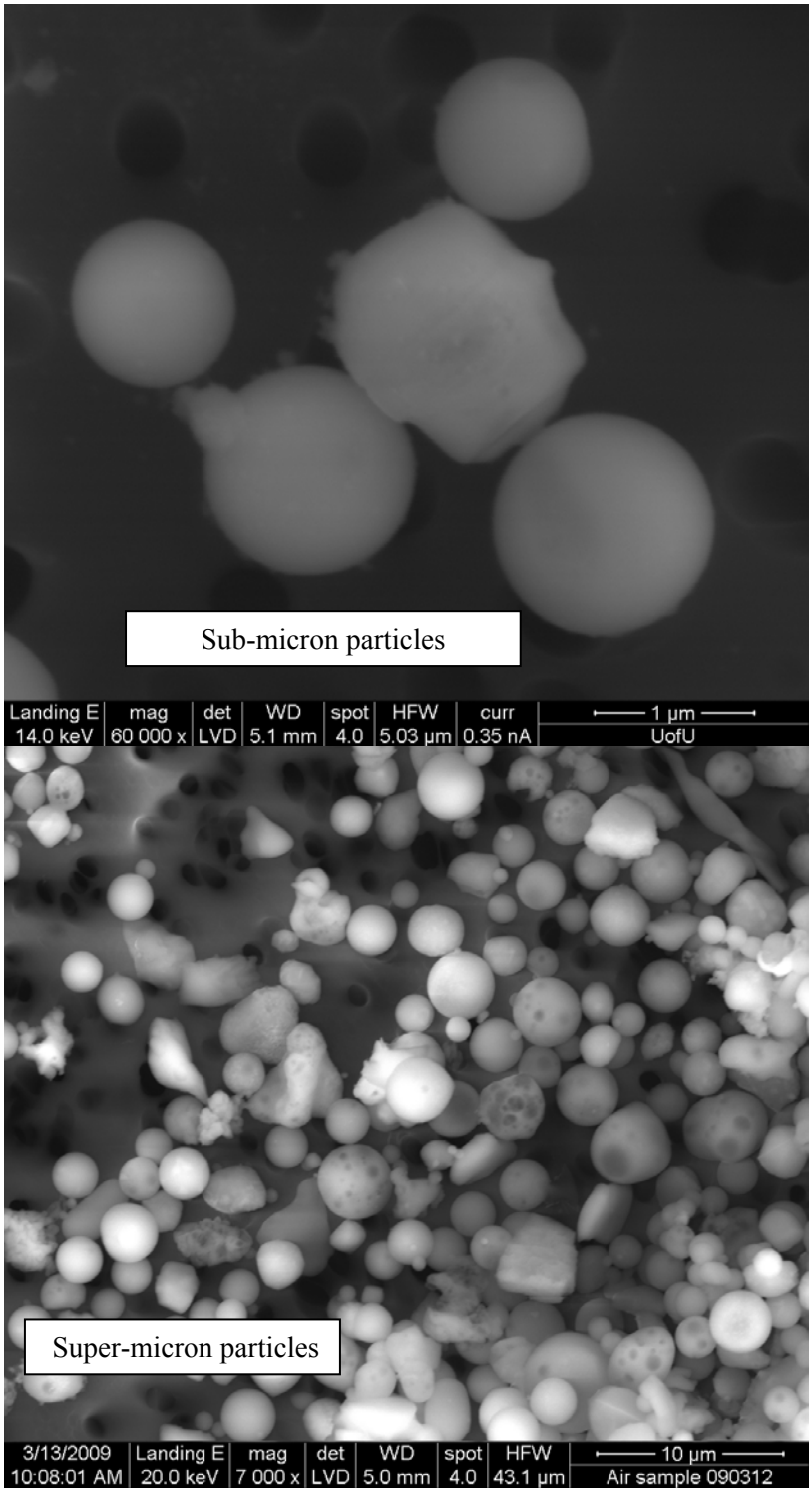

Figure 2.2-32. Ash aerosol SEM micrographs for Case 1 (air).

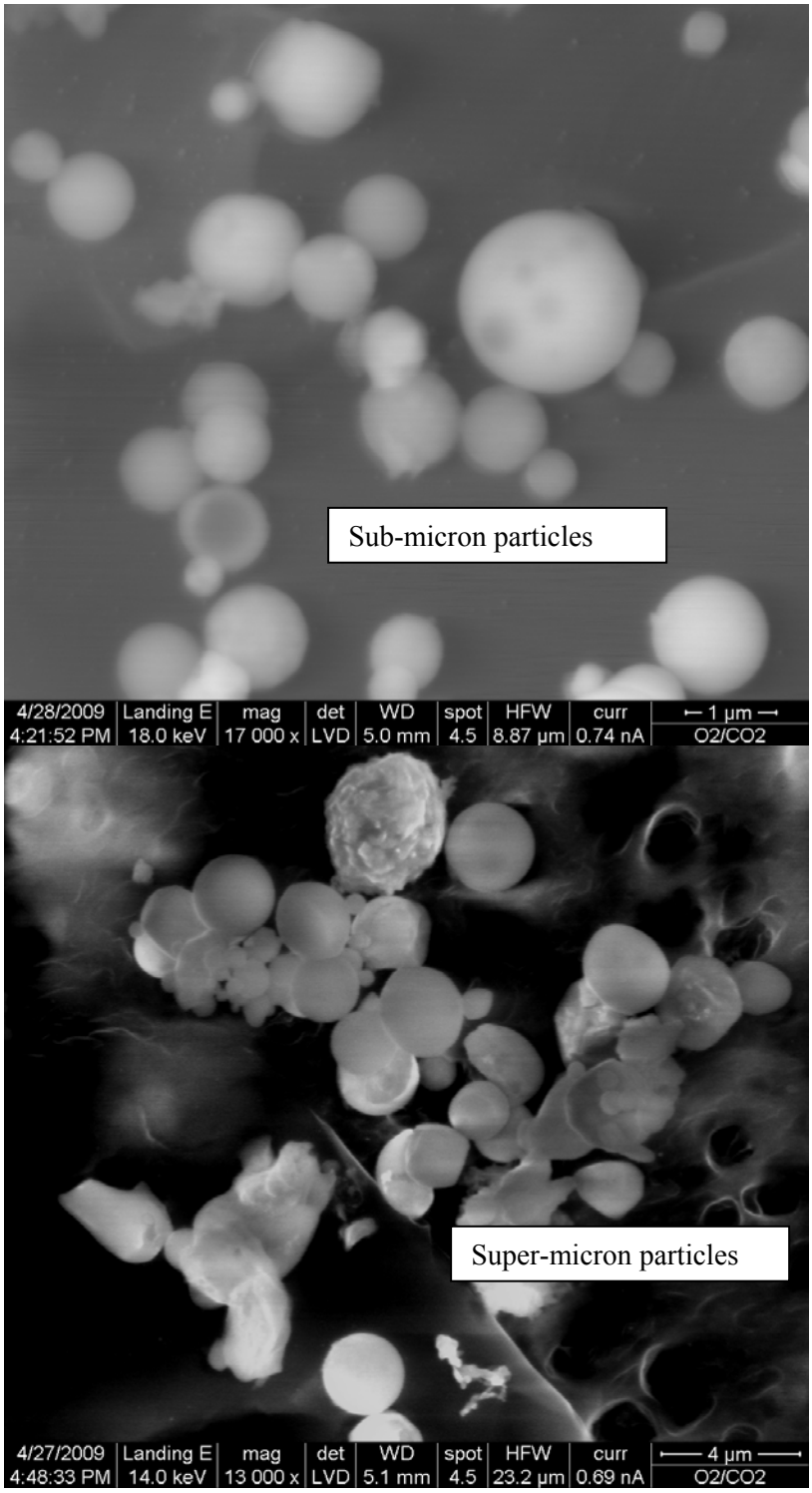

Figure 2.2-33. Ash aerosol SEM micrographs for Case 3 (oxy-coal, lower temperature).

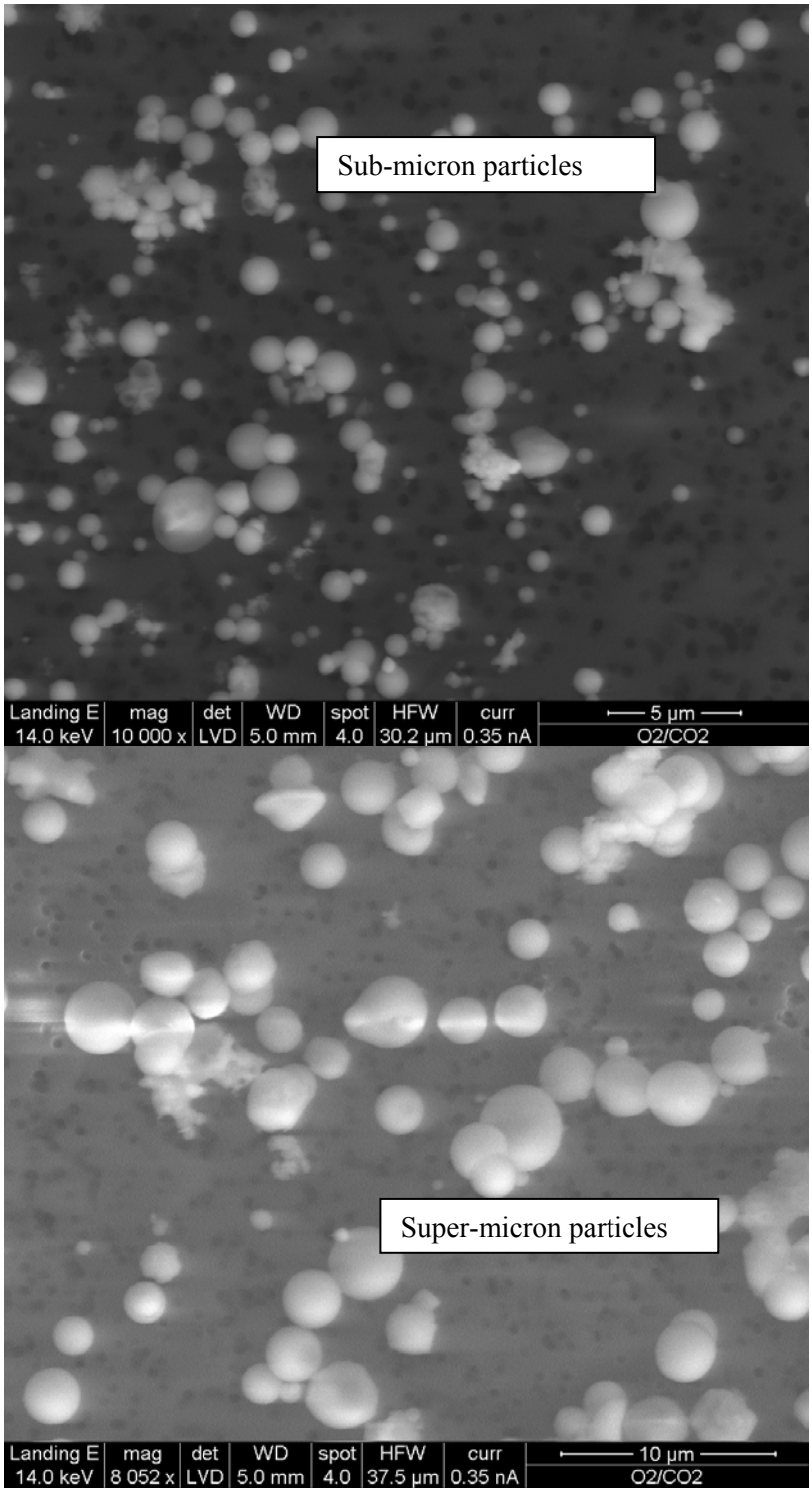

Figure 2.2-34. Ash aerosol SEM micrographs for Case 4 (oxy-coal, higher temperature).

Validation of EDS composition measurements using XRF data. Validation of our EDS technique was performed by comparing our EDS of bulk particulate samples with samples previously analyzed by Xray Fluorescence (XRF) by a laboratory at The University of Stuttgart, Germany. The bulk (non-size segregated) samples consisted of the ash of a Powder River Coal, the ash from a Bituminous Coal and a special Sorbent Powder called "Arizona Sorbent". The comparison results are plotted in Figure 2.2-35.

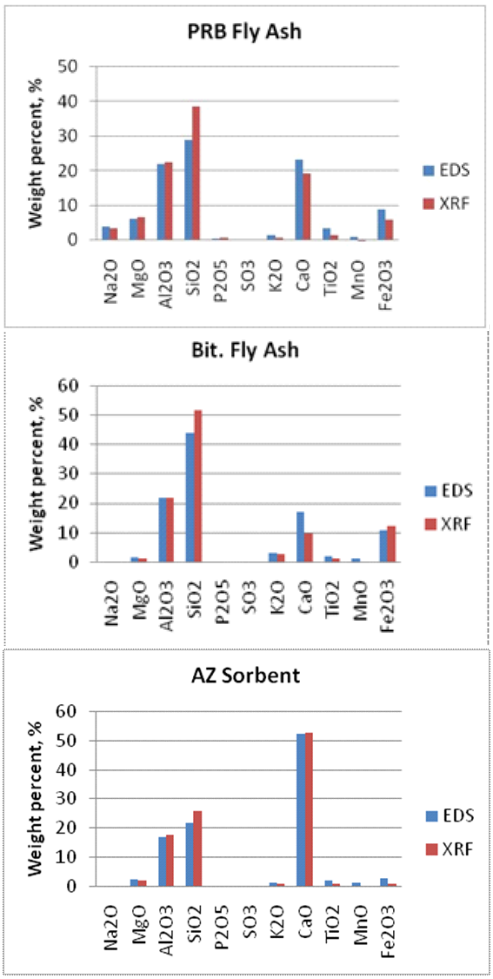

Figure 2.2-35. Comparison of EDS and (University of Stuttgart) XRF analyses of particulate constituents.

Generally, the results from EDS are comparable to those from XRF. XRF often gives a higher concentration of SiO_2. It seems that EDS and XRF agree better for simple chemical systems, e.g. AZ sorbent. It should be noted that both EDS and XRF analyses methods are based on similar physical principles and therefore might be prone to common inaccuracies.

Future work will involve validation using standard reference fly ash samples from NIST.

We do not present comparisons of our EDS and digestion followed by ICP-OES data at this time, because these data are still undergoing evaluation and it would be premature to present them now. We are aware that the silicon values from the digestion and ICP-OES are probably in error because of digestion issues. We have greater confidence in the EDS analysis.

Ash Composition. Figure 2.2-36 through Figure 2.2-45 show ten size segregated ash composition plots, namely for Na_2O, K_2O, MgO, CaO, P_2O_5, Fe_2O_3, Al_2O_3, SiO_2, SO_3, and TiO_2.

The Na_2O concentrations (see Figure 2.2-36) for the three cases are similar in the size range of larger than 2μm. But in the size range of less than 0.5 μm, the Na_2O concentration for the air case is higher than those for Cases 3 and 4 except for the very tiniest particles. The concentration of Na in the smallest particles is significantly lower than that measured by ICP (Figure 2.2-28). Reasons for this discrepancy are unclear. The high temperature enhanced increased enrichment of Na on large particles is in agreement with Gallagher et al [1990] and is due to increased reaction of Na vapor with alumino-silicates at higher temperatures. However, these data, if confirmed in subsequent experiments, suggest that the change of air-fired condition to oxy-fired condition may have some effects on Na partitioning.

Fe (Figure 2.2-41) seems abnormally high for the very smallest particles, and this disagrees with the ICP measurements (Figure 2.2-22). One might conclude from Figure 2.2-36 through Figure 2.2-45 that the combustion atmosphere of O_2/CO_2 may have significant effects on oxide size distributions, especially basic oxides. For particles less than 1μm MgO, CaO and P_2O_5 increase with decreasing particle size, while SiO_2 decreases with particle size. As expected, sulfate is predominately found in the small particle size range.

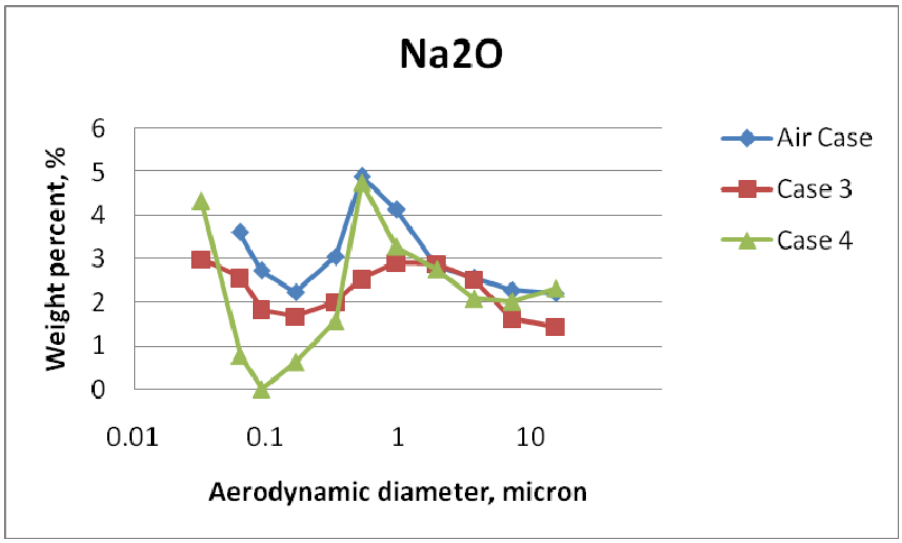

Figure 2.2-36. Size segregated distribution of Na_2O.

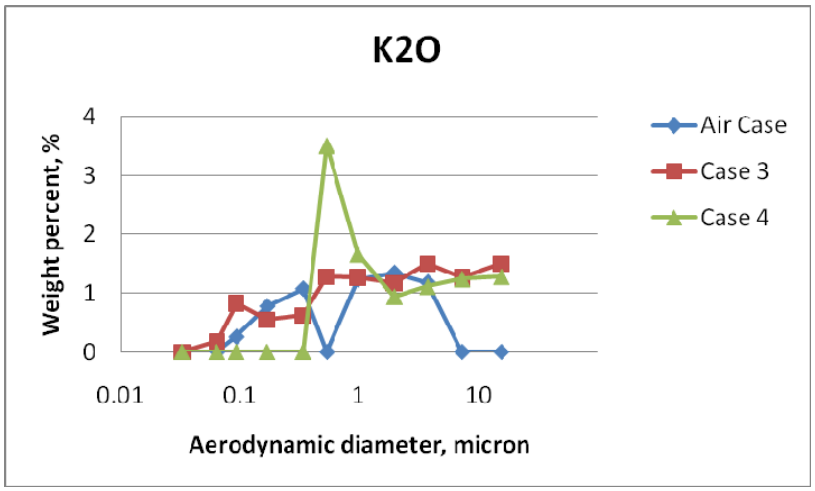

Figure 2.2-37. Size segregated distribution of K_2O.

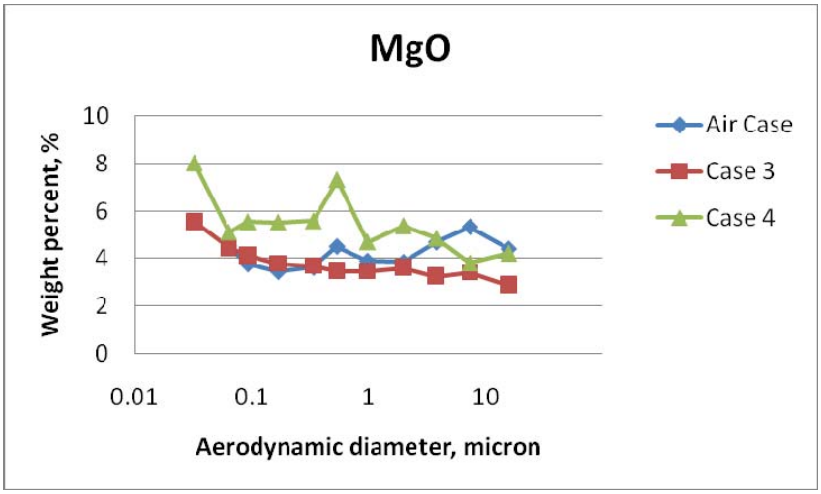

Figure 2.2-38. Size segregated distribution of MgO.

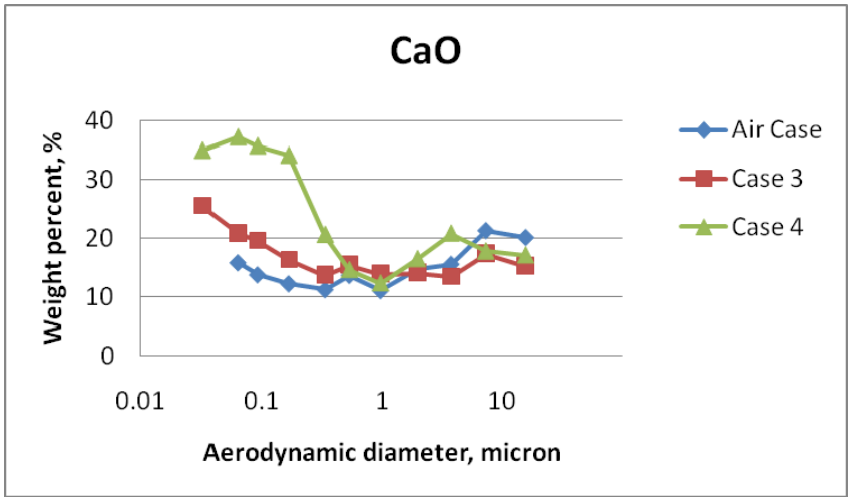

Figure 2.2-39. Size segregated distribution of CaO.

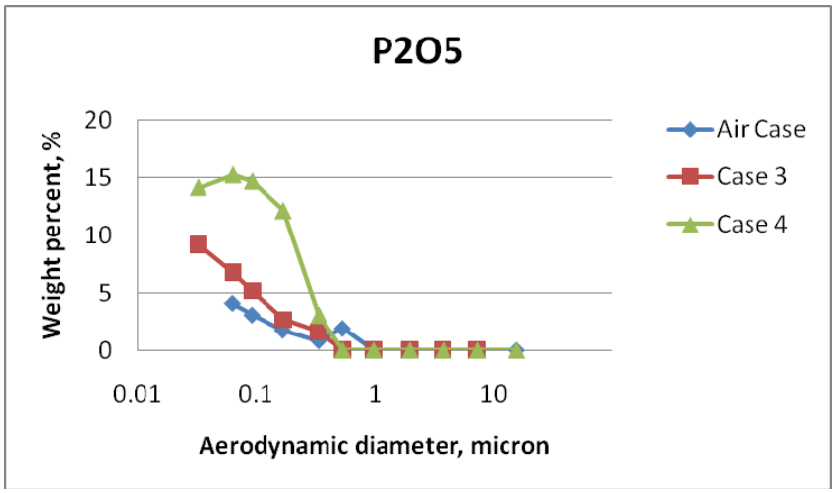

Figure 2.2-40. Size segregated distribution of P_2O_5.

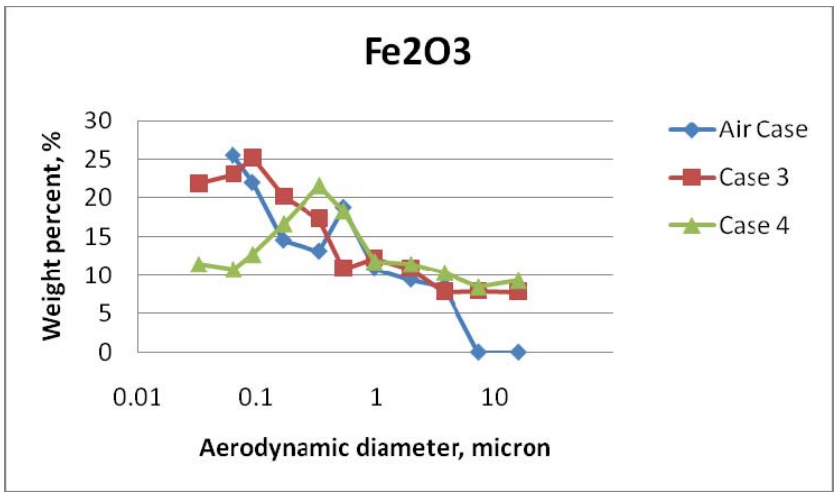

Figure 2.2-41. Size segregated distribution of Fe_2O_3.

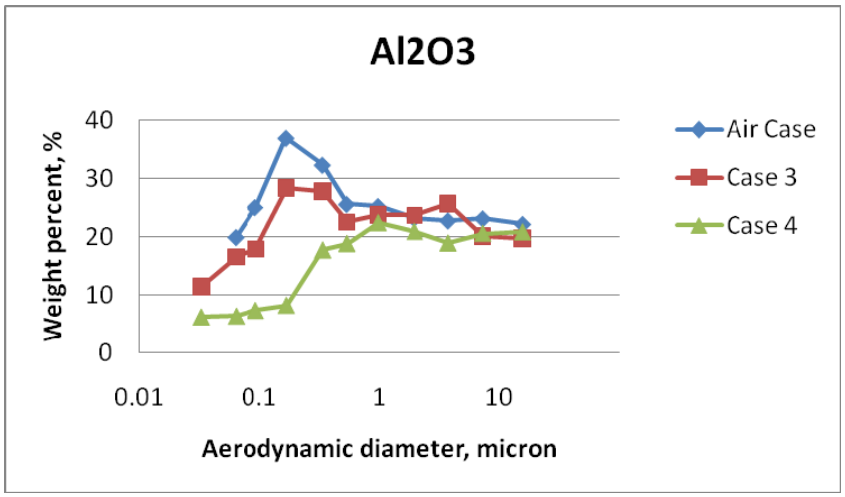

Figure 2.2-42. Size segregated distribution of Al_2O_3.

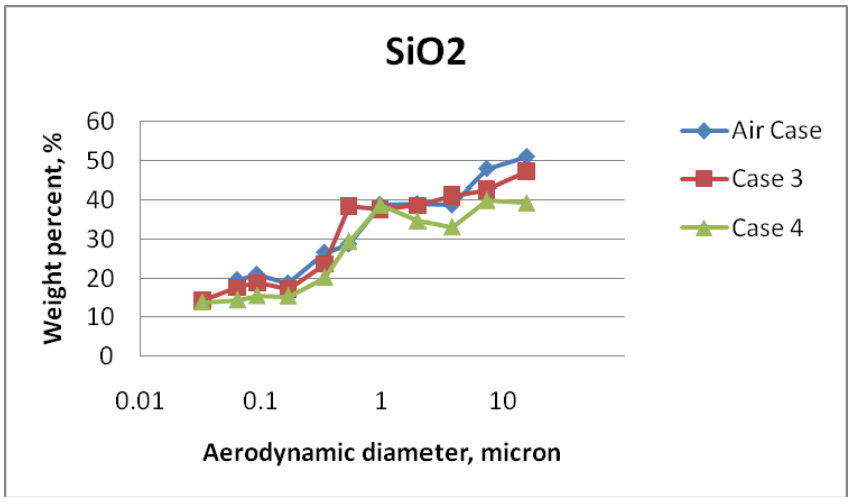

Figure 2.2-43. Size segregated distribution of SiO_2.

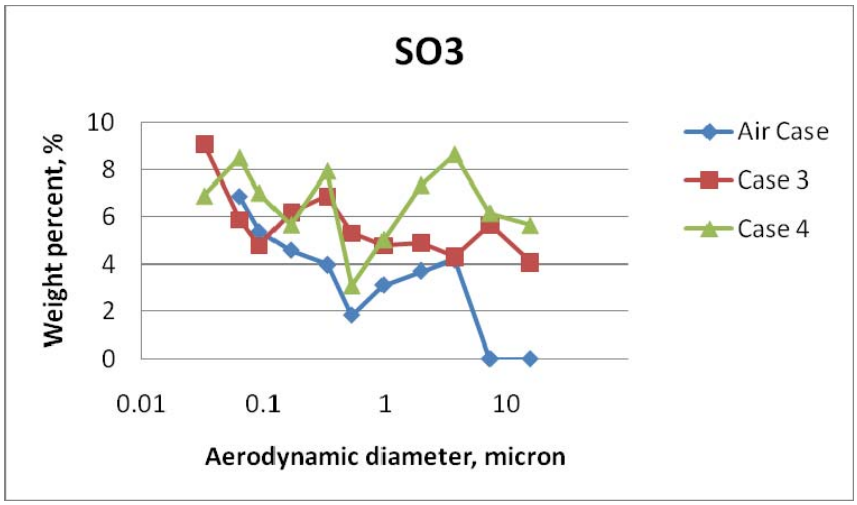

Figure 2.2-44. Size segregated distribution of SO_3.

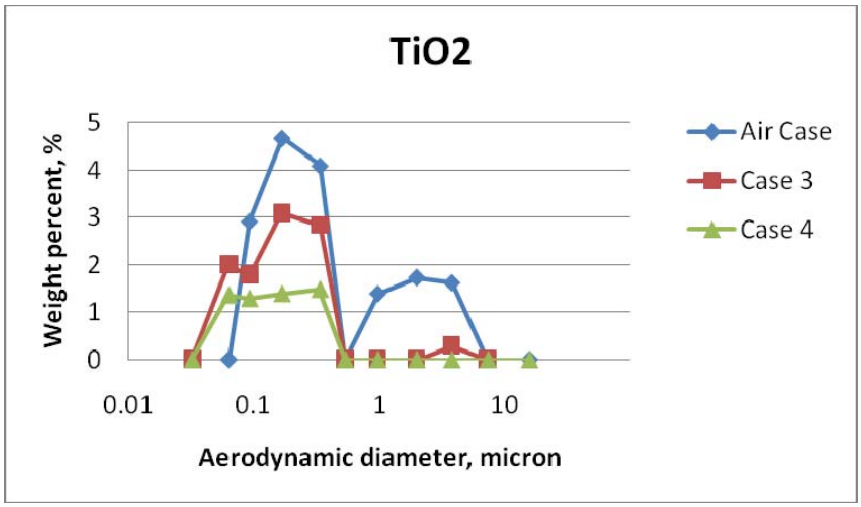

Figure 2.2-45. Size segregated distribution of TiO_2.

Individual particle analysis. One of the advantages of EDS is that the composition of individual particles can be examined, and from this mineralogical analyses hypothesized. Table 2.2-2 below shows the number of particles analyzed per case, and the combinations of groups of three elements explored. Results can be plotted on ternary diagrams, shown below.

Table 2.2-2. Individual particle analyses. Systems explored.

		Air Case	Case 3	Case 4
particle number analyzed	stage			
	6	22	22	21
	7	21	22	22
	8	22	21	22
	9	23	22	23
	10	22	21	21
	11	22	21	22
	total	132	129	131
Na-Al-Si particle number	stage			
	6	16	19	8
	7	14	22	13
	8	14	21	10
	9	16	17	21
	10	5	20	13
	11	12	18	12
	total	77	117	77
Mg-Al-Si particle number	stage			
	6	12	22	18
	7	15	22	15
	8	16	19	21
	9	17	14	17
	10	13	21	13
	11	8	20	17
	total	81	118	101
K-Al-Si particle number	stage			
	6	3	6	4
	7	1	9	2
	8	0	6	4
	9	4	14	10
	10	4	9	4
	11	3	7	5
	total	15	51	29

Table 2.2-2 continued

		Air Case	Case 3	Case 4
Ca-Al-Si particle number	stage			
	6	11	22	19
	7	16	22	14
	8	18	21	21
	9	15	22	20
	10	12	21	14
	11	11	20	16
	total	83	128	104

Fe-Al-Si particle number	stage			
	6	2	22	18
	7	3	22	10
	8	5	8	13
	9	3	16	11
	10	6	15	8
	11	4	17	14
	total	23	100	74

Figure 2.2-46 through Figure 2.2-60 show results of individual particle analyses. These data are still undergoing evaluation. The immediate point that is evident is that compared to air combustion, a larger number of particles with a basic Al-Si composition are formed under O_2/CO_2 combustion conditions. This suggests that classical fouling and slagging indices should be considered, such as:

1. Basic to acid oxides ratio
   B/A=(Na2O+MgO+K2O+CaO+Fe2O3)/(Al2O3+SiO2+TiO2)
   - the higher B/A, the higher slagging tendency
2. Silica to alumina ratio
   Si/Al_R= SiO2/Al2O3
   - the higher Si/Al_R, the higher slagging tendency
3. Silica ratio
   Si_R=SiO2/(SiO2+MgO+CaO+Fe2O3)
   - the higher Si_R, the lower slagging tendency

We have completed a preliminary exploration of theses indices to determine how they depend on air-coal versus oxy-coal combustion, and how they might also depend on particle diameter. These data are still undergoing evaluation, and will be presented in a subsequent report.

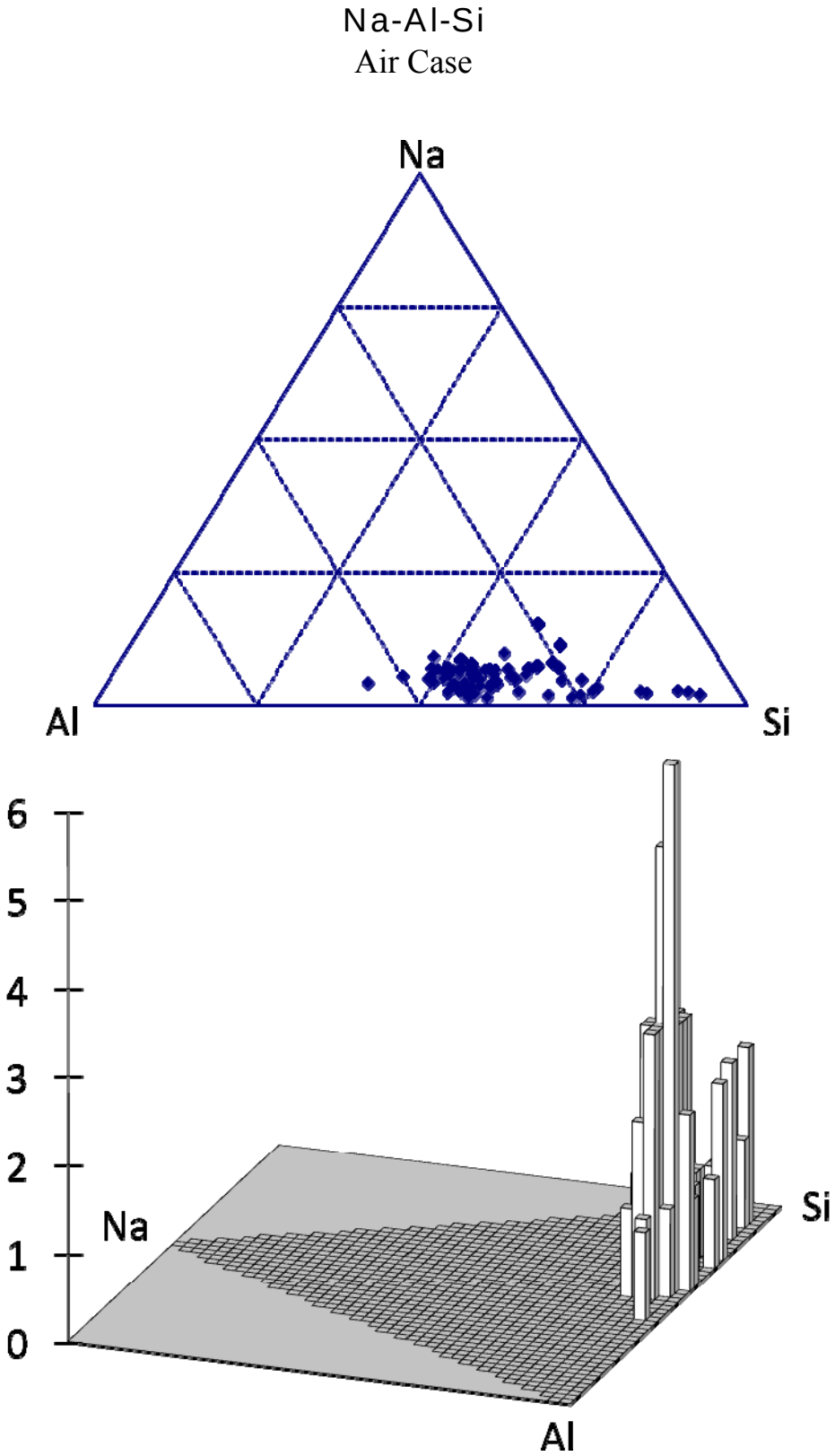

Figure 2.2-46. Na-Al-Si system. Air Case 1. Vertical bars in the lower panel give particle counts.

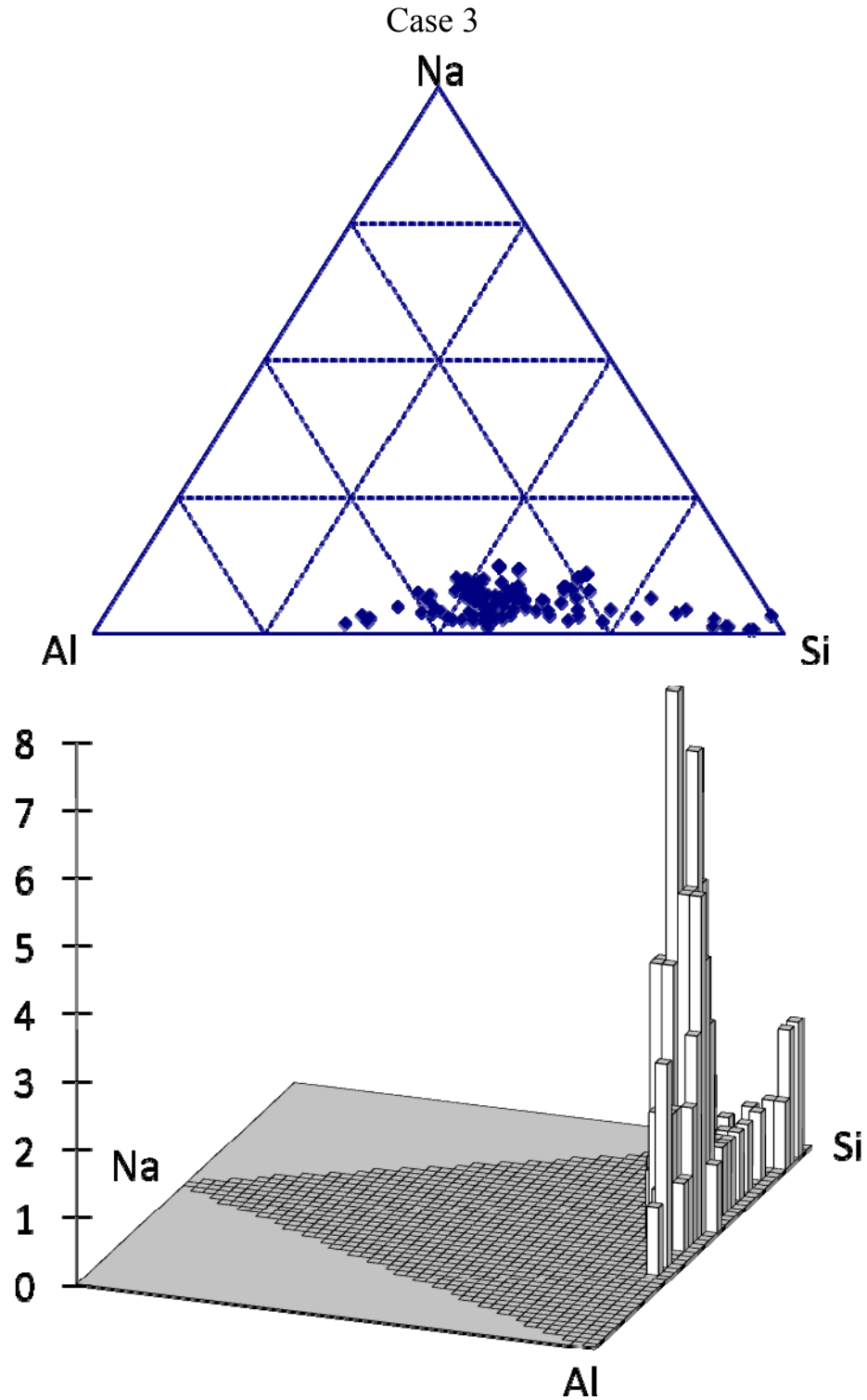

Figure 2.2-47. Na-Al-Si system. Oxy-coal Case 3. Vertical bars in the lower panel give particle counts.

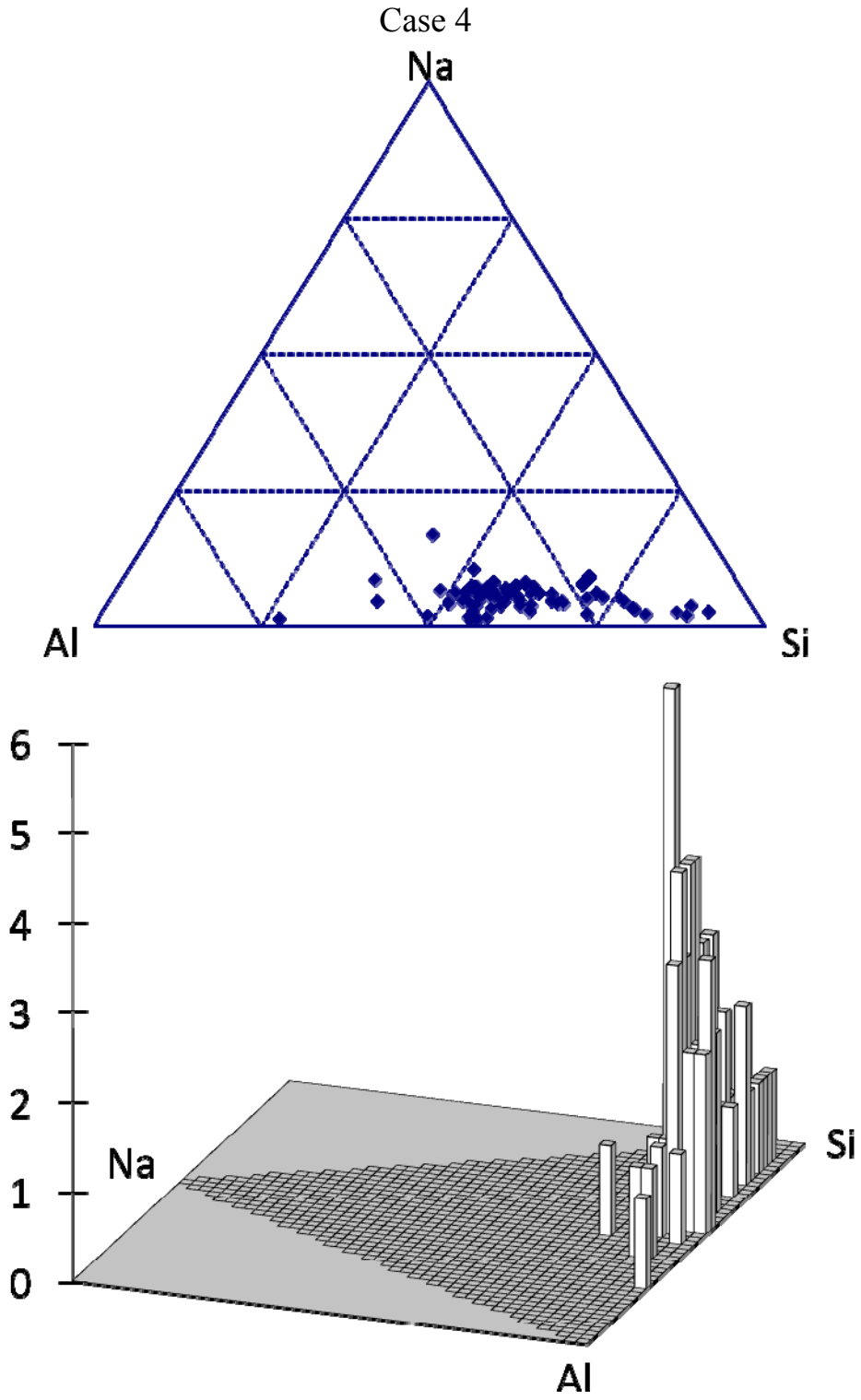

Figure 2.2-48. Na-Al-Si system. Oxy-coal Case 4. Vertical bars in the lower panel give particle counts.

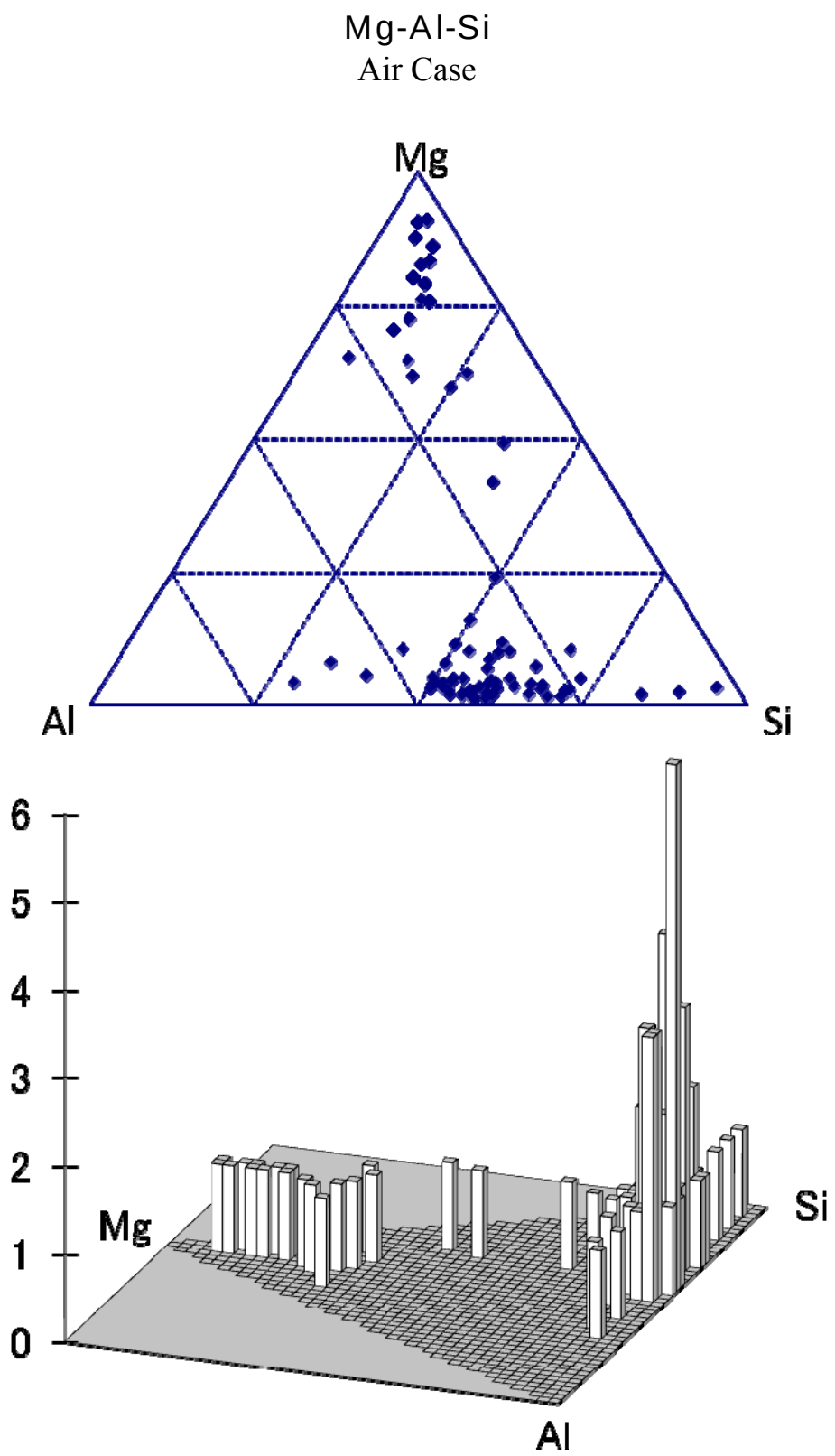

Figure 2.2-49. Mg-Al-Si system. Air Case 1. Vertical bars in the lower panel give particle counts.

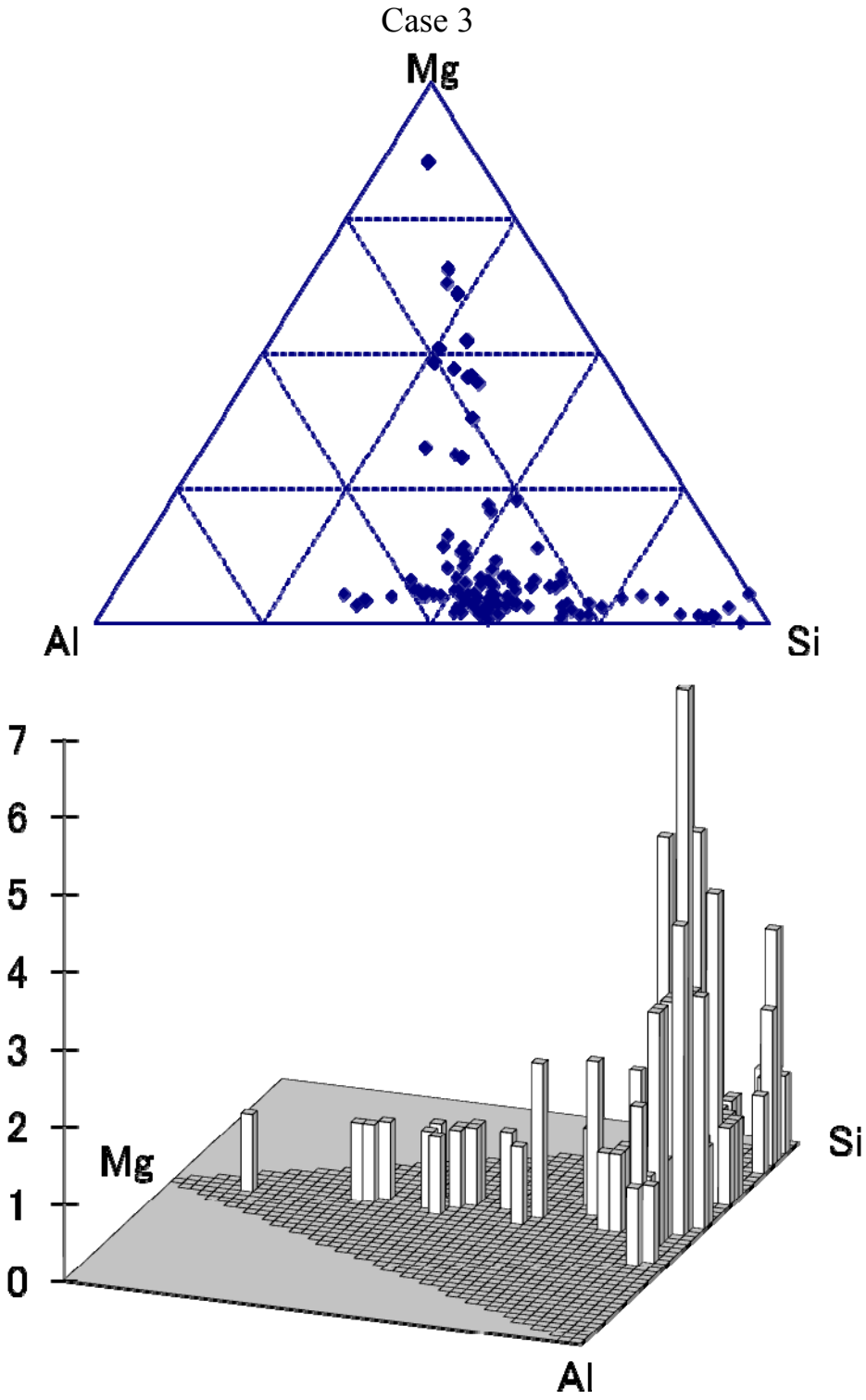

Figure 2.2-50. Mg-Al-Si system. Oxy-coal Case 3. Vertical bars in the lower panel give particle counts.

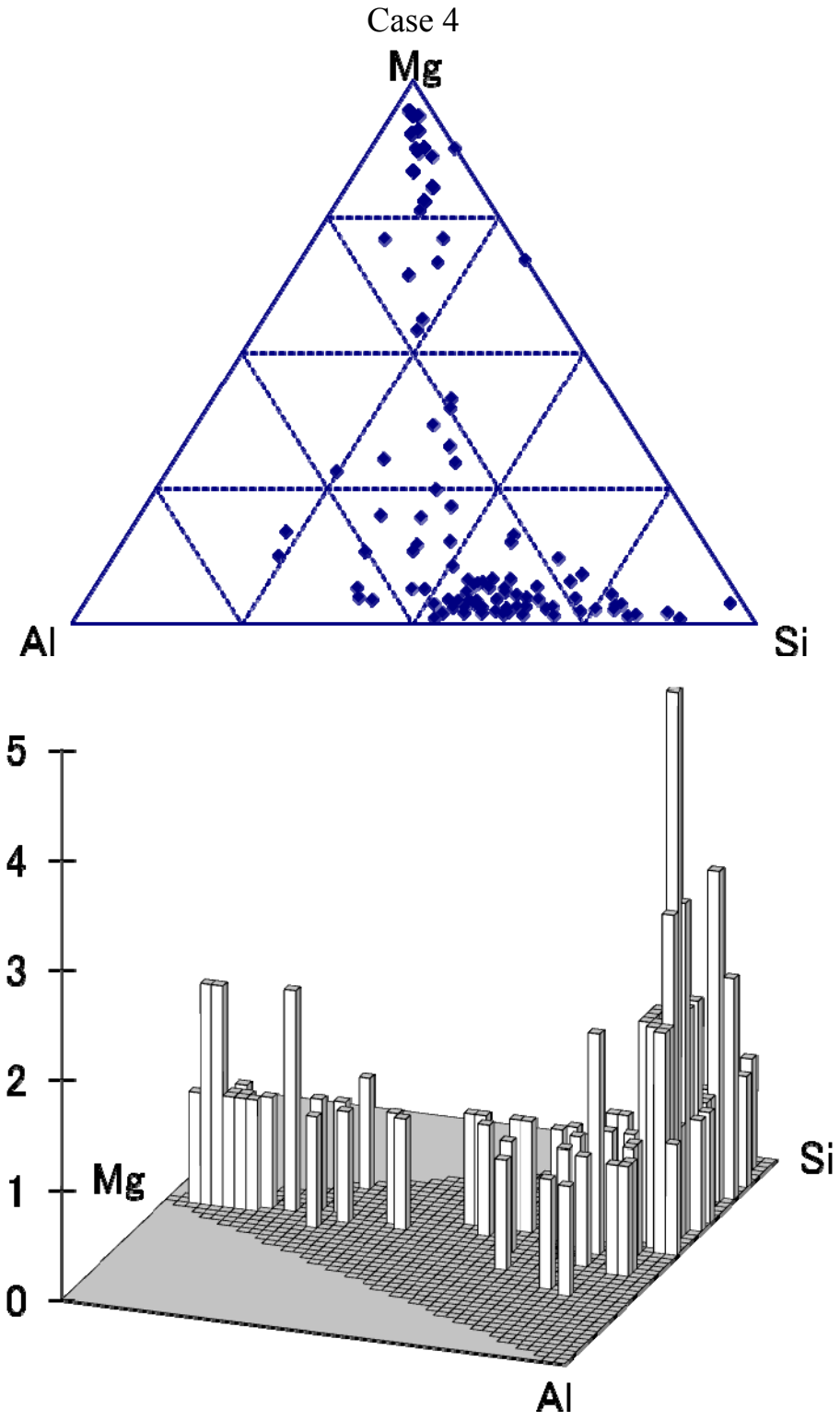

Figure 2.2-51. Mg-Al-Si system. Oxy-coal Case 4. Vertical bars in the lower panel give particle counts.

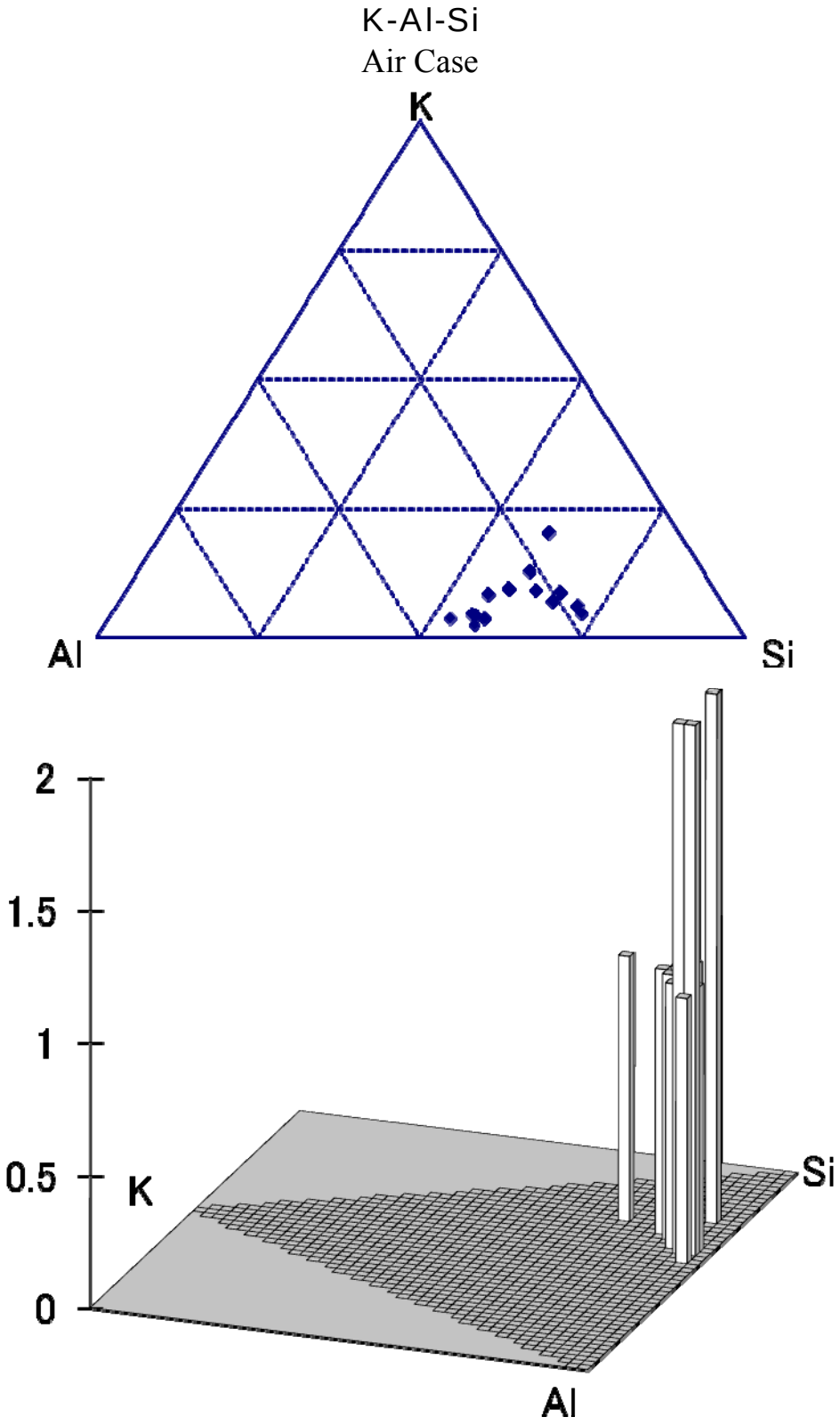

Figure 2.2-52. K-Al-Si system. Air Case 1. Vertical bars in the lower panel give particle counts.

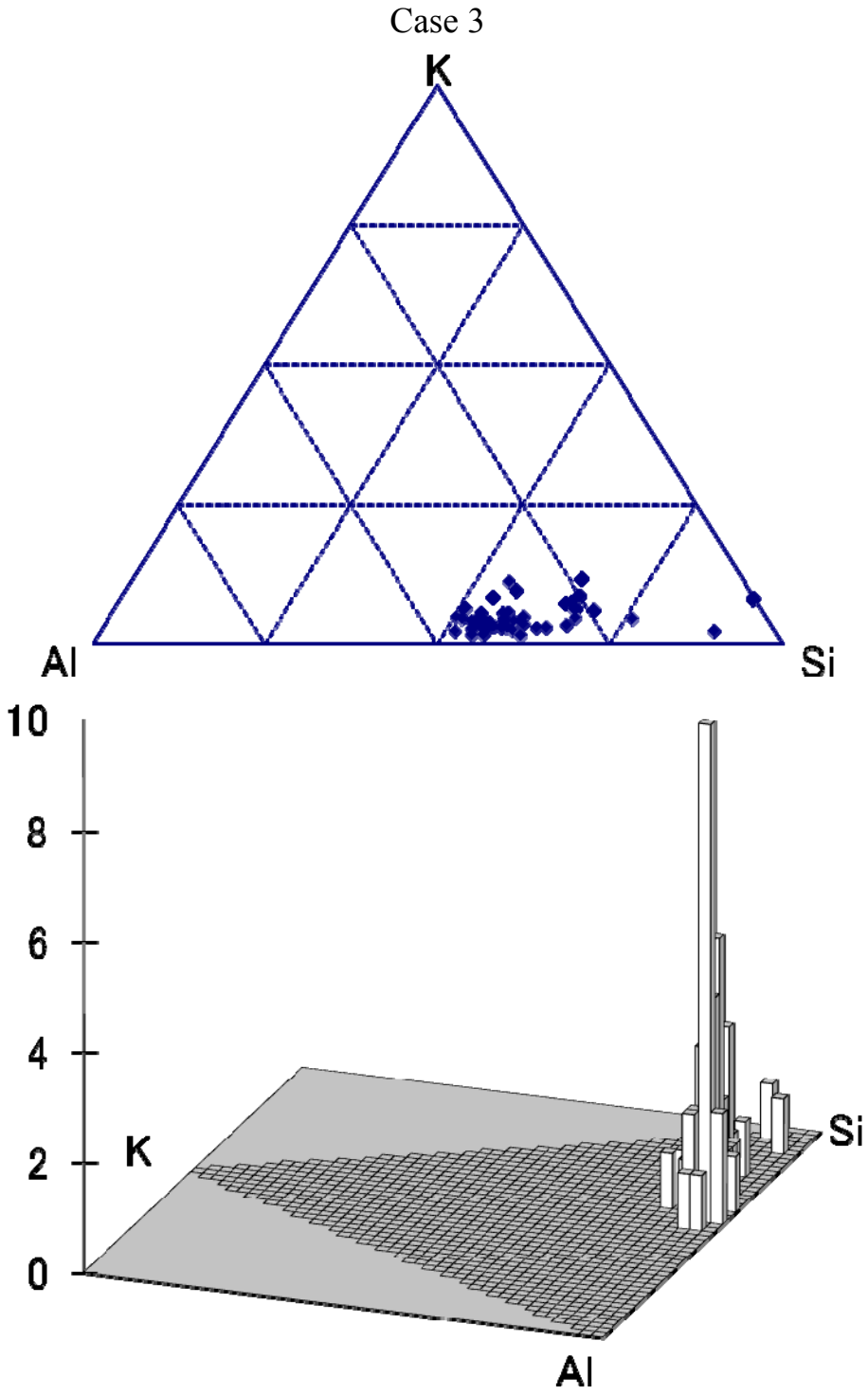

Figure 2.2-53. K-Al-Si system. Oxy-coal Case 3. Vertical bars in the lower panel give particle counts.

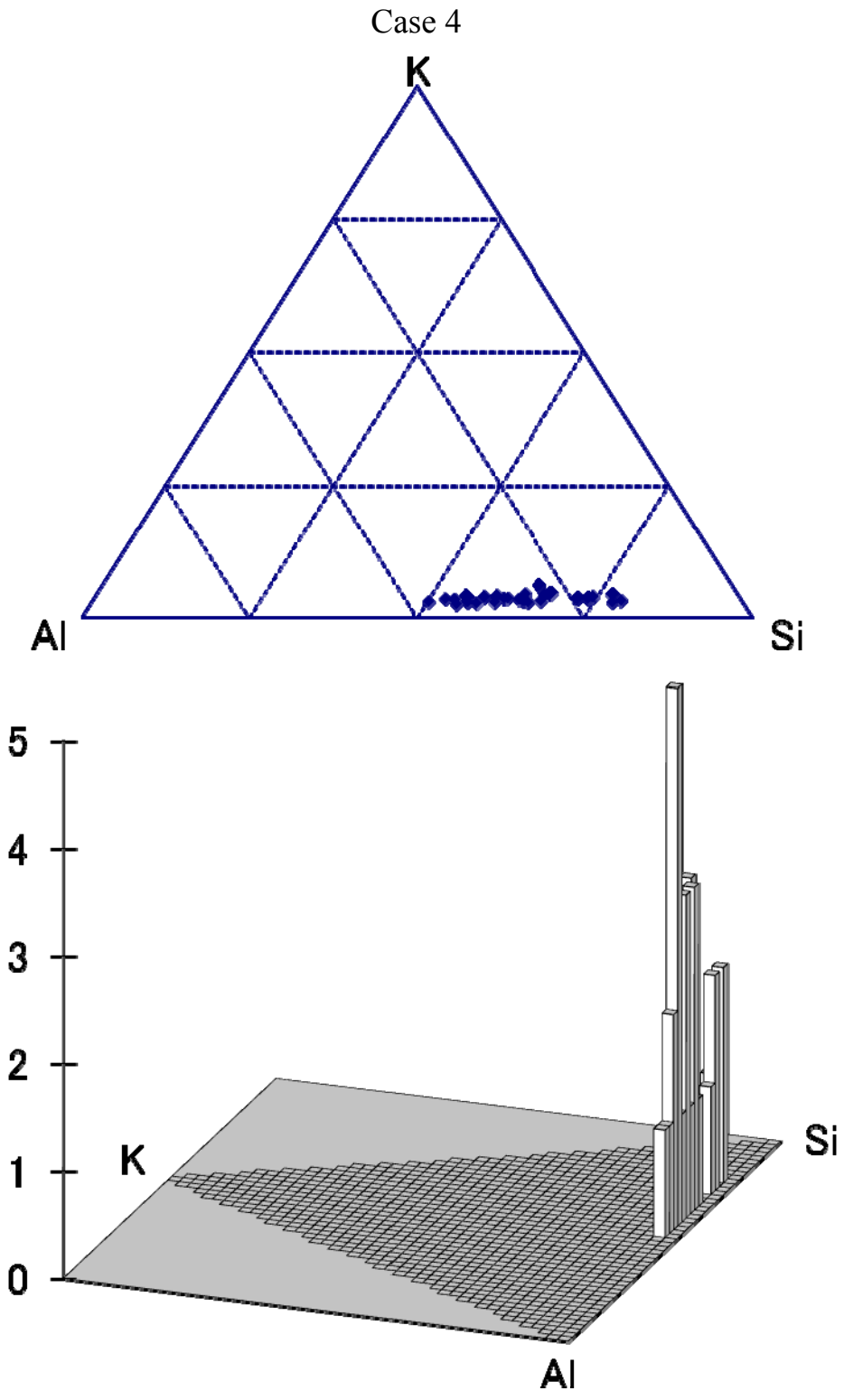

Figure 2.2-54. K-Al-Si system. Oxy-coal Case 4. Vertical bars in the lower panel give particle counts

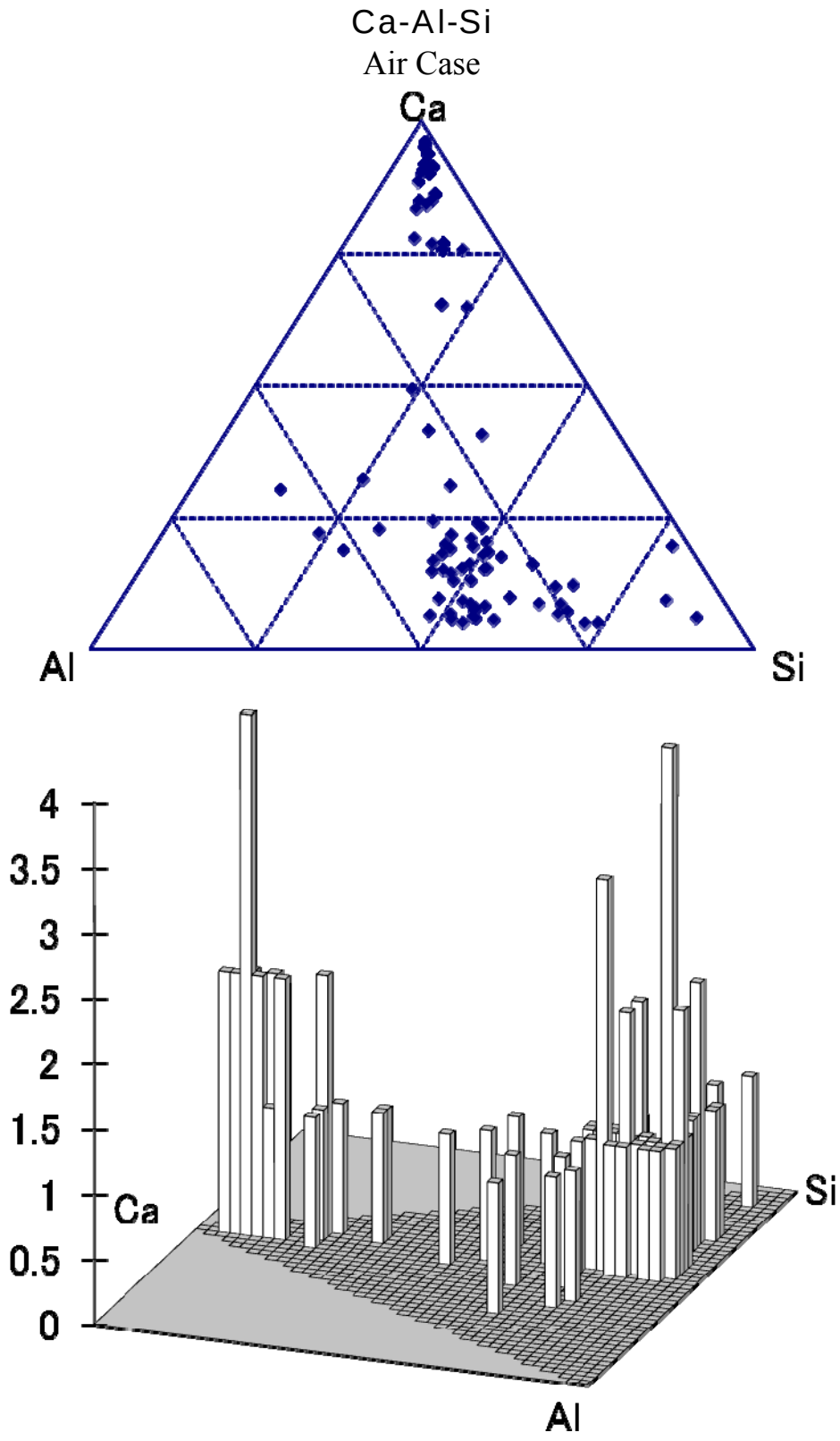

Figure 2.2-55. Ca-Al-Si system. Air Case 1. Vertical bars in the lower panel give particle counts.

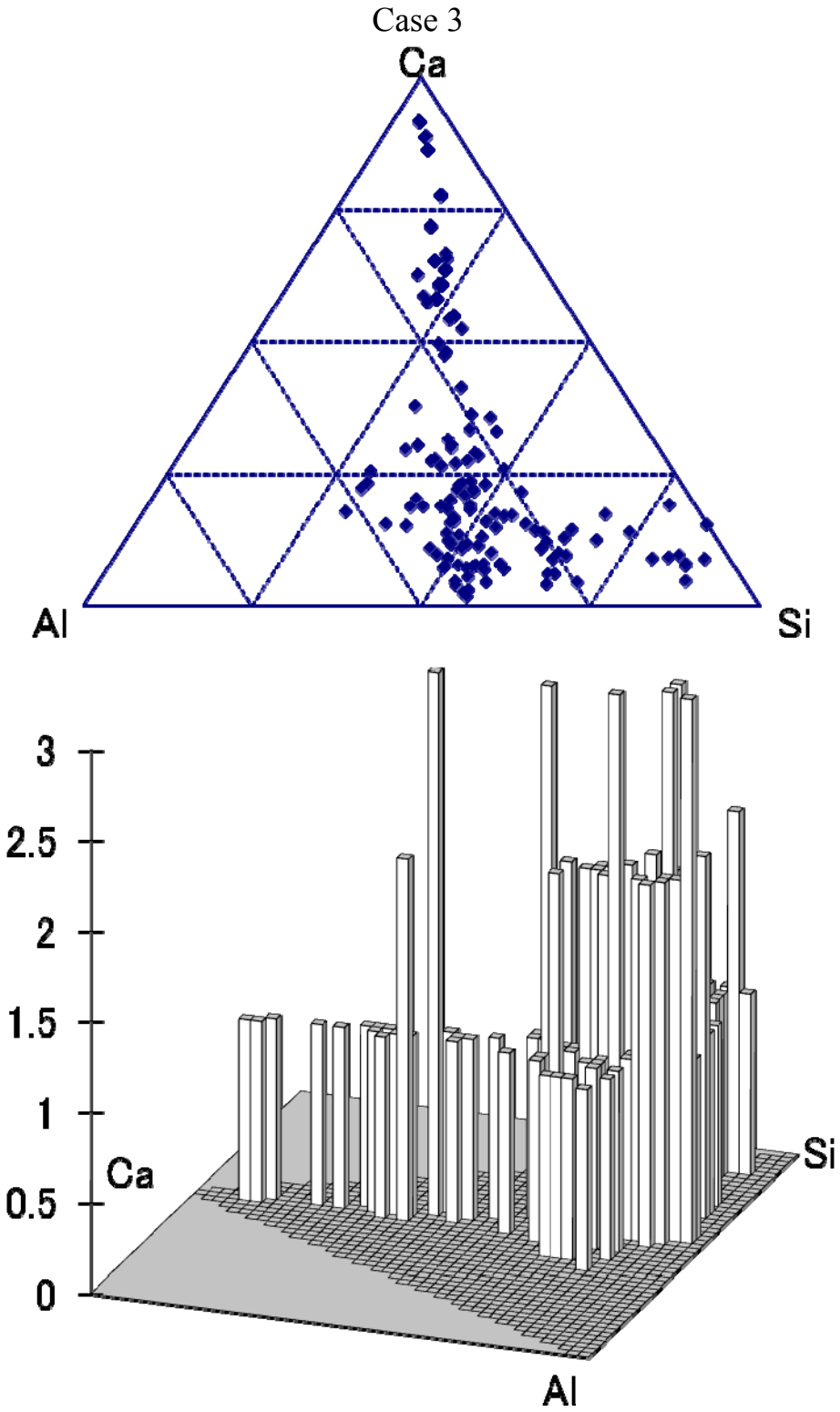

Figure 2.2-56. Ca-Al-Si system. Oxy-coal Case 3. Vertical bars in the lower panel give particle counts.

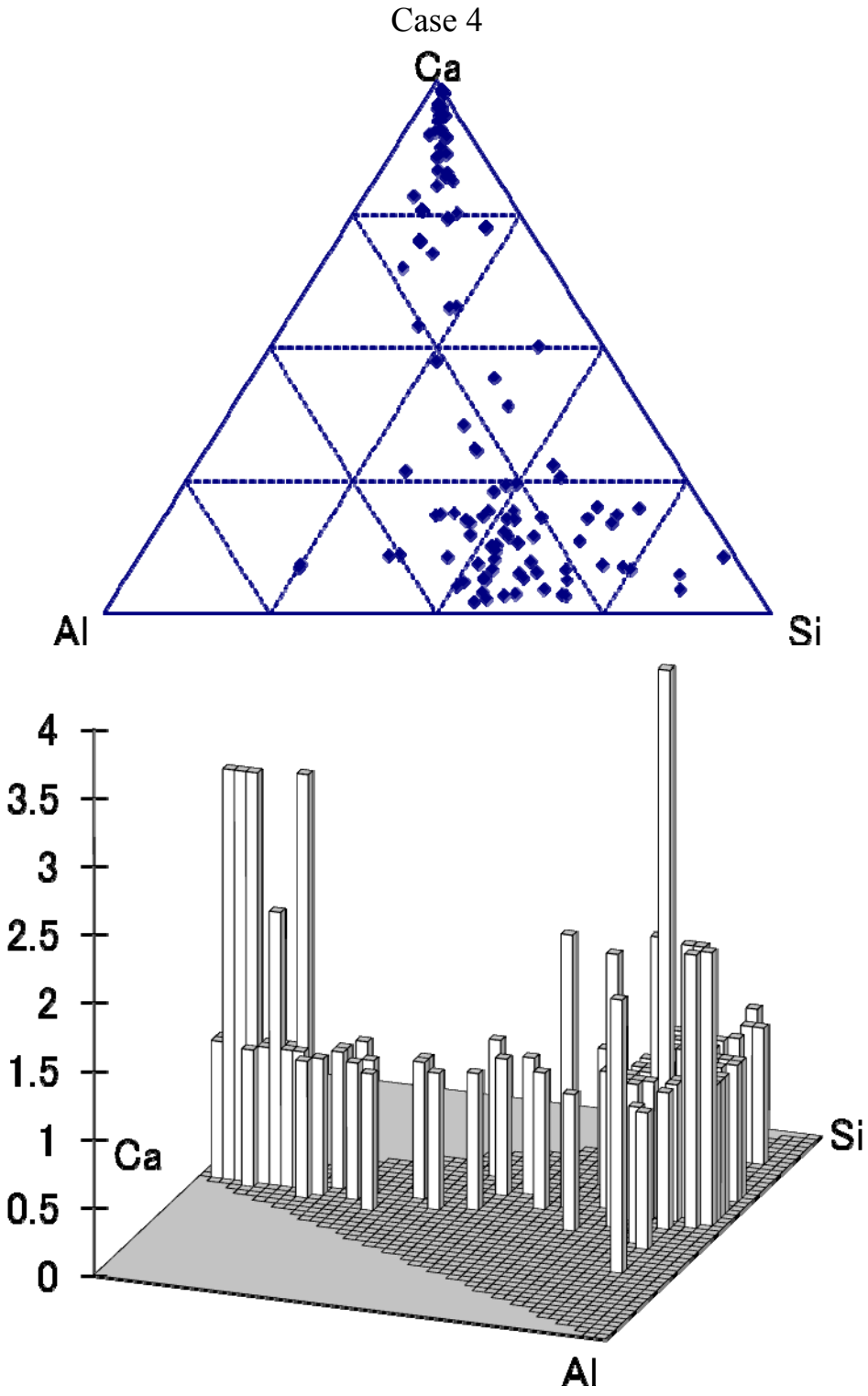

Figure 2.2-57. Ca-Al-Si system. Oxy-coal Case 4. Vertical bars in the lower panel give particle counts.

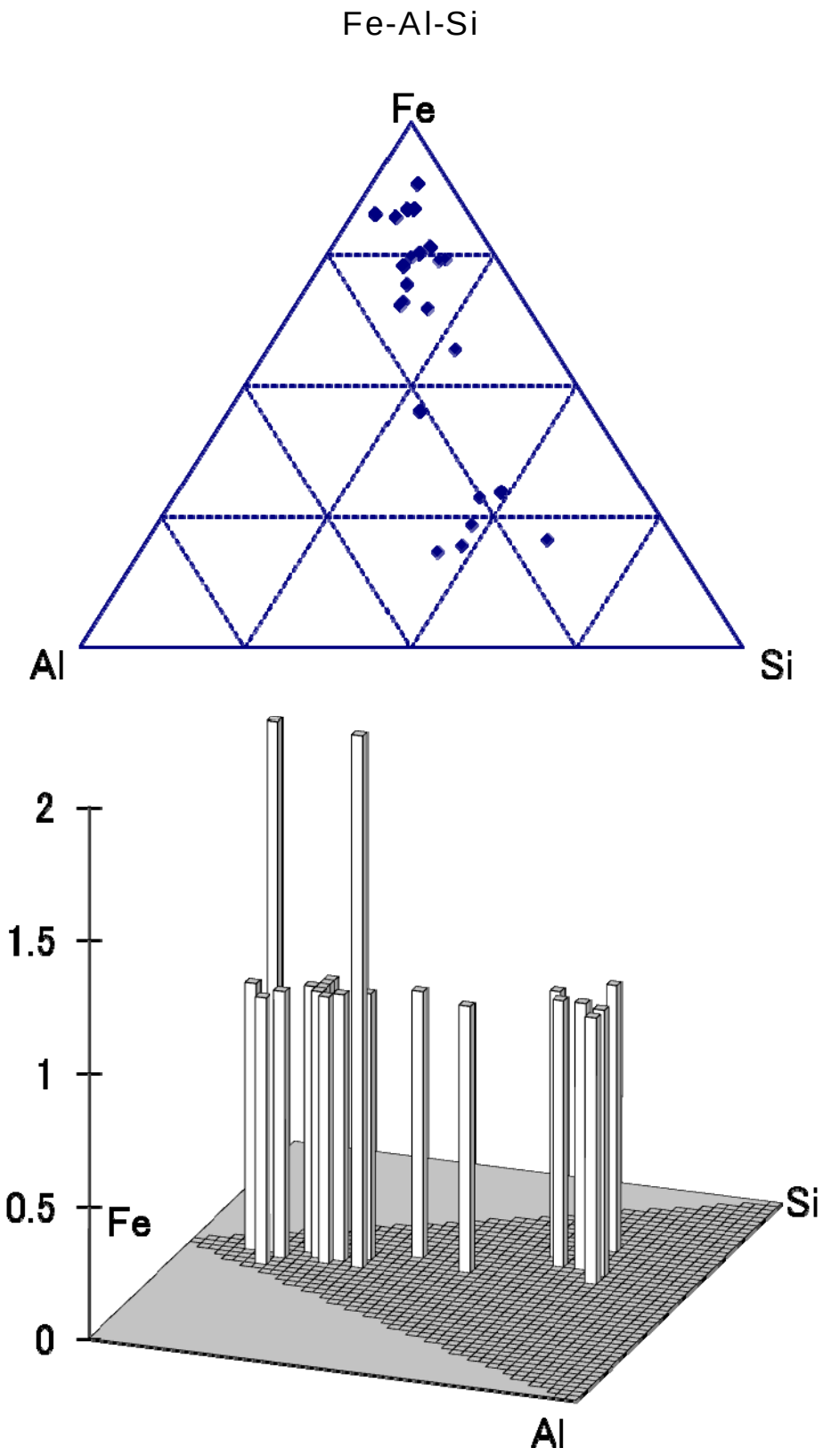

Figure 2.2-58. Fe-Al-Si system. Air Case 1. Vertical bars in the lower panel give particle counts.

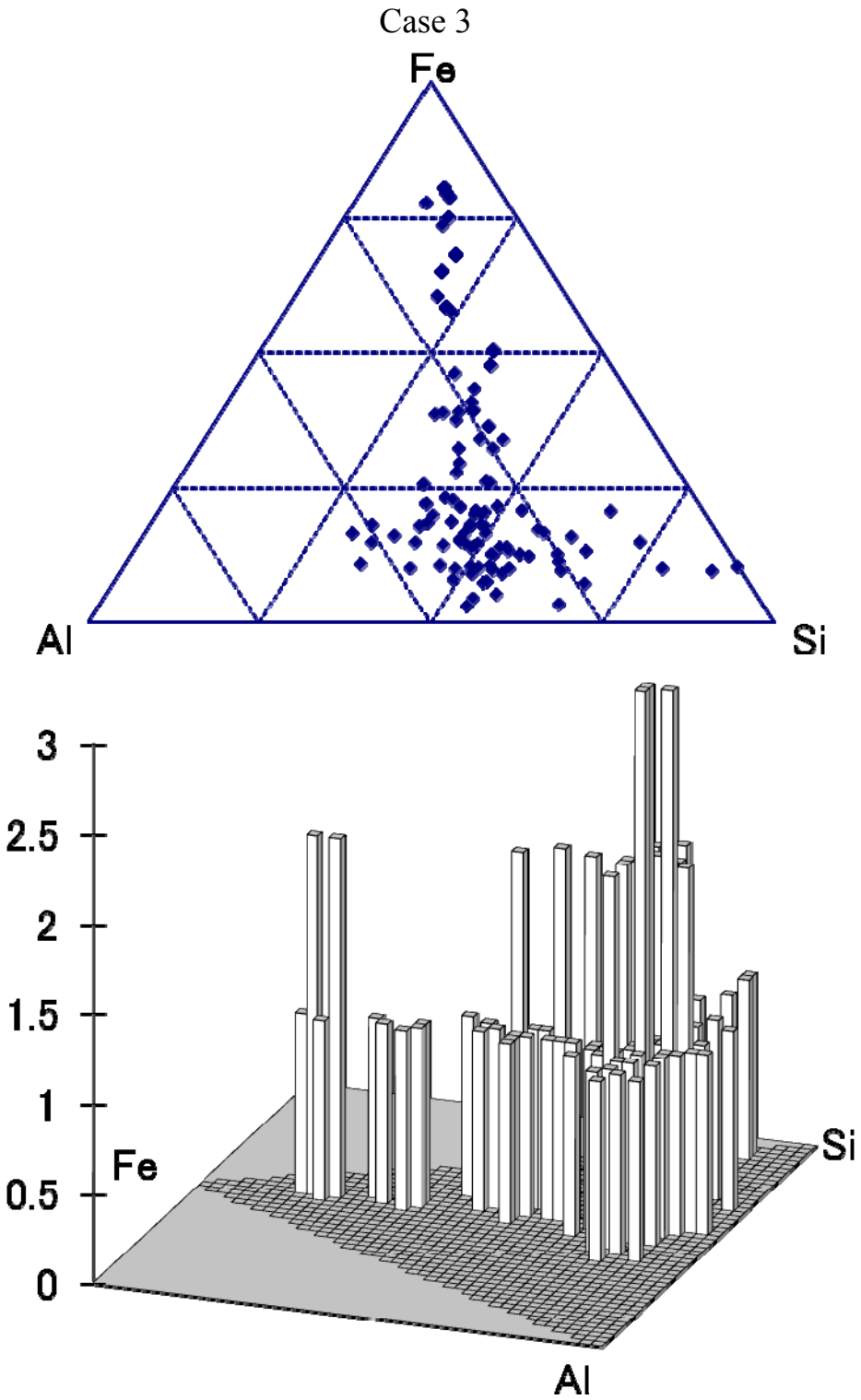

Figure 2.2-59. Fe-Al-Si system. Oxy-coal Case 3. Vertical bars in the lower panel give particle counts.

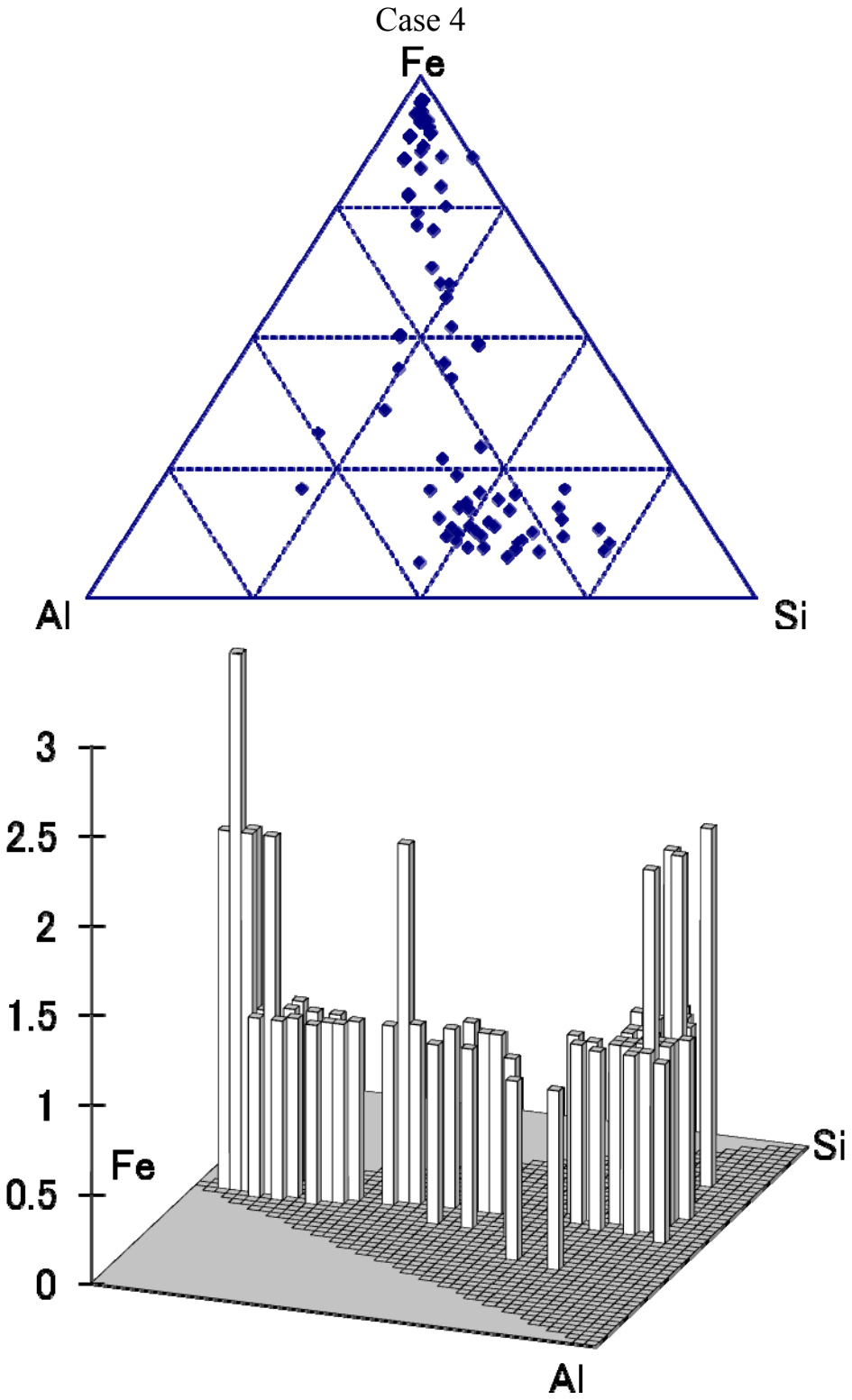

Figure 2.2-60. Fe-Al-Si system, Oxy-coal Case 4. Vertical bars in the lower panel give particle counts.

2.2.4 Conclusions and Future Work

Preliminary data comparing the size segregated ash composition arising from coal combustion in air and from two cases of oxy-coal combustion have been obtained. Experimental techniques have been developed for the extraction of representative samples using low pressure impactors, and for the measurement of sub-micron particle size distributions using electric mobility analyzers. In addition, measurement techniques for LOI and for soot have also been perfected. Remaining issues relate to discrepancies in the chemical analyses of particles collected, where there appears to be some dependence on the analysis method chosen.

These preliminary data suggest that the size segregated composition of fly ash may change when boilers are retrofitted from air-firing to oxy-firing. If confirmed in future work, this might potentially have important consequences on fouling and slagging.

Future work in the near term will focus on completing baseline experimentation with once-through CO_2 used as the diluents. These will use a more stable swirl based coal flame. Remaining analytical discrepancies will be resolved. A system to allow recycle of exhaust gases instead of using fresh carbon dioxide will be designed, and will form the basis for subsequent testing, where ash will be characterized under more realistic oxy-fuel retrofit conditions.

Work has continued on designing and implementing the flue gas recycle system for the OFC to be used in Year 2 testing. System components will include a blower, baghouse with fine bags for near total particulate removal, in-line condenser with caustic solution for SO_2 and water removal, valves installed to allow bypass of the condenser and the baghouse, ESP on the baghouse bypass line. The University of Utah has initiated design and construction of the blower, baghouse, condenser and bypass equipment.

2.2.5 Ash Characterization References

Arnott, W.P., Zielinska, B., Rogers, C.F., Sagebiel, J., Park, K., Chow, J., Moosmuller, H., Watson, J.G., Kelly, K., Wagner, D., Sarofim, A., Lighty, J., and G. Palmer (2005), "Evaluation of 1047-nm Photoacoustic Instruments and Photoelectric Aerosol Sensors in Source-Sampling of Black Carbon Aerosol and Particle-Bound PAHs from Gasoline and Diesel Powered Vehicles", *Envi. Sci. Technol*., 39:5398-5406.

Borrego, A.G., and Alvarez, D. (2007), "Comparison of Chars Obtained under Oxy-Fuel and Conventional Pulverized Coal Combustion Atmospheres", *Energy & Fuels*, **21**:3171-3179.

de Nevers, N.. (2000), Air Pollution Control Engineering, 2nd Edition, McGraw-Hill.

Gallagher, N.B., Bool, L.E., Wendt, J.O.L., Peterson, T.W. (1990), "Alkali Metal Partitioning in Ash from Pulverized Coal Combustion", *Combust. Sci. and Technol*., 74:211-221

Hinds, W.. (1999), Aerosol Technology, 2nd Edition, John Wiley and Sons, Inc.

Seames, W.S., (2003) "An initial study of the fine fragmentation fly ash particle mode generated during pulverized coal combustion", *Fuel Proc Technol.* **81**:109-125.

Seames, W.S., (2000) The Partitioning of Trace Elements During Pulverized Coal Combustion, Doctoral Dissertation, University of Arizona.

2.3 Task 3 – Baseline Char Oxidation Experiments

2.3.1 Summary of Progress

The reacting particle simulation code known as SKIPPY (Surface Kinetics in Porous Particles) was used to investigate particle size effects on the influence of boundary layer reactions on pulverized coal char during oxy-combustion. These effects are not accounted for in current CFD models of coal combustion. The results suggest that boundary layer effects begin to be important for particle sizes greater than 60 micrometers and are greatest for particles around 75 micrometers in size. For particles larger than 100 micrometers, the particles burn close to the diffusion limit and thermal feedback from the boundary layer conversion of CO has a diminishing impact on the char combustion rate. These results show that particle size has a strong influence on the relative importance of boundary layer chemistry to char combustion under oxy-combustion conditions. We anticipate that the range of sizes for which this effect is important will vary somewhat with the reactivity of the coal (i.e., the relevant size range will decrease as the reactivity increases relative to the Pittsburgh seam high-volatile bituminous coal reactivity used in these simulations).

Considering the available standard sieve sizes and the results from the SKIPPY simulations, pulverized samples of the two project coals (Utah Skyline high-volatile bituminous coal and North Antelope PRB subbituminous coal) were sieved into 54-74 μm, 75-105 μm, and 106-125 μm size cuts. In preparation for the conducting of char combustion experiments in our bench-scale optical entrained flow reactor, the particle-sizing pyrometer system was recalibrated for both particle size and particle temperature measurements, using a combination of an optical technique (blackbody source and a chopper wheel embedded with optical reticles) and graphite test particles. The two techniques yielded good agreement in determining the 2-color pyrometry calibration factor, lending confidence in the deduced char particle temperatures. During the remainder of FY09, optical measurements of char particle temperatures, velocities, and sizes will be collected for the three different size cuts of each coal for background oxygen levels varying from 12 – 36%, to provide the necessary data for detailed analysis by SKIPPY in FY10. Furthermore, collection of partially reacted char particles will be performed, to provide direct measurements of char burnout and available surface area.

2.3.2 Detailed Description of Results

Modeling of the steady-state combustion of single, isolated particles was performed using the SKIPPY (Surface Kinetics in Porous Particles) code developed by Brian Haynes of the University of Sydney [1,2]. This program solves the mass conservation equation, the energy equation, and the species conservation equation by considering a multi-component diffusion system and mass convection. From this solution, SKIPPY predicts species concentrations and temperature within the pores of the char, at the outer surface of the char, and within the boundary layer surrounding the char. Both heterogeneous (gas-solid) and gas-phase chemical reactions are considered. We have previously used this model to interpret experimental data on pulverized coal (pc) char NOx formation [3] as well as oxy-fuel combustion of pc char [4].

A particular focus of this task is to develop insight into the effect of boundary layer conversion of CO during oxy-combustion conditions and eventually to develop tractable kinetic expressions that at least approximately account for this effect. An unanswered question is what particle sizes are susceptible to substantial boundary layer chemistry effects. In general, larger particle sizes are expected to be more susceptible because the characteristic diffusion time through the boundary layer is longer for larger particle sizes, providing more time for CO reactions to proceed. However, the relative balance of convective and radiative energy loss and oxygen diffusion to the particle surface means that particle temperatures reach a peak for a certain size and fall-off for both larger and smaller sizes. This existence of a peak particle temperature will influence the size dependence of the boundary layer chemistry effect.

To begin to investigate this size dependence, and to provide guidance for the future conduct of char combustion experiments, SKIPPY simulations were conducted for a high-volatile bituminous coal char when burning in 36% O_2 at a gas temperature of 1723 K (1450 °C) with radiatively cool surroundings. These conditions correspond to typical oxy-combustion conditions in Sandia's entrained flow reactor. The char kinetic rate parameters used in SKIPPY have been adjusted to match the mean Pittsburgh seam high-volatile bituminous coal char particle combustion temperature measured under these conditions. To understand the effect of the elevated CO_2 concentrations on the char combustion process, separate simulations have been conducted for N_2-diluent conditions and CO_2-diluent conditions. Similarly, to understand the impact of boundary layer chemistry on char combustion, separate simulations have been conducted with full homogeneous and heterogeneous chemistry and with only heterogeneous chemistry (i.e., single-film model).

Figure 2.3-1 shows the results for SKIPPY simulations for particle sizes ranging from 50 to 150 μm in a N_2 bath gas. The 50 μm particles show no effect of homogenous chemistry throughout the radial profiles. In contrast, the simulations for larger size particles show substantial effects from homogeneous chemistry, which is seen to increase the particle burning temperature, decrease the oxygen concentrations through the boundary layer and into the particle, dramatically increase the CO_2 concentrations in the vicinity of the particle, and decrease the CO concentrations throughout the computational domain. Close examination of the oxygen profiles shows that particles that are 100 μm or larger are burning near the diffusion limit, with very little oxygen penetration through the particle surface.

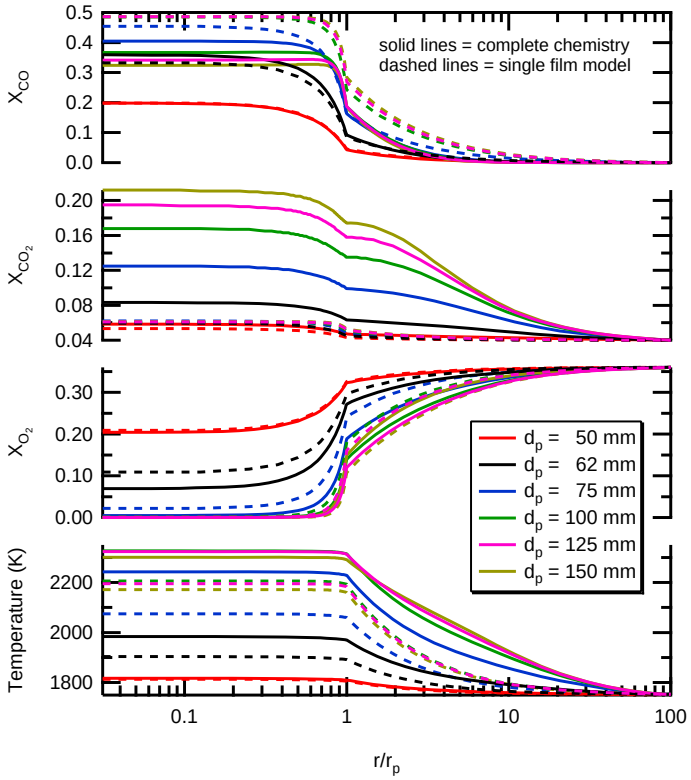

Figure 2.3-1. SKIPPY computed radial profiles of CO, CO_2, and O_2 concentrations and temperature for different particle sizes and for either full chemistry active (solid lines) or only heterogeneous chemistry active (dashed lines). Gas environment: 36% O_2 in N_2, with 14% H_2O.

Figure 2.3-2 shows comparable results for simulations in a CO_2 bath gas. The main differences from the N_2 bath simulations are the ~ 100 K lower particle temperatures during combustion in CO_2 (a consequence of the lower diffusivity of O_2 in CO_2 [4]), and the high free-stream concentration of CO_2, which results in a clear hump of CO_2 in the near-particle region when homogeneous chemistry is active, demonstrating CO_2 production in the gas phase.

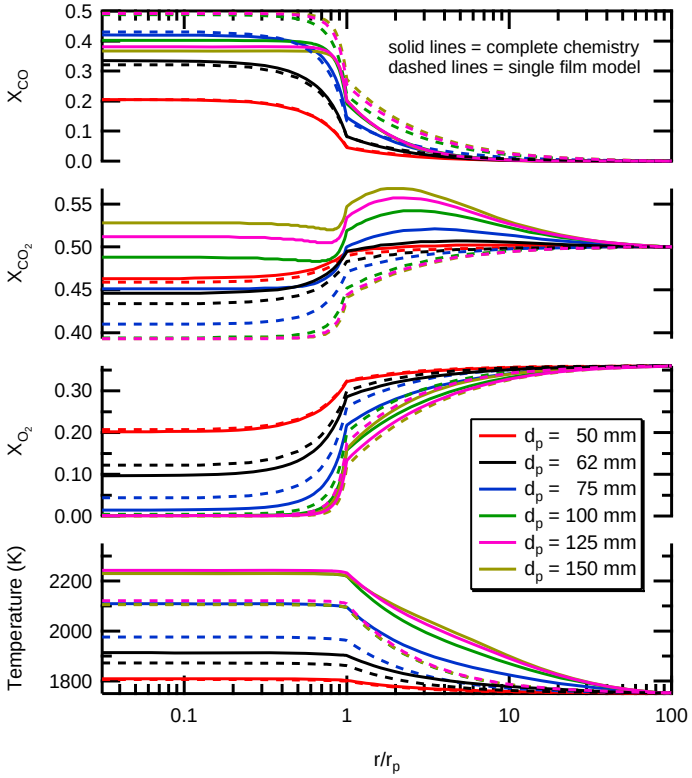

Figure 2.3-2. SKIPPY computed radial profiles of CO, CO_2, and O_2 concentrations and temperature for different particle sizes and for either full chemistry active (solid lines) or only heterogeneous chemistry active (dashed lines). Gas environment: 36% O_2 in CO_2, with 14% H_2O.

Figure 2.3-3 shows a comparison of the particle gasification rate (i.e., burning rate) as a function of the particle size, N_2 vs. CO_2 diluent gas, and the occurrence of gas-phase chemistry. As expected, the CO_2 diluent gas reduces the particle burning rate, except for particles small enough that they are burning with largely kinetic control. Similarly, the presence of homogeneous chemistry (which converts some of the CO to CO_2 in the boundary layer and thereby releases heat) results in higher burning rates, except for small particles (50 μm or smaller in size). Interestingly, the boundary layer chemistry has its largest impact for particles ~75 μm in size and then has a diminishing effect on the char burning rate for particles larger than 100 μm. For particle sizes approaching 150 μm the homogeneous chemistry has an almost negligible impact. This lack of influence for large particles presumably is a consequence of the burning rate approaching the diffusion limit for these larger particles, although the exact mechanism for this limiting influence is unclear.

The results from these SKIPPY simulations suggest that boundary layer chemistry primarily influences oxy-combustion of pc char between 62 and 125 μm in size, at least for high-volatile bituminous coal. For more reactive coal, such as subbituminous coal, we would expect the relevant size range to shift down slightly with size, because the particles burn hotter (and therefore have a higher film temperature where

the relevant homogeneous chemistry occurs) and run into the diffusion limit for smaller size particles. Considering the available standard sieve sizes, it makes the most sense to make measurements of char particle combustion temperatures and char particle burning rates for particles in the following three size ranges: 54-74 μm, 75-105 μm, and 106-125 μm, as they span the range of industrially relevant particle sizes wherein boundary layer chemistry is predicted to be important.

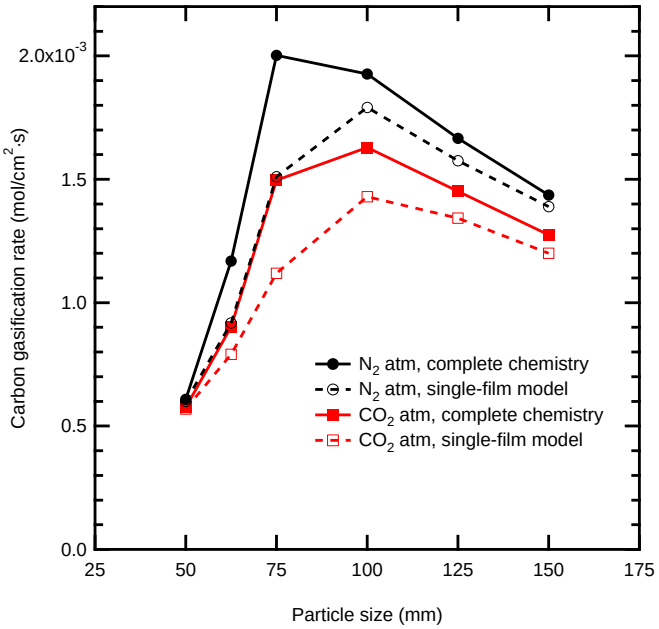

Figure 2.3-3. SKIPPY computed gasification rate, per unit external surface area, for combustion in 36% O_2 in N_2 or CO_2, with 14% H_2O, for either full chemistry active (solid lines) or only heterogeneous chemistry active (dashed lines).

Two low-sulfur coal types are being investigated in this project: Utah Skyline high-volatile bituminous coal and North Antelope PRB subbituminous coal. Samples of these coals were pulverized by Headwaters and have been sieved at Sandia into the three size bins described above.

Before initiating char combustion experiments with these samples, the particle-sizing pyrometer optical system needed to be calibrated for 2-color pyrometry measurements. This calibration has historically been performed using either a tungsten lamp source or a blackbody, in combination with a chopper wheel with embedded reticles that simulates the trajectory of burning particles in the furnace (see Figure 2.3-4). This calibration procedure requires precise optical alignment of the artificial light source with the detection optics and typically requires several days of work to achieve consistent, dependable results. This traditional calibration procedure was successfully completed, but, at the same time, a new and much simpler calibration procedure was developed, which is based on the measured signal ratios from the 2-color pyrometry photomultiplier tubes when unreactive test particles within a narrow size cut are fed into the furnace. This method of calibration is based on a detailed energy balance on these particles, including the thermal inertia, and an accurate measurement of the gas temperature profile through the furnace, as achieved with an ultrafine wire thermocouple with a suitable radiation correction. Unlike the purely optical method of calibration, this approach does not require any modification of the normal configuration for collecting char combustion data and can be easily performed in a few hours time. Figure 2.3-5 shows the results of a typical calibration that was performed with 60 μm graphite test particles. The derived two-color pyrometry calibration factor, shown to be 2.52, agrees with the optically derived calibration of 2.6 within the estimated +/- 0.1 uncertainty in determining the calibration.

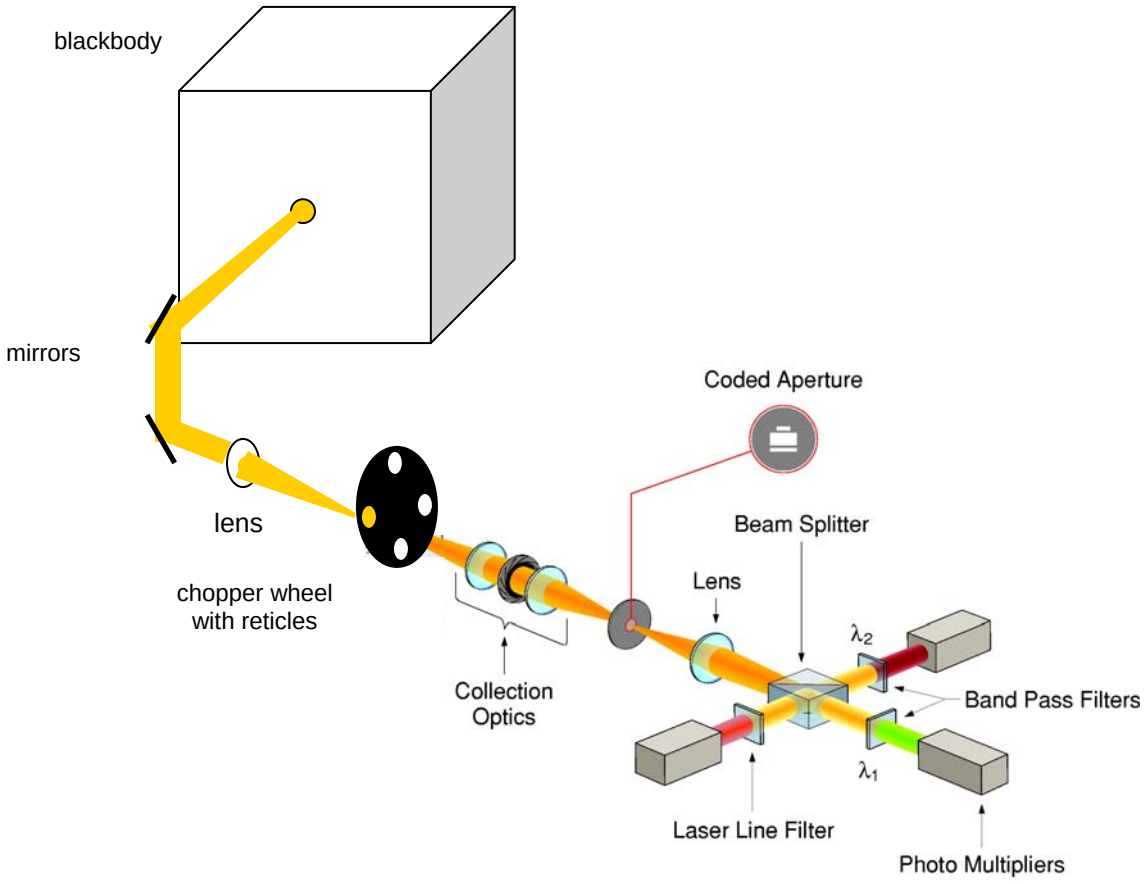

Figure 2.3-4. Schematic diagram of the particle-sizing pyrometry diagnostic, to the right, and the blackbody-based optical calibration system.

Having established the two-color pyrometry calibration factor, experiments will be performed in July and August on combustion of the sieved coal samples. Optical data on particle temperatures, sizes, and velocities will be collected at several different heights during char combustion in 12% O_2, 24% O_2, and 36% O_2 in a simulated flue gas composed of CO_2 and H_2O. Furthermore, a water-cooled, helium-quench sampling probe will collect partially reacted coal char samples at several heights, for determination of char burnout and for analysis of the available surface area, an important factor in making comparisons to SKIPPY modeling predictions. Having collected this important data on particle size effects, work in FY10 will focus on comparing the data to SKIPPY simulations and on developing simplified char combustion expressions that approximately compensate for the deficiencies inherent in using a single-film char combustion model (in which boundary layer chemistry is assumed to be frozen).

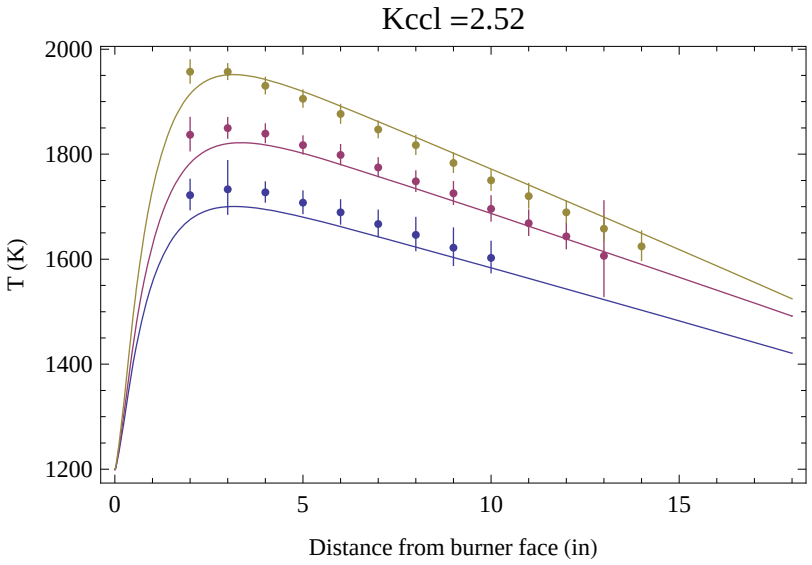

Figure 2.3-5. Best-fit graphite particle temperatures (solid points, derived from the photomultiplier signals) and calculated particle trajectories in the furnace for three different characteristic furnace temperatures.

2.3.3 Char Oxidation References

1. P. J. Ashman, B. S. Haynes, *Improved techniques for the prediction of NOx formation from char nitrogen*, Project No. C4065; Australian Coal Association. CSIRO Energy Technology: North Ryde NSW, Australia, 1999.
2. A. Molina, A.F. Sarofim, W. Ren, J. Lu, G. Yue, J.M. Beer, B.S. Haynes, Combust. Sci. Technol. 174 (2002) 43-71.
3. A. Molina, J.J. Murphy, F. Winter, B.S. Haynes, L.G. Blevins, C.R. Shaddix, Combust. Flame 156 (2009) 574-587.
4. C.R. Shaddix, A. Molina, "Effect of O_2 and High CO_2 Concentrations on PC Char Burning Rates during Oxy-Fuel Combustion," *Proceedings of the 33rd International Technical Conference on Coal Utilization and Fuel Systems*, Clearwater FL, June 1-5, 2008.

2.4 Task 4 – Pilot-Scale Burner Development

2.4.1 Introduction

The existing burner on the University of Utah's pilot-scale furnace is a dual-register, low-NOx burner with a nominal firing rate of 1.47 MW (5 MBtu/hr). The existing low-NO_x burner is detailed in Figure 2.4-1.

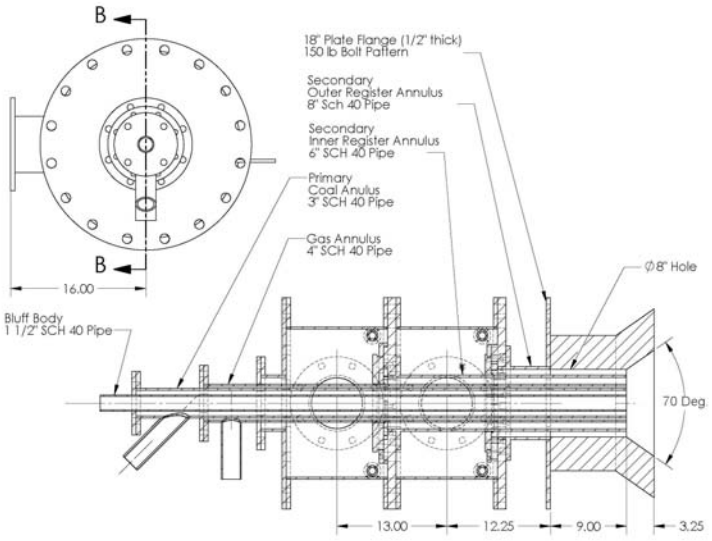

Figure 2.4-1. Low-NO_x burner currently installed on the L1500.

Recently, some effort was focused on more tightly controlling the temperature profile of the furnace and eliminating transient thermal behavior. In accordance with this effort, new cooling panels were installed on the walls of the first four sections of the furnace and the furnace was derated to 1.03 MW (3.5 MBtu/hr). These adjustments were successful in producing a stable furnace temperature profile. However, the velocities at the burner face are now somewhat low, resulting in a stable and attached flame almost irrespective of operating condition. A burner designed for a firing rate of 1.03 MW (3.5 MBtu/hr) would allow stability response to burner operating conditions that is representative of a full-scale commercial burner. In addition to size benefits, the new burner should have integrated hardware for targeted oxygen injection in the primary and in the inner secondary registers.

Directly stated, the design criteria for the oxy-research burner were:

- Flexible mixing strategies for FGR, O_2 and fuel. This capability is inherent in the gas train of the L1500, where O_2 and FGR can be mixed in any ratio, in any register of the burner.
- The flame should be attached within the quarl at operating conditions of 1.03 MW (3.5 MBtu/hr) for both air and oxy-fired operation.
- Hardware should be incorporated for targeted oxygen injection within the primary and the inner secondary registers.

The initial design of the oxy-research burner was based on a patented commercial-scale design by Siemens Energy Inc. This design was reduced to a 1.03 MW (3.5 MBtu/hr) firing rate using a constant velocity scaling technique evaluated by the IFRF [1,2]. The initial design was evaluated and compared to operation of the existing burner using CFD modeling. CFD modeling was then used to evaluate a series of geometry and operational modifications that would allow the burner to meet the design criteria.

2.4.2 Burner Modeling Overview

The following discussion is an overview of the cases that were modeled in support of the design of the oxy-research burner. A total of 19 cases have been modeled. These cases are listed in chronological order in Table 2.4-1 including an identifier and a brief case description. The case identifier includes information about the operating conditions unique to each case for clarity in reporting the results.

The first two cases modeled, LNB-A and LNB-O, were of the existing low-NO_x burner under air and oxy-fired conditions. The purpose of these cases was to identify typical temperatures and radiative heat transfer in the near burner region of the furnace. This information was used in the design of the new burner.

Table 2.4-1. Description of all cases modeled.

Case Identifier	Case Description
LNB-A	Existing Low-NOx Burner (Air-Fired)
LNB-O	Existing Low-NOx Burner (Oxy-Fired)
OXY-A	Oxy-Research Burner, Design 1 (Air-Fired)
OXY-O	Oxy-Research Burner, Design 1 (Oxy-Fired)
OXY-Vel80A	Oxy-Research Burner, Design 1, 24.4 m/s (80 ft/s) Primary (Air-Fired)
OXY-Vel80O	Oxy-Research Burner, Design 1, 24.4 m/s (80 ft/s) Primary (Oxy-Fired)
OXY-Vel70A	Oxy-Research Burner, Design 1, 21.3 m/s (70 ft/s) Primary (Air-Fired)
OXY-Vel70O	Oxy-Research Burner, Design 1, 21.3 m/s (70 ft/s) Primary (Oxy-Fired)
OXY-Vel60A	Oxy-Research Burner, Design 1, 18.3 m/s (60 ft/s) Primary (Air-Fired)
OXY-Vel60O	Oxy-Research Burner, Design 1, 18.3 m/s (60 ft/s) Primary (Oxy-Fired)
OXY-ParA	Oxy-Research Burner, Design 2, 21.3 m/s (70 ft/s) Primary (Air-fired)
OXY-ParO	Oxy-Research Burner, Design 2, 21.3 m/s (70 ft/s) Primary (Oxy-Fired)
OXY-ParLO2	Oxy-Research Burner, Design 2, Low Primary O2 (Oxy-Fired)
OXY-ParPRBA	Oxy-Research Burner, Design 2, PRB Fuel (Air-fired)
OXY-ParPRBO	Oxy-Research Burner, Design 2, PRB Fuel (Oxy-Fired)
OXY-ParREFA	Oxy-Research Burner, Design 2, Refined Mesh (Air-Fired)
OXY-Qua4A	Oxy-Research Burner, Design 2, 10.16 cm (4 in.) Quarl (Air-Fired)
OXY-Qua6A	Oxy-Research Burner, Design 2, 15.24 cm (6 in.) Quarl (Air-fired)
OXY-Qua4O	Oxy-Research Burner, Design 2, 10.16 cm (4 in.) Quarl (Oxy-Fired)

The cases OXY-A and OXY-O were the first air and oxy-fired cases, respectively, modeled of the initial design of the oxy-research burner and the conditions used in the model were those recommended by Siemens for operation of this burner. Based on the OXY-A and OXY-O modeling results it was determined that lower primary velocities should be investigated for a burner of this scale. The next six cases, OXY-Vel80A through OXY-Vel60O, were designed to investigate the behavior of the burner as a function of velocity, under air and oxy-fired conditions. The results of these cases indicated that the air-fired conditions could be used to establish the stability of the burner for specific design criteria and that a 21.3 m/s (70 ft/s) primary velocity was a reasonable compromise between flame stabilization location and typical burner velocities.

The next step in burner design was to reassign the burner shape parameters to accommodate a 21.3 m/s (70 ft/s) primary, a bluff body for targeted oxygen injection in the primary and hardware to inject oxygen

in the inner register of the secondary. Based on these design modifications, five conditions were modeled. The OXY-ParA and OXY-ParO cases incorporated conditions that were expected to be "typical". The OXY-Par LO2 case was used to determine the flame stabilization location at a low primary O_2 concentration. The OXY-ParPRBA and OXY-ParPRBO cases were air and oxy-fired combustion of the PRB coal (resulting in a slightly higher primary velocity). The OXY-ParREFA was designed to investigate the sensitivity of the model to mesh refinement. This case uses identical conditions to the OXY-ParA case but the meshing scheme was refined from about 900,000 cells to approximately 1.9 million cells to evaluate the sensitivity of results to computational grid refinement.

Based on the parametric modeling, it was determined that the flame stabilization location could be pulled closer to the burner by lengthening the quarl. The cases OXY-Qua4A and OXY-Qua6A have identical operating conditions to OXY-ParA with the quarl adjusted from 2 inches to 4 and 6 inches, respectively. The OXY-Qua4O case uses identical conditions to OXY-ParO but with a 4-inch quarl.

2.4.3 Burner Modeling Conditions

The geometry of the oxy-research burner is characteristic of Siemens patented burner design, including a flower shaped primary, flame stabilization tabs and straightening vanes on the inner secondary. A diagram of the burner geometry and key design parameters is detailed in Figure 2.4-2. The values of the key design parameters for cases OXY-A through OXY-Vel60O are included in Table 2.4-2. A 1-inch quarl was used for the OXY-A and OXY-O cases and a 2-inch quarl was used for the remainder of these cases.

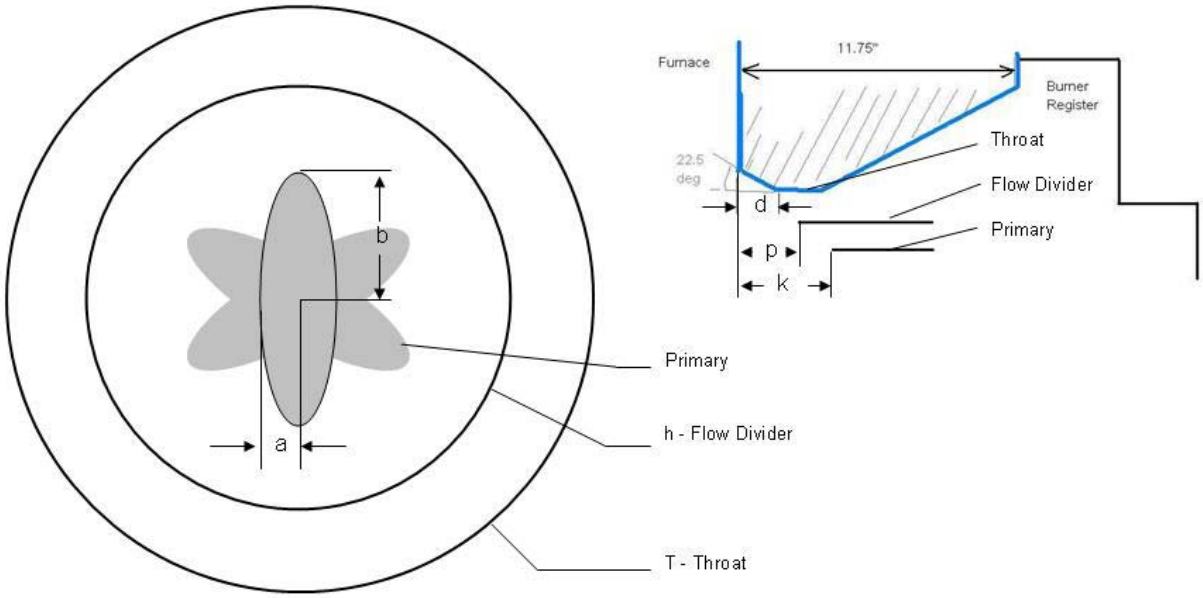

Figure 2.4-2. Initial geometry for the oxy-research burner.

Table 2.4-2. Initial geometry parameters for the oxy-research burner

Parameter	Description	Value (cm)	Value (in.)
a	Ellipse Short Axis	1.12	0.44
b	Ellipse Long Axis	3.71	1.46
	Primary Wall Thickness	0.51	0.2
d	Quarl Depth	2.54 or 5.08	1.0 or 2.0
p	Divider Setback	7.62	3.0
k	Burner Setback	10.16	4.0
h_i	Divider ID	11.44	4.51
h_o	Divide OD	12.40	4.88
t	Throat Diameter	17.15	6.75

Assumed coal compositions were used for the burner design modeling. Although coal suppliers had been determined at this point in the project, analyses of the delivered coals were not yet available. As received analyses from the coal suppliers were used, with the bituminous coal assumed to be dried to 3% moisture and the PRB dried to 10% moisture in the milling process. The compositions used for the purposes of design modeling are detailed in Table 2.4-3.

Table 2.4-3. Assumed coal compositions for all modeling cases.

	After Drying (Fired)	
	Bit. Coal	PRB Coal
C (wt %)	71.31%	63.51%
H (wt %)	5.04%	4.17%
O (wt %)	10.14%	14.42%
N (wt %)	1.28%	0.77%
S (wt %)	0.57%	0.37%
Ash (wt %)	8.66%	6.76%
Moisture (wt %)	3.00%	10.00%
Volatiles (wt %)	40.47	37.24
HHV (kJ/kg)	29114.5	25339.4
HHV (Btu/lb)	12517	10894

The coal particle size distribution was assigned by using size distributions of coals previously processed by Headwaters Energy Services, who is also processing the coals for this project. The size distribution used is detailed in Table 2.4-4 and is assumed to be the same for both coals.

Inlet temperatures for both FGR and Air in the secondary registers were assumed to be 533 K (500 °F) for all cases modeled. The primary gases were assumed to be 338.7 K (150 °F) for all cases. These temperatures are typical operating conditions for the L1500. The conditions for heat transfer were held constant for all cases modeled. These conditions are detailed in Table 2.4-5.

Table 2.4-4. Assumed coal particle size distribution for all modeling.

Size Bin	Diameter (micron)	Mass Fraction
1	6.7	0.025
2	13.4	0.05
3	19.0	0.075
4	25.4	0.1
5	34.1	0.15
6	48.2	0.2
7	69.1	0.15
8	93.6	0.1
9	124.7	0.075
10	173.6	0.05
11	272.2	0.025

Table 2.4-5. Assumed heat transfer conditions for all modeling.

Refractory Wall Emissivity	0.7
Inlet Boundary Emissivity	1.0
Refractory Wall Thermal Resistance (m^2K/W)	0.13
Refractory Wall Skin Temperature (K)	355.4
Inlet Boundary Temperature For Radiation	Gas Temperature
Convective Coil Equivalent Emissivity	0.7
Convective Coil Thermal Resistance (m^2K/W)	0.001
Convective Coil Fluid Temperature (K)	322.0

For the purposes of this modeling effort, the composition of the flue gas recycle was assumed to be constant for all cases, independent of fuel type. A summary of the FGR compositions used is presented in Table 2.4-6.

Table 2.4-6. Recirculated flue gas composition for all modeling.

Based on Bituminous Coal	
O2 (vol %)	3.2
N2 (vol %)	0.6
CO2 (vol %)	83.6
H2O (vol %)	12.4
SO2 (vol %)	0.1

Operating conditions that are unique to cases LNB-A through OXY-O are presented in Table 2.4-7 and conditions that are unique to cases OXY-Vel60A through OXY-Vel80O are presented in Table 2.4-8.

Table 2.4-7. Unique modeling conditions for the existing low-NO_x burner and the initial modeling of the oxy-research burner.

	LNB-A	LNB-O	OXY-A	OXY-O
Firing Rate (MBtu/hr)	3.5	3.5	3.5	3.5
Fuel	Bit. Coal	Bit. Coal	Bit. Coal	Bit. Coal
Oxidizer	Air	O2 + FGR	Air	O2 + FGR
Burner SR	0.9	0.9	0.9	0.9
Total Coal Flow (kg/s)	0.03523	0.03523	0.03515	0.03515
Total Coal Flow (lb/hr)	279.6	279.6	279.0	279.0
Primary Gas / Fuel	1.8	1.8	1.86	2.36
Primary Velocity (m/s)	20.5	14.4	26.8	25.3
Primary Velocity (ft/s)	67.2	47.2	88	83
Primary Flow (kg/s)	0.06342	0.06342	0.06539	0.08281
Primary Flow (lb/hr)	503.3	503.3	519.0	657.2
Inner Sec. Flow (kg/s)	0.06007	0.06656	0.03561	0.02320
Inner Sec. Flow (lb/hr)	476.8	528.3	282.6	184.1
Outer Sec. Flow (lb/hr)	0.18022	0.19968	0.20178	0.21942
Outer Sec. Flow (lb/hr)	1430.3	1584.8	1601.4	1741.4
Primary Feed O2 (wt %)	N/A	24.6%	N/A	17.7%
Inner Sec. Feed O2 (wt %)	N/A	24.6%	N/A	41.9%
Outer Sec. Feed O2 (wt %)	N/A	24.6%	N/A	17.7%

Table 2.4-8. Unique modeling conditions for the oxy-research burner with varying primary velocity.

	OXY-Vel60A	OXY-Vel70A	OXY-Vel80A	OXY-Vel60O	OXY-Vel70O	OXY-Vel80O
Firing Rate (MBtu/hr)	3.5	3.5	3.5	3.5	3.5	3.5
Fuel	Bit. Coal	Bit. Coal	Bit. Coal	Bit. Coal	Bit. Coal	Bit. Coal
Oxidizer	Air	Air	Air	O2 + FGR	O2 + FGR	O2 + FGR
Burner SR	0.9	0.9	0.9	0.9	0.9	0.9
Total Coal Flow (kg/s)	0.035154	0.035154	0.035154	0.035154	0.035154	0.035154
Total Coal Flow (lb/hr)	279.0	279.0	279.0	279.0	279.0	279.0
Primary Gas / Fuel	1.24	1.45	1.65	1.62	1.91	2.21
Primary Velocity (m/s)	18.29	21.33	24.38	18.29	21.33	24.38
Primary Velocity (ft/s)	60	70	80	60	70	80
Primary Flow (kg/s)	0.04355	0.05080	0.05805	0.05707	0.06731	0.07755
Primary Flow (lb/hr)	345.6	403.2	460.7	452.9	534.2	615.5
Inner Sec. Flow (kg/s)	0.03597	0.03597	0.03597	0.02390	0.02390	0.02390
Inner Sec. Flow (lb/hr)	285.5	285.5	285.5	189.7	189.7	189.7
Outer Sec. Flow (kg/s)	0.22637	0.21911	0.21186	0.25705	0.24679	0.23655
Outer Sec. Flow (lb/hr)	1796.6	1739.0	1681.4	2040.1	1958.7	1877.4
Primary Feed O2 (wt %)	N/A	N/A	N/A	27.2%	22.6%	19.3%
Inner Sec. Feed O2 (wt %)	N/A	N/A	N/A	41.0%	41.0%	41.0%
Outer Sec. Feed O2 (wt %)	N/A	N/A	N/A	14.9%	15.7%	16.4%

Following completion of the modeling OXY-Vel60A through OXY-Vel80O, the burner geometry was modified to incorporate a bluff body for targeted oxygen injection in the primary and the parameters for the primary geometry were modified to produce a primary velocity of 21.3 m/s (70 ft/s). The revised burner geometry is detailed in Figure 2.4-3. The geometric parameters for the revised oxy-research burner are included in Table 2.4-9.

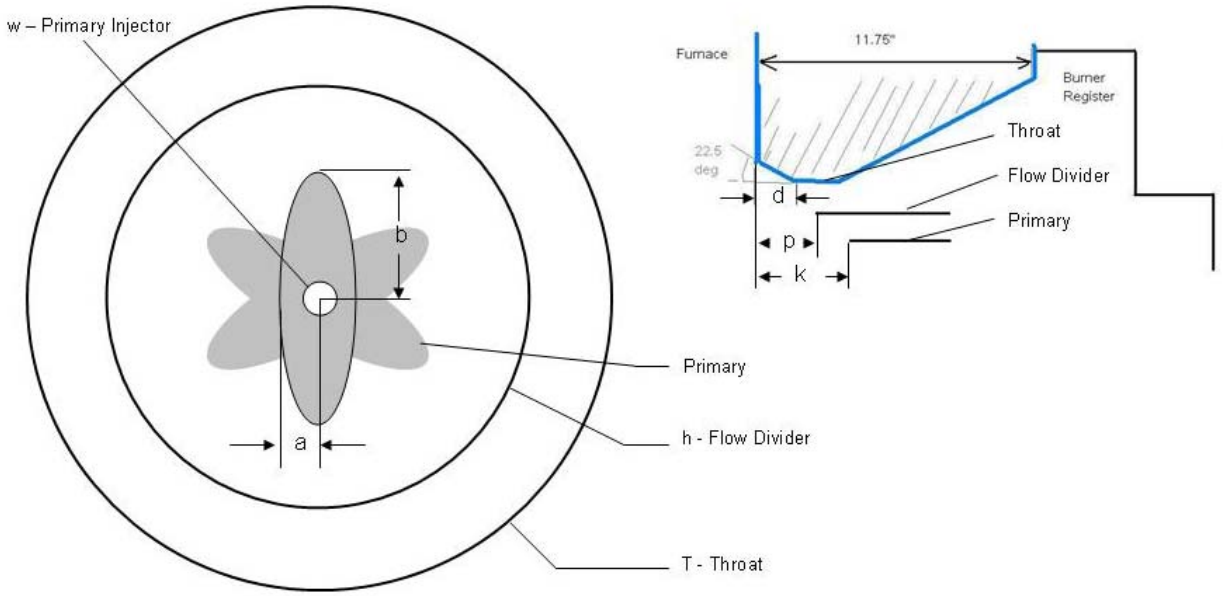

Figure 2.4-3. Revised geometry for the oxy-research burner.

Table 2.4-9. Revised geometry parameters for the oxy-research burner

Parameter	Description	Value (cm)	Value (in.)
a	Ellipse Short Axis	1.40	0.55
b	Ellipse Long Axis	4.29	1.69
	Primary Wall Thickness	0.76	0.3
d	Quarl Depth	5.08*	2.0*
p	Divider Setback	7.62	3.0
k	Burner Setback	10.16	4.0
h_i	Divider ID	12.26	4.825
h_o	Divide OD	13.21	5.2
t	Throat Diameter	17.15	6.75
w	Primary Injector OD	2.13	0.84

*unless otherwise specified.

Operating conditions that are unique to cases OXY-ParA through OXY-ParREFA are presented in Table 2.4-10 and operating conditions that are unique to cases OXY-Qua4A through OXY-Qua4O are presented in Table 2.4-11.

Table 2.4-10. Unique modeling conditions for the oxy-research burner for 21.3 m/s primary velocity and parametric conditions.

	OXY-ParA	OXY-ParO	OXY-ParLO2	OXY-ParPRBA	OXY-ParPRBO	OXY-ParREFA
Firing Rate (MBtu/hr)	3.5	3.5	3.5	3.5	3.5	3.5
Fuel	Bit. Coal	Bit. Coal	Bit. Coal	PRB	PRB	Bit. Coal
Oxidizer	Air	O2 + FGR	O2 + FGR	Air	O2 + FGR	Air
Burner SR	0.91	0.91	0.91	0.91	0.91	0.91
Total Coal Flow (kg/s)	0.03515	0.03515	0.03515	0.04048	0.04048	0.03515
Total Coal Flow (lb/hr)	279.0	279.0	279.0	321.3	321.3	279.0
Primary Gas / Fuel	1.88	2.45	2.52	1.88	2.44	1.88
Primary Velocity (m/s)	21.9	21.0	21.0	25.0	24.4	21.9
Primary Velocity (ft/s)	72	69	69	82	80	72
Primary Flow (kg/s)	0.06606	0.08606	0.08859	0.07610	0.09877	0.06606
Primary Flow (lb/hr)	524.3	683.0	703.1	604.0	783.9	524.3
Inner SA Flow (kg/s)	0.03597	0.02390	0.02500	0.03401	0.02201	0.03597
Inner SA Flow (lb/hr)	285.5	189.7	198.4	269.9	174.7	285.5
Outer SA Flow (kg/s)	0.20384	0.22805	0.22442	0.19272	0.20968	0.20384
Outer SA Flow (lb/hr)	1617.8	1809.9	1781.1	1529.5	1664.1	1617.8
Primary Feed O2 (wt %)	N/A	17.1%	5.6%	N/A	17.3%	N/A
Inner Sec. Feed O2 (wt %)	N/A	41.0%	47.0%	N/A	41.2%	N/A
Outer Sec. Feed O2 (wt %)	N/A	17.1%	20.8%	N/A	17.3%	N/A
Primary SR	0.1961	0.2133	0.0919	0.2297	0.2515	0.1961

Table 2.4-11. Unique modeling conditions for the oxy-research burner for 21.3 m/s primary and varying quarl depth.

	OXY-Qua4A	OXY-Qua6A	OXY-Qua4O
Firing Rate (MBtu/hr)	3.5	3.5	3.5
Fuel	Bit. Coal	Bit. Coal	Bit. Coal
Oxidizer	Air	Air	O2 + FGR
Burner SR	0.91	0.91	0.91
Total Coal Flow (kg/s)	0.03515	0.03515	0.03515
Total Coal Flow (lb/hr)	279.0	279.0	279.0
Primary Gas / Fuel	1.88	1.88	2.45
Primary Velocity (m/s)	21.9	21.9	21.0
Primary Velocity (ft/s)	72	72	69
Primary Flow (kg/s)	0.06606	0.06606	0.08606
Primary Flow (lb/hr)	524.3	524.3	683.0
Inner Sec. Flow (kg/s)	0.03597	0.03597	0.02309
Inner Sec. Flow (lb/hr)	285.5	285.5	189.7
Outer Sec. Flow (kg/s)	0.20384	0.20384	0.22805
Outer Sec. Flow (lb/hr)	1617.8	1617.8	1809.9
Primary Feed O2 (wt %)	N/A	N/A	17.1%
Inner Sec. Feed O2 (wt %)	N/A	N/A	41.0%
Outer Sec. Feed O2 (wt %)	N/A	N/A	17.1%

2.4.4 Burner Modeling Results

The first step in the design process was to model the existing burner and the initial oxy-research burner under air and oxy-fired conditions. Temperature and CO concentration plots were generated from the modeling results and used to determine the flame stabilization location. A temperature plot of the furnace cross section (viewed from the side) in the near burner region is presented in Figure 2.4-4 for cases LNB-A through OXY-O. The CO concentration plots for the same cases are presented in Figure 2.4-5. It is apparent from comparing the LNB-A and LNB-O cases that the adiabatic flame temperature is slightly lower for the oxygen case. This is an expected result since a 27 vol% O_2 is used in the overall mixture of the O_2 and FGR. This condition is chosen to match overall heat transfer, not flame temperature and the results are consistent with results in other studies.

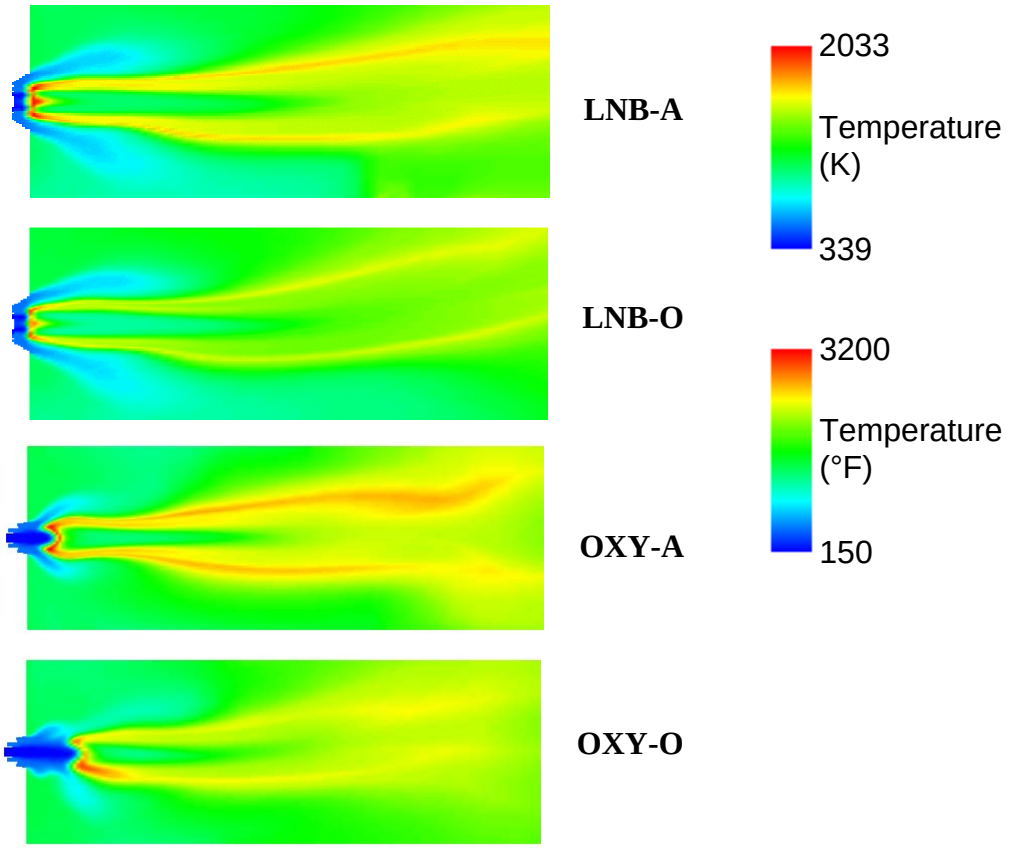

Figure 2.4-4. Temperature plots for cases LNB-A through OXY-O.

It is also apparent from the modeling results that the flame stabilizes at the quarl outlet with the existing, low-NO_x burner for both the air and oxy-fired cases. The initial oxy-research burner design has a flame stabilization location that is well outside the quarl for both the air and the oxygen cases, but the standoff distance is much greater for the oxygen case. The CO concentration plots provide a clear picture of the flame stabilization location and indicate that the initial oxy-research burner design requires modification. Some factors that are expected to contribute to this standoff distance include: a very short quarl, 2.54 cm (1 in.) compared to 8.9 cm (3.5 in.) in the LNB, high primary velocities, almost 27.4 m/s (90 ft/s) compared to 15.2 and 21.3 m/s (50 to 70 ft/s), and significant space within the LNB for the gases to expand, caused by a large bluff body and an unused gas annulus between the primary and inner secondary registers.

The asymmetry of the flame in all conditions is due to buoyancy of the hot flue-gas and the effect of gravity on large versus small particles (large particle are actually deposited on the floor of the furnace, where they continue to oxidize).

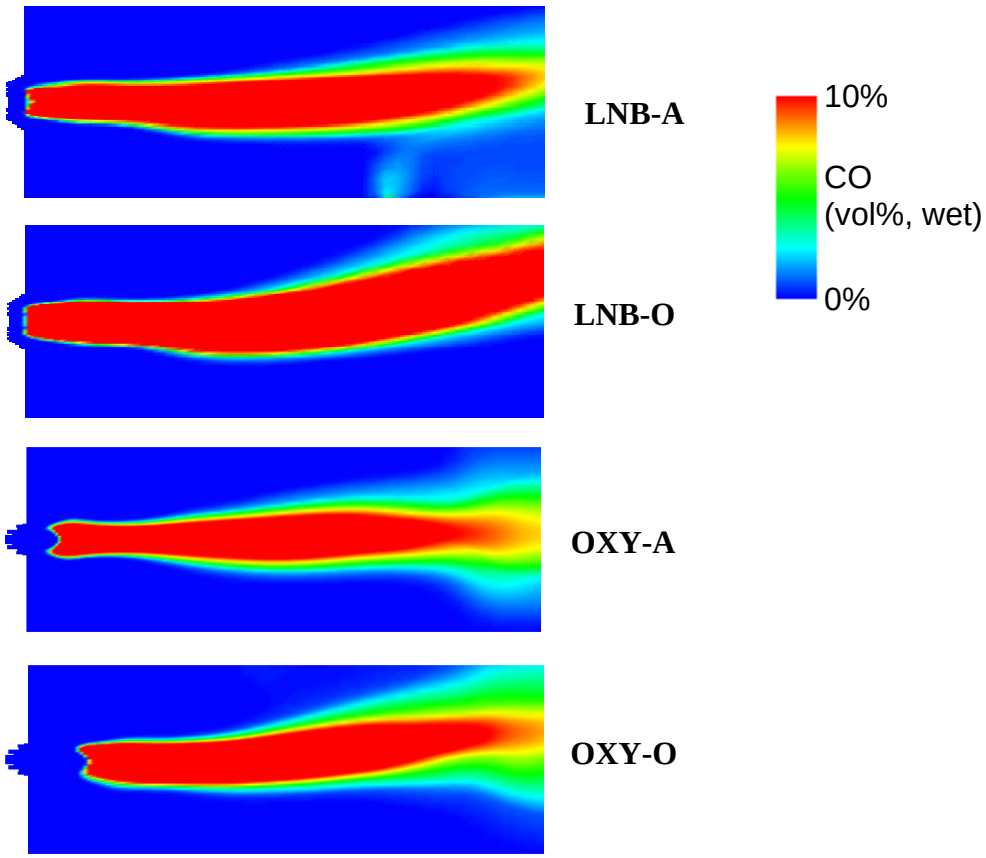

Figure 2.4-5. CO concentration plots for cases LNB-A through OXY-O

The next round of modeling investigated the impact of primary gas velocity on flame stabilization location. The geometry of the burner was held static for these simulations, with the exception of the quarl depth which was increased from 2.54 to 5.08 cm (one to two inches). Gas was removed from the primary and distributed to the inner and outer secondary registers, while maintaining the ratio of flow between the inner and outer register. The drawback to this approach is that the primary oxidizer gas / fuel ratio is not constant for each case. As the primary velocity decreases, there is less oxidant available to the fuel in the primary. These two variables were expected to counteract each other to a degree. The temperature plots for cases OXY-Vel80A through OXY-Vel60O are presented in Figure 2.4-6 and the CO concentration plots are provided in Figure 2.4-7.

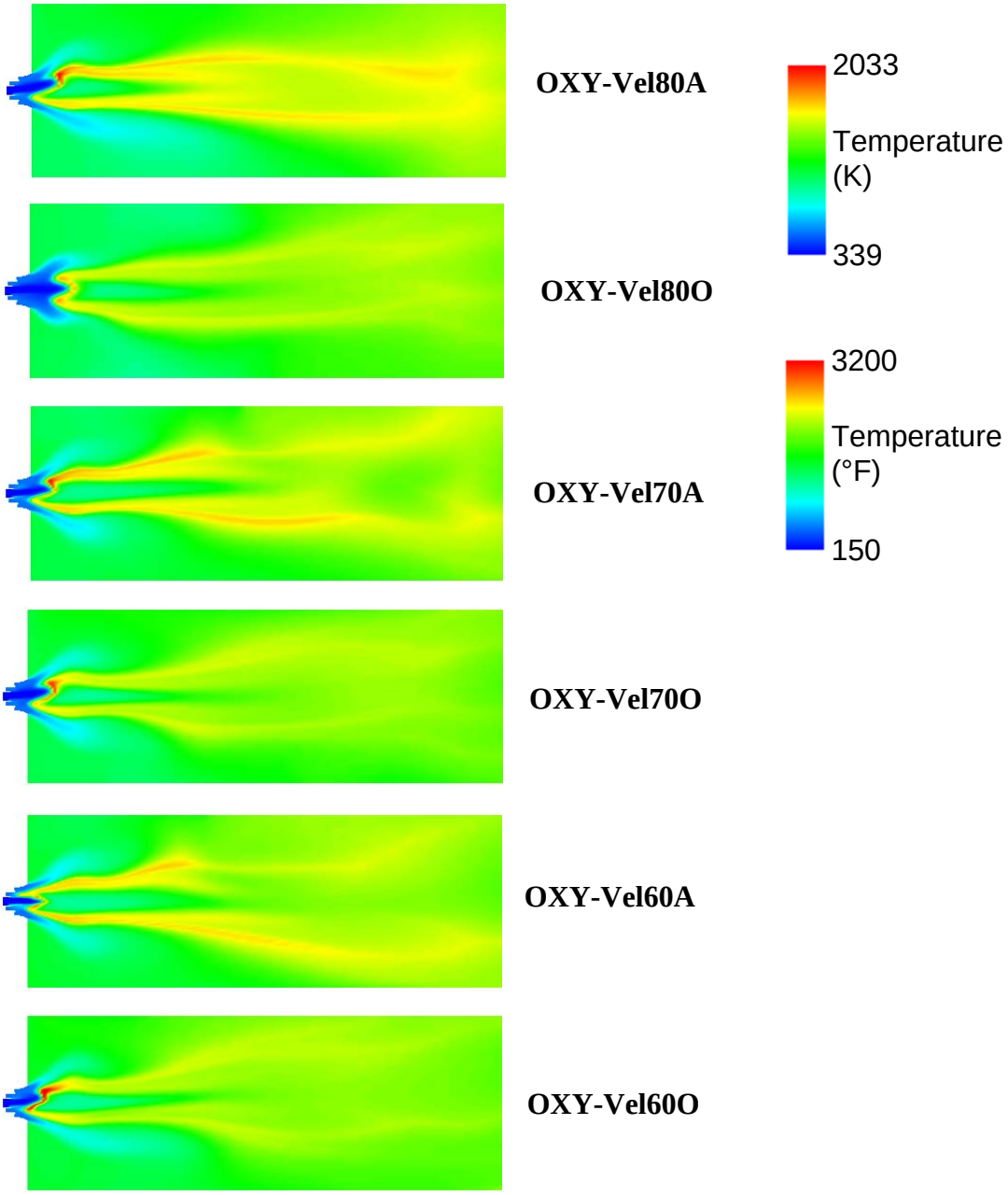

Figure 2.4-6. Temperature plots for cases OXY-Vel80A through OXY-Vel60O.

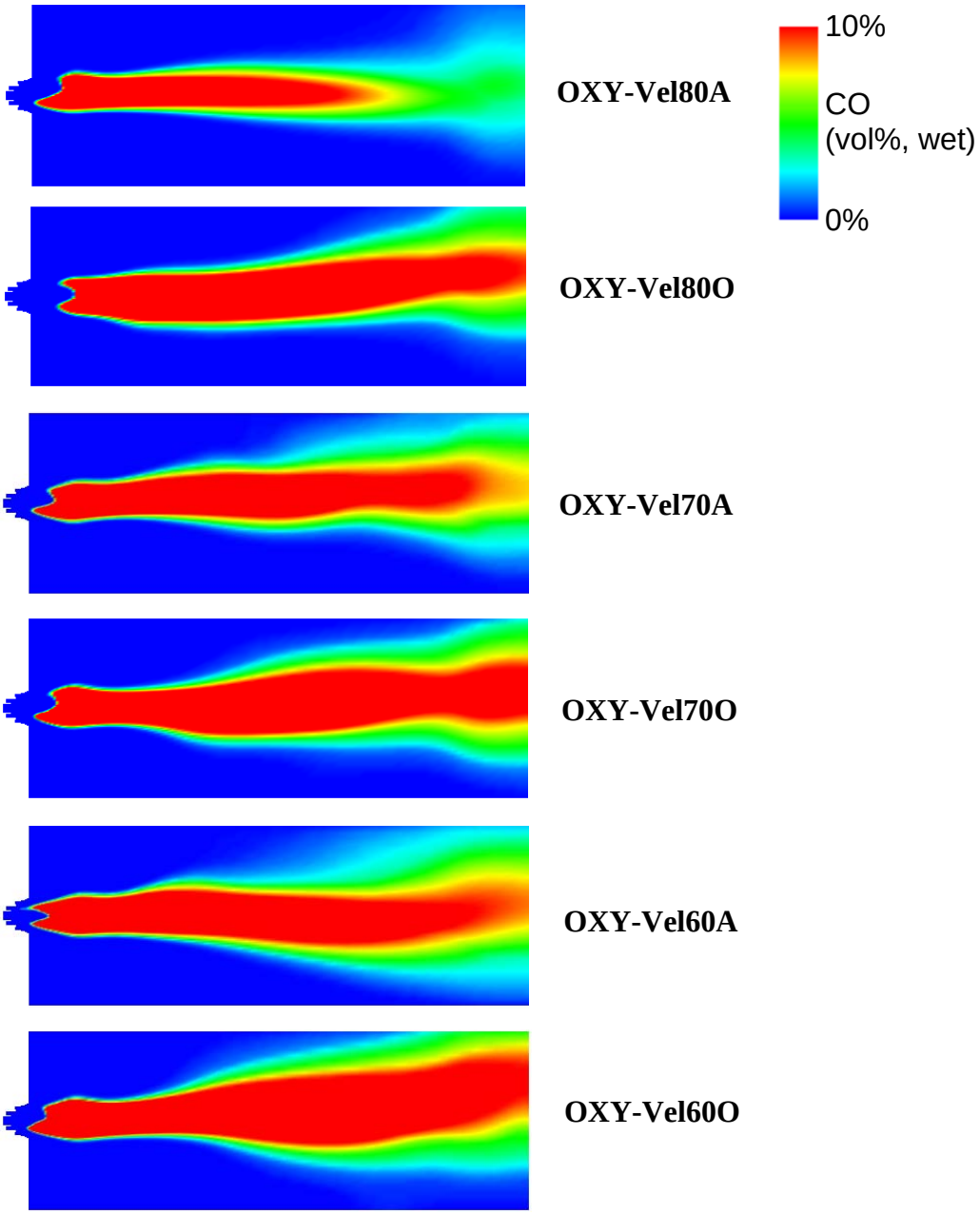

Figure 2.4-7. CO concentration plots for cases OXY-Vel80A through OXY-Vel60O.

The results from the primary velocity cases show that the flame stabilization location is more strongly tied to the primary velocity than to the primary gas / fuel ratio. While the 24.4 m/s (80 ft/s) air-fired case shows that the flame originates inside the quarl, the oxy-fired case is still detached. Both of the 21.3 m/s (70 ft/s) cases have flames originating in the quarl. Although the 18.3 m/s (60ft/s) case is well attached inside the quarl, this velocity is too low to represent full-scale burner behavior. Based on these results, it was decided that a primary velocity of 21.3 m/s (70 ft/s) could provide an appropriate flame stabilization location. Another curious trait of the velocity modeling is the asymmetry of the burner in the near-quarl region. This is likely due to operating conditions that could result in an unstable (fluttering) flame location.

The next step was to redesign the burner geometry to include a bluff body for targeted oxygen injection in the primary and to produce a primary gas velocity of 21.3 m/s (70 ft/s). This new geometry was modeled for typical air and oxygen conditions and for conditions where the flame standoff distance may be greater. These conditions included firing with a PRB coal and a condition where a minimum concentration of oxygen was used in the primary during oxy-combustion. The minimum concentration of oxygen was determined using patents for low-NO_x burner operation by Anderson [3]. The OXY-ParA case was also re-run with significant refinement in the meshing strategy in order to determine the impacts of modeling approach on flame stabilization location. The temperature plots for cases OXY-ParA through OXY-ParREFA are presented in Figure 2.4-8 and the CO concentration plots for the same cases are presented in Figure 2.4-9.

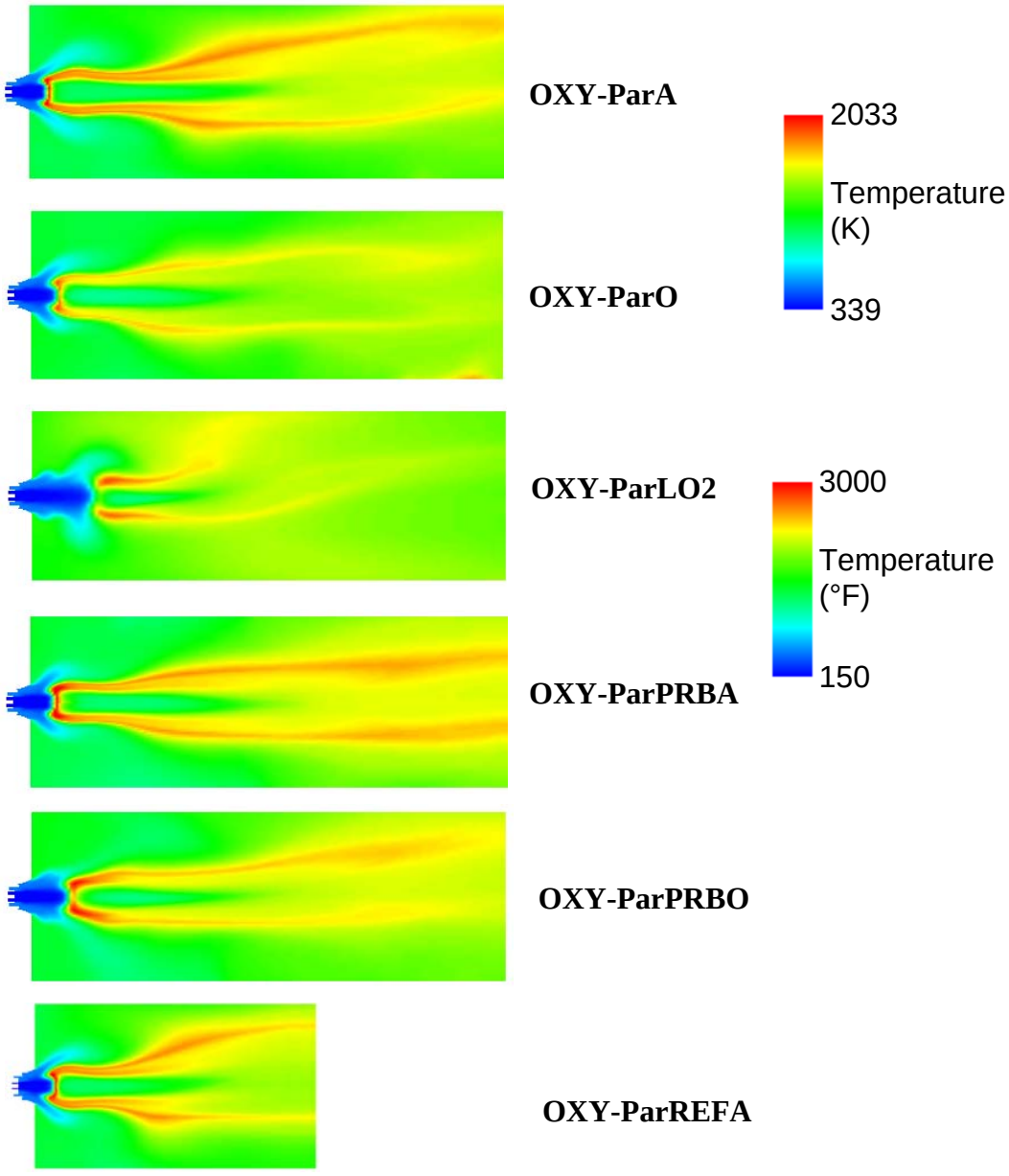

Figure 2.4-8. Temperature plots for cases OXY-ParA through OXY-ParREFA.

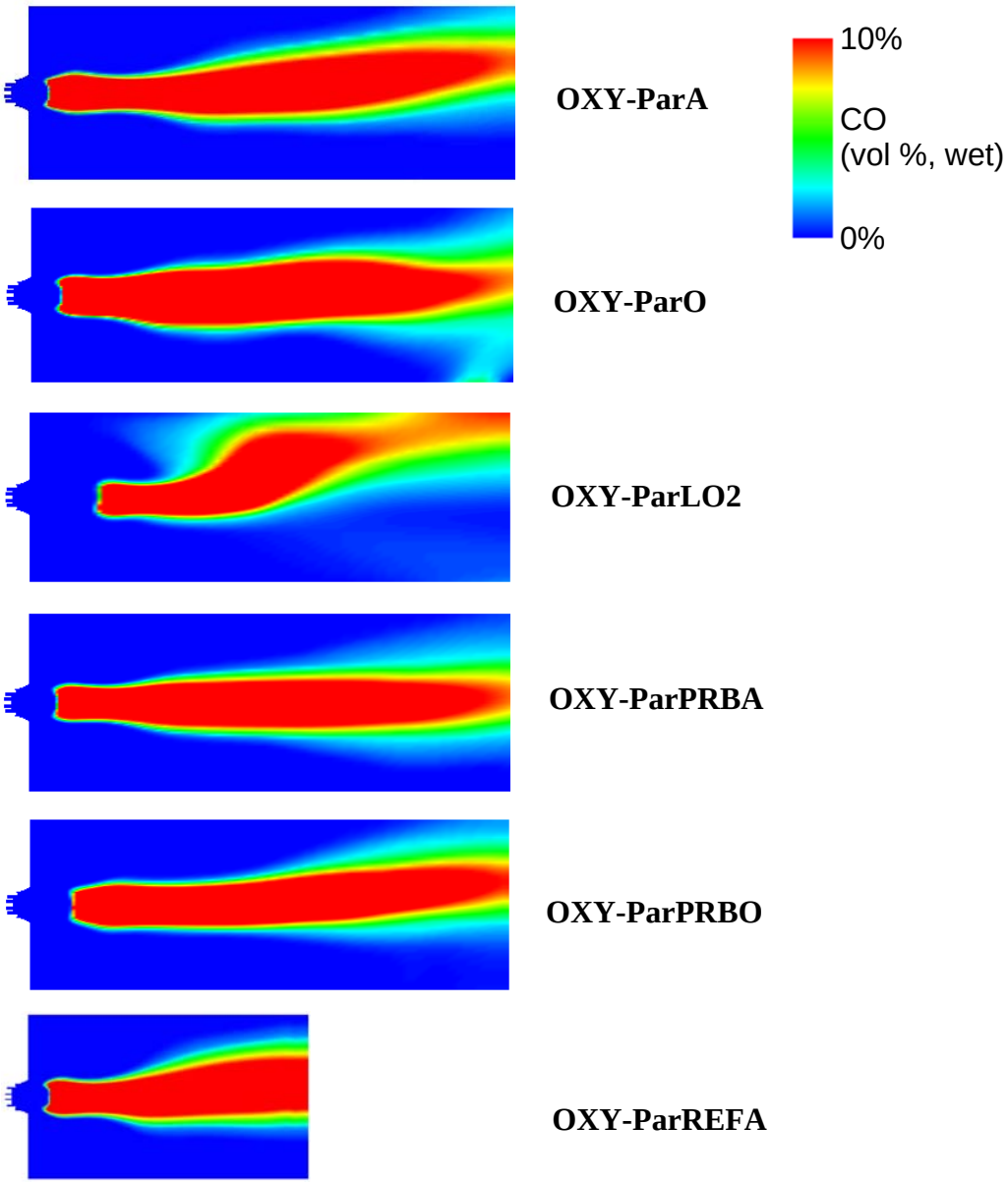

Figure 2.4-9. CO concentration plots for cases OXY-ParA through OXY-ParREFA.

These results indicate that the revisions to the geometry are not sufficient to attach a flame inside the quarl. Cases Oxy-ParA and OXY-ParO have flames that are still detached. In addition, the low-oxygen case has a flame that is substantially blown off. Firing the PRB coal pushed the flame back slightly for the air case and more significantly for the oxygen case. The refined mesh model produced essentially the same results for the flame position as the coarse mesh model, indicating that the chosen level of refinement used in the model is appropriate.

The next step was to investigate the impact of quarl depth on flame stabilization location. In the previous modeling, the quarl depth was 5.08 cm (two inches). The existing low-NO_x burner has a quarl depth of

8.9 cm (3.5 inches). For the next modeling runs, 10.16 and 15.24 cm (four and six inch) quarls were tested. The temperature plots for cases OXY-Qua4A through Oxy-Qua4O are presented in Figure 2.4-10 and the CO concentration plots for the same cases are presented in Figure 2.4-11. The OXY-ParA case is also included in these plots to include the 5.08 cm (2 in.) quarl for comparison. These plots are aligned such that the face of the burner in each plot is aligned and therefore the face of the quarl (and end wall of the furnace) is in a different relative position. In this way the distance from the burner face to the flame stabilization location can more easily be seen.

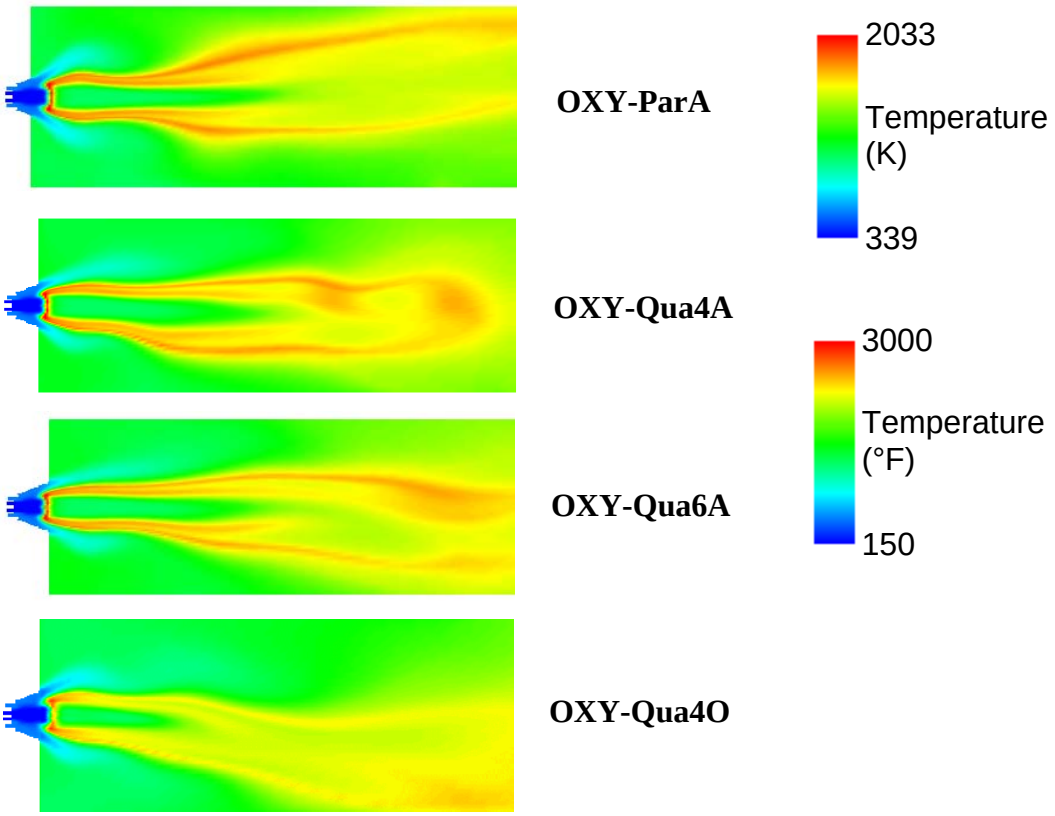

Figure 2.4-10. Temperature plots for cases OXY-Qua4A through OXY-Qua4O, with case OXY-ParA plotted for comparison.

As the burner quarl is extended, the quarl moves out toward the flame and the flame moves slightly back toward the face of the burner. A more quantitative analysis displayed that a 5.08 cm (two inch) increase in the depth of the burner quarl moves the flame back towards the burner face by approximately 1.27 cm (half inch), in a linear relationship. These results show that the 10.16 cm (4 inch) quarl promotes flame stabilization at the outlet of the quarl and the 15.24 cm (six inch) quarl has a flame well inside.

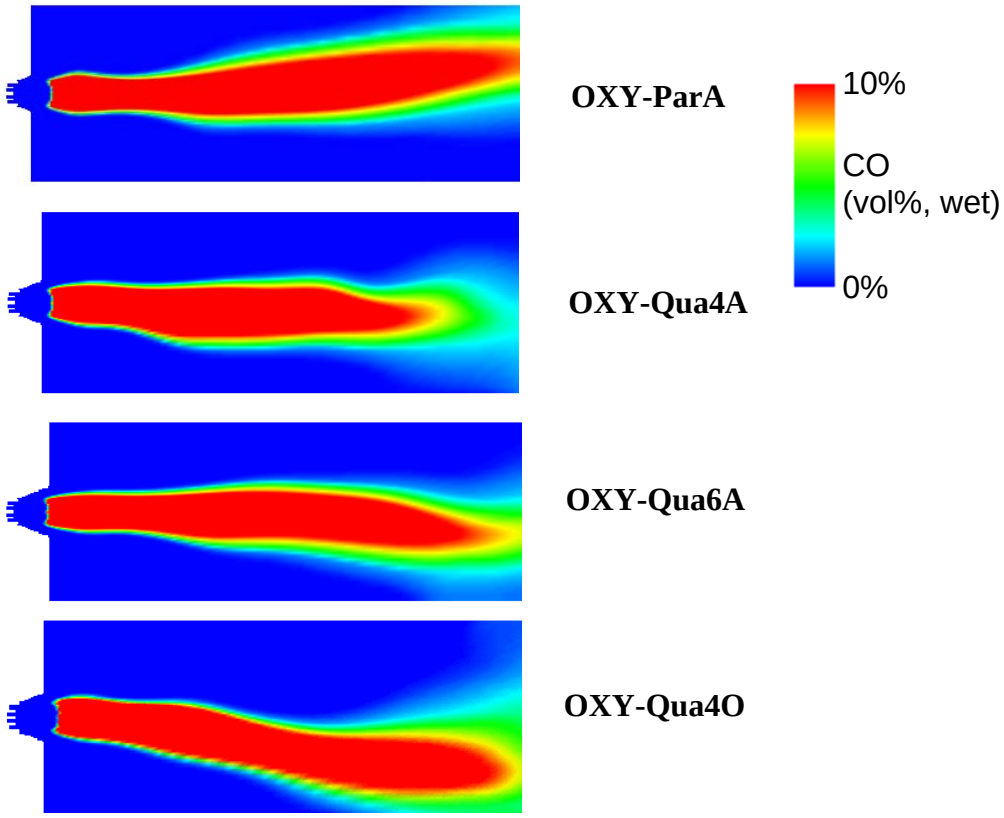

Figure 2.4-11. CO concentration plots for cases OXY-Qua4A through OXY-Qua4O, with case OXY-ParA plotted for comparison.

Based on these modeling results it was decided that the modified geometry with the 4 inch quarl would meet the criteria for flame stabilization location. Finally, the behavior of the existing low-NO_x burner and the oxy-research burner are compared with temperature plots in Figure 2.4-12 and with CO concentration plots in Figure 2.4-13.

From these results it can be seen that the flame stabilization location is very similar for the existing and the oxy-research burner. However, it appears that the flame length is shorter for the oxy-research burner.

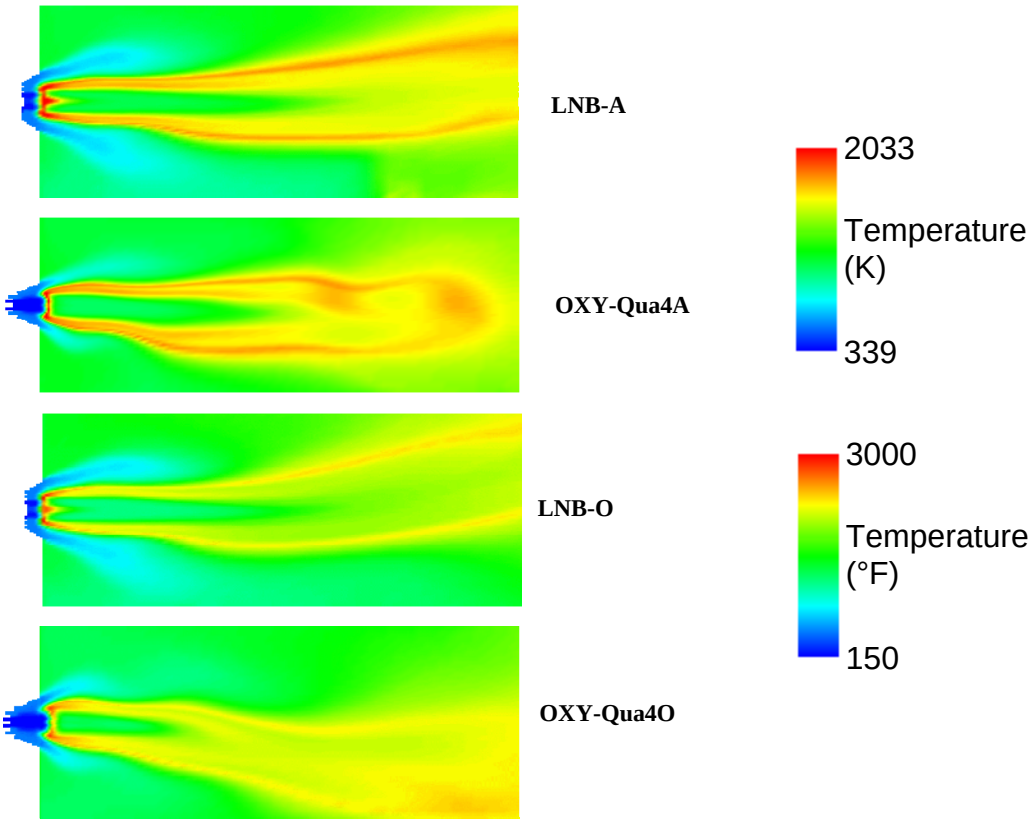

Figure 2.4-12. Temperature plots for the existing low-NO_x burner compared to the finalized design of the oxy-research burner under air and oxy-fired conditions.

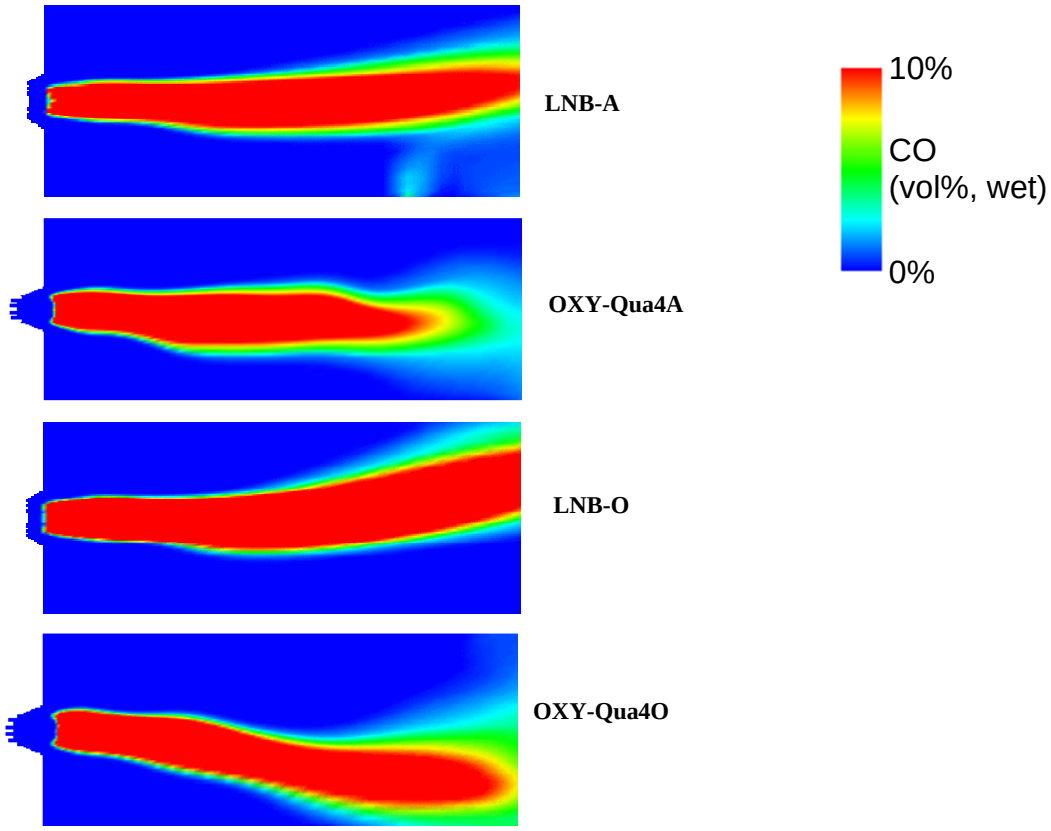

Figure 2.4-13. CO concentration plots for the existing low-NO_x burner compared to the finalized design of the oxy-research burner under air and oxy-fired conditions.

2.4.5 Burner Modeling Summary

CFD modeling results suggested that the constant velocity scaling method did not produce the desired flame behavior for the oxy-research burner. Using this method of design resulted in a flame stabilization location that was well outside the burner quarl. In an effort to correct this behavior, the primary gas velocity was reduced, the quarl was lengthened and the burner face setback relative to the quarl was lengthened. These modifications produced a flame stabilization location that was in the desired location at the quarl outlet.

These results suggest that the dominating parameter governing flame shape and stability is not solely velocity. In an effort to more plainly understand the burner behavior, the modeling results were analyzed for average particle temperature as a function of position in the furnace. These data were generated and plotted for the existing low-NO_x burner, for the original oxy-research burner design and for the final oxy-research burner design, both for air and oxy-fired conditions. Figure 2.4-14 presents these results in a comparison of the existing low-NO_x burner and for the original oxy-research burner design. The location of the quarl location is indicated in this plot for clarity.

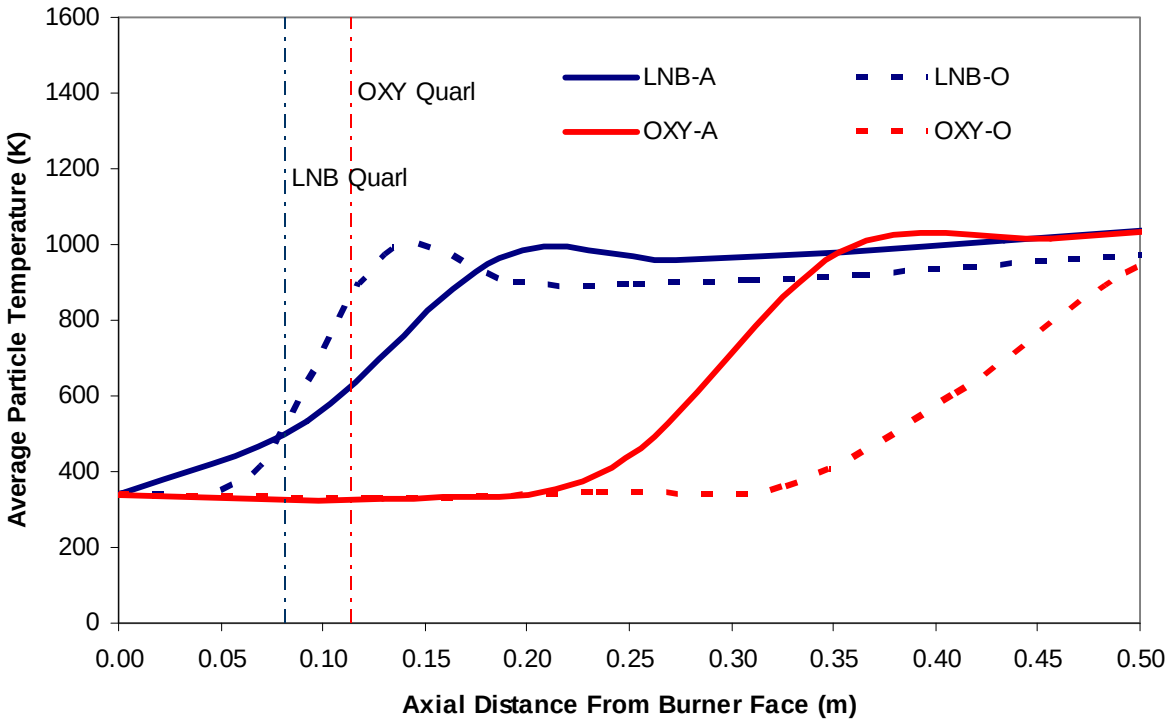

Figure 2.4-14. Particle temperature profile for the existing burner and the original oxy-research burner design.

Figure 2.4-14 shows that the steep increase in average particle temperature matches the observed flame stabilization location from the temperature profile and CO plots. For the existing burner, the flame stabilizes at the quarl exit for both the air and the oxygen cases. The flame for the oxy-research burner as originally designed is far outside the quarl. The low-NO_x burner behaves differently than the original oxy-research burner with respect to air and oxygen. The oxy-fired curve for the low-NO_x burner heats up much more quickly than the air case, whereas the behavior is opposite for the original oxy-research burner design. This can be explained by two factors. First, the velocities for the two oxy-research burner cases are similar, but the velocity for the low-NO_x burner oxy-fired case is significantly lower than the air case. This explains why the particles in the oxy-fired case heat up at a shorter distance from the low-NO_x burner face than in the air-fired case. The second factor explains why the temperature of particles in the oxy-fired case is slower to heat than in the air-fired case for the oxy-research burner. This is likely due to the lower temperature flame in the oxy-fired case providing a lower radiant intensity to the particles. It is apparent from this plot that the original oxy-research burner design does not meet the design criteria.

Figure 2.4-15 compares the particle temperatures for the low-NO_x burner and the final oxy-research burner design. Again, the behavior represented by the particle temperatures very closely matches the behavior of the flame stabilization location relative to the quarl exit that was observed in the temperature and CO concentration plots. This indicates that the flame behavior is very closely related to the rate that the particles are heated. In order to maintain similar burner behavior when scaling a burner, the particle temperature profile should be maintained. The particle temperature profile is influenced by many factors including: gas velocity, radiation intensity, particle size and hot flue gas recirculation characteristics inside of the quarl. Figure 2.4-15 also indicates that the flame stabilization location for the oxy-research burner, in its final design configuration, is expected to fulfill the design criteria.

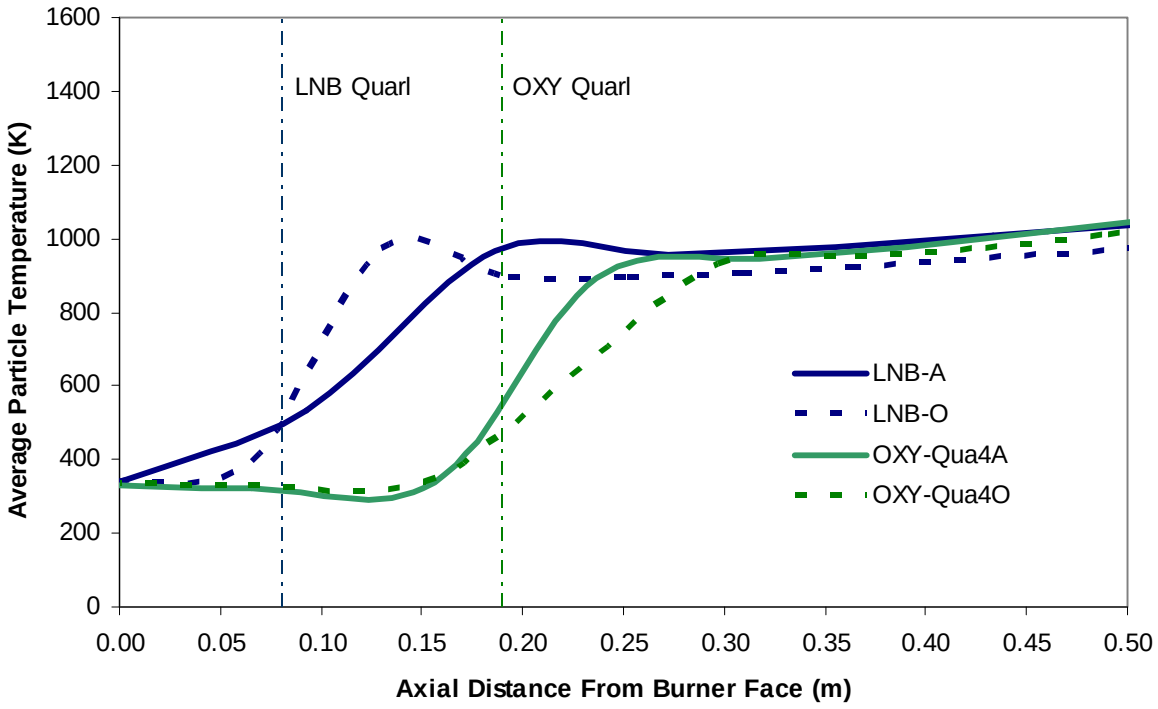

Figure 2.4-15. Particle temperature profile for the existing burner and the final oxy-research burner design.

2.4.6 Burner Final Design Summary

Following the extensive CFD work, the final geometry requirements for the oxy-research burner were sent to the Siemens designer for modifications and detailing. Additional considerations were made in the overall design to allow the burner and burner plate to be installed on the L1500 with minimal modification to the existing infrastructure, while allowing the original burner to be easily interchanged for future and existing programs. These considerations included:

- Installation of a pilot burner and a natural gas plenum and distributor within the quarl for overnight operation and for furnace heat up and cool down.
- Inner and outer secondary air plenum design to accommodate the existing gas train connections.
- Connectors and penetrations for flame scanners and thermocouples in the quarl region to integrate with the furnace control system.
- Overall dimensions of the burner plate to meet tight installation tolerances.
- Configuration of the burner plate refractory to accommodate the oxy-research burner's quarl, natural gas distribution system and plate design.

These modifications to the burner design have been completed and virtual pictures of the oxy-research burner were generated by the designers with CAD software. These pictures are presented as Figure 2.4-16 through Figure 2.4-19. In these pictures, some of the major components have been labeled. Figure 2.4-16 is a view from the top of the furnace looking down at the burner and burner plate. In this figure, the existing gas train connections to the inner and outer secondary plenums are shown along with the pilot burner penetration and the swirl control.

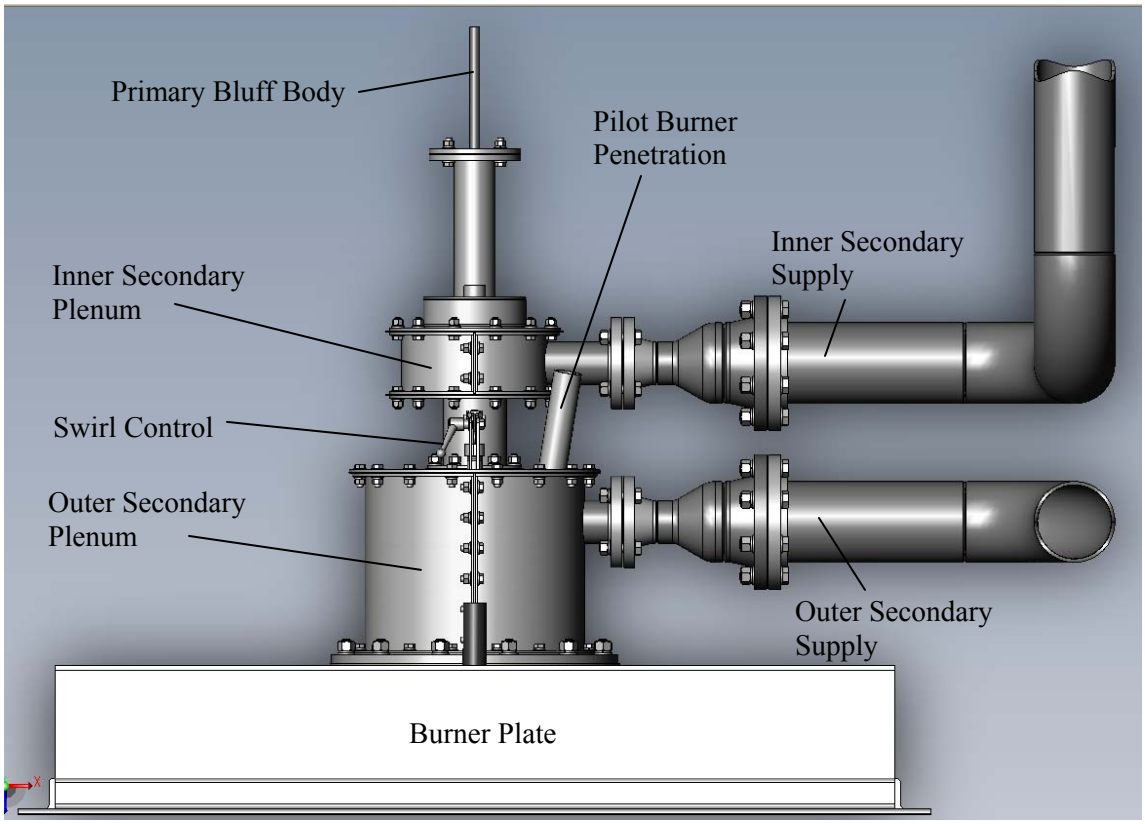

Figure 2.4-16. Top view of the oxy-research burner.

Figure 2.4-17 provides a side view of the oxy-research burner. In this view the natural gas and coal pipe connections can be seen.

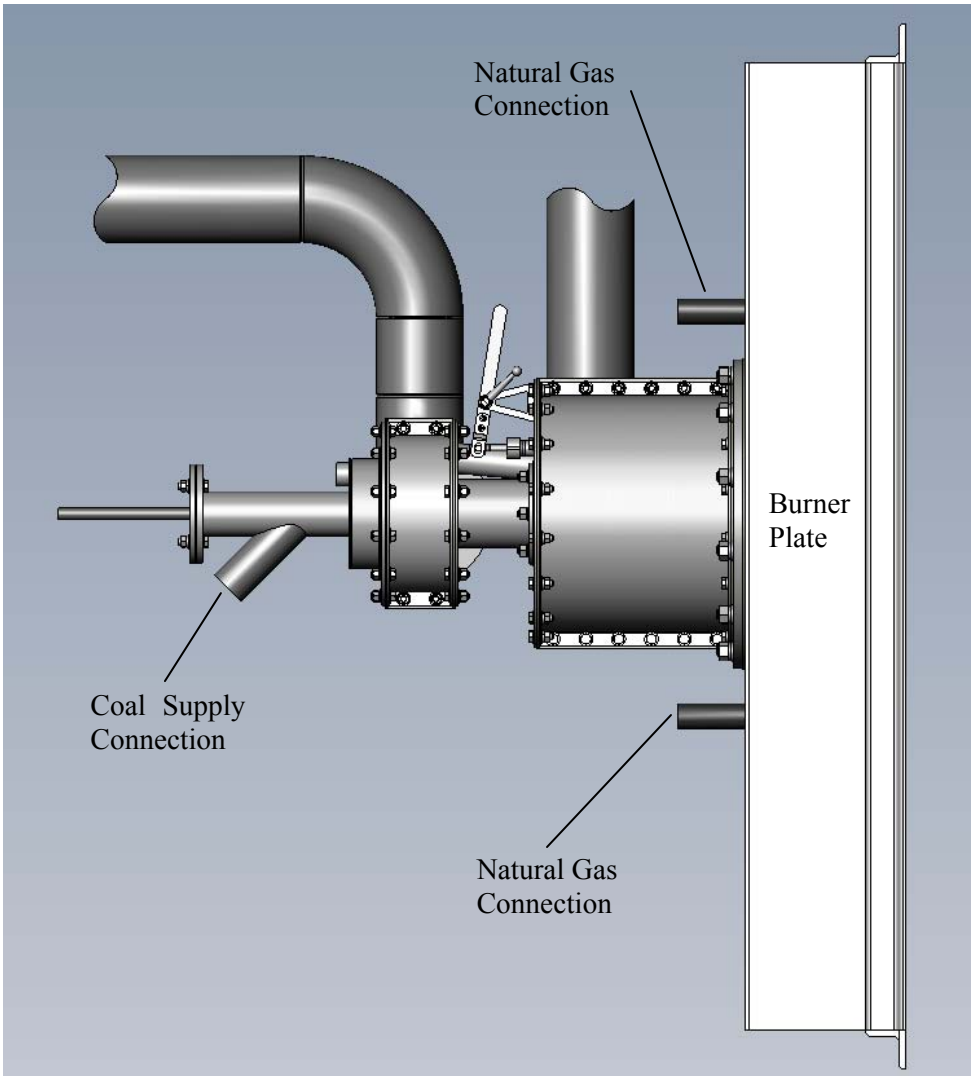

Figure 2.4-17. Side view of the oxy-research burner.

Figure 2.4-18 is a side cross section of the burner and Figure 2.4-19 is an expanded cross sectional view. These views provide some insight on the arrangement of each of the annulus in the burner throat.

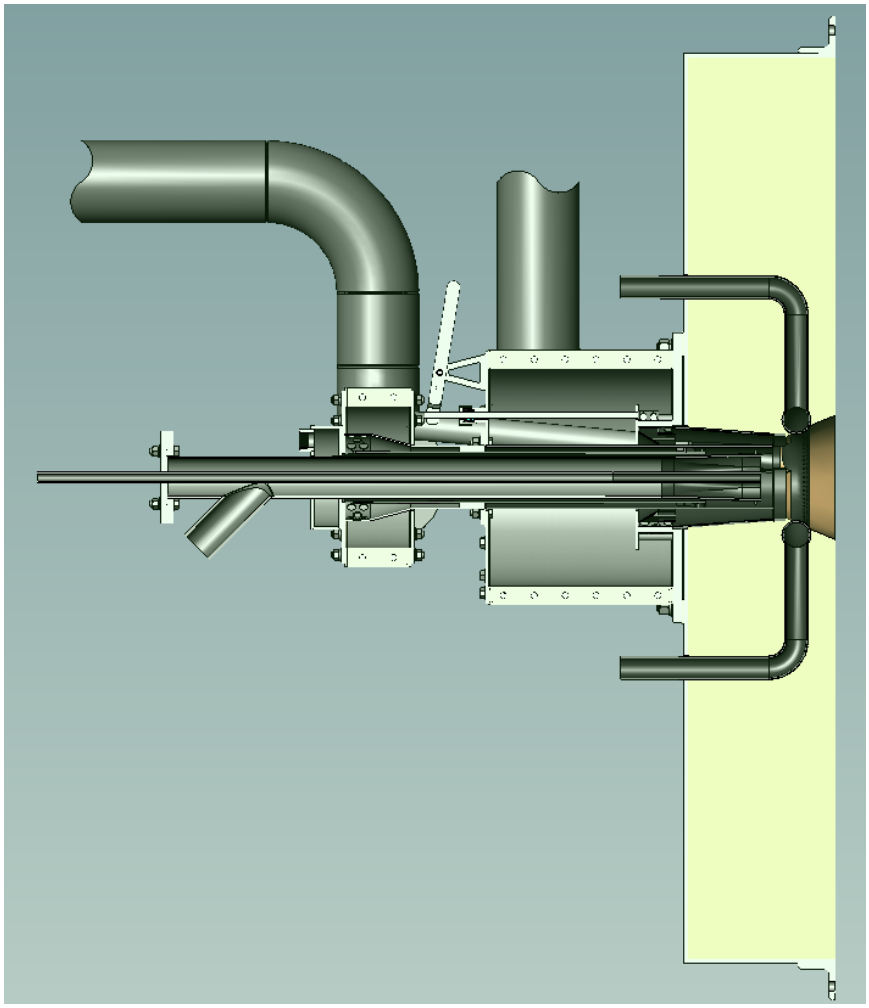

Figure 2.4-18. Side cross-section view of the oxy-research burner.

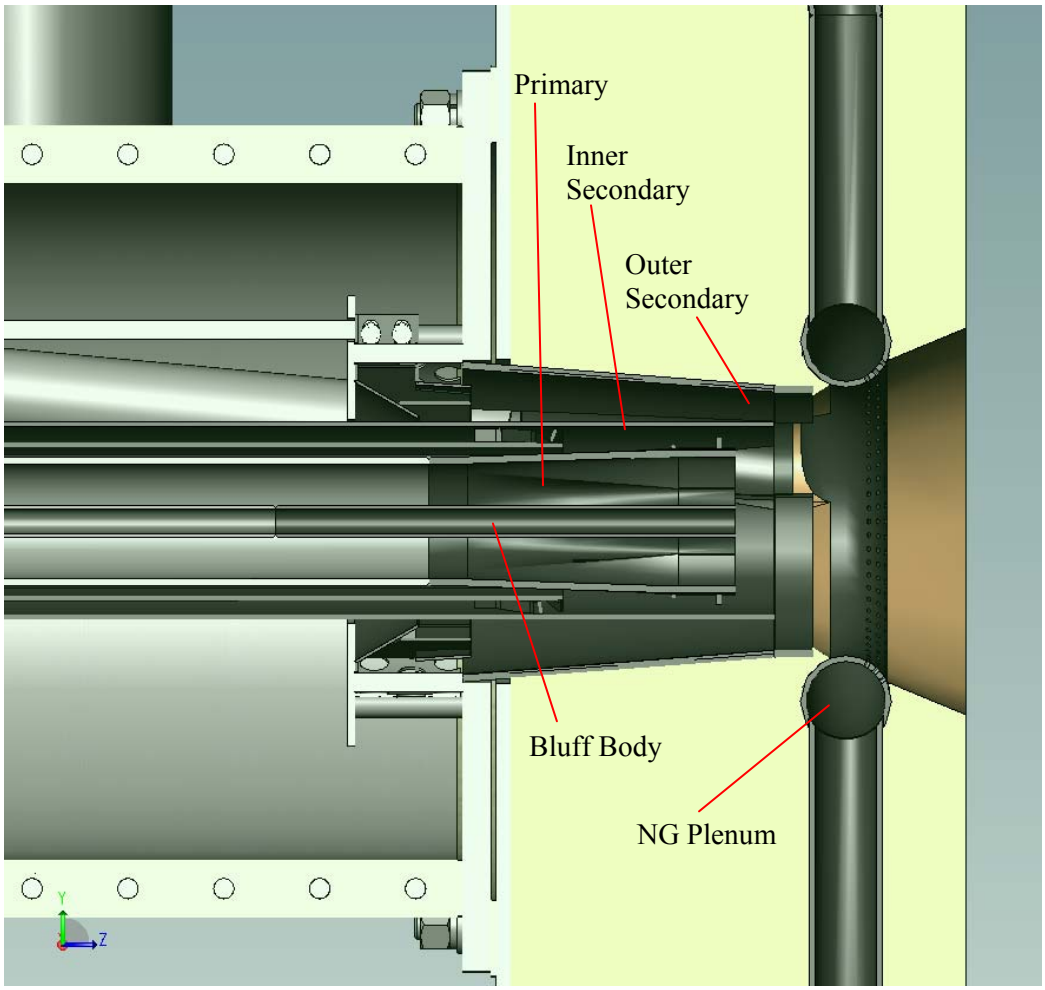

Figure 2.4-19. Side cross-section view of the oxy-research burner throat.

2.4.7 Schedule of Fabrication and Delivery

The final fabrication blueprints were completed and transmitted to the burner and burner plate manufacturers on July 15, 2009. The delivery of these items to the University of Utah is scheduled for September 21, 2009.

2.4.8 Pilot-Scale Burner References

1. Smart, J.P., van de Kamp, W. L., and Morgan, M. E., The Effect of Scale on the Performance of the Aerodynamically Air Staged Burner. International Flame Research Foundation, Livorno, Italy, December 1989.
2. Smart, J.P., Morgan, D.J., The Comparison Between Constant Velocity and Constant Residence Time Scaling of the Aerodynamically Air Staged Burner. International Flame Research Foundation, Livorno, Italy, January 1992.
3. Anderson, J.E., Fuel Jet Burner and Combustion Method. U.S. Patent # 4,878,829. November 7, 1989.

2.5 Task 5 – Mechanism Exchange

REI personnel met with Vattenfall managers and engineers in Sweden to review previous oxy-combustion R&D testing and modeling work that has been completed under Vattenfall funding (Vattenfall is a team member on this program). Vattenfall is pursuing several RD&D programs in oxy-combustion in support of their carbon capture and sequestration (CCS) initiatives. For example, Vattenfall has sponsored test programs at Chalmers University, IVD (Univ of Stuttgart), and University of Newcastle to provide data to develop and validate correlations which describe oxy-combustion mechanisms. Vattenfall has attempted to use the Fluent CFD code to model oxy-combustion for coal-fired combustors and found that the current Fluent capabilities are inadequate. They are trying to upgrade their Fluent sub-models using the new correlations. Key data and mechanisms/correlations they agreed to share with this program were:

- Gas-phase radiation property data from Chalmers University
- Soot testing and mechanism from Cranfield University (focused on single-phase gas flames)
- Gas phase combustion and NOx kinetics from Denmark Technical University (DTU) (Glarborg)

There is also some related gas-phase radiation modeling data from Terry Wall's group at University of Newcastle which REI has obtained through the literature. Unfortunately there is little data on radiation or sooting properties under coal-fired oxy-combustion conditions. Most if not all of this will need to be developed during this testing program. Vattenfall are willing to continue to share data published by EU collaborators such as IVD, but are currently restricted by Alstom from sharing any data from the 30 MW_{th} oxy-combustion unit in Schwarze Pumpe, Germany.

Combined with the visit to Vattenfall, REI also attended (and presented at) the International Flame Research Foundation (IFRF) Topically Oriented Technical Meeting (TOTeM) on oxy-combustion held in Pisa, Italy. This provided an up-to-date review of many oxy-combustion research programs in Europe. Among the most relevant for this program was oxy-coal research work done by Guenter Scheffknecht at IVD. He agreed to provide us with data from his programs as it was published.

REI will continue to watch for new data and mechanism descriptions from other research programs and from the literature to utilize in our R&D work.

2.6 Task 6 – Slagging and Fouling Mechanism Review and Development

2.6.1 Slagging Modeling Approach

2.6.1.1 Overall Approach

The overall approach of slagging modeling is to use the slagging submodel together with a comprehensive CFD combustion model, as shown in Figure 2.6-1. The comprehensive CFD simulation provides the flame side information and deposition rate. The slagging submodel performs the deposit growth, sintering and properties calculation and updates the wall boundary condition for comprehensive CFD simulation. Total deposition time is discretized into several time steps during which the deposition rate is assumed to be constant and the steady-state comprehensive CFD model can be used. The transient deposition build up process in the furnace can be addressed with this approach with adequate accuracy and manageable computational time. The two key elements in this approach are how to predict the deposition rate and how to predict the deposit property and growth. The deposition rate calculation is presented in detail first, followed by the discussion of the approach used to predict deposit property and growth.

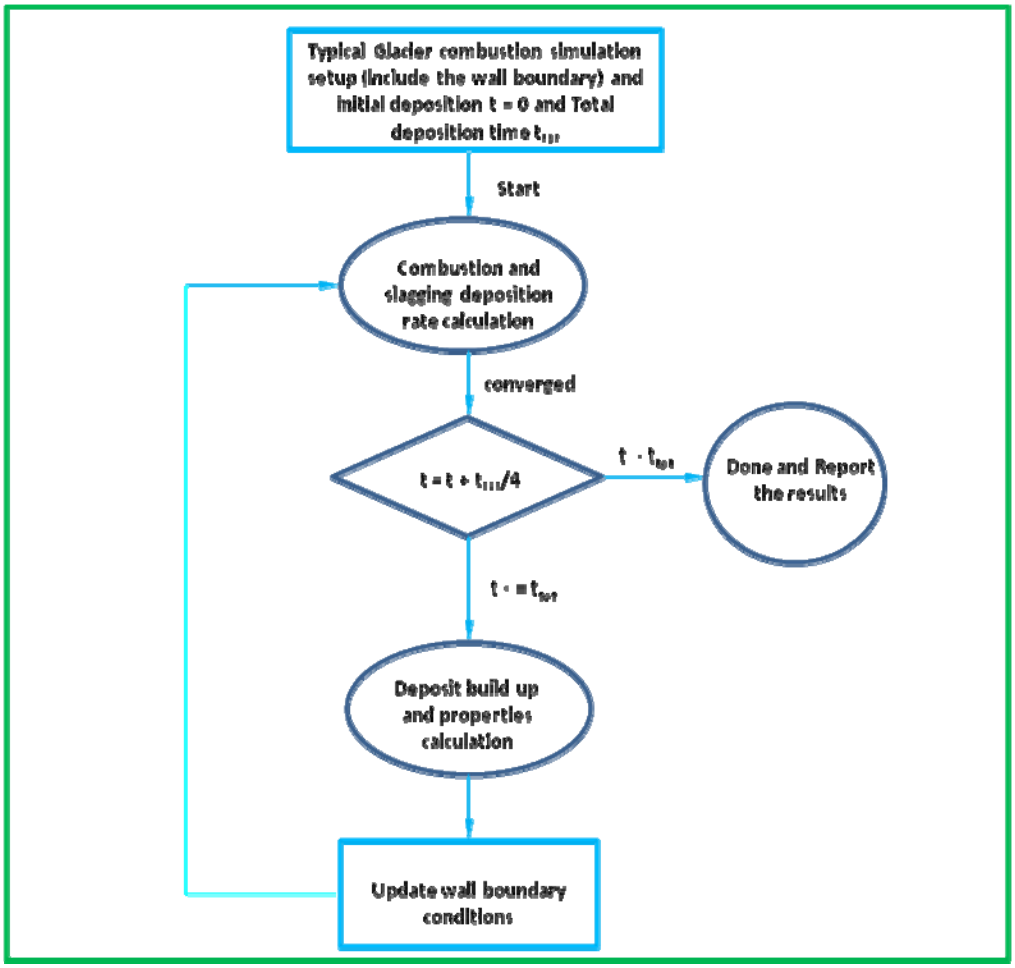

Figure 2.6-1. Overall approach to slagging model.

2.6.1.2 Slagging Deposition Rate

The initial ash composition distribution of each coal particle is assumed to be known and is estimated by a fly ash transformation model, expressed by *n* groups of compositions with a weighing factor w^i for each group. When the coal particle cloud interacts with wall cells, the fraction that sticks on the wall surface (capture efficiency $f_{dep}{}^i$) for a particle with composition of group *i* was expressed by Walsh *et al*. (1990):

$$f_{dep}{}^i = p^i(T_p) + [1 - p^i(T_p)]p_{sur}(T_s) - k_e[1 - p^i(T_p)][1 - p_{sur}(T_s)] \qquad \textbf{(2.6-1)}$$

where, $p^i(T)$ is the sticking probability (the probability that an impacting particle will stick on a clean wall surface) for an incoming particle of group *i* evaluated at temperature *T*, and T_p and T_s are the incoming particle and deposit surface temperatures, respectively, k_e is the erosion coefficient for the particular system and is assumed to be 0 at present, and p_{sur} is the sticking probability for dry particles on the deposit surface.

Particle viscosity μ^i has been found to provide a reasonable representation of the particle properties that affect sticking probability as shown:

$$\begin{aligned} p^i(T) &= \frac{\mu_{ref}}{\mu^i} && \mu^i > \mu_{ref} \\ p^i(T) &= 1 && \mu^i \le \mu_{ref} \end{aligned} \qquad \textbf{(2.6-2)}$$

A value of 10^5 poise for μ_{ref} was suggested by Richards *et al*. (1993), based on the relative deposition rates observed for two different coals in a laminar drop tube furnace and is used here.

A viscosity model developed by Senior and Srinivasachar (1995) is used to calculate the viscosity of silicate glass particles as a function of both temperature and composition.

The viscosity calculation is based on the ash composition and particle temperature, the influence of unburned carbon on particle viscosity is accounted in such a way that when the particle burnout is larger than a critical burnout, the ash tends to be explored at the outer surface of the particle, thus the viscosity of ash particle is representative of the particle in calculating the sticking probability. When particle burnout is less than a critical burnout, the ash tends to be buried in the carbon matrix, thus, a large viscosity is assigned to the particle in calculating the sticking probability.

The sticking probability of the deposit surface $P_{sur}(T_s)$ was approximated by the following expression by using the deposit surface temperature and deposit composition:

$$P_{sur}(T_s) = \frac{\sum_{i=1}^{N} w^i P^i(T_s)}{\sum_{i=1}^{N} w^i} \qquad \textbf{(2.6-3)}$$

where, $P^i(T_s)$ is the sticking probability of ash composition *i* in the deposit at surface temperature T_s, w^i is the weighting factor associated the composition *i* in the deposit.

Thus the average capture efficiency of coal particles is expressed as:

$$f_{dep} = \frac{\sum_{i=1}^{N} w^i f_{dep}{}^i}{\sum_{i=1}^{N} w^i} \qquad \textbf{(2.6-4)}$$

where, f^i_{dep} is the capture efficiency of ash composition i and w^i is the weighting factor associated the composition i in the coal particles.

After deposition, the deposit compositions in the wall cells are recorded and the ash composition in the coal particle along the trajectory is adjusted based on the ash composition balance by recalculating the weighting factor w^i for ash composition in the coal particles.

The outlined approach is completed for all the coal particle trajectories to calculate the slagging deposition rate and size and composition distribution of deposited particles in the comprehensive CFD combustion simulation.

2.6.1.3 Deposit Properties and Growth

2.6.1.3.1 Deposit Properties

A quantitative description of deposition properties is necessary in order to assess the effect of the ash deposition on heat transfer and to assess deposit strength. Key physical properties related to heat transfer are the emissivity, absorptivity, and thermal conductivity. The viscosity, porosity and surface tension of the deposit are related to sintering and deposit strength.

The emissivity and absorptivity of the deposit were found to decrease with temperature and to increase with particle size or iron content prior to sintering. A sintered or fused deposit was found to have high emissivity and absorptivity of approximately 0.9 (Wall *et al*., 1993). A quantitative method for calculation of deposit emissivity and absorptivity was reported by Wall *et al*. (1993). In this method, spectral data for the complex index of refractive of coal slags (Goodwin, 1986) was estimated as a function of iron-oxide content. A two-flux model (Bohren, 1987; Brewster, 1992) was used to solve the radiative transport equation through the opaque particulate deposit. The spectral emissivity and absorptivity were assumed to be equal and were calculated for the deposit at several wavelengths. The spectral values were then weighted by the relevant Planck distribution and integrated to yield the desired radiative properties. Once the deposit began to sinter, the emissivity and absorptivity were assumed to increase linearly with temperature to a maximum value, for a completely sintered deposit, of 0.9 (Wall *et al*., 1993). The values of emissivity and absorptivity are also dependent on the structure of the heat transfer surface. For example, a thin deposit on boiler tubes will follow the curvature of the tubes with an emissivity ε related to the flat emissivity ε_f by Eq. 2.6-5 (Wall *et al*., 1979):

$$\varepsilon = \frac{\pi\varepsilon_f}{1+(\pi-1)\varepsilon_f} \qquad \textbf{(2.6-5)}$$

The thermal conductivity of ash deposits was reviewed by Gupta *et al*. (1997) who recommended methods for determination of the effective thermal conductivity for different types of deposits as follows. The effective thermal conductivity K_e of a particulate deposit can be calculated by Eq. 2.6-6

$$K_e = K_c\,[r\phi_s^{2/3} + (1-\phi_s^{2/3})]/[r(\phi_s^{2/3} - \phi_s) + (1-\phi_s^{2/3} + \phi_s)] \qquad \textbf{(2.6-6)}$$

where, K_c is thermal conductivity of the continuous phase (gas), r is the ratio of discrete phase conductivity K_d to continuous phase conductivity K_c, and ϕ_s is the volume fraction of the discrete solid phase.

The thermal conductivity of the partially sintered deposit is more complex, and can be estimated by Eq. 2.6-7

$$K_e = K_2\,[\zeta + (\zeta^2 + 8K_1/K_2)^{0.5}]/4.0 \qquad \textbf{(2.6-7)}$$

where $\zeta = (3\phi_1 - 1)(K_1/K_2) + (3\phi_2 - 1)$. The thermal conductivities K_1 and K_2 in Eq. 2.6-7 correspond to the thermal conductivities of gas-continuous-phase and solid-continuous-phase, respectively, and can be determined by Eq. 2.6-6 using gas and solid as continuous phase, respectively. In the expression of ζ,, ϕ_1 and ϕ_2 are the volume fractions of gas-continuous-phase and solid-continuous-phase. An empirical correlation to estimate the volume fraction of gas-continuous-phase ϕ_1 and solid-continuous-phase ϕ_2 from the volume fraction of gas phase ϕ is given by Eq. 2.6-8

$$\phi_1 = \phi[\alpha + (1-\alpha)\phi] \qquad \phi_2 = 1 - \phi \qquad \textbf{(2.6-8)}$$

where α is a parameter related to the structure of the deposit.

The thermal conductivity of a completely sintered or molten deposit has a high value, close to the thermal conductivity of the solid deposit. A deposit is characterized by particulate (or partially sintered) deposit layers near the heat transfer surface and highly sintered layers exposed to the flame. Therefore, all the formulas mentioned above need to be used together in order to describe the effective thermal conductivity of a deposit.

The development of deposit strength is due primarily to the viscous flow sintering, which is determined by particle surface tensions and viscosities. Methods for estimating the surface tension of a slag deposit have been summarized by Mill (1987). A viscosity model developed by Senior and Srinivasachar (1995) is used to calculate the viscosity of silicate glass particles as a function of both temperature and composition.

Deposit properties (porosity, thermal conductivity, emissivity, absorptivity, etc.), which are determined by the deposit morphology, composition, and temperature, are critical in the prediction of heat transfer and deposit growth. Equilibrium is not reached locally in the deposit, and viscous flow sintering is the main mechanism responsible for the change of deposit morphology and properties. Sintering changes the pore structure of a deposit and causes an increase of deposit cluster size or connectivity. However, the porosity of a deposit appears to decrease significantly only in the outer region of the deposit where the temperature is sufficiently high.

2.6.1.3.2 Sintering in Deposit

Viscous flow sintering in the deposit is largely determined by viscous forces and surface tension forces. Surface tension forces cause adjacent particles to sinter together by increasing the width of the neck between particles and by decreasing the distance between the centers of the particles. Viscous forces are required to be low enough not to hinder the sintering from occurring. The extent of sintering is described by the sintering percentage or the densification parameter, ψ, as shown in the following expression:

$$\psi = \frac{V_s - V_G}{1 - V_G} \qquad \textbf{(2.6-9)}$$

where V_s is the volume fraction of solid phase (or relative density), and V_G is the initial volume fraction of solid phase. Thus $V_s = \rho/\rho_s$ and $V_G = \rho_o/\rho_s$, where, ρ is the deposit density, ρ_o is the initial deposit density, and ρ_s is the theoretical density for the solid material. The porosity of the deposit (ϕ) is related to the relative density through Eq. 2.6-10:

$$\phi + V_s = 1 \qquad \textbf{(2.6-10)}$$

The sintering between particles with uniform size and uniform composition can be predicted by using Frenkel's model (1945) for the initial stage of sintering, Scherer's model (1977) for middle and initial stages of sintering, and Mackenzie and Shuttleworth's model (1949) for the final stage of sintering. All these models predict the relative density as a function of particle size, viscosity, surface tension and time. The

influence of particle shape and size distribution on the sintering rate has been discussed in the literature (Coble, 1973; Chappell and Ring, 1986). The effect of the non-uniform composition on the sintering rate has also been recognized as important, although it has not been discussed quantitatively in the literature (German, 1996). Unfortunately, ash deposits are formed from fly ash particles that come in a wide variety of sizes, shapes, and compositions. Thus, accurate prediction of the sintering rate in an ash deposit is a very difficult task. Also, sintering predictions must be simple enough computationally to permit integration with a comprehensive combustion code for the simulation of deposition behavior in large-scale boilers. An attempt has been made here (Wang, 1998) to track the sintering in the deposit and to represent the experimental results at a minimal computational cost.

Viscous-flow sintering is the principal mechanism responsible for changing the structure of a deposit. Based on experimental observations (Wang, et. al., 1999), initial sintering tends to increase the connectivity of the deposit without making significant changes in the deposit porosity. Observations also indicate substantial porosity changes in the later stages of sintering. These observations have been incorporated into the sintering model developed here. Fly ash particles that adhere to the surface and form the ash deposit are assumed to be spherical for the purpose of simplification. This assumption is not expected to have a large effect on the predicted results. Before the calculation of sintering in the deposit, particles that adhere to the surface and form the deposit are divided into a finite number of groups (according to their sizes and compositions) in order to represent the behavior of a large number of particles. Grouping of the particles is required in order to make the sintering calculations computationally feasible. The following key assumptions were made in order to predict overall sintering of the deposit, which is responsible for an increase of deposit connectivity, and to predict the porosity (or relative density) of the deposit:

1) the extent of sintering of a particular particle group depends only on the size and composition of particles in that group;
2) the overall sintering can be calculated as a weighted average of the extent of sintering of individual particle groups;
3) high-viscosity particles will not mix and react with the surrounding species unless other smaller or equally sized particles have completely sintered;
4) the extent of sintering affects the cluster size or connectivity of the deposit, not the deposit porosity, until a critical viscosity is reached;
5) when the critical viscosity is reached, an increase of sintering will result in a decrease in the deposit porosity or an increase in the relative density of the deposit.

The first two assumptions are key simplifications. As shown in Figure 2.6-2, the contribution of particle A to the sintering is through the movement of flow coming from particle A to the area between particle A and B or between particle A and A'. In the present implementation, the contribution of particles of a particular size and composition to the overall sintering of a deposit is approximated as that which would be observed from a deposit made up entirely of those particles. The overall sintering of the deposit is then calculated as the weighted average of sintering extent of individual particle groups.

The first two assumptions preclude the need to deal with individual pairs of particles of different size and/or composition. Instead, a combination of Scherer's model (Scherer, 1977) and the model of Mackenzie and Shuttleworth (1949) can be used to predict the sintering extent of a particular group of particles, as described in Figure 2.6-3. In other words, overall sintering of the deposit is estimated as the weighted average of the sintering which would occur for groups of monosized particles of a particular composition.

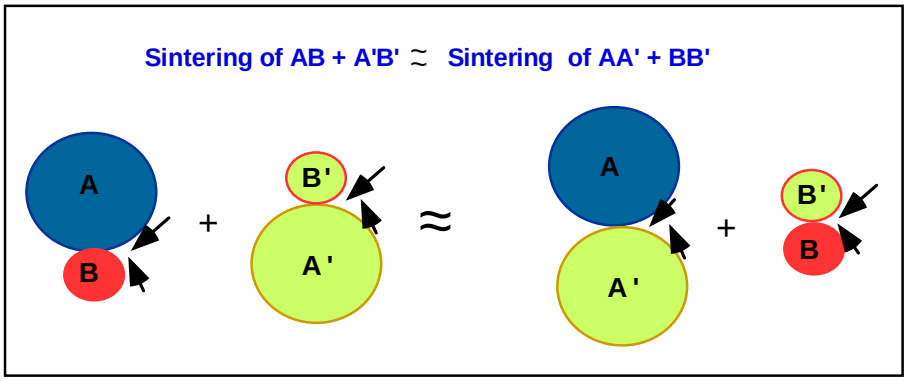

Figure 2.6-2. Movement of viscous flow.

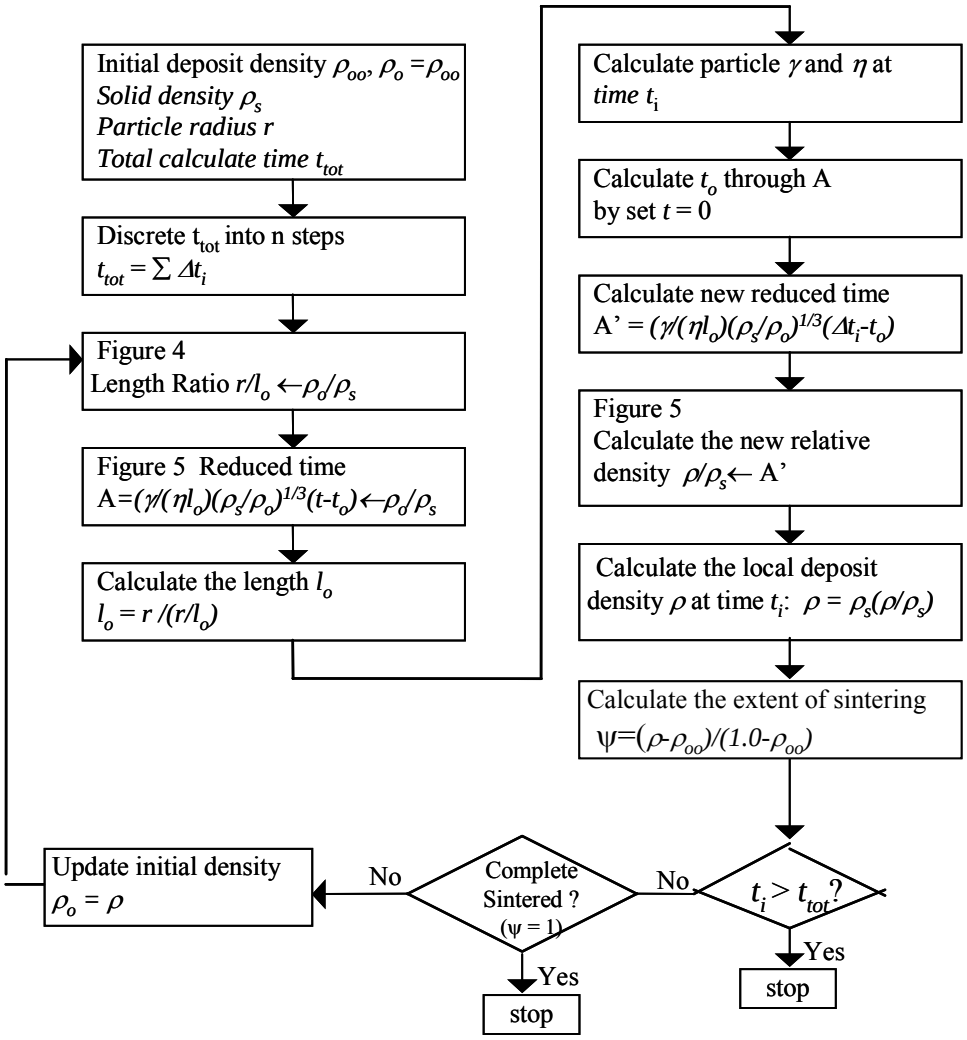

Figure 2.6-3. The procedure to calculate the extent of sintering for a particular group as a function of time.

It is well known (Frenkel, 1945; Mackenzie and Shuttleworth, 1949; Scherer, 1977) that sintering of monosized particles leads to a reduction in porosity and hence a change in relative density. Therefore, a relative density change can be used to characterize the sintering extent of the monosized groups. However, overall porosity of the deposit does not change significantly until well after significant sintering has occurred. This phenomenon was confirmed by experimental observation and was mainly due to the fact that a deposit was formed from fly ash particles with varied size, shape, and compositions. The possible reasons for a deposit to maintain porosity as sintering occurs are explained later in this section together with assumptions 3 and 4. Therefore, the relative density (ρ) in Figure 2.6-4 is merely a way of quantifying the extent of sintering (ψ) of the monosized groups. The relationship between the relative density (ρ/ρ_s) and reduced time ($\gamma/(\eta l_o)(\rho_s/\rho_o)^{1/3}(t- t_o)$) and the relationship between the length ratio (r/l_o) and relative density (ρ/ρ_s) for the monosized groups were developed by Scherer (1977) and are plotted in Figure 2.6-4 and Figure 2.6-5.

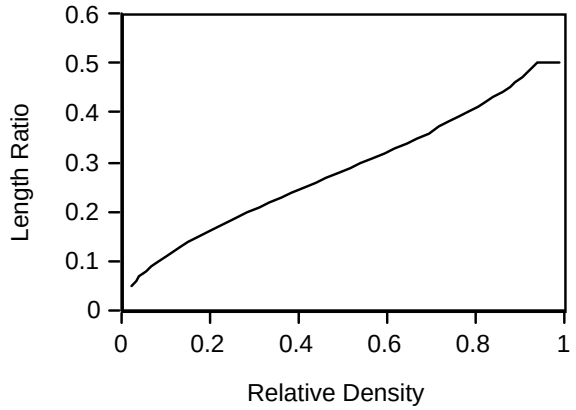

Figure 2.6-4. Length ratio (r/l_o) versus relative density (ρ/ρ_s) used to estimate extent of sintering for individual particle groups.

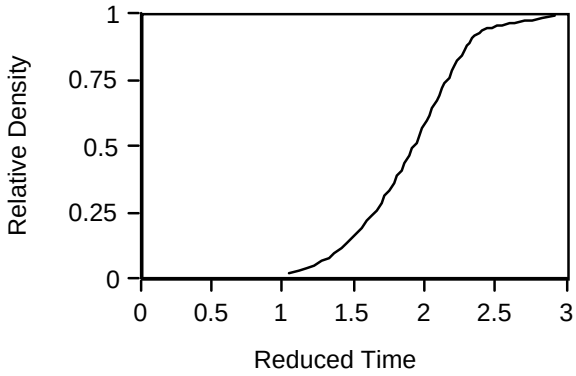

Figure 2.6-5. Relative density (ρ/ρ_s) versus reduced time $(\gamma/(\eta l_o)(\rho_s/\rho_o)^{1/3}(t - t_o))$ used to estimate extent of sintering for individual particle groups.

These two figures provide a simple way to get the deposit length and reduced time when the relative density is known (or vice versa). The corresponding values from these two figures were tabulated in a computer program for the purpose of computer simulation. In Figure 2.6-3 through Figure 2.6-5, γ is the surface tension, and η is the viscosity of the particle group. The viscosity model of Senior and Srinivasachar (1995) was used to calculate the viscosity of particles as a function of particle composition and temperature. The surface tension of particles was estimated using the method of Mills (1986). Once the sintering extent of the

individual groups (ψ_j) was calculated, the overall sintering extent of the deposit (ψ) was estimated through Eq. 2.6-11, which is a mass weighted average of the sintering of individual groups:

$$\psi = \frac{\sum_{j=1}^{N} m_j \psi_j}{\sum_{j=1}^{N} m_j} \qquad \textbf{(2.6-11)}$$

where m_j is the mass associated with the particle group j, and N is the total particle groups in the deposit.

The third and fourth assumptions recognize that high viscosity particles, due to their relative immobility, play a very important role in maintaining the porosity of the deposit during the sintering of other particles. These high-viscosity particles were assumed to have a viscosity greater than 10^{11} poise at a temperature of 1250 K. The high-viscosity particles tend to hold their original positions to maintain the porosity of the deposit during the sintering of other particles until mixing occurs with basic "flux" components that surround them. The mixing between high-viscosity particles and the surrounding basic "flux" components only occurs at high temperature. In the current model, the high-viscosity particles are not allowed to mix with other species and sinter until smaller or equally sized particles have sintered completely.

The fifth assumption recognizes that the deposit porosity begins to decrease in the outer region of the deposit where the temperature is sufficiently high. The viscosity of the bulk deposit at the deposit surface temperature was calculated and compared to a critical value, 10^5 poise, chosen based on the viscosity of formation of non-flowing slag (Raask, 1986). The porosity of the deposit was assumed to decrease once the viscosity calculated from the bulk deposit composition reached the critical value. If ψ_{cri} represented the overall sintering percentage when the viscosity of bulk deposit at the deposit surface temperature reached the critical value, a linear relationship between the extent of sintering and the deposit porosity ϕ was assumed as described in Eq. 2.6-12:

$$\begin{aligned} \phi &= \phi_o && \psi \le \psi_{cri} \\ \frac{\phi_o - \phi}{\phi_o} &= \frac{\psi - \psi_{cri}}{100\% - \psi_{cri}} && \psi > \psi_{cri} \end{aligned} \qquad \textbf{(2.6-12)}$$

where, ϕ, and ϕ_o are the deposit porosity and initial deposit porosity, respectively; ψ is the overall extent of sintering of the deposit.

The local overall extent of sintering in the deposit as a function of time was calculated by dividing the deposit into discrete layers. The extent of sintering for each layer during the time step Δt_i was approximated by the mass average of the extent of sintering for each of the relevant particle groups. High-viscosity particle groups were not allowed to mix and sinter until other groups of equal or smaller size had completely sintered. Once the sintering of a particular particle group was complete, the mass of this group was distributed among the high-viscosity particle groups. This procedure permitted approximation of the local extent of sintering as a function of time, particle size, and composition, and was used to estimate the deposit properties.

One complication of this approach is the influence of unburned carbon in the deposit on the deposit growth and sintering. The effect of unburned carbon on deposit growth is determined by the release rate of unburned carbon in the deposit, which in turn influences the deposit surface sticking probability. The release rate of deposited unburned carbon is dependent on the local gas environment where the deposit is

located. If the local gas is very fuel lean, quick lease of all unburned carbon in the deposit is assumed. If the local gas is very fuel rich, none of unburned carbon in the deposit is released into gas phase. Under normal conditions, the release rate of unburned carbon in the deposit creates a near stoichiometric local gas environment.

Deposited partially-burned carbon particles are treated in a same way as other deposited ash particles in surface sticking probability calculation and in sintering calculation through their viscosity identities. The viscosity of a partially burned-carbon particle is calculated in such a way that when the particle burnout is larger than a critical burnout, the ash tends to be exposed on the outer surface of the particle, thus the viscosity of ash particle is representative of the particle. When particle burnout is less than a critical burnout, the ash tends to be buried in the carbon matrix, thus, a high viscosity is assigned to the particle.

Crystallization in the deposit at sufficiently high temperatures was not considered in the current model. Crystal formation would affect deposit properties and deposit strength. However, as a first effort, this sintering model approximated the overall extent of sintering and deposit porosity as a function of time, particle size, and composition in the deposit, which in turn was used to estimate the deposit properties.

Deposit properties include deposit porosity, local thermal conductivity, emissivity, and absorptivity. The porosity (ϕ) of the deposit was discussed previously. The initial deposit porosity was assumed to be 0.6 in the model, a typical value for the particulate deposit and consistent with values measured by Anderson *et al.* (1987).

The local thermal conductivity (K_e) of an ash deposit depends on the extent of sintering, the deposit porosity and the temperature. As discussed previously, the local thermal conductivity of a particulate deposit (K_e) was calculated by Eq. 2.6-6. The local thermal conductivity of a partially or completely sintered deposit was calculated by Eq. 2.6-13.

$$K_e = \psi K_{sc} + (1-\psi)K_{gc}$$

$$K_{sc} = K_s[r_s\phi^{2/3} + (1-\phi^{2/3})]/[r_s(\phi^{2/3} - \phi) + (1-\phi^{2/3} + \phi)] \qquad \textbf{(2.6-13)}$$

$$K_{gc} = K_g[r_g\phi_s^{\,2/3} + (1-\phi_s^{\,2/3})]/[r_g(\phi_s^{\,2/3} - \phi_s) + (1-\phi_s^{\,2/3} + \phi_s)]$$

where K_{gc} and K_{sc} correspond to the thermal conductivities of gaseous continuous phase and solid continuous phase, respectively; r_s is the ratio of gas conductivity K_g to solid conductivity K_s and r_g is the ratio of solid conductivity K_s to gas conductivity K_g; ϕ and ϕ_s are the volume fractions of gas and solid, respectively; ψ is the extent of sintering. The value of thermal conductivity calculated for the completely sintered deposit using Eq. 2.6-13 will be close to the thermal conductivity of the solid deposit phase.

The thermal conductivity of the gas phase (in W/(m K)) was approximated as that of nitrogen at the local deposit temperature, which is expressed in Eq. 2.6-14,

$$K_g = 1.14\text{x}10^{-2} + 5.108\text{x}10^{-5}T_{dep} \qquad \textbf{(2.6-14)}$$

where, T_{dep} is the temperature of the deposit in Kelvin. The thermal conductivity of the solid deposit phase was assumed to be constant at 4 W/(m K), a value representative of silica-containing materials at high temperature (Kingery *et al.*, 1976).

The emissivity and absorptivity of the particulate deposit surface were determined by the particle size and composition distribution as per Harb *et al.* (1993). The method assumed multiple independent scattering and utilized the scattering albedo and the scattering asymmetry factor from single particle calculations

performed with the Mie code of Bohren and Huffman (1983). Once the surface deposit began to sinter, the emissivity was assumed to increase linearly with temperature. These thermal and physical properties of the deposit were then used to predict the deposit growth and heat flux through the deposit as discussed in the next section.

2.6.1.3.3 Deposit Growth and Heat Flux

Deposit growth and the heat flux through the deposit are simulated for a time period in which the deposition rate and the incident heat flux are assumed to remain constant. Figure 2.6-6 illustrates the procedure used for simulation of deposit growth and heat flux through the deposit (Wang, *et al*., 1997). The simulated time is divided into a finite number of time steps and the amount of deposit, which accumulates during the i^{th} time step, is referred as the i^{th} deposit layer.

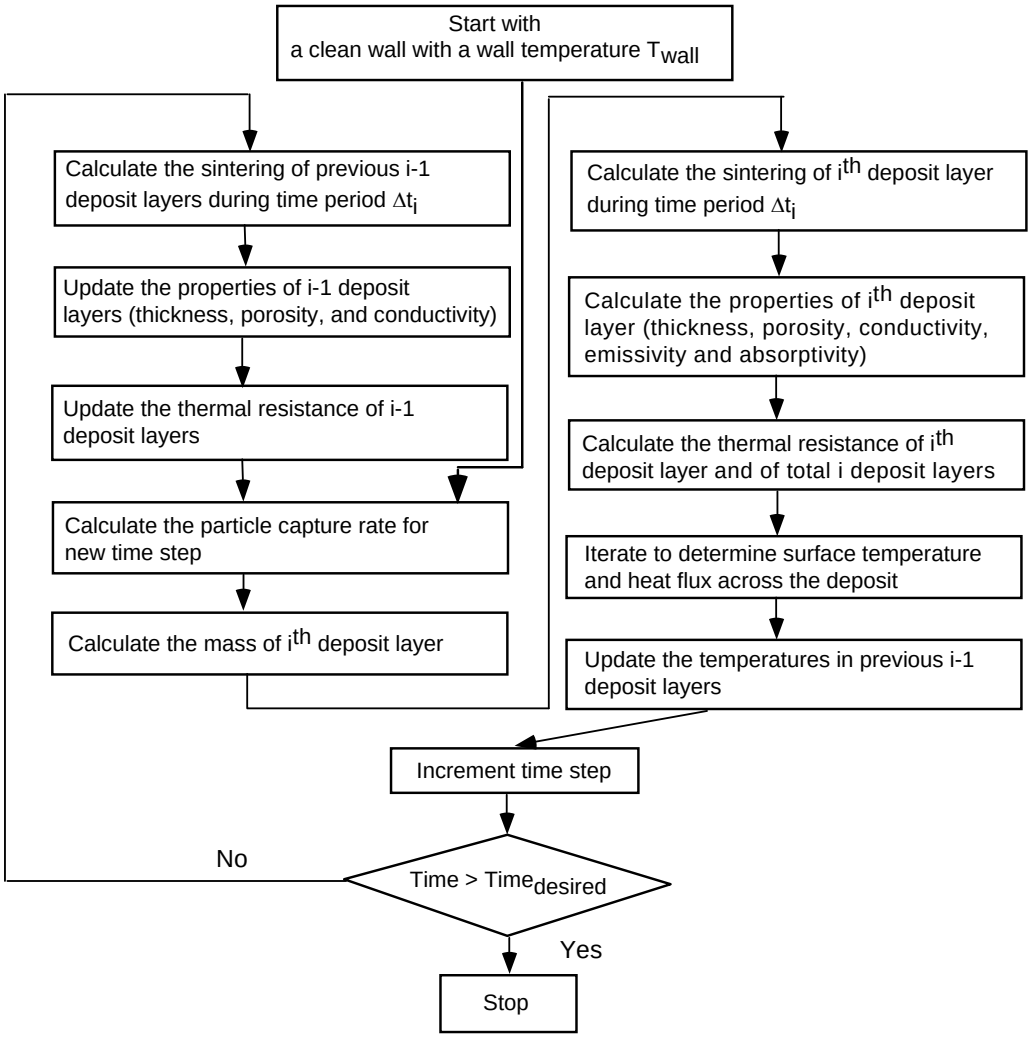

Figure 2.6-6. Flowchart illustrating the procedure used to simulate deposit growth.

First, the extent of sintering that occurs during the time step *i* is calculated for each layer of the existing deposit (layers *1* to *i-1*) and the deposit thermal conductivities for each of these layers are updated. Next, the mass of the deposit, which accumulates during the time step *i*, is determined. The thickness and sintering of the new deposit layer is then calculated and the thermal conductivity, emissivity, and absorptivity of the new deposit layer are approximated as discussed in the previous section.

Once the thermal resistance of the deposit and the emissivity and absorptivity of the deposit surface have been calculated, it is then possible to calculate the deposit surface temperature and the net heat flux through the deposit by solving Eqs. 2.6-15 and 2.6-16 together:

$$T_s = q_{net} R_i + T_{wall} \quad \textbf{(2.6-15)}$$

$$q_{net} = h(T_g - T_s) + \alpha q_{inc} - \varepsilon \sigma T_s^4 \quad \textbf{(2.6-16)}$$

where, T_s is the deposit surface temperature, q_{net} is the net heat flux through the deposit, q_{inc} is the incident radiation heat flux on the deposit surface, T_{wall} is the wall surface temperature, T_g is the near deposit gas temperature, h is the convection coefficient, α is the absorptivity of deposit surface, ε is the emissivity of deposit surface, and σ is the Stefan-Boltzmann constant. In these two equations, q_{inc}, h, T_g, T_{wall} are provided by the combustion simulation, whereas α, ε, and R_i are predicted as discussed previously. Finally, an iterative procedure is performed to solve for the surface temperature T_s and heat flux q_{net}. Once the new surface temperature and flux have been determined, the temperatures in the deposit layers are recalculated by Eq. 2.6-17:

$$T_k = T_{wall} + q_{net} R_k \quad \textbf{(2.6-17)}$$

These temperatures at different layers are saved and used to calculate the sintering in these deposit layers at the next time step. The entire process is repeated until the total time specified for deposit growth has been reached.

2.6.2 Fouling Modeling Approach

2.6.2.1 Introduction

This analysis will generally follow the analysis of Walsh *et al.* (1992). The major assumptions used are as follows:

- Alkali species (Na, K) vaporize during combustion, and some of the vaporized alkali species persist in the gas phase in the convective pass;
- Sodium sulfate condenses on cooled surfaces when the surfaces are below the dew point;
- When the surface temperature of the deposit is between the sodium sulfate dew point and the melting temperature of sodium sulfate (884°C or 1623°F), the surface will be sticky;
- When the gas temperature reaches the sodium sulfate dew point, sodium begins to condense on suspended ash particles;
- Homogeneous nucleation of sodium sulfate is neglected;
- When the gas temperature is between the sodium sulfate dew point and the melting temperature of sodium sulfate (884°C), the ash particle surface will be sticky (if sodium sulfate has condensed);
- Deposits grow most rapidly when their surfaces are sticky, at surface temperatures between 884°C and the dew point;
- Erosion of a dry surface by dry particles competes with deposit growth.

Thus, the region in which significant fouling will occur is that in which the gas temperature lies between the dew point of sodium sulfate and the melting point of sodium sulfate. Local gas temperatures and velocities in the back pass will be calculated by the CFD model. The amount of sodium vaporization will be calculated using a correlation between organically bound sodium and SiO_2 in the coal. The size distribution of the ash particles will be calculated by the mineral matter transformation model.

2.6.2.2 Estimation of sodium vaporization in pc-combustion

Prediction of fouling in the convective pass of a coal-fired boiler requires knowledge of the amount of sodium (Na) (and potassium (K)) vaporized in the boiler and carried over into the convective pass. In previous work (Gallagher *et al*., 1990; Gallagher *et al*., 1996), the amount of acid-soluble Na (Boni *et al*., 1990) was found to be an important parameter correlated with vaporization of Na under pulverized coal combustion conditions. The amount of acid-soluble Na and K should correspond to the amount of organically-bound element. Published data on chemical fractionation (selective leaching) of calcium (Ca), magnesium (Mg), Na, and K were assembled (Benson *et al*., 1985; Bool *et al*., 1995; Senior *et al*., 2001) as shown in Table 2.6-1.

Table 2.6-1. Chemical fractionation data (Benson *et al*., 1985; Bool *et al*., 1995; Senior *et al*., 2001).

	Falkirk NDL	Beulah, NDL	Bryan, TXL	Black Thunder	Wyodak	Rochelle	Rosebud	Ohio 5/6/7
Chemical fractionation results (% of element)								
	Removed by NH4Ac	Removed by NH4Ac	Removed by NH4Ac	Removed by H2O + NH4Ac	Removed by NH4Ac	Removed by H2O + NH4Ac	Removed by NH4Ac	Removed by NH4Ac
Ca	40	76	62	59	45	67	57	30
Mg	50	90	94	72	55	64	65	10
Na	85	84	75	86	90	93	81	25
K	10	20	9	15	30	49	2	0
Coal composition								
Coal C, wt% dry	60.15	64.13	53.67	69.80	69.00	69.04	70.70	72.77
Coal O, wt% dry	19.53	20.07	15.86	17.07	16.57	18.83	16.62	8.29
Coal Ash, wt % dry	14.63	9.55	24.50	5.94	8.13	5.95	4.90	9.93
Coal C/O	3.08	3.20	3.38	4.09	4.17	3.67	4.25	8.77

The organically bound elements should be correlated with the oxygen available for ion exchange in the coal. Thus, the more oxygen the coal has, the more organically bound cations the coal should have. In Figure 2.6-7, the C/O ratio is plotted against the fraction of organically bound elements. For Na and Mg, the correlations are good. For Ca, the correlation is not as good, while for K, the correlation is poor. However, the amount of K associated with organically bound elements is generally low; the poor correlation might be due, in part, to the difficulty in accurately measuring the amount of ion-exchangeable K in coals.

Gallagher *et al.* (1990) carried out pilot-scale combustion experiments in which he reported results on vaporization. In particular, vaporization of Na could be correlated with the ratio of acid-soluble Na to SiO_2 in the coal.

Table 2.6-2 gives selective coal composition and acid-soluble Na data reported by Gallagher *et al.* (1990). The amount of acid-soluble Na was sometimes greater than the amount of Na in the coal, as calculated from the ash composition and ash content. Thus, the amount of acid-soluble Na reported in (Gallagher *et al*., 1990; Boni *et al*., 1990) is suspect. For this reason, the amount of organically bound Na was estimated using the correlation in Figure 2.6-7; this is also shown in Table 2.6-2.

Table 2.6-2. Sodium in coal and acid-soluble or organically bound forms.

	Upper Freeport	Beulah NDL	Eagle Butte	KY 9	San Miguel TXL	KY 11	IL 6	Loy Yang
From Gallagher et al., 1990, Table 4								
wt fr. Ash	0.232	0.0965	0.048	0.143	0.2025	0.202	0.1331	0.02
g SiO2/g ash	0.506	0.216	0.284	0.446	0.659	0.458	0.461	0.132
g Na2O/g ash	0.003	0.061	0.02	0.009	0.025	0.003	0.013	0.492
g acid sol. Na/g coal	0.00036	0.00738	0.00082	0.00525		0.00383		0.00530
From Gallagher et al., 1996								
g acid sol. Na/g coal	0.00032	0.00750	0.00082	0.00055	0.00897	0.00037	0.00218	0.00290
Calculated								
g Na/g coal	0.00052	0.00437	0.00071	0.00095	0.00376	0.00045	0.00128	0.00730
Fraction of org. Na	0.00100	0.92039	0.87004	0.41833	1.00000	0.41537	0.47906	0.98652
g org. Na/g coal	0.00000	0.00402	0.00062	0.00040	0.00376	0.00019	0.00061	0.00720

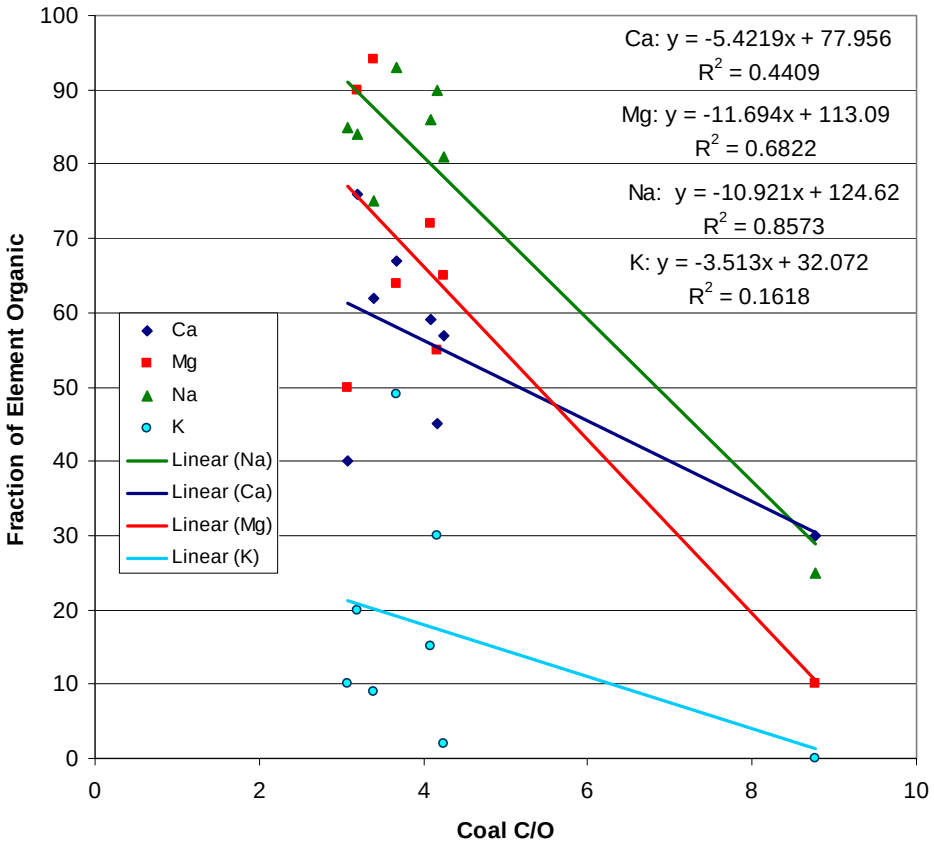

Figure 2.6-7. Fraction of elements that are ion-exchangeable (organically bound) as a function of C/O ratio.

The result is a plot of g acid-soluble Na/g SiO_2 versus fraction of Na vaporized in Figure 2.6-8. The scatter in the data is probably because of different peak temperatures in the experiments. In oxy-combustion, there may be a different relationship to express sodium vaporization as a function of Na/Si ratio.

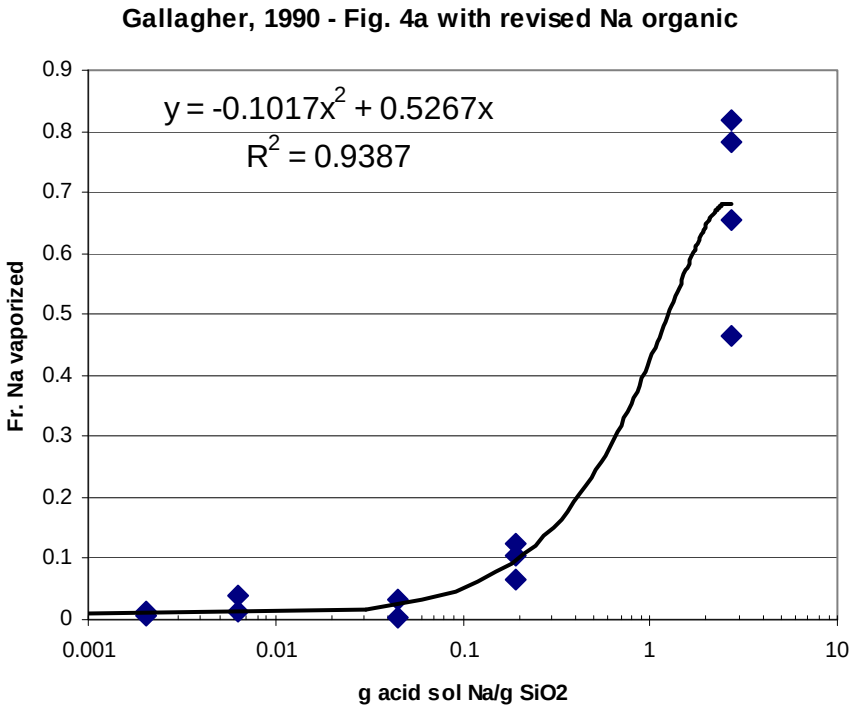

Figure 2.6-8. Na vaporization as a function of acid-soluble (organic) Na/SiO_2, re-interpretation of data of Gallagher *et al.* (1990) with estimated organic Na fraction.

Gallagher observed a good correlation between the fraction of Na vaporized and the fraction of K vaporized, as shown in Figure 2.6-9. This can be used to calculate the fraction of K vaporized.

The correlations described in Figure 2.6-7, Figure 2.6-8, and Figure 2.6-9 allow prediction of the fractional vaporization of Na and K for any coal, given an ultimate analysis and an ash composition. Examples of these calculations are shown in Figure 2.6-10 for many different U.S. coals.

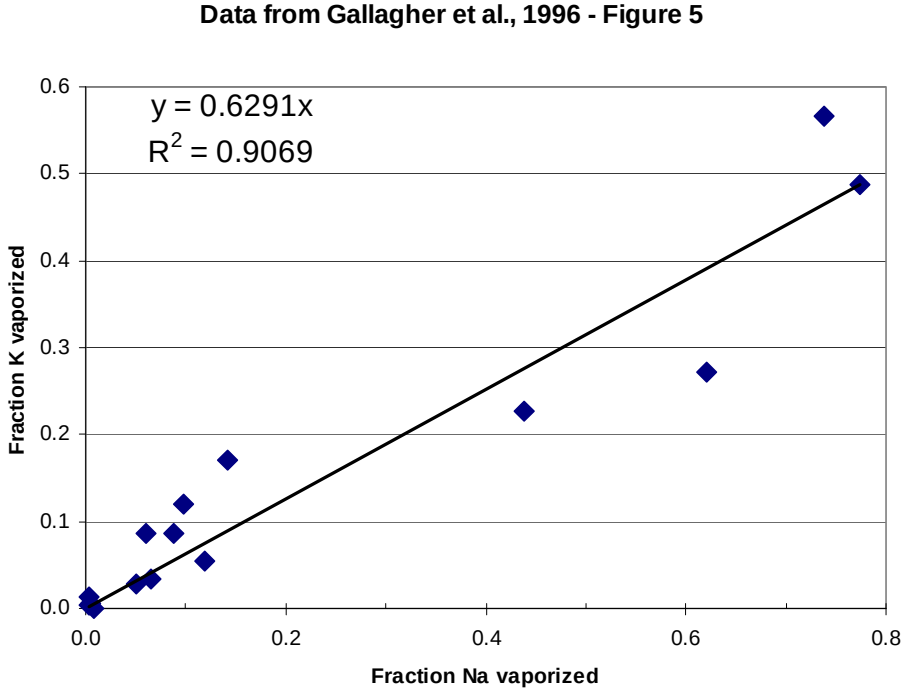

Figure 2.6-9. Fraction of K vaporized during combustion as a function of fraction of Na vaporized from data of Gallagher *et al.* (1996).

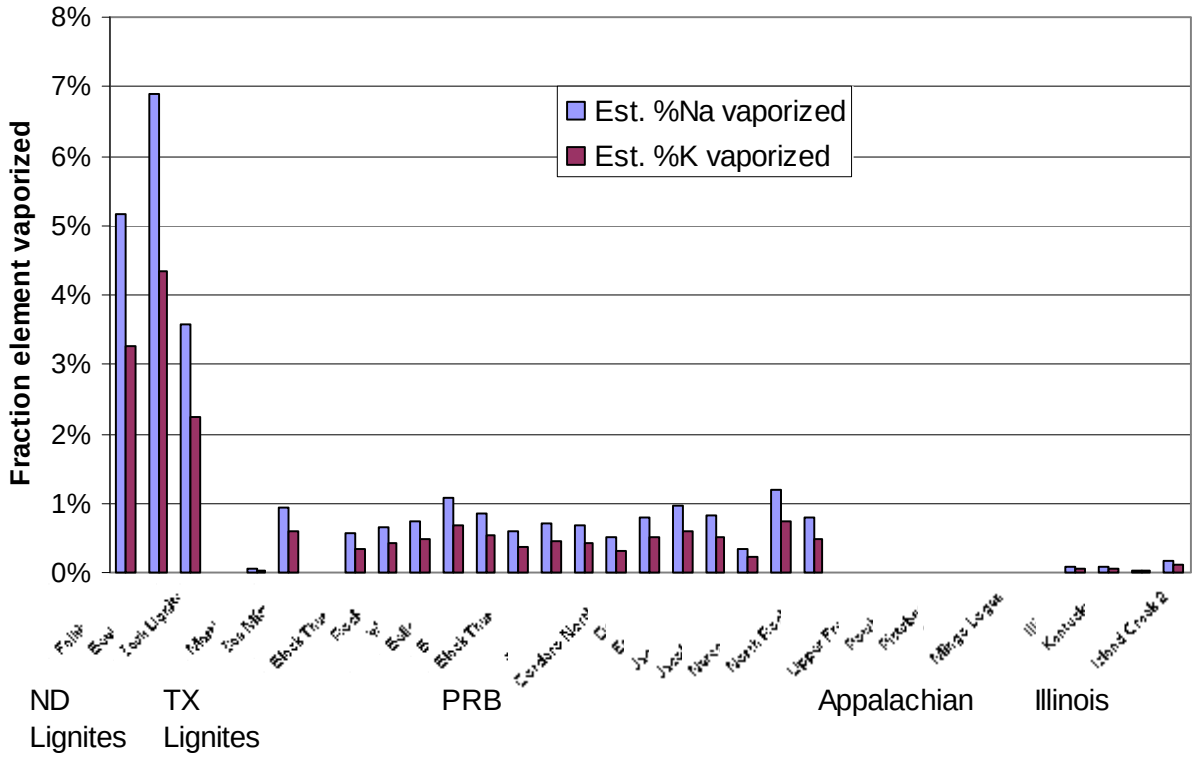

Figure 2.6-10. Calculated vaporization of Na and K for different U.S. coals.

The amount of Na vaporization predicted is 4-7% for North Dakota lignites and 0.5-1% for PRB coals. This is much lower than what was observed by Quann (1992) in single-particle combustion experiments in a drop tube furnace. Figure 2.6-11 and Figure 2.6-12 show results from Quann's combustion experiments on an Illinois bituminous coal and a Montana lignite, respectively. The fractional vaporization was calculated from the measured amount of the element in a final filter (after an impactor) and the coal composition.

Figure 2.6-11 (Illinois bituminous) suggests that 15% to 20% of the Na will vaporize, but the calculations and Gallagher's experiments on bituminous coals (Kentucky and Upper Freeport) suggest less than 1%. Figure 2.6-12 (Montana lignite) shows about 20% Na vaporization, Gallagher's data shows 5% to 12% Na vaporization.

Quann's experiments were very different from Gallagher's. One important difference is that Quann's experiments were dilute in nature, while Gallagher's experiments had a self-sustained flame. In the former experiments, vaporized Na that escaped the burning char particle would be less likely to interact with ash particles at high temperatures than in the latter experiments. In Gallagher's experiments, Na vapors could be adsorbed on ash particles once the vapors diffused out of the burning char particle.

Gallagher *et al*. (1990) mixed kaolinite with coal in some of his experiments and he observed a decrease in apparent Na vaporization when he did so. The kaolinite particles are obviously external to the burning char particles. This provides some support for this hypothesis.

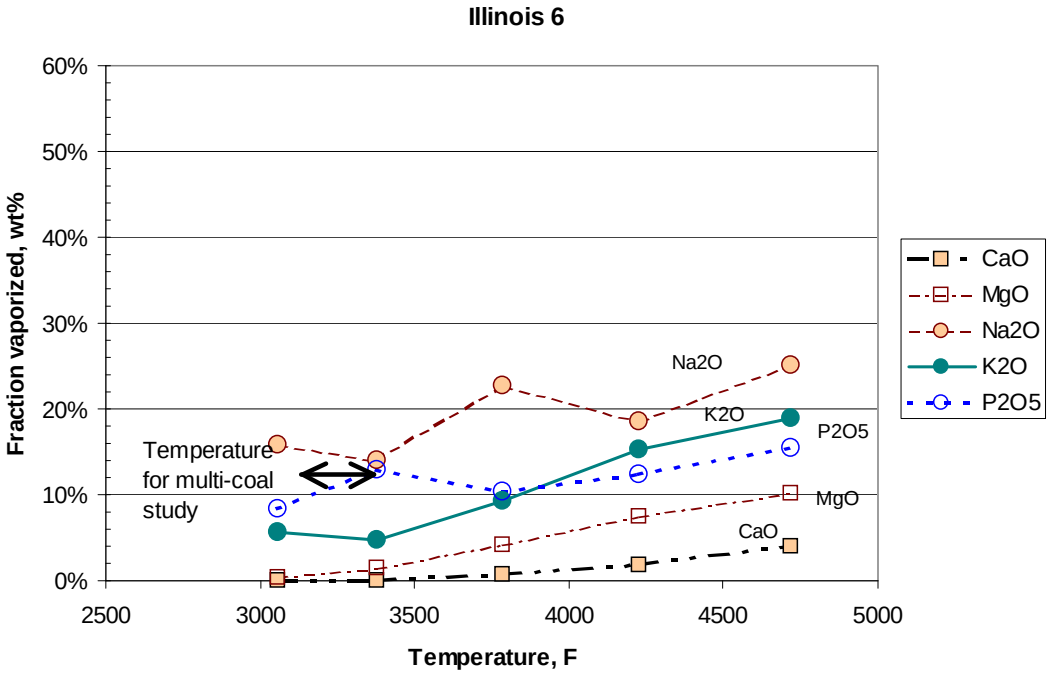

Figure 2.6-11. Fraction of element vaporized as a function of particle temperature for Illinois 6 bituminous coal calculated from data of Quann (1992)

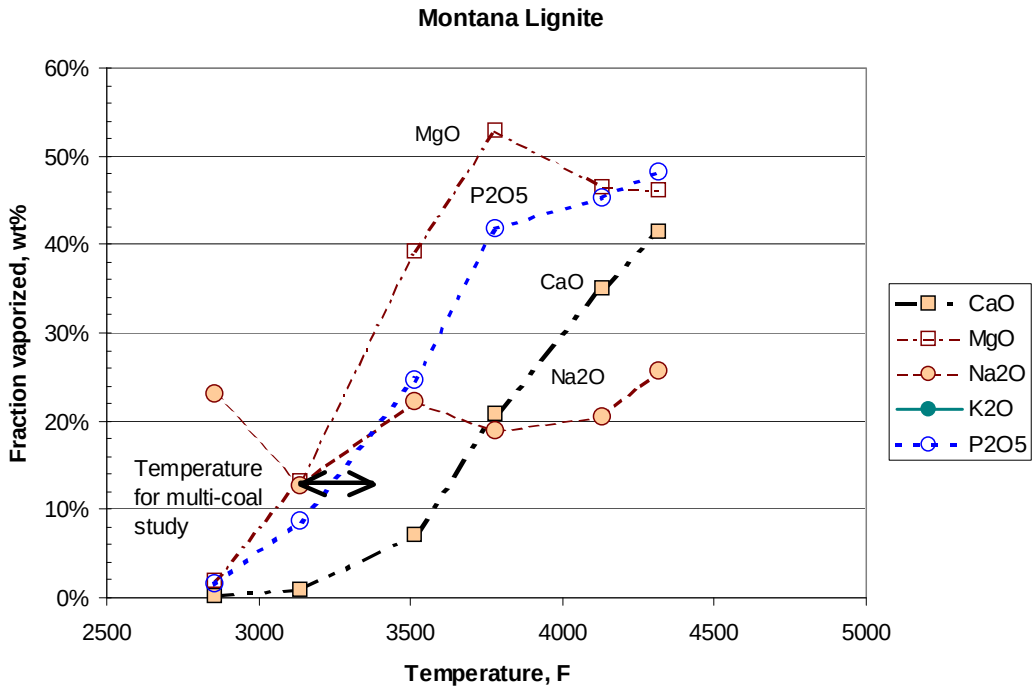

Figure 2.6-12. Fraction of element vaporized as a function of particle temperature for Montana lignite coal calculated from data of Quann (1992).

2.6.2.3 Dew point of Alkali Species

The dew point of alkali species in the flue gas can be calculated from equilibrium calculations based on the amount of *vaporized* alkali. As an example, this calculation was carried out for the Rochelle coal, a subbituminous Powder River Basin coal. Table 2.6-3 summarizes the composition of this coal.

Table 2.6-3. Coal information for Rochelle-North Antelope coal.

Composition	Rochelle-North Antelope
Ultimate (as-fired)	
C	51.47
S	0.21
H	3.49
Moisture	27.30
N	0.65
O	12.51
Ash	4.36
Total	99.99
Proximate	
Moisture	27.30
Ash	4.36
VM	32.10
FC	36.20
HHV, Btu/lb	8,800
Ash composition	
SiO_2	33.80
Al_2O_3	17.40
Fe_2O_3	5.60
TiO_2	1.40
CaO	23.80
MgO	5.60
Na_2O	1.90
K_2O	0.30
P_2O_5	1.10
SO_3	8.20
Total	99.10

In Table 2.6-4, the concentrations of Na_2O and K_2O in the ash have been estimated based on the coal properties of Table 2.6-3, along with the amount of vaporization of Na and K. Assuming 3% (dry) O_2 in the flue gas, the coal composition was used to create compositions for equilibrium calculations to approximate the sulfate deposition in the back pass.

Table 2.6-4. Calculated compositions for equilibrium composition calculation.

	Rochelle-North Antelope
HHV, wet, mineral-matter free	9,201
C/O Ratio	4.114
Estimated Na/K ratio	2.745
Fraction of org. Na	0.797
Fraction of org. K	0.176
Na, g/g coal	0.000614557
K, g/g coal	0.000108584
SiO_2, g/gcoal	0.0147368
Organic Na/g SiO_2 coal	0.033231513
Fraction Na vaporized	0.017390727
Fraction K vaporized	0.010940507
g Na vap/g S	0.005089332
g K vap/g S	0.000565699
Molar Na/S	0.007083582
Molar K/S	0.000462953
Composition for Equilibrium calculation	
CO_2	0.142346
SO_2	0.000218
O_2	0.025911
N_2	0.695379
H_2O	0.136146
Na	1.54E-06
K	1.01E-07

The results of the equilibrium calculations (using HSC) are shown in Figure 2.6-13. For the Rochelle-North Antelope coal the dew point of sodium sulfate is 990°C (1814°F). This temperature is below the melting point of sodium sulfate of 884°C (1623°F). Thus for this coal, we would expect sodium sulfate deposits to be sticky in the convective pass at temperatures between 884°C and 990°C.

The equilibrium calculation for potassium sulfate (not shown) gives a dew point of 850°C (1562°F). The melting point K_2SO_4 is 1069°C (1955°F). Potassium sulfate is predicted to deposit at temperatures below the melting point, and therefore would not be expected to be sticky.

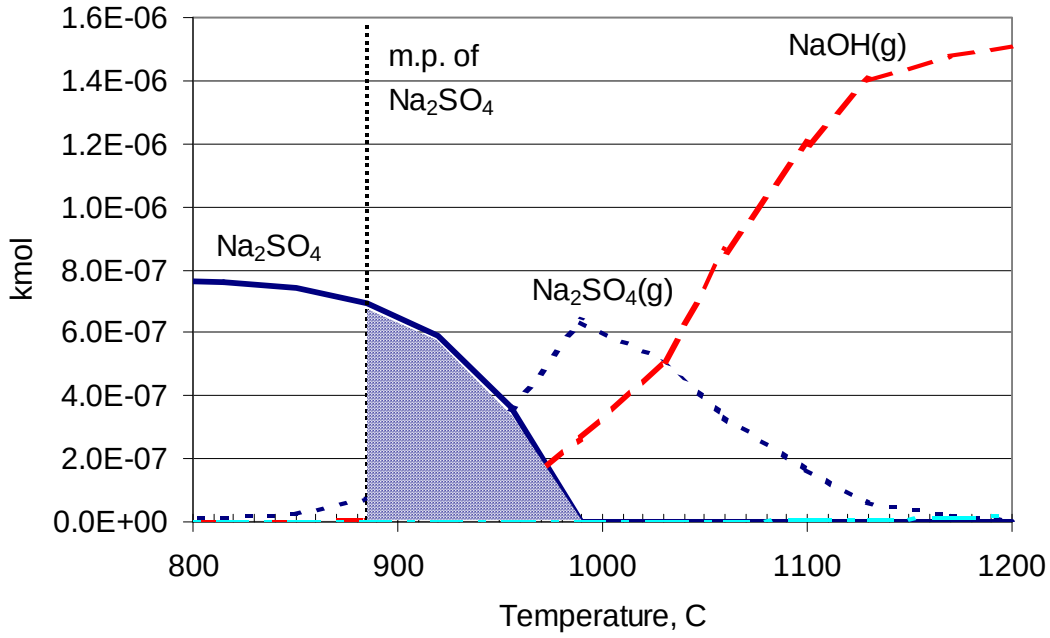

Figure 2.6-13. Sodium equilibrium calculation for Rochelle-North Antelope coal.

2.6.2.4 Ash Particle Size Distribution and Impaction

The convective pass can be thought of as a series of tubes in cross flow. Much work has been done concerning heat and mass transfer in banks of tubes, which should be investigated at some point in the future. For now, the analysis will be limited to a single tube.

As the flue gas flows across the tube, larger ash particles will impact the tube, while smaller ash particles will flow around the tube. From the mineral matter transformation model, the ash size distribution can be calculated.

When this is implemented in the CFD code, the ash size distribution will be calculated from the mineral matter transformation code. As an example in this section, a simpler (and less accurate estimate) is to use the coal particle size distribution and the coal ash content to calculate the size distribution, assuming one ash particle per coal particle. Given the ash contents of the coals, an ash particle size distribution can be calculated, as follows. First, the volume fraction of fly ash in the coal is calculated from the mass fraction of ash:

$$f_{vol} = \frac{1/\rho_{ash}}{1/\rho_{ash} + (1 - f_{mass})/\rho_{carbon} f_{mass}} \qquad \textbf{(2.6-18)}$$

The ash density was assumed to be 2500 kg/m^3 and the carbon density, 1050 kg/m^3. Assuming one ash particle per coal particle, the ash size distribution can be calculated from the coal particle size distribution and the ash content. For each coal particle diameter, D_{ci}, the ash particle diameter, D_{ai}, is computed:

$$D_{ai} = D_{Ci} (f_{vol})^{1/3} \qquad \textbf{(2.6-19)}$$

The results of these calculations are plotted in Figure 2.6-14.

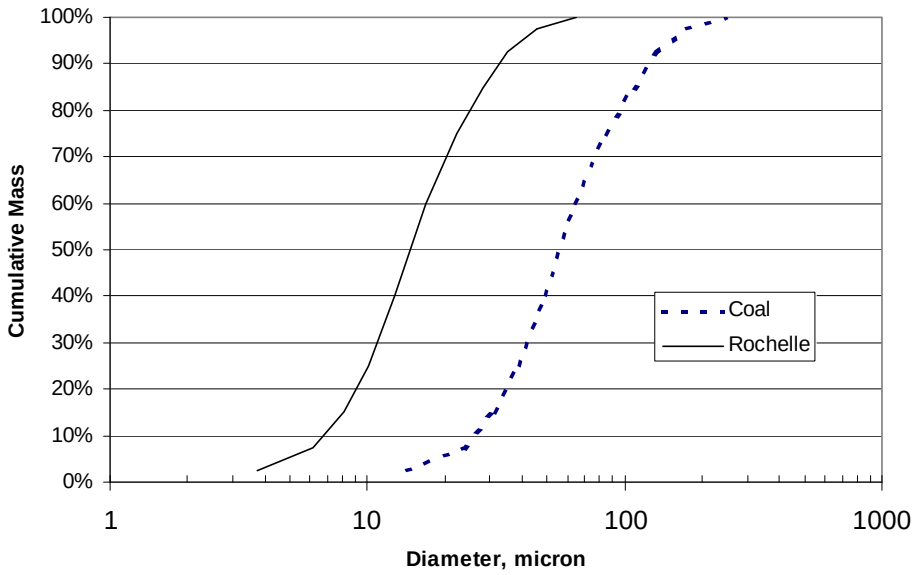

Figure 2.6-14. Predicted ash particle size distributions.

The impaction efficiency of ash particles on a tube (at 884°C, the sodium sulfate dew point) is then calculated. The impaction efficiency for a given particle size *i* can be calculated from the Stokes number (*St*) and particle Reynolds number for impaction on tubes in cross flow:

$$St_i = \frac{\rho_{ash} V D_{ai}^2}{9 \mu D_{tube}} \qquad \textbf{(2.6-20)}$$

$$\mathrm{Re}_p = \frac{D_{ai} V \rho}{\mu} \qquad \textbf{(2.6-21)}$$

The Reynolds number is used to calculate the Stokes correction factor:

$$\Psi = \frac{18}{\mathrm{Re}_p}\left[\mathrm{Re}_p^{1/3} - \sqrt{6}\,\tan^{-1}\left(\frac{\mathrm{Re}_p^{1/3}}{\sqrt{6}}\right)\right] \qquad \textbf{(2.6-22)}$$

$$St_{eff} = \Psi St \qquad \textbf{(2.6-23)}$$

Using the correlation of Israel and Rosner (1983), we can calculate the impaction efficiency:

$$\eta_{imp} = \left[1 + \frac{1.25}{St_{eff} - 0.125} - \frac{0.014}{(St_{eff} - 0.125)^2} + \frac{0.000508}{(St_{eff} - 0.125)^3}\right]^{-1} \qquad \textbf{(2.6-24)}$$

This is calculated from a correlation from Israel and Rosner (1983) and shown in Figure 2.6-15 below.

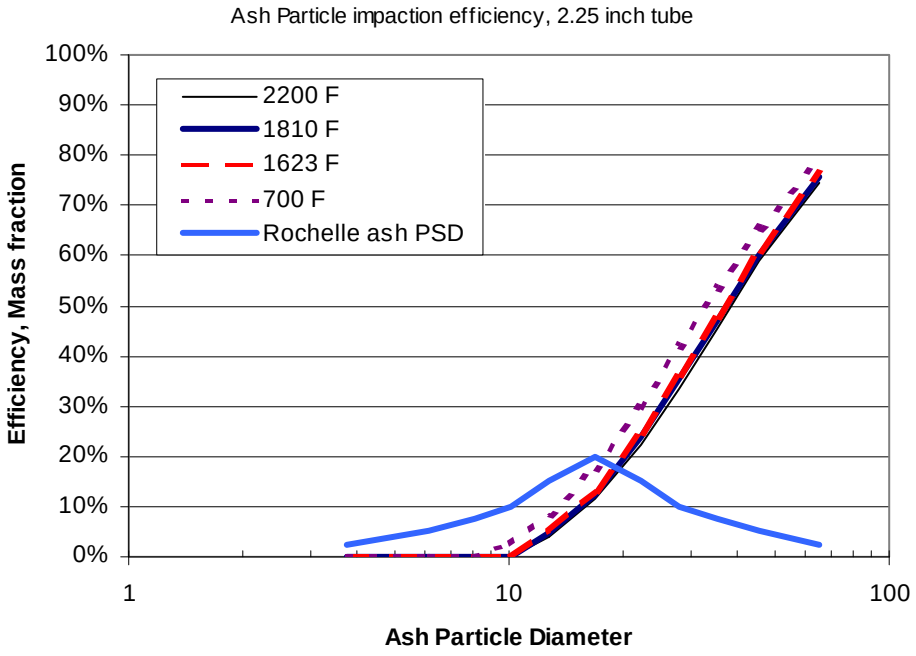

Figure 2.6-15. Impaction efficiency on 2.25 inch tube.

As Figure 2.6-15 shows, the impaction efficiency depends on the diameter of the tube as well as on the particle size. Figure 2.6-15 also contains the estimated particle size distribution for the Rochelle coal. In general, particles less than 10 microns will not impact on the leading edge of the tubes. Note that this analysis does not take into account thermophoresis or deposition from the turbulent wake behind the tube.

The impaction efficiency is somewhat dependent on temperature, but in most of the convective pass, the impaction efficiency varies little with temperature, except at the lowest temperatures. The dependences on velocity and particle diameter are more pronounced.

The impaction rate R_I (kg/m^2-s) can be calculated from

$$R_I = VM_{ash}\left(\sum_i f_i \eta_i\right) \qquad \textbf{(2.6-25)}$$

where f_i is the mass fraction of ash in the ith diameter, η_i is the impaction efficiency for that diameter, V is the gas velocity, and M_{ash} is the total ash loading in kg/m^3.

In the CFD simulations conducted with the *Glacier* code for this project, each "panel" (row of tubes) is modeled as a plate, so that a tube bank is modeled as a series of plates parallel to the flow direction (see Figure 2.6-16). At the leading edge of a tube bank, the velocity and ash loading in the computational cell just before the "plate" or row of tubes can be used to calculate the impaction rate at the leading edge of the "plate". There will be impaction on the tubes within each panel or "plate". Assuming that there is minimal interference with the flow field by upstream tubes, the impaction efficiency for the second, third, etc. tubes can be computed by using the local velocity and ash loading from the leading edge values and the local temperature.

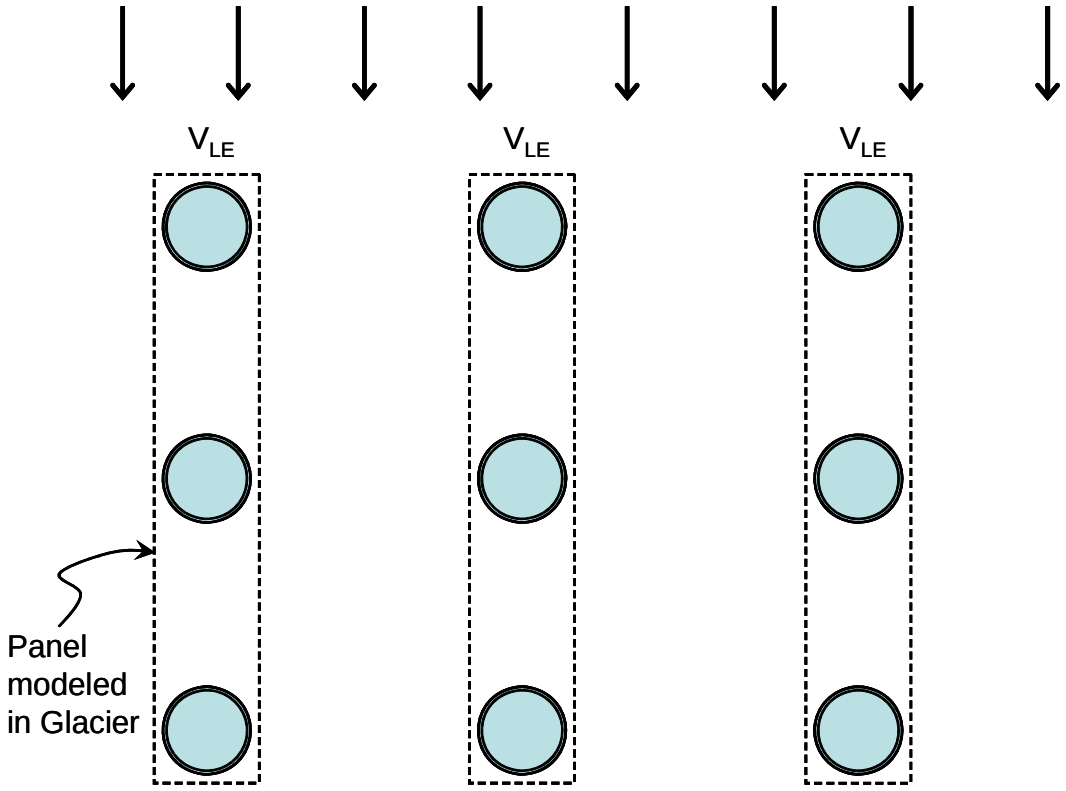

Figure 2.6-16. Representation of tube banks in CFD model.

2.6.2.5 Regions of Deposition

The deposit surface temperature is related to the thickness of the deposit and the deposit heat transfer coefficient. Walsh *et al.* (1992) assume a Nusselt number of 40 for the tube. Given that and assuming a uniform thickness of ash layer (which is probably not the case), the tube surface temperature can be estimated from

$$T_s = T_g - \frac{\left(T_g - T_t\right)}{0.5Nu \ln\left(r_2 / r_1\right) + 1} \qquad \textbf{(2.6-26)}$$

where Nu is the Nusselt number , r_2 is the radius of the tube plus deposit and r_1 is the radius of the clean tube. The local gas temperature is calculated assuming a fixed rate of temperature decrease in the convective pass.

Figure 2.6-17 plots results from an example calculation, assuming a dew point temperature of about 990°C and a tube metal temperature of 627°C. The figure shows that the thicker the ash deposit on the tube, the higher the surface temperature. The figure also indicates the region where the gas temperature lies between the dew point and the melting temperature. Sodium sulfate will condense on the ash particles, and therefore the ash particles that impact the deposit in this region will be sticky and thus more likely to stick. Furthermore, as the deposit thickens and accumulates sodium sulfate, the surface temperature will exceed the melting point of sodium sulfate and the surface will become sticky.

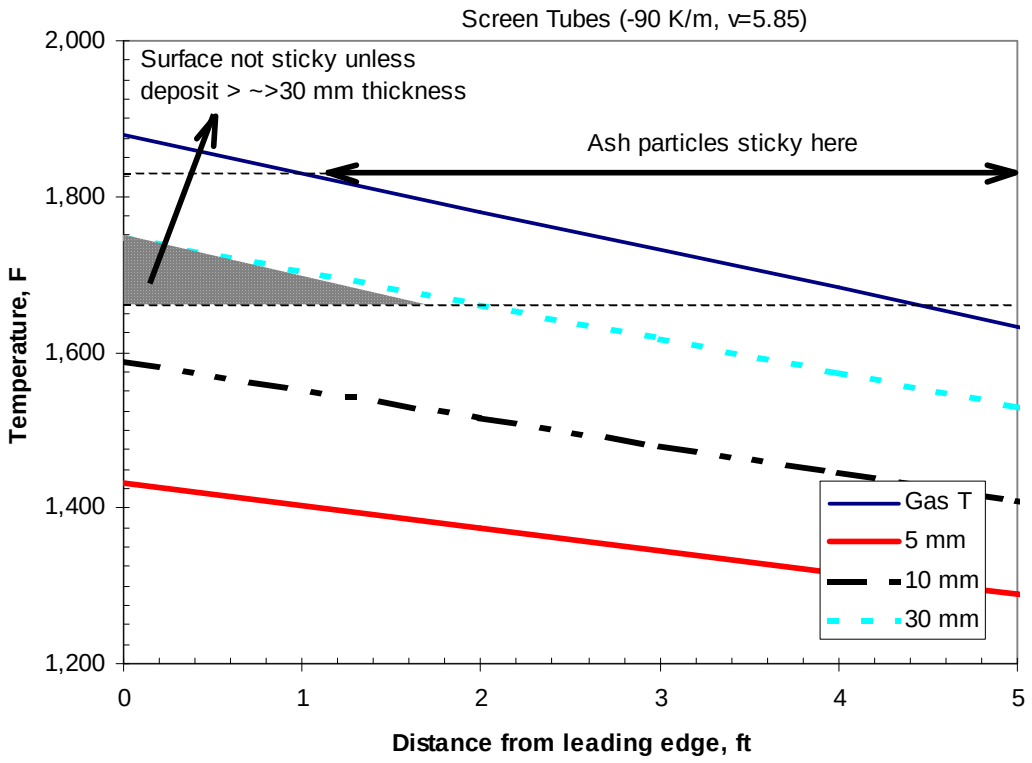

Figure 2.6-17. Gas and surface temperatures as a function of length in convective pass.

Thus, the fraction of the ash particles likely to impact the surface and the regions in which these particles are more likely to stick can be estimated. More quantitative estimates can be made using the formulae given by Walsh *et al*. (1992).

Walsh assumes that erosion is caused by large quartz particles. Assuming the distribution of both quartz and silicates in the deposit are known, the fraction of particles (of a given size) impacting the surface that will be incorporated into the deposit can be calculated. This is given by the difference between sticking and erosion, and is intended to be for dry deposition (when the surface is not sticky):

$$f_{deposit} = \left(1 + R_{Na_2SO_4}\right)\left(f_{Silc}\left(d_p\right)P_{Stick} - f_Q\left(d_p\right)k_{erosion}\right) \qquad \textbf{(2.6-27)}$$

where R_{Na2SO4} is the fraction of Na_2SO_4 on the particle, $f_{Silc}(d_p)$ and $f_Q(d_p)$ are the fractions of the ash size distribution of a given diameter of silicates and quartz, respectively, and P_{stick} is calculated from Eq. 4 in Walsh *et al*. (1992). $k_{erosion}$ is an erosion coefficient, i.e., the mass of deposit removed by erosion per unit mass of quartz particles impacting.

The rate of wet deposition (that is, when the surface is above the melting point of sodium sulfate) will be higher, since the probability of sticking is higher on a wet surface. The rate of impaction (in kg/m^2-s) in a give size range can be estimated as

$$F_{imp} = Uf_{imp}f_{ash}C_{ash} \qquad \textbf{(2.6-28)}$$

where U is the gas velocity in m/s, f_{imp} is the impaction efficiency (see Figure 2.6-15), f_{ash} is the fraction of mass of diameter d_p, and C_{ash} is the concentration of ash in the flue gas in kg/m^3. The fraction of mass depositing in a given size range can be calculated from Eq. 2.6-27 and 2.6-28.

The wet deposition rate can be used to calculate the thickness of a triangular deposit on the leading edge of a tube, as shown in Figure 2.6-18. In this calculation, about 5 days are required to produce a deposit thickness of 5 mm.

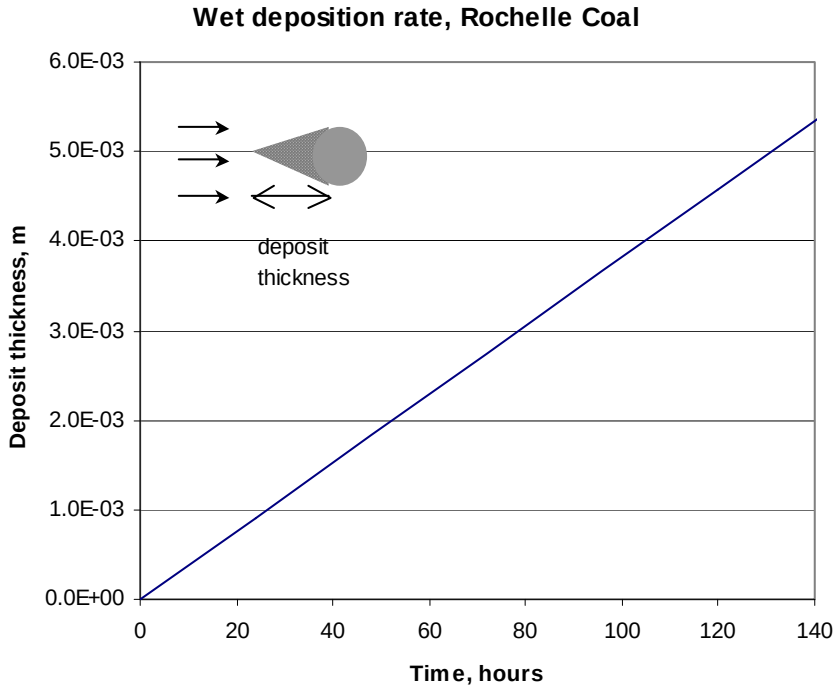

Figure 2.6-18. Estimated thickness of deposit on leading edge of tube as a function of time, Rochelle coal at 988°C (after Walsh *et al.*, 1992).

It is then possible to estimate the fraction of particles that are likely to stick because of sodium sulfate and, thus, the fraction of the ash particles likely to impact the surface and the regions in which these particles are more likely to stick. More quantitative estimates can be made using the formulas given by Walsh *et al*. (1992).

Condensation of sodium sulfate on suspended particles is assumed to begin when the gas has cooled to below the sodium sulfate dew point, which is assumed to be 990°C (1814°F) for the Rochelle coal. Sodium sulfate also deposits on the tubes, but the mass-transfer coefficient for transport to suspended particles is greater than that for transport to the tubes. The partial pressure of sodium sulfate in the gas is assumed to decay exponentially with time following the onset of condensation. The time-constant for condensation of sodium sulfate on particles depends on the specific surface area weighted mean particle size ($<d_s>$) and the concentration of particles, M_{ash}:

$$\tau = \frac{\rho_{Na_2SO_4} \left\langle d_s \right\rangle^2}{6 Sh_p D_{Na_2SO_4} M_{ash}} \qquad \textbf{(2.6-29)}$$

where the Sherwood number Sh_p of the particles is assumed to be 2, $\rho_{Na_2SO_4}$ is the density of condensed sodium sulfate, and $D_{Na_2SO_4}$ is the diffusivity of sodium sulfate in the gas. For the Rochelle coal the area-mean diameter is about 10 microns if just calculated from the one-ash-per-coal particle assumption

(Figure 2.6-14); in reality, however, there will be some smaller particles that will shift the area-mean diameter to a smaller size. The area-mean diameter will be assumed to be 5 microns. Using this diameter, the characteristic time is estimated to be ~0.1 seconds. This suggests that ash particles might not acquire a sticky, sodium sulfate layer immediately after the flue gas temperature drops below the dew point of sodium sulfate, but there might be an induction period of a hundred milliseconds.

The thickness of the sulfate layer on a particle of diameter d_p is calculated as

$$\delta = Y_{Na_2O} \frac{MW_{Na_2SO_4} \rho_{ash} \langle d_s \rangle^2}{MW_{Na_2O} \rho_{Na_2SO_4} 6 d_p} \left[1 - e^{-t/\tau}\right] \qquad \textbf{(2.6-30)}$$

where $Y_{Na_2SO_4}$ is the mass fraction of sodium oxide in the ash and MW_i are the molecular weights. For example, the surface layer on a 10 micron particle would be about 0.01 microns.

Walsh *et al*. (1990) incorporated the analysis of Wall *et al*. (1979) to calculate the probability that an ash particle with a condensed sodium sulfate layer (of diameter d_p) would stick (the dry sticking probability) as

$$\eta_{dry} = 4\gamma \frac{Y_{Na_2O} MW_{Na_2SO_4} \langle d_2 \rangle^2}{\rho_{Na_2SO_4} MW_{Na_2O} d_p^3 v^2} \left[1 - e^{-t/\tau}\right] \qquad \textbf{(2.6-31)}$$

where γ is the surface tension and v is the particle velocity. For the Rochelle coal, the dry sticking probability was estimated at t=150 milliseconds as shown in Figure 2.6-19.

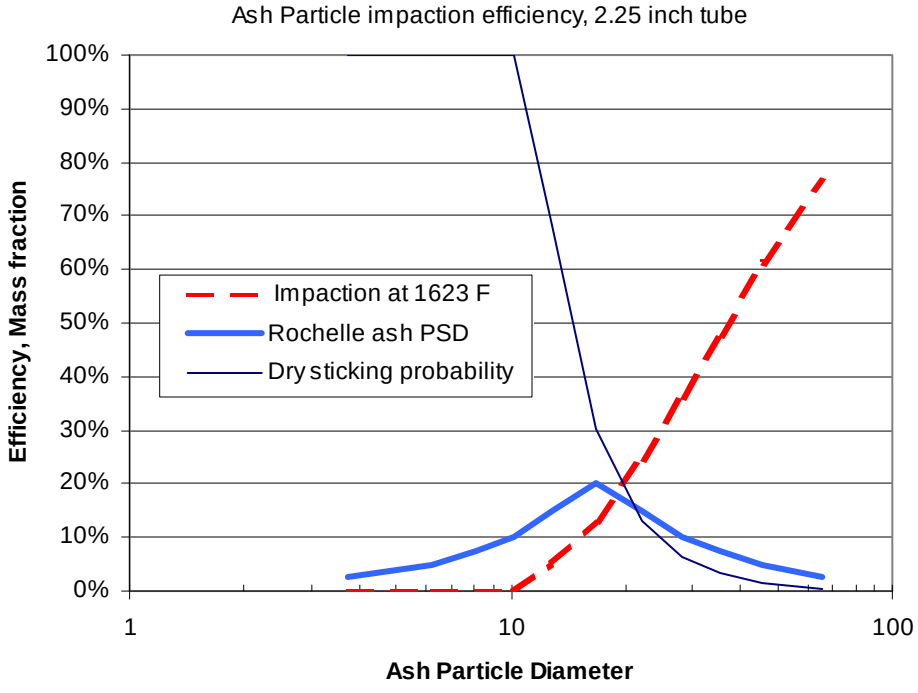

Figure 2.6-19. Impaction efficiency, dry sticking probability, and ash size distribution for Rochelle coal at 150 milliseconds after dew point, 5.85 m/s velocity.

The ratio of the mass of condensed sulfate to the particle mass, for a given particle diameter is

$$R_{Na_2SO_4} = Y_{Na_2SO_4} \frac{MW_{Na_2SO_4} \langle d_s \rangle^2}{MW_{Na_2O} d_p^2} \left[1 - e^{-t/\tau}\right] \quad \textbf{(2.6-32)}$$

Walsh *et al.* (1992) assume that erosion is caused by large quartz particles. Assuming one knows the distribution of both quartz and silicates in the ash, one can calculate the fraction of particles (of a given size) impacting the surface that will be incorporated into the deposit. This information can be obtained when the mineral matter transformation model is used to calculate the fly ash particle size distribution and composition. This is given by the difference between sticking and erosion, and is intended to be for dry deposition (when the surface is not sticky):

$$f_{deposit} = \left(1 + R_{Na_2SO_4}\right)\left[f\left(d_p\eta_{dry} - f_Q\left(d_p\right)k_{erosion}\right)\right] \quad \textbf{(2.6-33)}$$

where $R_{Na_2SO_4}$ is calculated from Eq. 2.6-32, $f(d_p)$ and $f_Q(d_p)$ are the fractions of the ash size distribution of a given diameter of the total ash and quartz, respectively, and η_{dry} is calculated from Eq. 2.6-31. $k_{erosion}$ is an erosion coefficient, i.e., the mass of deposit removed by erosion per unit mass of quartz particles impacting.

The fraction of the ash particles incorporated into the deposit by dry deposition of sticky particles is estimated in Figure 2.6-20. The erosion term in Eq. 2.6-33 was not included, since we do not know anything about the mineralogy of this coal. Figure 2.6-20 shows that the fraction of particles likely to stick because of dry deposition is small and centered around 20-30 microns.

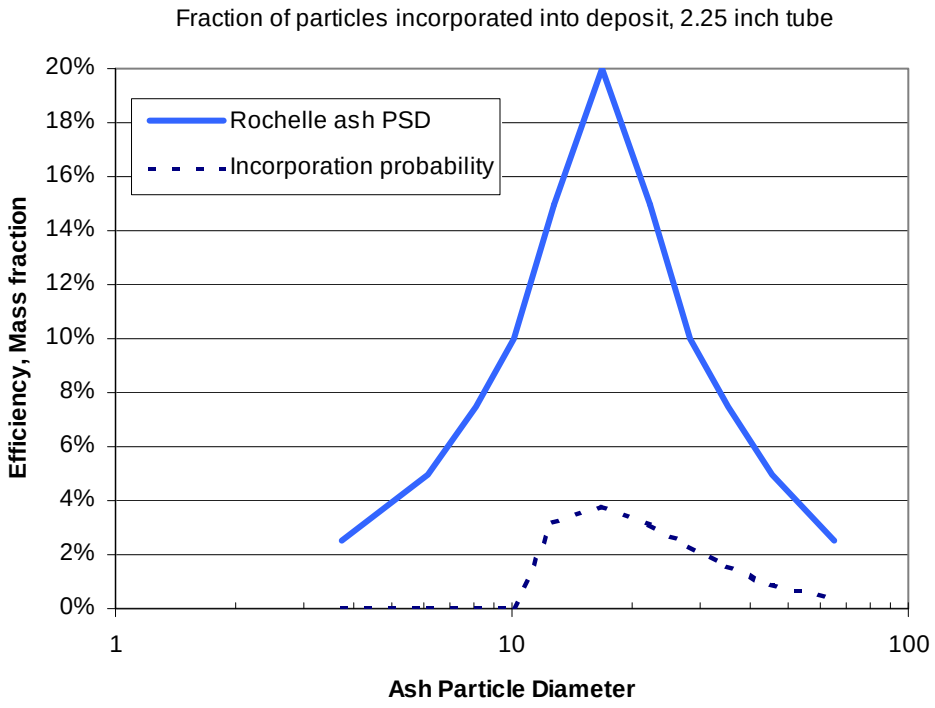

Figure 2.6-20. Fraction of particles sticking by dry deposition (at 150 milliseconds from dew point).

Sodium sulfate can also deposit directly on the tube, when the gas temperature is below the dew point. This deposition rate (in kg/m^2-s) is given by

$$F_{Na_2SO_4} = \frac{Sh_t D_{Na_2SO_4}}{d_t} \frac{\pi}{2} M_{ash} Y_{Na_2O} \frac{MW_{Na_2SO_4}}{MW_{Na_2O}} e^{-t/\tau} \qquad \textbf{(2.6-34)}$$

where the subscript *t* denotes the tube. The Sherwood number of the tube is assumed to be 40.

The rate of direct sodium sulfate deposition on tubes was estimated to be 3x10^{-7} kg/m^2-s at 900^{o}C (1650^{o}F). The sodium sulfate concentration in the flue gas for the Rochelle coal is estimated to be 2x10^{-7} kg/m^3. The sodium sulfate would be expected to preferentially deposit on the fly ash, not on the tubes.

The dry ash deposition flux for the Rochelle coal was estimated to be 2x10^{-5} kg/m^2-sec at 900^{o}C (1650^{o}F), without taking into account any erosion by fly ash. This would remove about 0.4% of the ash from the flue gas and in an eight-hour period result in a wedge of ash at the leading edge of the tube with a maximum thickness of 0.7 mm. This suggests that deposits in areas of the convective pass that are reached by soot blowers can be controlled effectively, but deposits in areas that are not reached by soot blowers would grow.

The preceding example illustrated how fouling calculations would be carried out. In order to integrate these calculations with the CFD model, assumptions must be included as to how often the tubes in the convective pass are cleaned. This will allow the calculation of the steady-state deposit thickness in the convective pass.

2.6.3 Summary

2.6.3.1 Slagging Model

A slagging modeling approach has been provided here. The approach utilizes both a comprehensive CFD combustion code and a slagging submodel and should be able to predict the deposit build up and strength development in the furnace. The key elements of the proposed slagging prediction approach are (see Figure 2.6-6):

1. Calculate particle capture based on particle deposition rate (from CFD code) and particle viscosity and outermost deposit layer viscosity (based on ash composition, ash and deposit temperature, gas composition).
2. Calculate mass of new deposit layer.
3. Calculate sintering of all deposit layers.
4. Calculate all deposit layer properties (thickness, porosity, thermal conductivity, emissivity, absorptivity).
5. Calculate deposit layer thermal resistance.
6. Calculate heat flux through all deposit layers and temperature of each deposit layer.
7. Repeat for next time step.

Potential improvements to the proposed approach include, but are not limited to, the following:

1) Coal particle fragmentation

In the *Glacier* CFD model, an ash composition distribution is assigned to a coal particle size bin based on the fly ash transformation model and the coal particle is tracked along the trajectory with the assumption that one fly ash particle is formed from a coal particle. A coal fragmentation model can be added in the future if it is determined to be necessary in oxy-combustion conditions.

2) Excluded pyrite transformation model
Excluded pyrite transformation is unique in comparison with included mineral matter transformation and other excluded mineral matter. An approach to track excluded pyrite transformation and deposition should be included in the proposed approach when dealing with a coal with an abundance of excluded pyrite. The transformations of excluded pyrite in a combustion environment will depend on the local temperature and oxygen concentration, which may be different in an oxy-combustion environment. Thus, attention should be paid to adaptation of the excluded pyrite transformation model to oxy-combustion.

3) Improved sintering and deposit properties calculations
The approach proposed here can be modified if more accurate calculations of sintering and deposit properties have been identified from the literature. In oxy-combustion systems, the local temperature and oxygen concentrations in the combustion zone might differ than in air-combustion systems. Oxygen concentrations will affect the viscosity of the ash particles, particularly for ash with high amounts of iron oxide. The impacts of local oxygen concentrations and temperatures will be accounted for in the existing ash viscosity model.

2.6.3.2 Fouling Model

A model for fouling in the back pass has been outlined, and can be summarized as follows:

1) Vaporization of sodium during the combustion process
A model for vaporization of sodium in coal combustion systems was developed, based on the ratio of the organically bound sodium to SiO_2 in the coal. This empirical model was based on pulverized coal combustion in air. The net sodium vaporization might be different in oxy-combustion, and thus measurements need to be made in the pilot-scale rig during this program to quantify the validity of the current model under oxy-combustion conditions.

2) Deposition of sodium sulfate on fly ash particles and tube surfaces
The dew point of sodium sulfate in the flue gas entering the convective pass can be calculated once the net sodium sulfate vaporization is calculated. At temperatures that fall between the dew point of sodium sulfate and the melting temperature of Na_2SO_4, condensation of sodium sulfate will result in a sticky surface. The dew point is calculated from an equilibrium calculation, which will take into account any differences in composition of the flue gas between oxy-combustion and air-combustion.

3) Deposit growth rate on convective pass tubes
Once the range of sticking temperatures is calculated as a function of temperature and fly ash particle size, the deposition and erosion rates as a function of location in the back pass can be calculated. The local temperature and velocity in the back pass of the boiler will come from the CFD model. The size distribution of the fly ash will come from the mineral matter transformation model.

2.6.4 Slagging and Fouling References

Anderson, D.W.; Viskanta, R.; Incropera, F.P. Effective Thermal Conductivity of Coal Ash Deposits at Moderate to High Temperatures. *Journal of Engineering for Gas Turbine and Power* **1987**, *109*, 215-221.

Benson, S. A.; Holm, P.L. Comparison of Inorganic Constituents in Three Low-Rank Coals. *Ind. Eng. Chem. Prod. Res. Dev.* **1985,** *24*, 145-149.

Bohren, C.F. Multiple Scattering of Light and Some of its Observable Consequences. *American J. of Physics* **1987**, *55*, 524-532.

Bohren, C.F.; Huffman, D.R. *Absorption and Scattering of Light by Small Particles*, John Wiley & Sons, 1983.

Boni, A.A. *et al*. (1990) *Transformations of Inorganic Coal Constituents in Combustion Systems*, Phase I Final Report, DOE Contract DE-AC22-86PC90751, Physical Sciences, Inc., Andover, MA, March 1990.

Bool, L.E. *et al*. *Fundamental Study of Ash Formation and Deposition: Effect of Reducing Stoichiometry*, Final Report, DOE Contract DE-AC22-93PC92190, Physical Sciences, Inc., Andover, MA, September 1995.

Brewster, M.Q. *Thermal Radiation Transfer and Properties*. John Wiley, 1992.

Chappell, J. S.; Ring, T. A. Particle Size Distribution Effects on Sintering Rates. *Journal of Applied Physics* **1986**, *60(1)*, 383-391.

Coble, R.L. Effects of Particle-Size Distribution in Initial-Stage Sintering. *Journal of the American Ceramic Society* **1973**, *56(9)*, 461-466.

Frenkel, J. Viscous Flow of Crystalline Bodies Under the Action of Surface Tension. *J. Phys*. (Moscos) **1945**, *9*, 385-390.

Gallagher, N. B.; Bool, L. E.; Wendt, J. O. L.; Peterson, T. W., Alkali Metal Partitioning in Ash from Pulverized Coal Combustion. *Comb. Sci. and Tech.* **1990**, *74*, 211-221.

Gallagher, N. B.; Peterson, T. W.; Wendt, J. O. L., Sodium Partitioning in a Pulverized Coal Combustion Environment. *Proc. Combustion Institute* **1996**, *26*, 3197-3204.Goodwin, D.G. "Infrared Optical Constants of Coal Slags." Ph.D. thesis, Stanford University, 1986.

German, R. M. *Sintering Theory and Practice*. New York, Wiley (1996).

Gupta, R.P.; Wall, T.F.; Baxter, L. The Thermal Conductivity of Ash Deposits: Particulate and Slag Structures. A paper presented at *Impact of Mineral Impurities in Solid Fuel Combustion.* An Engineering Foundation Conference, Kona, Hawaii, Nov. 2-7 (1997).

Harb, J.N.; Slater, P.N.; Richards, G.H. A Mathematical Model for the Build-Up of Furnace Wall Deposits. In *the Impact of Ash Deposition on Coal Fired Plants*. J. Willamson and F. Wigley (Eds), Solihull, Taylor & Francis press, 637-644, 1993.

Israel, R.; Rosner, D. E., Use of a Generalized Stokes Number to Determine the Aerodynamic Capture Efficiency of Non-Stokesian Particles from a Compressible Gas Flow. *Aerosol Sci. Technol.* **1983**, *2*, 45-51.

Kingery, W.D.; Bowen, H.K.; Uhlmann, D.R. *Introduction to Ceramics*, 2nd ed., John Wiley & Sons, New York, 1976.

Mackenzie, J.K.; Shuttleworth, R. Phenomenological Theory of Sintering. *Proc. Phys. Soc. London*. **1949**, ***62*** (12-B), 833-852.

Mills, K.C. Estimation of Physicochemical Properties of Coal Slags and Ashes. In *Mineral Matter and Ash* in Coal, K.S. Vorres (Ed), American Chemical Society, Washington, D.C., 195-214, 1986.

Quann, R.J., PhD Thesis, MIT, 1992.

Raask, E. *Mineral Impurities in Coal Combustion*. Hemisphere Publishing Company, Washington D.C, 1985.

Richards, G.H.; Slater, P.N.; Harb, J.N. Simulation of Ash Deposit Growth in a Pulverized Coal-Fired Pilot Scale Reactor. *Energy & Fuels* **1993**, *7*, 774-781.

Scherer, G.W. Sintering of Low-Density Glasses: 1, Theory. *Journal of The American Ceramic Society* **1977**, *60*, 236-239.

Senior, C.L. *et al*. *Toxic Substances from Coal Combustion – A Comprehensive Assessment*, Final Report, DOE Contract DE-AC22-95PC95101, Physical Sciences, Inc., Andover, MA, July 2001.

Senior, C. L.; Srinivasachar, S. Viscosity of Ash Particles in Combustion Systems for Prediction of Particle Sticking. ***Energy & Fuels*** **1995**, *9*, 277-283.

Wall, T.F.; Lowe, A.; Wibberley, L.J.; Stewart, I.M. Mineral matter in Coal and the Thermal Performance of Large Boilers. *Prog. Energy Combust. Sci*. **1979**, 5, 1-29.

Wall, T.F.; Bhattacharya, S.P.; Zhang, D.K.; Gupta, R.P.; He, X. The Properties and Thermal Effects of Ash Deposits in Coal-Fired Furnaces. *Prog. Energy Combust. Sci*. **1993**, *19*, 487-505.

Walsh, P.M.; Sayre, A.N.; Loehden, D.O.; Monroe, L.S.; Beér, J.M.; Sarofim, A.F., Deposition of Bituminous Coal Ash on an Isolated Heat Exchanger Tube: Effects of Coal Properties on Deposit Growth. *Prog. Energy Combust. Sci.* **1990**, *16*, 327-346.

Walsh, P. M.; Sarofim, A. F.; Beer, J. M., Fouling of Convection Heat Exchangers by Lignitic Coal Ash. *Energy & Fuels* **1992**, *6*, 709-715.

Wang, H., *Modeling of Ash Formation and Deposition in PC Fired Utility Boilers*. Ph.D. dissertation, Brigham Young University, 1998.

Wang, H.; Harb, J.N., Modeling of Ash Deposition in Large Scale Combustion Facilities Burning Pulverized Coal. *Progress in Energy and Combustion Science* **1997**, *23*, 267-282.

Wang, H.**;** Harb, J. N. Modeling of Ash Deposit Growth and Sintering in PC-Fired Boilers. 1997 Engineering Foundation Conference on *The Impact of Mineral Impurities in Solid Fuel Combustion* at Kona, Hawaii, November 2-7, 1997, Edited by Gupta *et al*., pp 697-708, 1999.

Wang, H.**;** West, J.; Harb, J.N., Microanalytical Characterization of Slagging Deposits in a Pilot-Scale Combustor. *Energy & Fuels* **1999**, *13* , 570-578.

2.7 Task 7 – Corrosion Mechanism Review and Development

2.7.1 Introduction

Since fire side water tube and steam tube corrosion was first recognized in the late 1950s, this problem has been the subject of many studies to identify mechanisms and to control corrosion propensities [1, 2]. As a result of these studies, the number of fire-side corrosion problems has been reduced. However the problem has not been solved but just avoided by adjusting operating parameters such as steam temperature. It has also been reported that no known tube material is free of corrosion [3]. Recently, interest in fire-side corrosion has re-emerged due to an unexpected increase in corrosion in the furnaces modified for low NOx operation. Additional interest has been generated by efforts to increase boiler efficiency using advanced combustion system such as ultra-supercritical boilers and, more recently, to assess boiler suitability for oxygen-firing combustion.

Fire-side corrosion can be categorized based on the location: waterwall, superheater/reheater, and low temperature corrosion as shown in Figure 2.7-1. Waterwall and superheater/reheater corrosion are considered high temperature corrosion and are of primary concern in this project. Low temperature corrosion refers to acid dew point corrosion occurring in the boiler back pass.

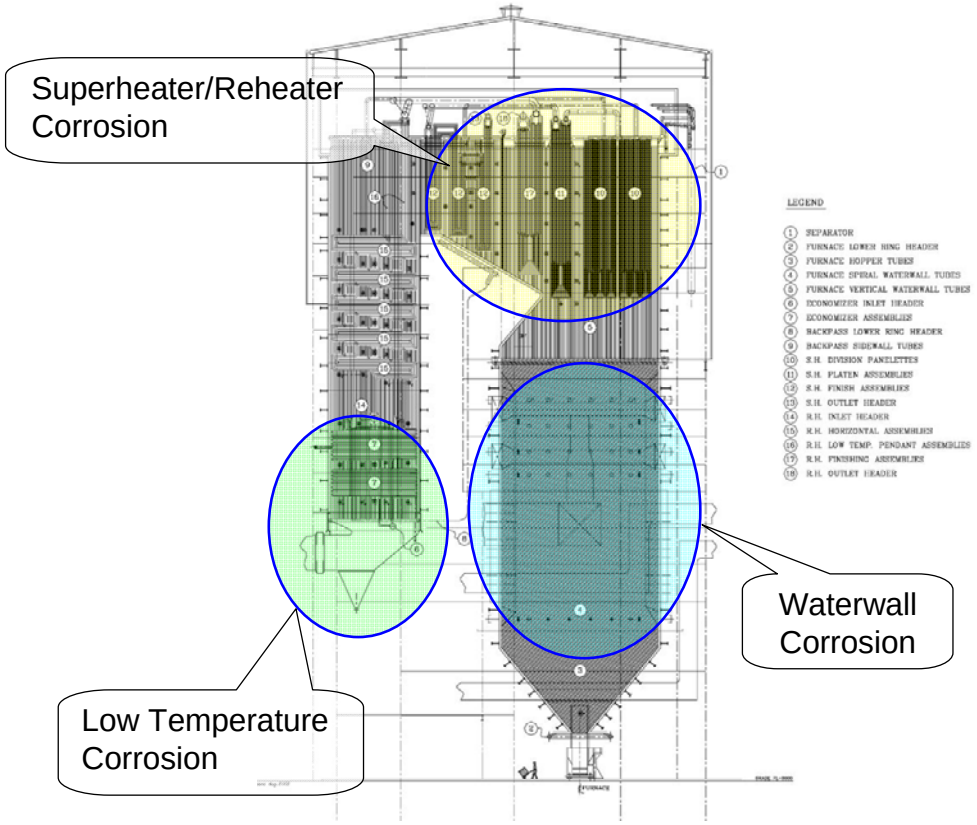

Figure 2.7-1. Fire-side corrosion based on the location in the furnace.

Fire-side corrosion can occur through a combination of various physicochemical phenomena occurring near the tube metal surface. Several corrosion mechanisms have been identified as relevant in coal-fired boilers: oxidation, sulfidation, and chloridation. The acting corrosion mechanism depends on local environment, determined by various key parameters and can occur through one dominant mechanism or a combination of multiple mechanisms. These mechanisms have been developed for air-fired conditions.

The local environment in a furnace retrofit for oxy-combustion is expected to be very different from air-fired boilers. Therefore known corrosion mechanisms need to be re-visited and potentially revised to account for the modified environment. As a part of this effort, the published research studies relevant to oxidation, sulfidation, chloridation, carburization, and the issues related to oxy-firing conditions are summarized here.

2.7.2 Corrosion Parameters and Mechanisms

It is useful to summarize various key corrosion parameters before a discussion of corrosion mechanisms. Fireside corrosion may be induced by combinations of many boiler parameters. These parameters include:

- Sulfur, vanadium, chlorine, alkali and alkaline metal contents in fuel.
- Local deposition and deposit characteristics including: thermal gradients, chlorine, SO_2 and metal species concentrations and deposit physiochemical properties.
- Local stoichiometry and fluctuations in stoichiometry.
- Local flue gas composition.
- Local heat flux.
- Tube metal temperature (determined by steam side temperature).
- Flue gas temperature, temperature fluctuations and flue gas temperature gradient.

These parameters can determine active corrosion mechanism(s) and the extent and rate of corrosion, and should be considered in understanding corrosion in oxy-fired pulverized coal combustion conditions.

The main corrosion phenomena on the fireside of the boiler tubes can be classified as oxidation, sulfidation, and chloridation. In oxy-firing conditions, carburization may also occur due to high concentration of CO_2 in flue gas. In the following sections, these mechanisms are discussed in detail.

2.7.3 Oxidation

Oxidation is typically the most common high temperature corrosion mechanism in the boiler. Under an oxidizing environment, tube metal (M) can react with gaseous oxidant such as O_2, CO_2, or H_2O to form metal oxides on the bare tube:

$$M + \frac{1}{2}O_2 \rightarrow MO \qquad \textbf{(2.7-1)}$$

$$2MO + \frac{1}{2}O_2 \rightarrow M_2O_3 \qquad \textbf{(2.7-2)}$$

Oxidation is not always detrimental to the metal surface as the oxide scale can provide protection from attacks of corrosive species. Therefore, the tube metal surfaces with oxide scale are more corrosion resistant than those metal surfaces exposed to corrosive gases without oxide scale. Metal temperature is an important parameter in this mechanism, as oxidation rates of the tube metals will increase with increasing temperature. The most common oxide scale that provides corrosion protection is chromium oxide (Cr_2O_3). Therefore, increasing chromium content in the tube metal is one of the ways to increase corrosion resistance. Other alloy components that can provide corrosion resistance are aluminum, silicon, nickel, and rare-earth metals. However, if the metal is exposed to conditions where continuous oxidation can occur, oxidation can result in metal wastage. To avoid continuous oxidation, the corrosion product, oxide scale, should remain attached to the metal surface without flaking or spalling and have a high melting temperature, a low vapor pressure, similar thermal expansion coefficients as the tube metal, some plasticity at high temperature, and low diffusion coefficients for metal ions and oxygen.

2.7.4 Sulfidation

2.7.4.1 Corrosion by Gaseous H_2S

Under oxidizing conditions, a protective Fe_3O_4 scale forms on tube surfaces and metal wastage generally occurs at extremely low rates. The Fe_3O_4 scale adheres strongly to the underlying metal, is impermeable to gases, and inhibits further metal loss. Under oxidizing conditions, fuel sulfur is converted primarily to SO_2 which typically has little effect on the tube metal. However, under reducing conditions, existing in the lower furnace when combustion is staged, fuel sulfur is preferentially converted to a reducing sulfur species such as H_2S, CS_2, or COS. High temperature metal corrosion may occur in the presence of these species through sulfidation of the metal surface. FeS forms on the tube surface in addition to or in place of Fe_2O_3. The weak FeS or mixed FeS / Fe_2O_3 scale is not as protective as the Fe_2O_3 scale, is more permeable to gases, and is subject to spalling, resulting in metal loss. A schematic of this corrosion mechanism is shown in Figure 2.7-2 and this corrosion occurs through the following steps:

1. Under a reducing environment, non-uniform oxide scale is formed on the metal surface
2. Reduced sulfur species such as H_2S are formed and diffused to the metal surface
3. Sulfidation occurs and FeS forms on the tube surface
4. FeS scale does not provide any protection against corrosive gas access

Tube material can also affect the sulfidation behavior. The presence of chromium in tube metal results in the formation of a protective chromia rich scale, as chromium can be relatively easily oxidized under even low partial pressure of oxygen compared to iron and nickel. This chromia can inhibit sulfidation.

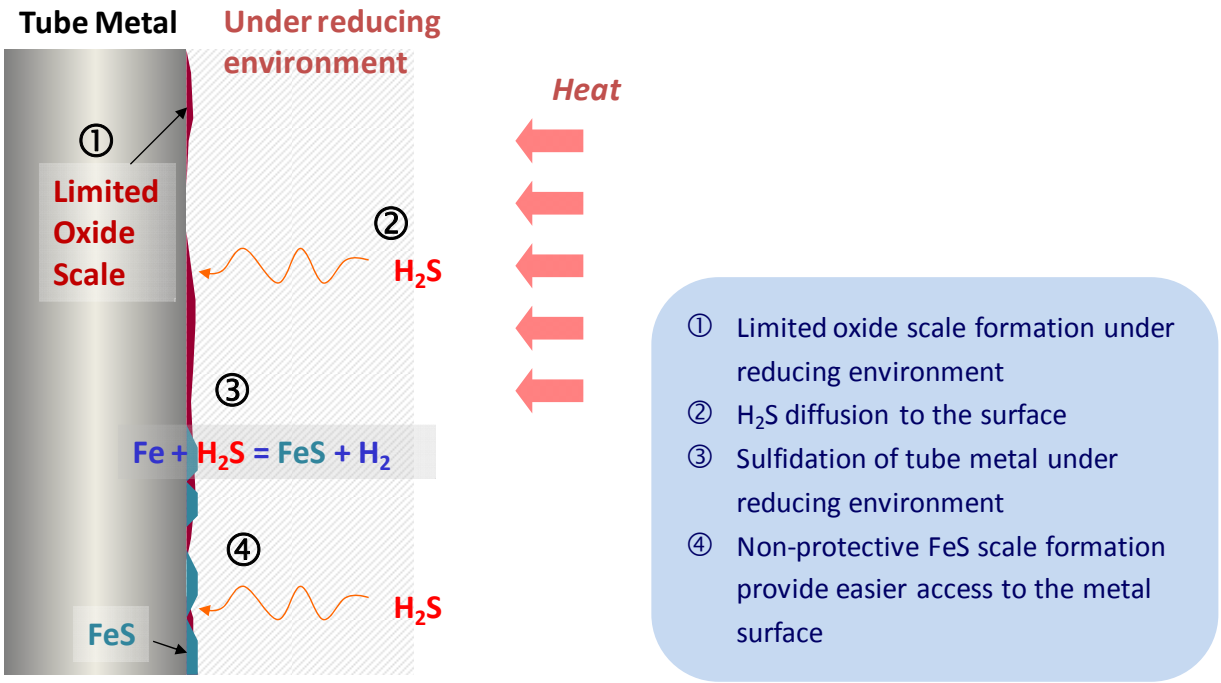

Figure 2.7-2. Schematic of H_2S corrosion mechanism.

Kung's [4] empirically developed correlations for H_2S corrosion for low and high chromium steels are

$$CR = 3.2\times10^{5}\exp\left(-\frac{15{,}818}{1.987T}\right)\times[H_2S]^{0.574}\times\frac{1}{(Cr\%+10.5)^{1.234}}\pm 2.2 \qquad \textbf{(2.7-3)}$$

for carbon and low-alloy steels with $0 \le$ Cr wt% ≤ 10, and

$$CR = 1.04\times10^{7}\exp\left(-\frac{19{,}230}{1.987T}\right)\times[H_2S]^{0.29}\times\frac{1}{(Cr\%+1.40)^{1.37}}\pm 1.2 \qquad \textbf{(2.7-4)}$$

for high-alloy steels with $10 \le$ Cr wt% ≤ 16, where CR is the corrosion rate in mil/yr, T is the tube metal temperature in Kelvin, H_2S is the flue gas concentration of H_2S in mg/kg, and Cr% is the % metal Cr content by weight.

Kung recommends that use of these correlations be limited to tube temperatures up to 482°C. (755 K), metal Cr contents up to 25% by weight, and H_2S concentrations of 500 mg/kg to 5000 mg/kg. According to these correlations, corrosion rate is more dependent on temperature than on H_2S concentration.

The H_2S corrosion rate, according to Kung's correlation for low alloy steel, is plotted for two metal temperatures in Figure 2.7-3. Corrosion rate increases with increasing temperature and the H_2S dependence of corrosion rate increases at higher temperature. However, even at the higher temperature, the predicted corrosion rate is far below the highest rates approaching 100 mil/yr that have been observed in some utility boilers. This observation has led to examination of other corrosion mechanisms for these cases.

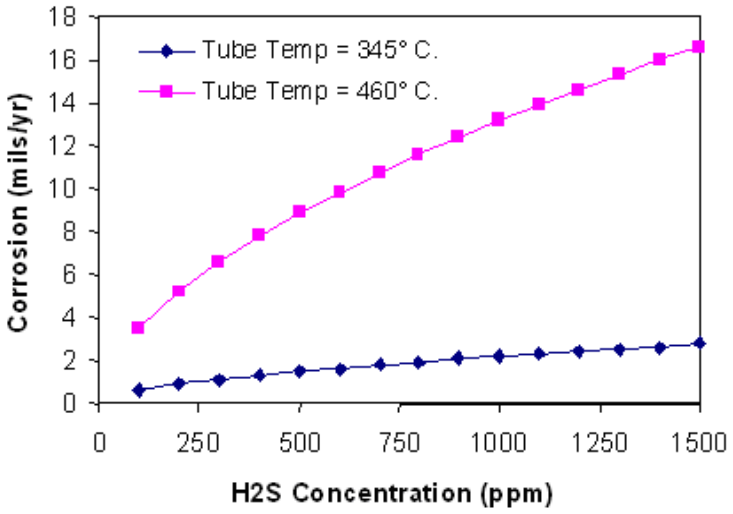

Figure 2.7-3. Plots of Kung's H_2S corrosion correlation as a function of temperature and H_2S concentration.

Perkins *et al*. [5] had previously developed an empirical expression for H_2S corrosion of carbon steel under conditions simulating those of syngas coolers on coal gasifiers,

$$CR = 2.23 \times 10^5 \exp\left(-\frac{4{,}723}{T}\right) \times [H_2S]^{0.23} \quad \textbf{(2.7-5)}$$

where *CR* is the corrosion rate in mil/yr, *T* is the tube metal temperature in Kelvin, and H_2S is the flue gas concentration of H_2S in atm. However, Kung notes that under utility boiler conditions, this expression predicts a corrosion rate approximately four times too high.

Davis *et al*. [6] have developed an empirical expression for a parabolic corrosion rate constant to describe sulfidation rate under reducing conditions (O_2 < 0.5%, CO > 2.%):

$$K_{pr} = B \times (\%CO)^n \times \exp\left(-\frac{Q_r}{RT}\right) \quad \textbf{(2.7-6)}$$

where K_{pr} is the parabolic sulfidation corrosion rate constant under reducing conditions, *B* and *m* are constants, *%CO* is the local CO concentration, and Q_r is the activation energy for sulfidation. This expression is less useful than the Kung correlation since it does not account for metal composition and, although local concentrations of reducing sulfur species correlate with CO concentration, the expression does not explicitly account for varying fuel sulfur.

Nava *et al*. [7] developed an empirical expression for low alloy steel weight loss in an H_2S environment at 500º C:

$$WeightLoss = 7.74 \times 10^{-3} \times (H_2S)^{0.54} \times (time)^{0.86} \quad \textbf{(2.7-7)}$$

where *Weight Loss* is the metal loss in mg/cm^2, H_2S is the local H_2S concentration in ppmv, and *time* is the exposure time in hours. This expression is less general than Kung's correlation since it is applicable only at one temperature, but it does indicate that corrosion rate decreases with exposure time, an observation also made by other researchers [8, 9]. Nava also observes that metal corrosion resistance increases with increasing chromium content.

Huijbregts *et al*. [9] used experimental data to determine constants in an expression for a parabolic corrosion rate coefficient:

$$\log K = a_0 + a_1 \frac{1000}{T} + a_2 (\log(pS_s) + 0.5 \times \log(pCl_2) - 0.75(pO_2)) \quad \textbf{(2.7-8)}$$

where, *K* is corrosion rate coefficient in mm/hr$^{0.6}$, *T* is temperature, and pS_2, pCl_2, *and* pO_2 are the partial pressures of S_2, Cl_2, and O_2, respectively.

In addition to metal loss due to sulfidation, this expression also contains a term for metal loss due to chlorine attack. For 13CrMo4.4 steel at temperatures varying from 400º C. to 450º C., constants a_0, a_1, and a_2 were determined to be 2.78, -3.56, and -0.027, respectively.

John *et al*. [8] developed similar correlations for prediction of corrosion rates due to gaseous phase sulfidation. Although attack by gaseous phase reducing sulfur species contributes to corrosion of tube metal surfaces, at typical pc furnace temperatures this mechanism results in lower corrosion rates than those due either to deposition of sulfur containing material or to fuel chlorine.

2.7.4.2 Deposit based Corrosion (FeS)

When unreacted fuel is deposited on surfaces, impurities such as unoxidized sulfides may also be deposited. Sulfur present in coal is comprised of both organic and inorganic components. The inorganic component is primarily pyrite, which can be excluded (separate from the coal particles) or included (small particles that are trapped within the hydrocarbon matrix). When coal particles are heated, organic sulfur species evolve with other volatile species and, depending on conditions, some fraction of the included sulfur will remain with char. Sulfur can arrive at furnace heat transfer surfaces through the deposition of incompletely oxidized coal char or excluded pyrite, both of which can lead to sulfidation and material loss.

The deposit based corrosion mechanism is illustrated in Figure 2.7-4. Limited oxide scale is formed where reducing conditions prevail and where local conditions change from oxidizing to reducing or vice versa (step ①). Then deposit is formed on the surface of the tube metal or the oxide scale. A number of reports indicate that either an unburned carbon or an FeS deposit on a metal surface may increase corrosion rates, often significantly [7, 10, 11, 12]. It is believed that a fuel rich microclimate develops under the deposit surface and metal loss occurs through sulfidation (steps ③ and ④). FeS and carbon rich deposits have been observed in furnace high corrosion regions and it has been observed that impacting FeS can interact chemically with an existing protective iron oxide scale [13].

Model predictions of sulfur release from pyrite decomposition at three temperatures are compared with experimental data in Figure 2.7-5 [14]. The model included submodels for pyrite particle tracking, kinetics and decomposition. The model shows an initial rapid sulfur release due to thermal decomposition then a slower oxidation process. Sulfur species released at high temperatures are then involved in sulfidation of metal (step ⑤). Sulfide scale formed from iron sulfidation does not provide protection, has higher gas permeability, and is prone to spalling. These characteristics lead to metal wastage.

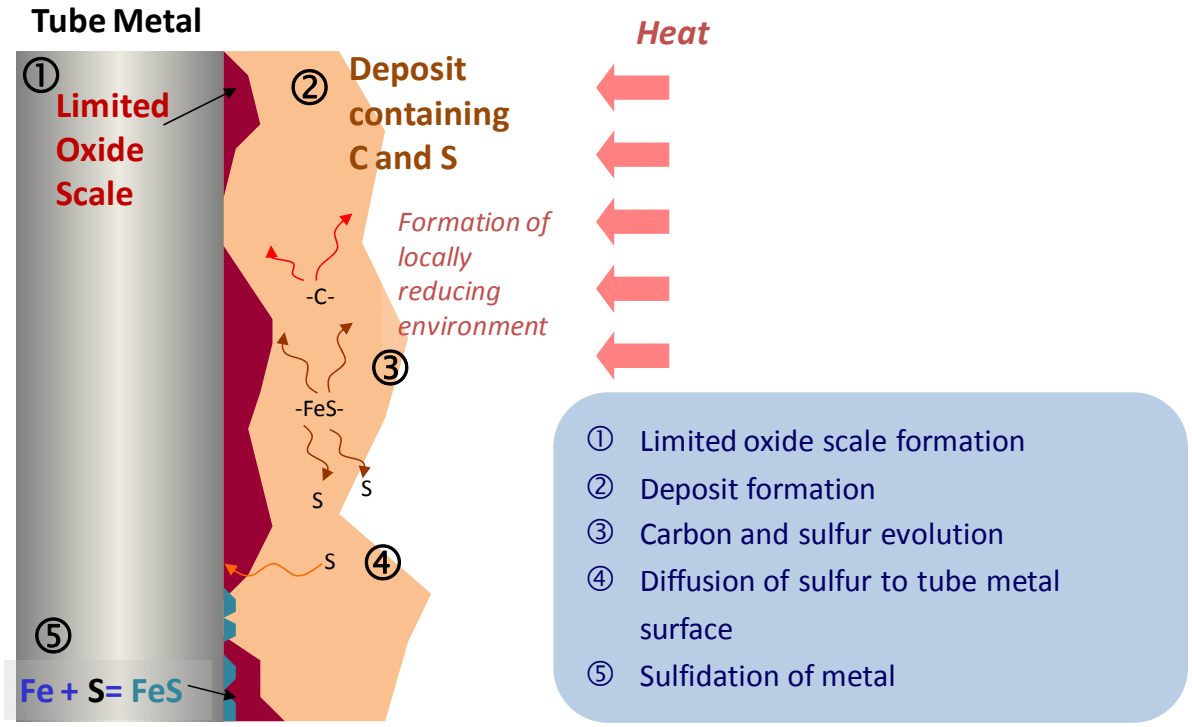

Figure 2.7-4. Schematic of deposit-based corrosion mechanism.

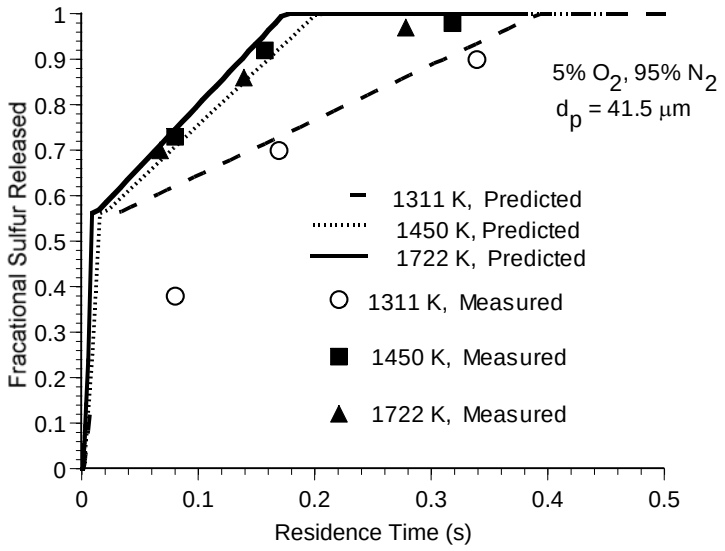

Figure 2.7-5. Comparison of predicted fractional sulfur from pyrite decomposition with laboratory measurements [14].

Laboratory tests have indicated that metal corrosion rates under an FeS layer can exceed 100 mil/yr [15]. However, under very reducing conditions (CO > 7%), the FeS deposit was inert and corrosion rates were low. Under mildly reducing conditions (0%< CO < 3%), corrosion rates increased somewhat, while the highest corrosion rates under an FeS deposit were measured for oxidizing conditions (O_2 > 1%). This indicates that corrosion may result from cycling of furnace operating conditions when regions go from substoichiometric (when FeS deposits occur) to oxidizing. Figure 2.7-6 shows the effect of local stoichiometry on corrosion rate under an FeS layer; as noted above, corrosion rates are highest under oxidizing gas phase conditions. Nava-Paz *et al*. [16] report that the microclimate under an unburned carbon layer in the presence of a sulfidizing gas atmosphere is as corrosive as that under an FeS layer.

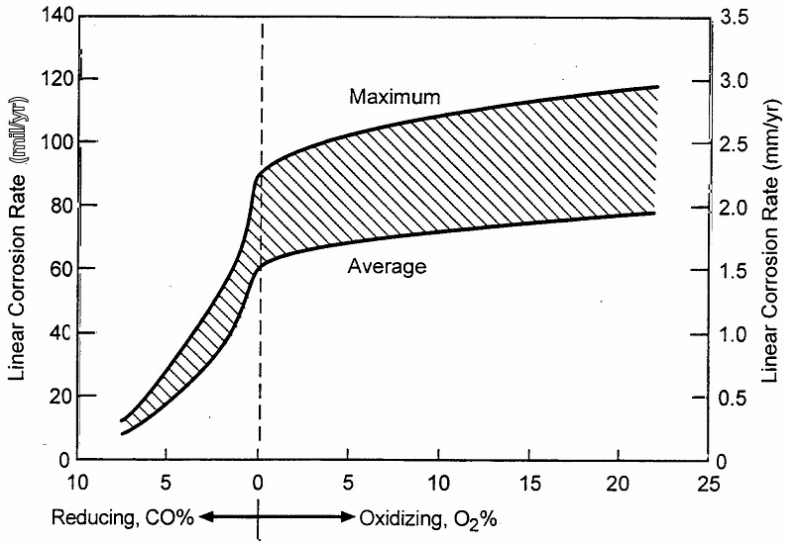

Figure 2.7-6. Corrosion rates predicted for low alloy steels under FeS rich deposits, as a function of O_2 and CO content of flue gas at 450°C [17].

Figure 2.7-7 shows predicted corrosion rates under an FeS layer and in a 1% O_2 gas environment as a function of temperature. Corrosion rates increase with temperature, so supercritical boilers with higher tube temperatures frequently suffer greater wastage than do subcritical boilers. Nava *et al*. [7] observed that metal temperature gradients (as opposed to the isothermal conditions) can accelerate wastage. Such gradients may arise from heat transfer through the surface deposit.

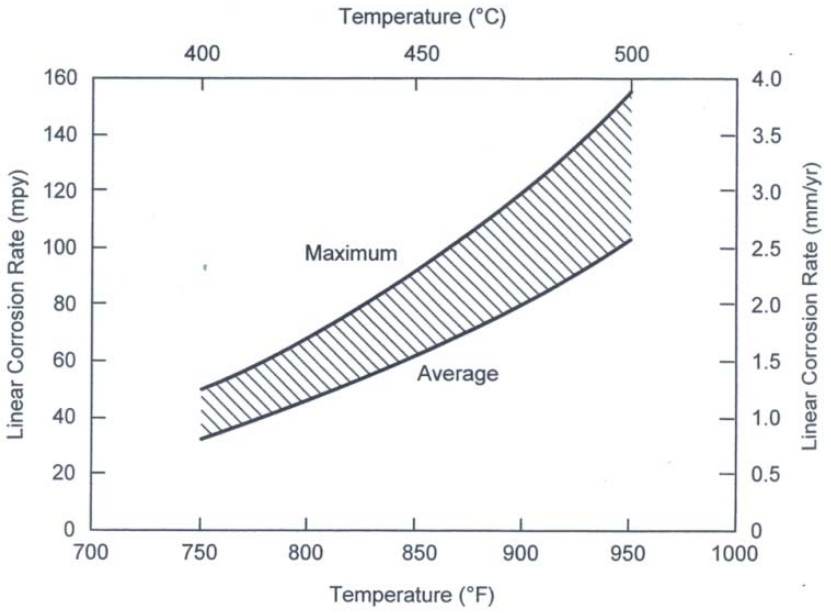

Figure 2.7-7. Corrosion rates as a function of temperature predicted for low alloy steels under FeS rich deposits and in a 1% O_2 gas environment.

2.7.4.3 Molten Sulfate Corrosion

One of the most common forms of corrosion found in coal-fired boilers is accelerated corrosion by molten alkali metal trisulfate [1, 2, 18, 19, 20]. Alkali iron trisulfate, $A_3Fe(SO_4)_3$ has often been found on corroded pendant tubes. There is much discussion on the role of alkali iron trisulfate in this corrosion process. The lowest melting point of Na-K sulfate system is known to be 1513°F (823°C). This temperature would be representative of significantly overheated pendant tubes. However, when iron sulfate is added into the system, alkali iron trisulfate is formed and its melting point is lowered to a typical superheater/reheater pendant tube metal temperatures. In its liquid form, alkali iron trisulfate is known to be highly corrosive. The melting points of $Na_3Fe(SO_4)_3$ and $K_3Fe(SO_4)_3$ are 1155°F (624°C) and 1144°F (618°C), respectively, and significant corrosion can occur at tube metal temperature higher than these temperatures. When these two materials are mixed, the melting point of the mixture can be lowered to 1022°F (550°C). Figure 2.7-8 shows variations in melting points in the alkali iron trisulfate system as a function of K and Na mole ratios. This figure clearly shows that alkali iron trisulfate can exist in the stable liquid form at the superheater tube temperature ranges. However, the stability of the alkali iron trisulfate in the liquid form decreases with increasing temperature. This is one of the reasons that the rates by molten sulfate corrosion have a bell-shape as a function of tube metal temperature (see Figure 2.7-11). Figure 2.7-9 shows the fire side corrosion of various alloys as a function of temperature [21]. As discussed, most alloys have a bell-shaped temperature dependency of the corrosion rates.

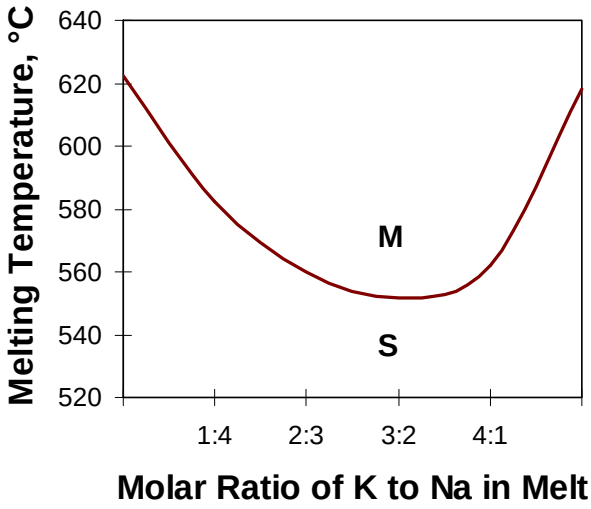

Figure 2.7-8. Solid/liquid equilibrium of $K_3Fe(SO_4)_3/Na_3Fe(SO_4)_3$ system. M, molten phase; S, solid phase (adapted from [2]).

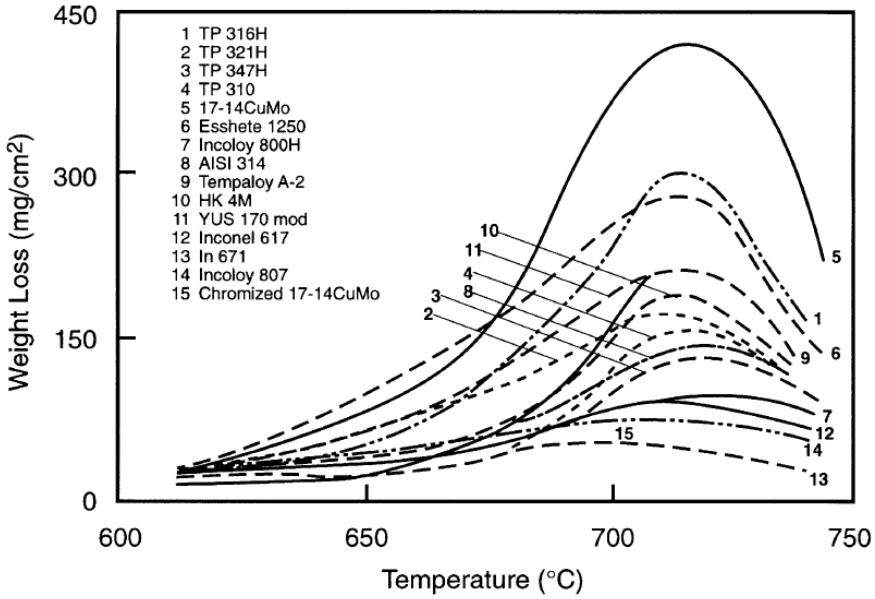

Figure 2.7-9. Weight loss as a function of temperature for various alloys.

Figure 2.7-10 illustrates overall molten sulfate corrosion reaction pathways. In this mechanism generally two surface reactions are considered:

a) Pyrosulfate ($A_2S_2O_7$) formation.

b) Alkali metal trisulfate formation through reactions of alkali sulfate and iron oxide in the presence of SO_2 under oxidizing environment.

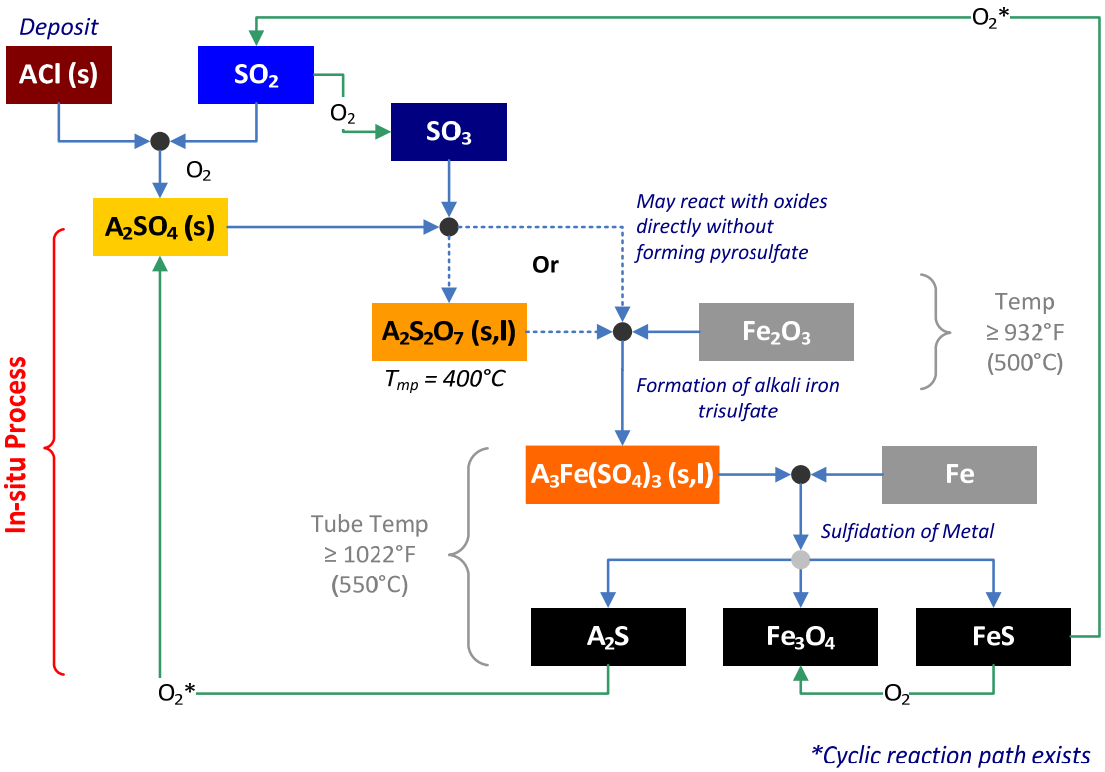

Figure 2.7-10. Overall reaction paths in molten sulfate corrosion mechanism (A: Na or K).

Pyrosulfate formation may start with the deposition of alkali chloride on the oxide scale surface. Then the alkali chloride deposit reacts with SO_2 under oxidizing environment to form pyrosulfate:

$$2(Na,K)Cl(s) + 2SO_2(g) + \frac{3}{2}O_2(g) = (Na,K)_2S_2O_7(s) + Cl_2(g) \qquad \textbf{(2.7-9)}$$

This reaction (9) can be explained by including sulfate and SO_3 formation. The alkali chlorides deposited on the boiler tube can react with SO_2 and O_2 to form alkali sulfates as in the following reaction:

$$2(Na,K)Cl(s) + SO_2(g) + O_2(g) = (Na,K)_2SO_4(s) + Cl_2(g) \qquad \textbf{(2.7-10)}$$

Then, the alkali sulfates can react with SO^3 to form pyrosulfates:

$$(Na,K)_2SO_4 + SO_3 = (Na,K)_2S_2O_7(s) \qquad \textbf{(2.7-11)}$$

However, the formation of pyrosulfates is still in question. Coats *et al.* [22] studied thermal stability of pyrosulfates in the presence of SO_3. This study showed that about 150 ppm of SO_3(g) would be needed to form molten $K_2S_2O_7$ at 765°F (407°C). In the case of $Na_2S_2O_7$, the study reported that more SO_3, about 2000 ppm, would be required to form molten phase.

Reid [23] studied potential roles of pyrosulfate in high temperature corrosion of furnace walls and superheaters and concluded that there was no direct evidence of $K_2S_2O_7$ or $Na_2S_2O_7$ formation in the boiler deposits. Therefore, molten sulfate formation through SO_3 absorption and its fluxing of protective oxide scale have been more emphasized. For example, at the temperature higher than 932°F (500°C), the following reaction can occur:

$$3(Na,K)_2SO_4(s) + Fe_2O_3(s) + 3SO_3(g) = 2(Na,K)_3Fe(SO_4)_3(s,l) \quad \textbf{(2.7-12)}$$

Pyrosulfate can be stabilized in the $(Na,K)Fe(SO_4)_3$ system and can expand the temperature range of the molten state.

The presence of SO_3 is required to form $(Na,K)Fe(SO_4)_3$ as mentioned before. Corey *et al*. [24] reported that at least 250 ppm of SO_3 would be required to form $K_3Fe(SO_4)_3$ at 1000°F (538°C) in the mixture of K_2SO_4 and Fe_2O_3. In the study by Anderson *et al*. [25], the required SO_3 is about 1000 ppm at 1175°F (635°C) in an equilibrium state. These values are much higher than 10 ppm typical in coal-fired boilers. However, it is reported that the SO_3 concentration can be much higher in ash deposits, through SO_2 oxidation by iron oxide catalysts on the metal surface (Equation 2.7-13). In this case, SO_3 concentration can be 50-100 ppm at 711 - 1341°F (377 - 727°C) [26]. Levy *et al.* [27] also reported SO_2 oxidation by catalysis of pure Fe_2O_3 and Krause *et al.* [28] validated the catalytic effect of Fe_2O_3. In this study, local SO_3 concentration is reported to be as high as 2000 ppm in a radioactive tracer experiment.

$$SO_2(g) + \frac{1}{2}O_2(g) \xrightarrow{Fe_2O_3} SO_3(g) \quad \textbf{(2.7-13)}$$

In addition, SO_3 can be formed in the deposit exposed to flame through the reaction between sulfate and silicate as shown in the following reaction:

$$Na_2SO_4 + SiO_2 \xrightarrow{k_1} Na_2OSiO_2 + SO_3 \xrightarrow{k_2} SO_2 + \frac{1}{2}O_2 \quad \textbf{(2.7-14)}$$

SO_3 dissociation can be low in these reactions ($k_1 > k_2$), then SO_3 concentration can be higher than 100 ppm on the deposit surface [26].

At the metal temperature of 550°C or higher, alkali metal trisulfate can attack metal surface through the following reactions. SO_3 evolved in these reactions can react with $(Na,K)_2SO_4$ again and then cyclic reaction path can be established.

$$2(Na,K)_3Fe(SO_4)_3(s,l) + 19Fe = 6Fe_3O_4 + 3FeS + 3Na_2S \quad \textbf{(2.7-15)}$$

$$Na_2S + 2O_2 = Na_2SO_4 \quad \textbf{(2.7-16)}$$

$$3FeS + 5O_2 = Fe_3O_4 + 3SO_2 \quad \textbf{(2.7-17)}$$

$$2SO_2 + O_2 = 2SO_3 \quad \textbf{(2.7-18)}$$

The temperature dependency of the molten sulfate corrosion mechanism is bell-shaped as shown in Figure 2.7-11 [29]. The temperature gradient existing in the deposit and the deposit characteristics are known to induce this bell-shaped temperature dependency. At the temperatures lower than 1022°F (550°C), the deposit is made of porous layers and free gas diffusion is possible through the pores between the flue gas and the metal surface. Then the temperature dependency of the corrosion rate is similar to that of gas phase oxidation. As the metal temperature increases, deposit forms molten alkali metal trisulfates on the tube surface. Then the corrosion rates significantly increase. The melting points of the sulfates are determined by SO_3 partial pressure, relative ratio of Na and K, and the presences of Ca and Mg. Ca and Mg can react with SO_3 to form the sulfates [2]:

$$CaO + SO_3 = CaSO_4 \quad \textbf{(2.7-19)}$$

$$MgO + SO_3 = MgSO_4 \quad \textbf{(2.7-20)}$$

These two sulfates can form more stable $K_2Ca_2(SO_4)_3$ or $K_2Mg_2(SO_4)_3$ and inhibit the formation of alkali iron trisulfate [30]. In addition, Ca and/or Mg containing deposits can cover the oxide scale reducing the catalytic effect of Fe_2O_3 in SO_2 oxidation [2].

When the metal temperature further increases, the alkali metal sulfate is not stable and the corrosion rate decreases.

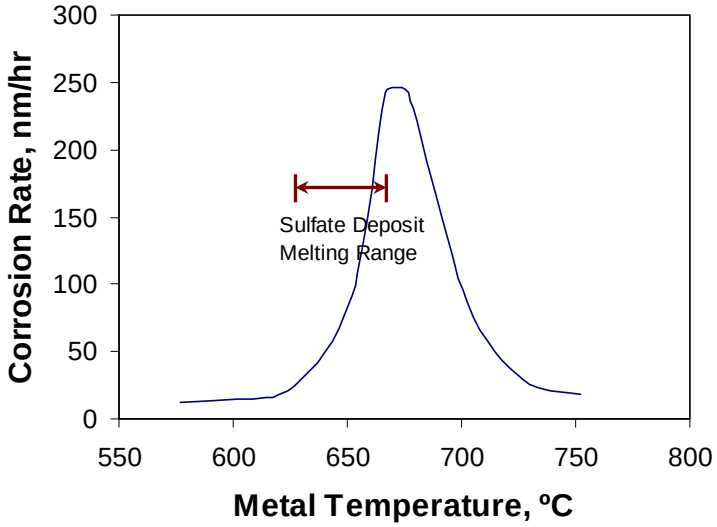

Figure 2.7-11. Bell-shaped curve for the temperature dependence of corrosion on superheater tubes in coal-fired boilers (adapted from [29]).

If the corrosion products of the tube metal are metal oxides such as Fe_2O_3 or Cr_2O_3, the protective scale is formed and metal wastage from the molten phase attach can be reduced. On the other hand, if the corrosion product can be dissolved in the molten deposit, then continuous corrosion in liquid form can occur. The solubility of the corrosion products is related to acidity of the molten salts [31]. For example, chrome in tube metal can be dissolved in acidic molten phase (high P_{SO3}) and generate Cr^{3+}. The layer of the molten salt on the tube metal surface is usually formed under acidic conditions (relatively high SO_3 concentration). As the dissolution of the metal progresses, the corrosion product is accumulated in the molten salt layer on the tube metal surface. If there is no driving force to move the corrosion product away from the metal surface and precipitate, the accumulation of the corrosion product can be saturated and the molten phase is solidified. Hendry *et al.* [32] observed the corrosion rate by molten sulfate at isothermal conditions (1112°F or 600°C) decreases significantly due to molten phase saturation. Continuous corrosion can occur when a negative solubility slope exists as shown Figure 2.7-12. This negative solubility slope can move the metal specie dissolved near the tube metal and precipitate away from the tube metal surface, which can avoid saturation near the metal surface. Under isothermal condition, the solubility of the corrosion product such as Fe^{3+} would increase with increasing SO_3 concentration. This implies positive solubility slope as SO_3 concentration is low at the interface between metal and molten salt and high at the interface between molten salt and flue gas. Therefore, this positive solubility slope from isothermal condition cannot maintain continuous corrosion.

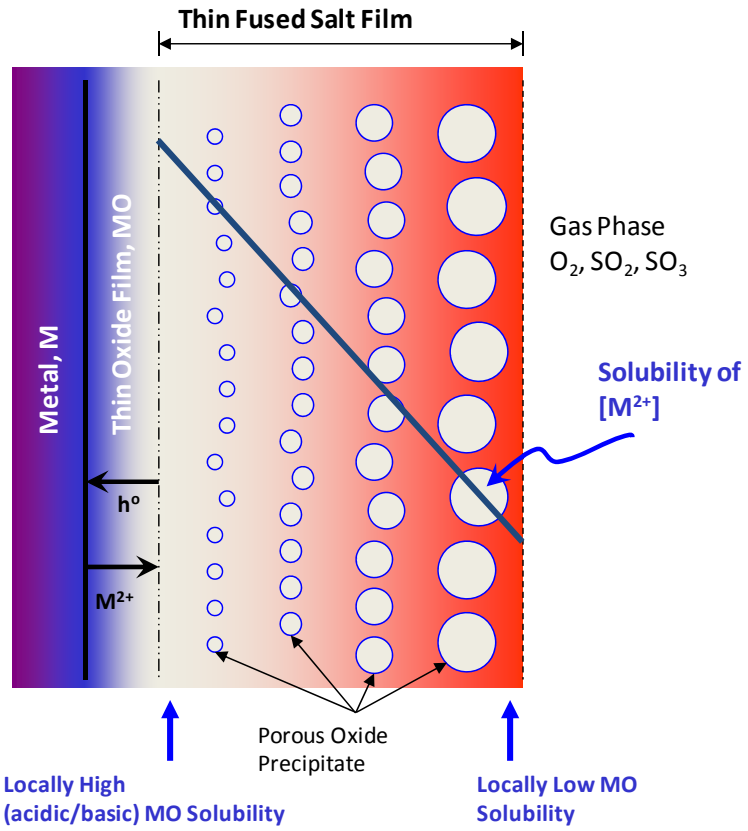

Figure 2.7-12. Precipitation of MO to form porous layer induced by the solubility gradient in a fused salt film (adapted from [31]).

However, actual conditions may be much more complex. A temperature gradient in the molten salt layer acts against the influence of SO_3 concentration distribution in the layer [29, 32]. Thermal gradient increases the solubility at the interface of metal and salt and decreases at the interface of salt and gas, as the corrosion product is more stable at lower temperature. The negative solubility slope from temperature gradient can overcome the positive solubility slope from SO_3 concentration gradient, providing conditions suitable for continuous corrosion. Therefore, temperature gradient is very important to have sustained corrosion. However, if there are more than two metal species (products from corrosion), with different stabilities, the situation can be much more complex. For example Cr_2O_3 is more stable against acid fluxing than Fe_3O_4 or Co_3O_4 [31].

Presence of chlorides can affect the molten sulfate corrosion mechanism in the following ways [18]:

1. Chloride can disintegrate the protective oxide scale. Normally SO_2 and SO_3 cannot diffuse through the scale, but, with disrupted oxide scale, SO_2 and SO_3 can react with tube metal directly.
2. Presence of chlorides in the alkali sulfate can decrease melting point and expand the temperature range that corrosion can occur as shown in Figure 2.7-11.

Many authors report that corrosion rate increases significantly when NaCl is added to alkali sulfate solution, even with only 1 wt% [33, 34, 35]. The impact of this small increase in chloride concentration is bigger for austenitic metal than ferritic metal.

McKee *et al.* [36] reported experimental results on the role of NaCl in high temperature corrosion by Na_2SO_4 at 1292-1472°F (700-800°C). They observed significant increase in corrosion at about 1382°F (750°C) when Na_2SO_4 exists with SO_2 and low concentrations of NaCl under an oxidizing environment. Without SO_2 and NaCl, only small corrosion occurred.

Hancock [37] reports that NaCl addition to Na_2SO_4 removes incubation time. Normally chrome enrichment in the metal can increase the resistance of alkali sulfate corrosion. However alkali metal chloride can destroy chromia allowing sulfur attack [35].

Cutler *et al*. [38] confirmed that addition of 500 ppm HCl to the flue gas of a pilot-scale could increase corrosion rate. When HCl is added, the corrosion temperature range was observed to be expanded. Authors report that adding 1 mol% NaCl does not have a large impact on corrosion. This contradicts Alexander [35]'s observation. The corrosion increase by HCl addition at the pilot-scale furnace may be from increased K release onto the deposit. Generally, the presence of chlorine specie can expand the bell shape temperature dependency shown in Figure 2.7-11.

James *et al*. [20] reports corrosion correlations for austenitic tube material:

$$CRate = A \cdot B \cdot \left(\frac{T_g}{1000} \right)^{\alpha} \cdot \left(\frac{T_m - 550}{100} \right)^{\beta} \cdot (Cl - 0.06) \qquad \textbf{(2.7-21)}$$

Where *CRate* is the corrosion rate, *A* is the tube location, *B* is chromium content in alloy (1 for 18% CR steel and 0.4 for Type 310), T_g is gas temperature (605°C<T_g<1200°C), T_m is metal temperature (870°C <T_m<680°C), *Cl* represents corrosivity of fuel (chlorine content).

Authors report that the corrosion behavior for low alloy ferritic material is elusive and transition from gaseous to molten corrosion may occur. Generally, 0.1% increase in chlorine gives 16 nm/h increases in corrosion rate.

2.7.5 Chloridation

Historically, high fuel chlorine content has been associated with high waterwall corrosion rates in UK pulverized coal furnaces. Recently, a similar problem has developed in US furnaces, although some studies have indicated that burning high chlorine coal does not always lead to accelerated metal corrosion [39]. Chlorine corrosion or chloridation may need proper transport mechanism for chlorine to the tube metal surface. Increased understanding of chlorine based corrosion is currently a very active area of research.

Nielsen *et al*. [40] and Baxter *et al*. [41] have investigated the mechanisms of chlorine based corrosion. Gaseous phase attack may occur through exposure to gaseous HCl or Cl_2. High rates of metal loss have been associated with the formation of alkali chloride deposits. In general, chlorine corrosion occurs in high heat flux, reducing regions when the fuel chlorine content is approximately 0.2% or higher [42, 43]. Gaseous phase chlorine based corrosion may occur under oxidizing conditions through an "active oxidation" mechanism [44].

Sulfur in the presence of chlorine can have different roles in corrosion depending on local environment. Under reducing conditions, metal loss through sulfidation may be accelerated by the presence of chlorine [45]. Under reducing conditions alkali chlorides are stable, but under oxidizing conditions the conversion of alkali chlorides to less corrosion alkali sulfates is favored. Thus, the presence of fuel sulfur can provide some protection against chlorine attack under oxidizing conditions, but may enhance sulfidation instead. Chlorine gas forming high temperature gases such as HCl, KCl, and NaCl can cause corrosion through

different mechanism from molten sulfate corrosion. Condensed chloride on the tube surface can also affect corrosion. Corrosion can occur by gaseous specie, deposit, or the combination of these corrosive materials [40].

In the following sections, thermodynamic stabilities of metal oxides and chlorides will be first discussed, followed by discussion on the more details of the chlorine corrosion mechanisms. Understanding thermodynamic stability of metal chlorides and oxides is useful in discussing chlorine related corrosion mechanisms. The corrosion mechanisms by chlorine containing species under various environments are well surveyed by Nielson *et al*. [40] and summarized here.

2.7.5.1 Thermodynamic Stability of Metal Oxides and Chlorides

Thermodynamic stability of the metal oxides and chlorides under a given temperature can be understood through an Ellingham-Pourbaix stability diagram which illustrates the type of corrosion product that would be stable under given oxygen and chlorine partial pressures. Figure 2.7-13 shows the stability of the corrosion products of the alloy with Fe, Cr, and Ni as main components at 727°C. It depends on actual chlorine and oxygen partial pressures, but oxides are more stable than chlorides under low chlorine partial pressure. On the other hand, metal chlorides are more stable at high chlorine and low oxygen partial pressures.

Metal chlorides exist as a solid at normal superheater metal temperatures, but they are known to have high vapor pressure even at relatively low temperature. This can lead to the vaporization of the metal chlorides and rapid metal wastage. It is suggested that when the vapor pressure of corrosion products is higher than 10^{-6} atm, the vaporization can affect corrosion mechanism significantly [46] and many authors agree that when the vapor pressure is higher than 10^{-4} atm, the material's vaporization can be main corrosion mechanism [46, 47]. When the chlorides melt due to increase in temperature, oxidation and chloridation can be accelerated. This is due to fluxing of the oxide scale on the metal surface. However, the melting of the metal chlorides occurs at narrow temperature range and the metal chlorides can evaporate when the temperature increases further.

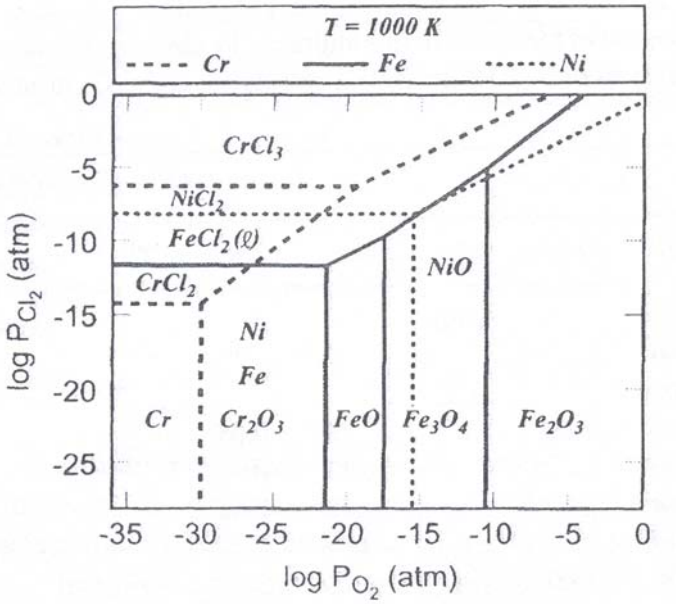

Figure 2.7-13. Stability diagram of Cr/Fe/Ni-O-Cl at 727°C (adapted from [47])

Table 2.7-1 shows the melting point and the temperature of various metal chlorides when the vapor pressure reaches 10^{-4} atm. Note that the melting temperature of $FeCl_3$ is significantly low. Figure 2.7-14 shows the vapor pressure of the condensed chlorides as a function of temperature. The vapor pressure of the metal chlorides as well as the stability of the oxides under given oxygen partial pressure can determine corrosion propensity. Chromium is usually added into the metal to increase corrosion resistance. Once chromium chloride is formed, however, the metal wastage can be accelerated even with low vapor pressure of chromium chlorides due to highly stable chromia (Cr_2O_3) formation under even low oxygen partial pressure. This type of enhanced corrosion depends on acting corrosion mechanism and will be discussed later. The stability and the vapor pressure of the metal oxides and chlorides can describe various metals' vaporization and therefore qualitative corrosion propensities.

Table 2.7-1. Melting point (T_m) and temperature (T_4) at which the chloride vapor pressure is equal to 10^{-4} atm (adapted from [47]).

Chloride	T_m, °C	T_4, °C
$FeCl_3$	303	167
$FeCl_2$	676	536
$NiCl_2$	1,030	607
$CoCl_2$	740	587
$CrCl_2$	820	741
$CrCl_3$	1,150	611

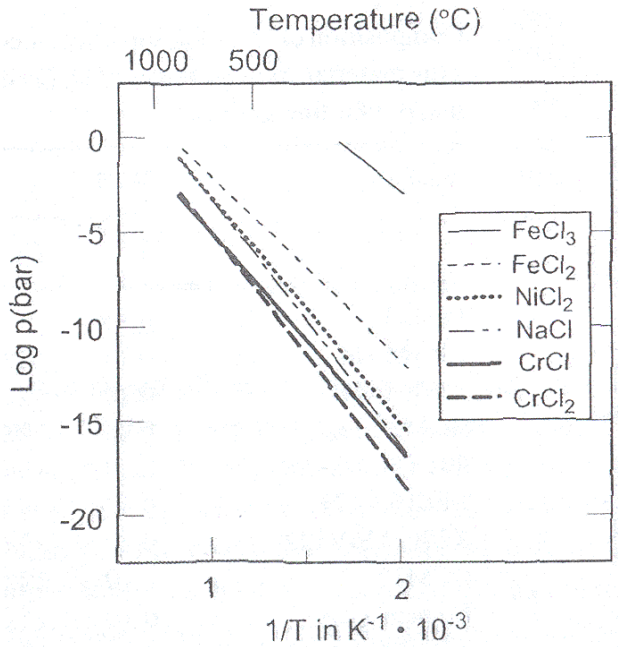

Figure 2.7-14. Vapor pressures of condensed chlorides (adapted from [47]).

2.7.5.2 Corrosion under Oxidizing Environment

When metal is exposed to high temperature oxidizing environment, the metal will form thermodynamically stable oxides that can provide protection from diffusion of oxygen or other gas species to the metal surface. However, in the presence of chlorine, the formation of protective oxide scale is inhibited and the corrosion of the metal can be accelerated [40, 48, 49, 50, 51, 52]. This is called "Active Oxidation." In this mechanism, the source of chlorine can be in the form of HCl or Cl_2, or in the combined form with Na, K, Zn, Pb, and Sn. Small changes in temperature or partial pressure of oxygen and chlorine are reported to affect the corrosion behavior. This active oxidation mechanism is known to be effective at the metal temperatures above 450°C. Overall reaction pathway of active oxidation mechanism is shown in Figure 2.7-15.

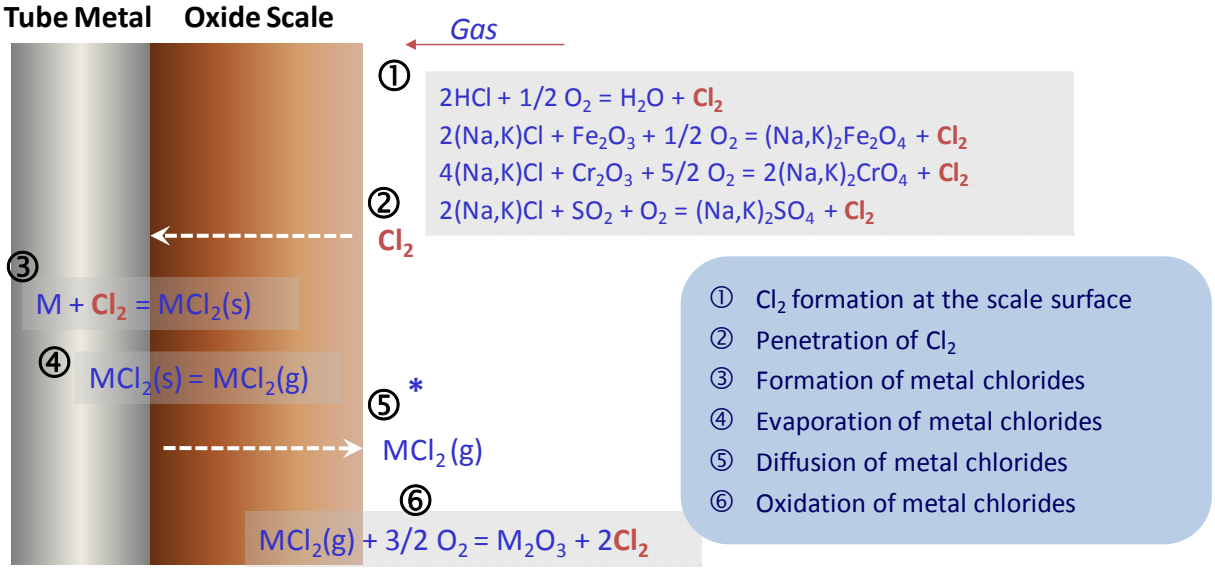

Figure 2.7-15. Overall reaction paths in active oxidation mechanism.

In this mechanism, Cl_2 is formed through either the oxidation of HCl on the oxide scale or the reaction of the oxide scale with NaCl or KCl condensed on the scale:

$$2HCl + \frac{1}{2}O_2 = H_2O + Cl_2 \qquad \textbf{(2.7-22)}$$

$$2(Na,K)Cl + Fe_2O_3 + \frac{1}{2}O_2 = (Na,K)_2Fe_2O_4 + Cl_2 \qquad \textbf{(2.7-23)}$$

$$4(Na,K)Cl + Cr_2O_3 + \frac{5}{2}O_2 = 2(Na,K)_2CrO_4 + 2Cl_2 \qquad \textbf{(2.7-24)}$$

The Cl_2 can access to the metal surface through the cracks or the pores of the oxide scale and react with iron or alloy component such as chromium and nickel to form metal chloride at the tube metal surface. This metal chloride is formed because oxygen partial pressure is low at the metal surface and relatively volatile $FeCl_2$ and $CrCl_2$ are thermodynamically stable (Figure 2.7-13 and Figure 2.7-14). This reaction at the interface of metal and oxide scale can be represented as:

$$M(s) + Cl_2(g) = MCl_2(s) \quad \textbf{(2.7-25)}$$

where M is metal component such as Fe, Cr, or Ni. Metal chloride can form through direct reaction between metal and HCl as in the following reaction:

$$M(s) + 2HCl(g) = MCl_2(s) + H_2(g) \quad \textbf{(2.7-26)}$$

Vapor pressure of metal chlorides at the interface of metal and oxide scale can be very high (ex. $FeCl_2$ vapor pressure is $4x10^{-5}$ atm at 500°C) and continuous vaporization can occur.

$$MCl_2(s) = MCl_2(g) \quad \textbf{(2.7-27)}$$

Vaporized chlorides can diffuse out through crack or pore of the oxide scale and reach a region that has high oxygen partial pressure. Then, the metal chloride is oxidized to from metal oxides (M_3O_4 or M_2O_3):

$$2MCl_2(g) + \frac{3}{2}O_2(g) = M_2O_3(s) + 2Cl_2(g) \quad \textbf{(2.7-28)}$$

$$3MCl_2(g) + 2O_2(g) = M_3O_4(s) + 3Cl_2(g) \quad \textbf{(2.7-29)}$$

These solid oxides form loose metal oxide layer and do not provide protection against further metal surface attack. The Cl_2 formed from these reactions can diffuse out to bulk gas or in to the metal surface to re-iterate the aforementioned reaction steps. This leads to migration of metal component from the metal surface to high partial oxygen pressure region without losing much of Cl_2 to bulk gas.

Among the metal chlorides, $FeCl_2$ is the main chloride that is vaporized due to its relatively high vapor pressure. However chromium can also participate in active oxidation mechanism and various studies report that main chloride can be chromium chloride [1, 50]. This is because chromium has more affinity to chlorine than other metal components such as Fe and Ni based on Gibb's free energy calculation and chromium chloride can be oxidized at relatively low oxygen partial pressure due to the chromium oxides' high stability (see Figure 2.7-13). Iron chloride with higher vapor pressure than chromium chloride move more toward outer area and is oxidized at higher oxygen partial pressure. Therefore iron chloride can form oxides near the outer surface of the scale than the chromium oxides. At low temperature, chromium chloride cannot vaporize, but iron chloride can still vaporize and accelerate active oxidation mechanism. At high temperature, high affinity to chlorine can lead to grain boundary corrosion and chromium does not provide protective oxide scale. With decreasing temperature, volatility of the metal chloride can become more important.

According to Grabke *et al*. [52], the governing reaction of active oxidation mechanism is the outward diffusion of metal chlorides through porous scale (Figure 2.7-15 step ⑤). Grabke *et al*. [52] also argues that the inward diffusion of the chlorine gas through the oxide scale is not clear (Figure 2.7-15 step ②). The active oxidation mechanism proceeds without any incubation time upon the introduction of the chlorine specie, based on their experiment. The authors said that the solid state diffusion, the grain boundary diffusion, or the molecular diffusion through the cracks or the pores of the oxide scales would not be fast enough to explain this result and concluded that the chlorine species would form a certain fast diffusion pathway such as the grooves and fissures at the grain boundary. Mayer *et al*. [53] and McNallan [54] also report similar phenomena. Mayer *et al*. [53] studied how the structure of the oxide scale changed when the HCl concentration increased in a flue gas. When there was no HCl in the flue

gas, continuous oxide scale without pores was observed. When the HCl concentration increased to 0.1 vol%, there were some pores in the hematite (Fe_2O_3) scale, but the scale was still continuous. With 0.2 vol% of HCl, more pores in the scale were observed and the scale was not continuous anymore. With 0.8 vol% of HCl, the hematite scale was totally disintegrated and the magnetite (Fe_3O_4) scale became irregular with many pores. When the HCl concentration was further increased to 2 vol%, all of the scales were disintegrated and the corrosive gases could access the metal surface freely. Other researchers report the internal attack after the exposure to chlorine environment. The internal attack can occur near the grain boundary and can be related to internal chromium carbide formation [54].

Sulfidation of the alkali chloride deposit can accelerate active oxidation [40, 52, 55]. The alkali chloride deposit can react with SO_2 in oxidizing environment to form Cl_2 or HCl in the presence of H_2O.

$$2(Na,K)Cl(s) + SO_2(g) + O_2(g) = (Na,K)_2SO_4(s) + Cl_2(g) \quad \textbf{(2.7-30)}$$

$$2(Na,K)Cl(s) + SO_2(g) + \frac{1}{2}O_2(g) + H_2O(g) = (Na,K)_2SO_4(s) + 2HCl(g) \quad \textbf{(2.7-31)}$$

Cl_2 and HCl can diffuse in toward the metal surface and form volatile metal chlorides ($FeCl_2$ or $CrCl_2$), and then corrosion reaction similar to active oxidation can occur. Then, some of the metal chlorides ($FeCl_2$ or $CrCl_2$) can diffuse out toward the high oxygen partial pressure region and be oxidized to form metal oxides and Cl_2 or HCl in the presence of H_2O:

$$4MCl_2(g) + 4H_2O(g) + O_2(g) = 2M_2O_3(s) + 8HCl(g) \quad \textbf{(2.7-32)}$$

Here, HCl can react with O_2 to form Cl_2:

$$2HCl(g) + \frac{1}{2}O_2(g) = Cl_2(g) + H_2O(g) \quad \textbf{(2.7-33)}$$

In the presence of HCl, the following reaction can occur in the sulfate mixture in the deposit:

$$(Na,K)_2Ca_2(SO_4)_3(s) + 2HCl(g) = 2(Na,K)Cl + 2CaSO_4 + SO_2(g) + \frac{1}{2}O_2(g) + H_2O(g) \quad \textbf{(2.7-34)}$$

This reaction can form metal chlorides at the interface of the scale and the deposit and the metal chloride can react with the scale to form Cl_2. Then, "Active Oxidation" can be accelerated. Sulfates and SO_2 from the aforementioned reactions can diffuse toward the interface of the metal and the scale and cause corrosion through "Molten Sulfate" corrosion mechanism. This pathway has been validated through identification of FeS after the experiment. Grabke [52] says that the sulfidation of the metal chloride occurs at the outer surface of the deposit and therefore Cl_2 and HCl are lost in the outer environment and only small parts diffuse toward the metal surface. Sulfidation in solid state can occur by SO_2 or SO_3 (much faster with SO_3). Small concentration of SO_3 can exist in the bulk, but can increase due to catalytic reaction with Fe_2O_3 in the deposit as discussed in the molten sulfate mechanism.

2.7.5.3 Corrosion under Reducing Environment

Schematic of the chlorine related corrosion under reducing environment is shown in Figure 2.7-16. Under reducing environment, the oxide scale does not exist or exists non-uniformly (step ①). Chlorine

can diffuse in and access the metal surface easily under this environment (step ②) and react with the metal surface to form metal chloride (step ③):

$$M(s) + Cl_2(g) = MCl_2(s) \quad \textbf{(2.7-35)}$$

$$M(s) + HCl(g) = MCl_2(s) + H_2(g) \quad \textbf{(2.7-36)}$$

The metal chloride formed on the metal surface can act as protective scale under stable condition, but mostly can lead to metal wastage due to relatively high vapor pressure of the metal chloride. Corrosion rate by chlorine specie is governed by the volatilization of the metal chloride (see Figure 2.7-14) and, therefore, has high dependency on the temperature (step ④ in Figure 2.7-16).

$$MCl_2(s) = MCl_2(g) \quad \textbf{(2.7-37)}$$

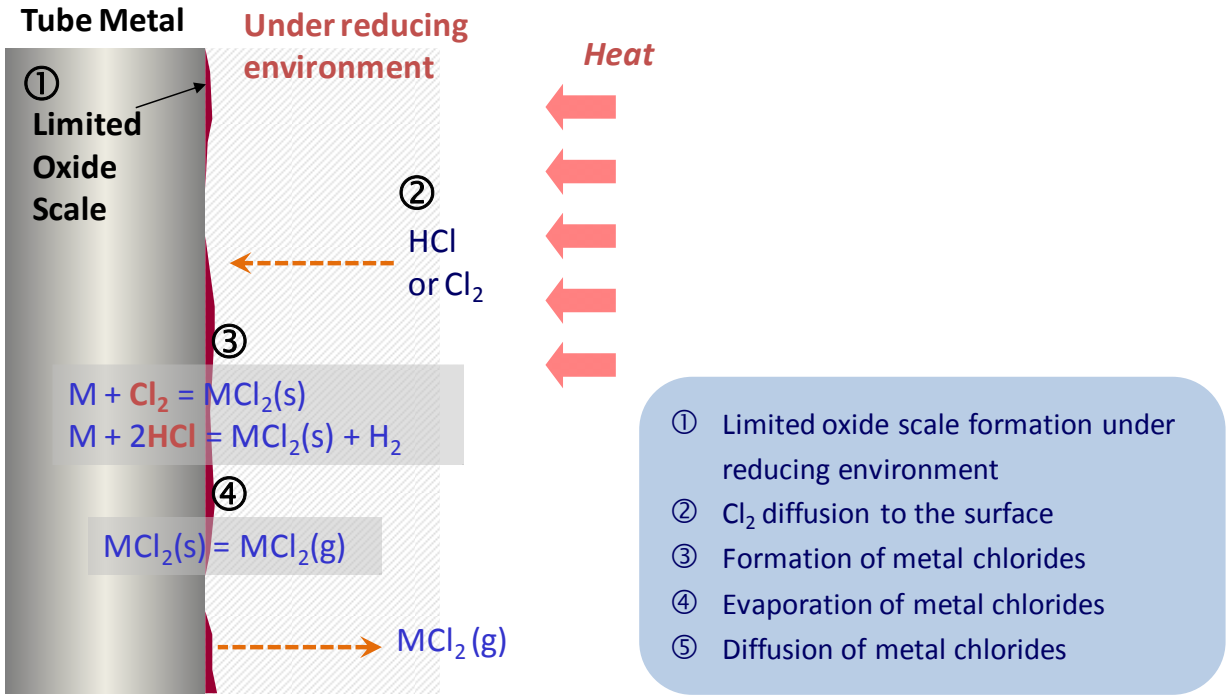

Figure 2.7-16. Schematic of Cl corrosion mechanism under reducing environment.

Chlorine corrosion correlation has been developed to predict waterwall corrosion rate. One of the rate correlations developed in U.K. is [42]:

$$CR = 1350 \times (\%Cl) + 780 \times (HF) + 413 \times (DF) - 743 \quad \textbf{(2.7-38)}$$

CR : corrosion rate (nm/hr)
%Cl : chlorine content in fuel (weight %)
HF : heat flux factor related to burner level heat transfer area
DF : deposit factor related to burner operating conditions, coal particle size, distance between burner and side wall.

Davis *et al*. [56] have developed empirical correlations for chlorine corrosion rate under reducing environment. When oxygen concentration is less than 0.5% and CO higher than 2%, the chlorine corrosion rate is a function of chlorine content in fuel and can be expressed as the following equation:

$$ACR = (C \times \%Cl) \times (HF)^m \times \exp\left(-\frac{Q_{cl}}{RT}\right) - d \qquad \textbf{(2.7-39)}$$

ACR : Corrosion rate (mil/yr)
C, m, d : constants
%Cl : chlorine content in coal (weight %)
Q_{cl} : activation energy for chlorination
T : tube metal temperature (Kelvin)
HF : wall heat flux (kW/m^2)

The rate correlations discussed above assume uniform distribution of chlorine gas specie in the furnace and do not consider local variations.

Whether or not chloride scale growth rate can provide enough amounts for volatilization can determine corrosion rate behavior [57]. At temperatures below 500°C, metal chloride formed on the metal surface can provide protective scale and show parabolic corrosion behavior as a function of time. At higher temperature, weight initially shows parabolic increase, but becomes linear as a function of time. When this transition occurs, the scale does not grow anymore and the scale thickness at the transition point is called critical thickness. This point depends on temperature, environment and nature of chlorides. At temperatures higher than 800°C, the growth rate of chlorides is not fast enough to be able to provide enough amounts for volatilization and corrosion rate shows linear weight loss as a function of time. Ihara *et al*. [58] reports that when oxygen is added in HCl gas, ferric chloride, $FeCl_3$ is formed from oxidation and chloridation. Ferric chloride with low melting point can show sublimation and the corrosion of iron metal can be significantly accelerated.

$$FeCl_2 + HCl + \frac{1}{4}O_2 = FeCl_3 + \frac{1}{2}H_2O \qquad \textbf{(2.7-40)}$$

Hupa *et al*. [59] reports the high corrosion rate by HCl under reducing environment due to limited formation of metal oxide scale. They also reports that the corrosion rate increases by a factor of 2.5 when about 2% CO concentration is added. When CO is added further up to 10%, the corrosion rates don't change much. Under reducing environments, destruction of oxide scale by HCl increases synergistically in the presence of CO and H_2 [1]. In addition, the destruction of the oxide scale by HCl can accelerate the corrosion rates by other corrosion mechanisms. Haanappel *et al*. [60] exposed various metals to 500 ppmv HCl in an environment similar to a coal gasifier. They report that the addition of 500 ppmv HCl in oxidizing-sulfidizing environment increases corrosion rate significantly and forms thick sulfide scale. The sulfide scale formed here cannot provide protection because the sulfide scale is porous and does not stick to the metal surface.

2.7.5.4 Corrosion by Molten Chlorides

Chloride mixture in chloride-chloride or chloride-sulfate system forms eutectic point and has relatively low melting point. Examples of the melting temperatures of pure material and mixtures of two materials are shown in Table 2.7-2.

Table 2.7-2. Melting temperatures of eutectic temperatures for different pure species and binary mixtures (adapted from [40]).

System	Melting/eutectic temperature, °C	Composition at eutectic point (mol% alkali)
NaCl	801	
KCl	772	
$FeCl_2$	677	
$FeCl_3$	300	
NaCl-$FeCl_2$	370-374	~56
NaCl-$FeCl_3$	151	45.3
KCl-$FeCl_2$	340-393	45.8-91.8
KCl-$FeCl_3$	202	24-47
$CrCl_2$	845	
$CrCl_3$	947	
NaCl-$CrCl_2$	437	53.7
NaCl-$CrCl_3$	544-593	68-95
KCl-$CrCl_2$	462-475	36-70
KCl-$CrCl_3$	700-795	54-89
Na_2CrO_4	792	
K_2CrO_4	980	
NaCl-Na_2CrO_4	557	
KCl-K_2CrO_4	650	68.4
$Na_2Cr_2O_7$	356.7	
$K_2Cr_2O_7$	398	
NaCl-$Na_2Cr_2O_7$	592	30
KCl-$K_2Cr_2O_7$	366-368	25-27.5

When corrosive material exists on the metal surface in liquid form, the corrosion rate can be significantly enhanced by the following reasons [61]:

1) Chemical reaction is generally faster in liquid state than in solid state ,
2) Liquid state act as electrolyte and provide ion transfer path for electrochemical attack.

Overall reaction paths of the corrosion by molten chlorides are shown in Figure 2.7-17 using KCl-$ZnCl_2$ system as an example [62]. Corrosion reaction starts with the formation of $ZnFe_2O_4$ on the scale, which leads to higher KCl concentration in molten chloride due to consumption of $ZnCl_2$. Large amount of K and small amount of Zn have been identified at the interface of metal and the scale, which means that molten material with high K diffused through the scale, reached to the metal surface, and formed metal chloride by dissolving iron and chromium. Oxidant, chlorine gas is formed through the following reaction and resides in molten material.

$$ZnCl_2(l) + Fe_2O_3 + \frac{1}{2}O_2 = ZnFe_2O_4 + Cl_2(diss.) \qquad \textbf{(2.7-41)}$$

Then, the molten material with chlorine in it moves toward metal surface and react with metal component.

$$Fe + Cl_2(diss.) = FeCl_2(diss.) \qquad \textbf{(2.7-42)}$$

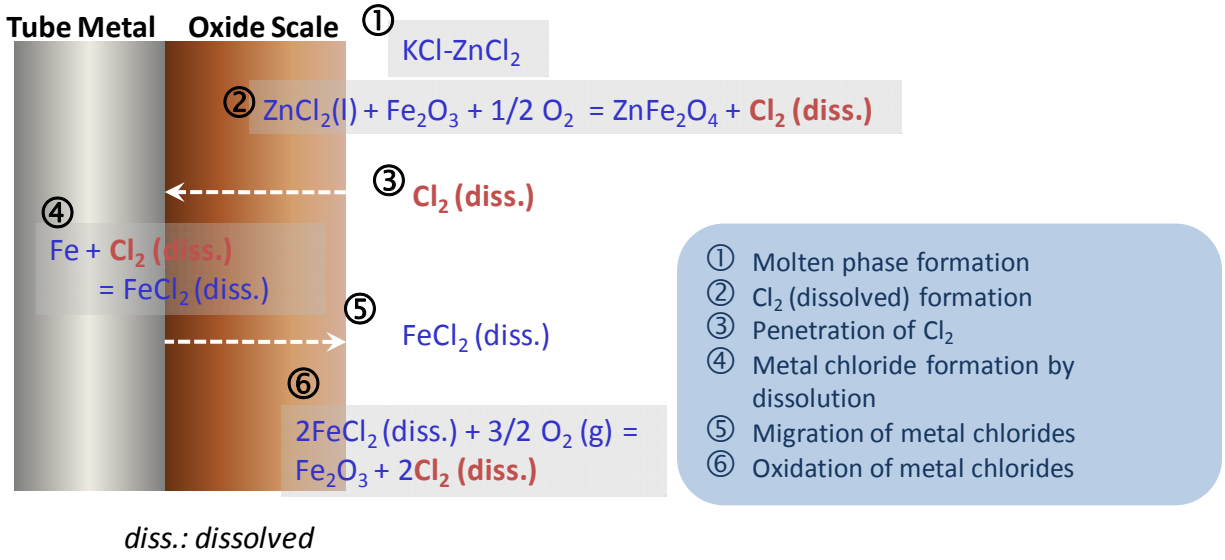

diss.: dissolved

Figure 2.7-17. Overall reaction paths in molten chloride corrosion.

Then, the dissolved $FeCl_2$ diffuses toward outside due to concentration gradient (high at the interface of metal and scale and low at the interface of scale and gas) and reacts with oxygen:

$$2FeCl_2(diss.) + \frac{3}{2}O_2(g) = Fe_2O_3 + 2Cl_2(diss.) \qquad \textbf{(2.7-43)}$$

Then, precipitation of Fe_2O_3 can occur in the oxide scale near the outside surface. Oxygen can diffuse through cracks and pores in the oxide scale toward the interface between the scale and the metal surface. Then solid oxide forms more at the interface and the corrosion rate can eventually decrease.

2.7.5.5 Reaction between Chromium Carbide and NaCl

When NaCl deposits on the superheater, the corrosion rate of the alloy is accelerated at the temperature over 550°C [63]. This was reported to be due to general metal wastage and deeper internal penetration. This internal attack was assumed to be related to grain boundary carbide and was increased with increasing carbon content in the metal. Chromium in the metal increased corrosion at the temperature lower than NaCl melting temperature (801°C), but reduced internal penetration attack. This was explained by the reaction of NaCl vapor and chromium carbide [63, 64]:

$$Cr_{23}C_6(s) + 46NaCl(g) + 52O_2(g) = 23Na_2CrO_4(s,l) + 6CO_2(g) + 23Cl_2(g) \qquad \textbf{(2.7-44)}$$

However, the chromium in the metal was reported to be an alloying component that increased corrosion resistance when the temperature was higher than NaCl melting point.

Reactions between NaCl and various metal chlorides have been studied by Mobin *et al.* [65]. TGA (Thermogravimetric Analyzer) was used in this study and the temperature ranges were 627-927°C. The weights of iron and chromium carbide showed initial decrease then increase afterward. Initial weight loss was reported to be from Cl_2 and CO_2 release [65]:

$$MC(s) + 2NaCl(s) + 2O_2(g) = MO(s) + Na_2O(s) + CO_2(g) + Cl_2(g) \quad \textbf{(2.7-45)}$$

Na_2O dissolves metal oxide and forms Na_2O-MO and Cl_2 reacts with metal oxide to form metal chloride:

$$MO(s) + Na_2O(s,l) = Na_2O \cdot MO(s,l) \quad \textbf{(2.7-46)}$$

$$MO(s) + \frac{1}{2}Cl_2(g) = MCl(s,l,g) + \frac{1}{2}O_2(g) \quad \textbf{(2.7-47)}$$

Some metal chloride can volatilize and show less weight increase.

2.7.6 Carburization

When the metal contains the component that can form carbide and is exposed to high temperature where thermodynamic activity coefficient (a_C) is high, then the metal can be carburized [66]. Flue gas mixture in many systems consists of CO, CO_2, CH_4, and H_2. In oxy-firing system, high CO_2 concentrations are expected due to flue gas recirculation. Carbide can form at or under the alloy metal surface. Carburization rate is often determined by the carbon transfer rate in the metal. Several possible reactions are:

$$7Cr + 3CH_4 = Cr_7C_3 + 6H_2 \quad \textbf{(2.7-48)}$$

$$23Cr + 6CH_4 = Cr_{23}C_6 + 12H_2 \quad \textbf{(2.7-49)}$$

$$3Cr + 2CH_4 = Cr_3C_2 + 4H_2 \quad \textbf{(2.7-50)}$$

$$2Mo + 2CO = Mo_2C + CO_2 \quad \textbf{(2.7-51)}$$

$$W + 2CO = WC + CO_2 \quad \textbf{(2.7-52)}$$

The stability of the carbide is determined by carbon activity coefficient, a_C, that is defined by various gas species' relative amount, such as H_2/CH_4 or CO/CO_2 ratios. Based on the alloy composition, various carbide compositions are possible. Carburization rate is expected to increase with increasing a_C and temperature. However, when P_{H2S} becomes about $1x10^{-4}$ atm, the carburization rate decreases. When H_2S concentration gets higher, then the major corrosion mechanism is changed to sulfidation.

2.7.7 Corrosion Under Oxy-firing Conditions

The flue gas environment in oxy-firing conditions contains high concentrations of CO_2 and H_2O compared to conventional air-firing conditions and these conditions can affect the corrosion behavior of the metal. Piron *et al*. [67] studied the oxidation behavior of martensitic 9-12%Cr steels under simulated gas mixture containing 70%CO_2-30% H_2O at the temperatures of 550-700°C in a laboratory. In their study, the iron-rich scales were formed at the metal surface instead of the more corrosion resistant Cr-rich scale under the simulated environment. They report enhanced internal oxidation of chromium in the H_2O-containing gases and carbide formation in the CO_2-rich gases caused a decreased flux of chromium toward the metal surface. The iron oxide scales formed in the simulated environment were reported to be permeable to CO_2 resulting in substantial carburization of the steel [67]. In addition, H_2O-rich environment has been reported to form wűstite (FeO) that does not provide protecting scale [68] and exposes the metal surface for other corrosion attacks as well. On the other hand, in a 500kW oxy-fuel

test rig study [69] where solid fuels were actually fired under oxy-firing condition and the comparison between the oxy- and air-firing modes were performed, the difference in corrosion behavior between two different operating modes was not significant. This implies that gaseous attack by enhanced CO_2 and/or H_2O concentrations may not be significant and the corrosion may be dominated by other corrosion mechanisms. Further study is needed to clarify the importance of the changed flue gas environment in oxy-firing mode on corrosion.

2.7.8 Future Work

The next step for the corrosion work is to use published data and theory to identify the mechanisms most important to oxy-coal firing. Correlations describing these mechanisms will then be selected or developed. Subsequent experimental data from this program will then be used to validate both the importance of the different mechanisms and the accuracy of the correlations.

2.7.9 Corrosion References

1. Harb JN, Smith EE, "Fireside Corrosion in Coal-Fired Boilers," Prog Energy Combust Sci 16, 169-190, 1990.
2. Raask E, "Mineral Impurities in Coal Combustion," Washington DC, Hemisphere Publishing, 1985.
3. Rehn IM, "Fireside corrosion of superheater alloys for advanced-cycel steam plants," EPRI Rep CS-5195, 1987.
4. Kung, S. C., "Prediction of Corrosion Rate for Alloys Exposed to Reducing/Sulfidizing Combustion Gases," Material Performance, 36(12), 36-40, (1997).
5. Perkins, R. A., Marsh, D. L., Clark, P. R., Bakker, W. T., "Corrosion in Syngas Coolers of Entrained Slagging Gasifiers," EPRI Report GS-6971, RP 2048-1 (1990).
6. Davis, C. J., James, P. J., Pinder, L. W., and Mehta, A. K., "Effects of Fuel Composition and Combustion Parameters on Furnace Wall Fireside Corrosion in Pulverised Coal-Fired Boilers," Materials Science Forums, Vols. 369-372, pp. 857-864, 2001.
7. Nava, J. C., Plumley, A. L., Knodler, R., "Wastage Control in Low Emission Boiler Systems," Third International Conference on Boiler Tube Failures in Fossil Plants," Nashville TN, November 11-13, 1997.
8. John, R. C., Thompson, W. T., Karakaya, I., "Predicting Corrosion Mechanisms and Rates for Alloys in High Temperature, Complex Gases," NACE Corrosion 90 Conference, Paper 279, Las Vegas NV, 1990.
9. Huijbregts, W. M. M., Janssen, J. B., Rens, O. C. J., "Corrosion in Low NOx Firing Conditions," Power Gen 98 Conference, Milan, 1998.
10. Kung, S. C., "Corrosion Studies for Low NOx Burner Technology," EPRI Report TR-108750, 1997.
11. Kung, S. C., and Bakker, W. T., "Effect of Sulfur and Chlorine on Furnace Wall Corrosion," NACE Corrosion/98 Conference, NACE, Houston, 1998.
12. Bakker, W. T., "The effect of deposits on waterwall corrosion in fossil fuel boilers," Materials at High Temperatures, 20(2), 161-168, 2003.
13. Mayoral, M. C., Izquierdo, M. T., Adrés, J. M., Rubio, B., "Mechanism of interaction of pyrite with hematite as simulation of slagging and fireside tube wastage in coal combustion," Thermochimica Acta, 390, 103-111, 2002.
14. Valentine, J. R., Davis, K. A., Adams, B. R., Heap, M. P., and Bakker, W., "Modeling Potential Waterwall Wastage Based on Pyritic Deposition and Wall Conditions," United Engineering Foundation Conference: Effects of Coal Quality on Power Plant Management: Ash Problems, Management and Solutions, Park City, Utah, May 8-11, 2000.

15. Bakker, W. T., Wastage in Low NOx Boilers, Root Causes and Remedies, EPRI Report TR111155, October 1998.
16. Nava-Paz, J. C., Plumley, A. L., Chow, O. K., and Chen, W., "Waterwall corrosion mechanisms in coal combustion environments," Materials at High Temperatures, 19(3), 127-137, 2002.
17. Bakker, W. T., Kung, S. C., Heap, M. P., Valentine, J. R., "Waterwall Corrosion in Low NOx Boilers Root Causes and Remedies," Proceedings of the EPRI-DOE-EPA Combined Utility Air Pollution Control Symposium: The MEGA Symposium, Volume 2: NOx and Multi-Pollutant Controls, pp.13-17 – 13-30, Atlanta, August 16-20, 1999.
18. Nielsen HP, Frandsen FJ, Dam-Johansen K, Baxter LL, "The Implications of Chlorine-associated Corrosion on the Operation of Biomass-fired Boilers," Prog Energy Combust Sci 26, 283-298, 2000.
19. James PL, Pinder LW, "Effect of coal chlorine on the fireside corrosion of boiler furnace wall and superheater/reheater tubing," Mat High Temp 14(3), 187-196, 1997.
20. James PJ, Pinder LW, "The Impact of Coal Chlorine on the Fireside Corrosion Behavior of Boiler Tubing: A UK Perspective," NACE 1997, Paper No. 133, 1997.
21. Viswanathan R, Bakker WT, "Materials for Boilers in Ultra Supercritical Power Plants," Proceedings of 2000 International Joint Power Generation Conference, July 23-26, 2000.
22. Coats AW, Dear DJA, Penfold D. J Inst Fuel 41, 129, 1968.
23. Reid WT. External Corrosion and Deposits. New York, Elsevier, 1971.
24. Corey RC, Cross BJ, Reid WT. Trans ASME 67, 289, 1945.
25. Anderson CH, Goddard CW. J Inst Fuel 41, 357, 1968.
26. Hedley AB. J Inst Fuel 40, 142, 1967.
27. Levy A, Merryman EL. Trans ASME Ser A J Eng Pwr 87, 374, 1965.
28. Krause HH, Levy A, Reid WT. Trans ASME Ser A J Eng Pwr 91, 216, 1969.
29. Cutler AJB, Raask E. Cor Sci 21, 789, 1981.
30. Borio RW, Hensel RP. Trans ASME Ser A J Eng Pwr 94, 142, 1972.
31. Rapp RA. Corrosion 42, 568, 1986.
32. Hendry A, Lees DJ. Cor Sci 20, 383, 1980.
33. Shirley HT. J Iron Steel Inst 182, 144, 1956.
34. Lucas DH. J Inst Fuel 36, 206, 1963.
35. Alexander PA. In: Johnson R, Littler DJ, eds. The mechanism of corrosion by fuel impurities, London, Butterworths, p.571, 1963.
36. McKee DW, Shores DA, Luthra KL. J Elecrochem Soc 125, 411, 1978.
37. Hancock P. Mat Sci Tech 3, 536, 1987.
38. Cutler AJB, Grant CJ, Laxton JW, Price DD, Stevens CG. In: Meadowcroft DE, Manning MI, eds. Corrosion resistant materials for coal conversion systems, Barking, Applied Science Publishers, p. 159, 1983.
39. Ho, K., and Doane, E. P., "Current Evidence Concerning Coal Chlorine Content and Fireside Corrosion in Coal-Fired PC and Fluidized-Bed Boilers," The Proceedings of the 26th International Technical Conference on Coal Utilization & Fuel Systems, Clearwater, Florida, March 5-8, 2001.
40. Nielsen HP, Frandsen FJ, Dam-Johansen K, Baxter LL, "The Implications of Chlorine-associated Corrosion on the Operation of Biomass-fired Boilers," Prog Energy Combust Sci 26, 283-298, 2000.
41. Baxter, L. L., Tree, D., Lokare, S., Dunaway, J. D., Moulton, D., Mehta, A., Bakker, W., Facchiano, A., "Mechanistic Investigation of Chlorine-based, High-temperature Boiler Corrosion," UEF Conference: Power Production in the 21st Century: Impacts of Fuel Quality and Operations, Snowbird UT, October 28 – November 2 2001

42. James PL, Pinder LW, “Effect of coal chlorine on the fireside corrosion of boiler furnace wall and superheater/reheater tubing,” Mat High Temp 14(3), 187-196, 1997.
43. James PJ, Pinder LW, “The Impact of Coal Chlorine on the Fireside Corrosion Behavior of Boiler Tubing: A UK Perspective,” NACE 1997, Paper No. 133, 1997.
44. Spiegel M, Zahs A, Grabke HJ, “Fundamental aspects of chlorine induced corrosion in power plants,” Proceedings of the 3rd International Workshop on Environmental Degradation in Advanced Energy Systems, 153-9, Woburn, UK, June 2002.
45. Uusitalo, M. A., Vuoristo, P. M. J., Mäntylä, T. A., “High temperature corrosion of coatings and boiler steels in reducing chlorine-containing atmosphere,” Surface and Coatings Technology, 161, pp. 275-285, 2002.
46. McNallan M, Modern Power 54, 95, 1998.
47. Grabke HJ. In : Bryers RW, editor. Incinerating municipal and industrial waste, New York, Hemisphere, p. 161, 1989.
48. Albina DO, Millrath K, Themelis NJ, “Effects of Feed Composition on Boiler Corrosion in Waste-to-Energy Plants,” Presented at 12th North American Waste To Energy Converence, May 17-19, 2004.
49. Sander B, Henriksen N, Jensen JN, Livbjerg H, Thellerfsen M, Dam-Johansen K, Frandsen F, van der Lans R, Hansen J, “Emissions, Corrosion and Alkali Chemistry in Straw-fired Combined Heat and Power Plants,” Presented at 1st World Conference on Biomass for Energy and Industry, 5-9 June 2000, Sevilla
50. Montgomery M, Larsen OH, Biede O, “Corrosion and Materials Performance in Biomass-Fired and Coal-Fired Power Plants, “ Paper 03356, presented at Corrosion/2003, San Diego, California.
51. Spiegel M, Zahs A, Grabke HJ, “Fundamental aspects of chlorine induced corrosion in power plants,” Proceedings of the 3rd International Workshop on Environmental Degradation in Advanced Energy Systems, 153-9, Woburn, UK, June 2002.
52. Grabke HJ, Reese E, Spiegel M, “The Effects of Chlorides, Hydrogen Chloride, and Sulfur Dioxide in the Oxidation of Steels below Deposits,” Corr Sci 37(7), 1023-43, 1995.
53. Mayer P, Manolescu AV. Influence of Hydrogen Chloride on Corrosion of Boiler Steels in Sysnthetic Flue Gas. Paper 80, Corrosion/NACE 1979.
54. McNallan M, Modern Power 54, 1994.
55. Miler PD, Krause HH, Zupan J, Boyd W. Corrosion-NACE 1972;28:222.
56. Davis, C. J., James, P. J., Pinder, L. W., and Mehta, A. K., “Effects of Fuel Composition and Combustion Parameters on Furnace Wall Fireside Corrosion in Pulverised Coal-Fired Boilers,” Materials Science Forums, Vols. 369-372, pp. 857-864, 2001.
57. Chang YN, Wei FI. Journal Mat Sci 26, 3693, 1991.
58. Ihara Y, Ohgame H, Sakiyama K, Hashimoto K. Corr Sci 21, 805, 1981.
59. Hupa M, Backman P, Backman R, Tran H. In: Bryers RW, editor. Incinerating municipal and industrial waste, New York: Hemisphere, 1989. 161.
60. Haanappel VAC, Haanappel NWJ, Fransen T, van Corbach HD, Gellings PJ. Corrosion 48, 812, 1992.
61. Kofstad P. High temperature corrosion. New York, Elsevier Applied Science, 1988.
62. Spiegel M, Zahs A, Grabke HJ, “Fundamental aspects of chlorine induced corrosion in power plants,” Proceedings of the 3rd International Workshop on Environmental Degradation in Advanced Energy Systems, 153-9, Woburn, UK, June 2002.
63. Fjujikawa H, Maruyama N, Mat Sci Eng A 120, 399, 1987.
64. Hiramatsu N, Uematsu Y, Tanaka T, Kinugasa M, Mat Sci Eng A 120, 319, 1989.

65. Mobin M, Malik AU. J Alloys Compounds 186, 1, 1992.
66. John RC, Thompson WT, Karakaya I, “Predicting Corrosion Mechanisms and Rates for Alloys in High Temperature, Complex Gases,” NACE 1990, Paper No. 279, 1990.
67. Pirón Abellán J, Olszewski T, Penkalla HJ, Meier GH, Singheiser L, “Scale formation mechanisms of maternsitic steels in high CO2/H2O containing gases simulating oxyfuel environments,” Mat High Temp 26(1), 63-72, 2009.
68. Huenert D, Kranzmann A, “Influence of Pressure and Chromium Content on Corrosion Reactions At 600°C In a CO2-H2O Atmosphere,” NACE 2008, Paper No. 08447, 2008.
69. Montgomery M, Hjörnhede A, Gerhardt A, “Short-term Corrosion Testing in a burner rig with oxyfuel and conventional firing,” EUROCORR 2009, Paper 7979, 2009.

3 SUMMARY AND CONCLUSIONS

Baseline Ash Characterization Tests. Initial ash characterization testing continued on the University of Utah Oxy-Fuel Combustor (OFC). As of June 30, 2009, preliminary experimental tests have been completed that allow comparison between the size segregated composition of the coal ash aerosol formed under air combustion and that formed under two different oxy-coal combustion conditions. These tests yielded the very first data currently available on size segregated composition, particle size distributions, soot content, and overall loss on ignition of ash from air and oxy-coal combustion. Additional tests to be performed from August 1 through September 30 of this year will complete the baseline data base for ash particle size, composition, and characteristics, with once through CO_2 from an external supply (no recycle). These additional tests will employ a newly designed swirl based burner to allow similarly stabilized pulverized coal flames under three previously specified inlet oxidant conditions, namely, air, 32% O_2 in CO_2 and 27% O_2 in CO_2.

In the experiments reported here, ash sample collection was isokinetic via a diluted, quenched sampling probe. The sample was then drawn through a low pressure impactor to allow for inertial separation on eleven impactor plates. Particle compositions on each plate were obtained by two methods in order to determine the most cost effective method to be used for subsequent work in this project. One set of samples was analyzed by a commercial lab using sample digestion followed by Inductively Coupled Plasma Optical Emission Spectrometry (ICP-OES). The other set of replicate samples was analyzed at the University of Utah directly by Electron Dispersion Spectrometry (EDS). The method to be used in subsequent work is still being determined, although preliminary data indicate that a combination of both methods would be best. Comparisons of fine particle size distributions were made using a Scanning Mobility Particle Sizer (SMPS). Comparisons of black carbon (soot) content were also performed using a Photo-Acoustic (PA) analyzer. In addition, loss on ignition (LOI), for bulk ash samples were made for all three conditions. Once a learning curve had been surmounted, all these experimental techniques were employed successfully to yield useful data, as reported in the body of this report.

Results show that the major effects of oxy-coal combustion on ash aerosol composition occur in the fine particle, or sub-micron particle size range. The larger super-micron particle size distributions appeared to be similar for air-fired and oxy-fired combustion alike. The volatilities of calcium and other elements are affected by flame temperature, with maximum concentrations of sub-micron particles being observed for the test conditions with the highest (theoretical) flame temperature. However changes in combustion environment may also be important for particles in the sub-micron region. There, the elements calcium, magnesium, and iron were all found in higher relative concentrations in the oxy-fired cases compared to the air-fired cases at the same adiabatic flame temperatures, while potassium and sodium were in relatively higher abundance in air-fired cases, and aluminum was similar throughout. If confirmed in future experiments, these results might have profound implications on the effects of oxy-coal retrofit on fouling and slagging mechanisms.

Ash loss on ignition results show that flame type (attached versus detached) is important. A detached oxy-coal flame led to lower LOI than both the detached air flame (at the same temperature) and the attached oxy-flame (at a higher temperature). These results indicate a switch to oxy-combustion may lead to a decrease in LOI. The black carbon data followed similar trends.

Baseline Char Oxidation Experiments. The reacting particle simulation code known as SKIPPY (Surface Kinetics in Porous Particles) was used to investigate particle size effects on the influence of boundary layer reactions on pulverized coal char during oxy-combustion. These effects are not accounted for in current CFD models of coal combustion. The results suggest that boundary layer effects begin to be important for particle sizes greater than 60 micrometers and are greatest for particles around 75 micrometers in size. For particles larger than 100 micrometers, the particles burn close to the diffusion

limit and thermal feedback from the boundary layer conversion of CO has a diminishing impact on the char combustion rate. These results show that particle sizes in the region of real coal combustion have a strong influence on the relative importance of boundary layer chemistry to char combustion under oxy-combustion conditions. It is anticipated that the range of sizes for which this effect is important will vary somewhat with the reactivity of the coal (i.e., the relevant size range will decrease as the reactivity increases relative to the Pittsburgh seam high-volatile bituminous coal reactivity used in these simulations).

Considering the available standard sieve sizes and the results from the SKIPPY simulations, pulverized samples of the two project coals (Utah Skyline high-volatile bituminous coal and North Antelope PRB subbituminous coal) were sieved into 54-74 μm, 75-105 μm, and 106-125 μm size cuts. In preparation for char combustion experiments in Sandia's bench-scale optical entrained flow reactor, the particle-sizing pyrometer system was recalibrated for both particle size and particle temperature measurements, using a combination of an optical technique (blackbody source and a chopper wheel embedded with optical reticles) and graphite test particles. The two techniques yielded good agreement in determining the 2-color pyrometry calibration factor, lending confidence in the deduced char particle temperatures. During the remainder of FY09, optical measurements of char particle temperatures, velocities, and sizes will be collected for the three different size cuts of each coal for background oxygen levels varying from 12 – 36%, to provide the necessary data for detailed analysis by SKIPPY in FY10. Furthermore, collection of partially reacted char particles will be performed, to provide direct measurements of char burnout and available surface area.

Pilot-scale Burner Design. REI and Siemens have completed the oxy-research burner design for use in the L1500 pilot-scale furnace. The initial design of the oxy-research burner was based on a patented commercial-scale burner design by Siemens Energy Inc. This burner design was reduced to 1.03 MW (3.5 MBtu/hr) firing rate using a constant velocity scaling technique. The initial design was evaluated and compared to operation of the existing L1500 low-NOx burner using CFD modeling. CFD modeling results suggested that the constant velocity scaling method did not produce the desired flame behavior for the oxy-research burner. Using this method of design resulted in a flame stabilization location that was well outside the burner quarl. In an effort to correct this behavior, the primary gas velocity was reduced, the quarl was lengthened and the burner face setback relative to the quarl was lengthened. These modifications produced a flame stabilization location that was in the desired location at the quarl outlet.

The modeling results suggested that the dominating parameter governing flame shape and stability was not solely velocity, but that the flame behavior was closely related to the rate at which the particles were heated. That is, in order to maintain similar burner behavior when scaling a burner, the particle temperature profile or particle heat-up rate profile should be maintained. The particle temperature profile is influenced by many factors including: gas velocity, radiation intensity, particle size and hot flue gas recirculation characteristics inside of the quarl. CFD simulations provided an excellent approach to evaluate the combined impacts of all of these factors.

Following the extensive CFD work, the final geometry requirements for the oxy-research burner were sent to the Siemens designer for modifications and detailing. Additional considerations were made in the overall design to allow the burner and burner plate to be installed on the L1500 with minimal modification to the existing infrastructure, while allowing the original burner to be easily interchanged for future and existing programs. The final fabrication blueprints were completed and transmitted to the burner and burner plate manufacturers on July 15, 2009. The delivery of these items to the University of Utah is scheduled for September 21, 2009.

Slagging and Fouling Mechanism Development. The literature on slagging and fouling mechanisms in coal-fired power plants was reviewed, with the objectives of understanding the state-of-the-art and applying this to the combustion conditions that are expected in an oxy-firing environment. Key issues

were identified that a fundamentally-based deposition model must address, including: 1) ash formation, 2) fluid dynamics and particle transport, 3) particle impaction and sticking, 4) deposit growth as a function of location in the combustion chamber, 5) deposit properties and strength development, 6) heat transfer through the deposit, 7) the effect of deposition on combustion conditions (e.g. temperatures and heat fluxes), and 8) deposit structure and its effect on flow patterns in the furnace. A number of slagging and fouling models were reviewed that describe these processes, including ash characterization and deposition/growth models that have been integrated with CFD codes.

Differences between combustion of coal in air and in O_2-CO_2 mixtures could result in differences in slagging and fouling in the two combustion regimes, including:

- Conditions in the flame zone of the furnace might change in the oxy-combustion regime, specifically the local values of temperature and O_2 in the flue gas. Sticking of ash particles depends on temperature and ash viscosity. The viscosity at a given temperature, in turn, is determined by the composition. If there is sufficient iron in a silicate-based ash particle, the viscosity will depend strongly on the local oxygen partial pressure, because this quantity affects the oxidation state of iron in the glassy silicate particle, which, in turn, affects viscosity.
- Fouling in the convective pass depends strongly on the dew point of sodium sulfate. The dew point of sodium sulfate depends on the amount of vapor-phase sodium entering the convective pass and on the concentration of SO_2 in the flue gas. Due to FGR in oxy-combustion, SO_2 levels in the flue gas might be higher. Sodium vaporization might be different as well, if the flame conditions are different. Finally, the size distribution of the ash might differ in an oxy-combustion system as compared to an air-combustion system.

The differences between air-combustion and oxy-combustion boilers can be accounted for in models for slagging and fouling, because fundamentally based models are available. Coal combustion experiments under oxy-combustion conditions will be used to provide necessary inputs and/or validation of slagging and fouling submodels. Key experimental data needed (and planned) are the size distribution of fly ash and the amount of vaporization of individual species.

A slagging modeling approach has been selected which utilizes both a comprehensive CFD combustion code and a slagging submodel. This approach is designed to predict the deposit build up and the strength of that deposit in the furnace. The key elements of the proposed slagging prediction approach are:

1. Calculate particle capture based on particle impaction rate (from CFD code) and particle viscosity and outermost deposit layer viscosity (based on ash composition, ash and deposit temperature, gas composition).
2. Calculate mass of new deposit layer.
3. Calculate sintering of all deposit layers.
4. Calculate all deposit layer properties (thickness, porosity, thermal conductivity, emissivity, absorptivity).
5. Calculate deposit layer thermal resistance.
6. Calculate heat flux through all deposit layers and temperature of each deposit layer.
7. Feed surface information back to CFD code for further iterations.

Potential future improvements to the proposed approach include coal particle fragmentation, excluded pyrite transformation model, sintering and deposit properties calculations.

A model for fouling in the back pass has been outlined, and can be summarized as follows:

1) Vaporization of sodium during the combustion process - A model for vaporization of sodium in coal combustion systems was developed, based on the ratio of the organically bound sodium to SiO_2 in the coal. This empirical model was based on pulverized coal combustion in air. The net sodium

vaporization might be different in oxy-combustion, and thus measurements need to be made in the University of Utah's Oxy Fuel Combustor (OFC) during this program to quantify the validity of the current model under oxy-combustion conditions.

2) Deposition of sodium sulfate on fly ash particles and tube surfaces - The dew point of sodium sulfate in the flue gas entering the convective pass can be calculated once the net sodium sulfate vaporization is calculated. At temperatures that fall between the dew point of sodium sulfate and the melting temperature of Na_2SO_4, condensation of sodium sulfate will result in a sticky surface. The dew point is calculated from an equilibrium calculation, which will take into account any differences in composition of the flue gas between oxy-combustion and air-combustion.

3) Deposit growth rate on convective pass tubes - Once the range of sticking temperatures is calculated as a function of temperature and fly ash particle size, the deposition and erosion rates as a function of location in the back pass can be calculated. The local temperature and velocity in the back pass of the boiler will come from the CFD model. The size distribution of the fly ash will come from the mineral matter transformation model.

Corrosion Mechanism Development. A review of corrosion mechanisms was performed. Several corrosion mechanisms were identified as relevant in coal-fired boilers: oxidation, sulfidation, chloridation and carburization. The acting corrosion mechanism depends on local environment, determined by various key parameters and can occur through one dominant mechanism or a combination of multiple mechanisms. Other than carburization, correlations describing these mechanisms have been developed for air-fired conditions. The local environment in a furnace retrofit for oxy-combustion is expected to be different from air-fired boilers, therefore known corrosion mechanisms need to be re-visited and potentially revised to account for the modified environment. The current work summarized the published research studies relevant to oxidation, sulfidation, chloridation and carburization.

Oxidation was identified as generally beneficial if the oxide layer can be maintained. Corrosion due to sulfidation can occur from H_2S gas attack, FeS based deposits, and molten sulfates. Presence of chlorides can affect the molten sulfate corrosion mechanism in that chloride can disintegrate the protective oxide scale. Normally SO_2 and SO_3 cannot diffuse through the scale, but, with disrupted oxide scale, SO_2 and SO_3 can react with tube metal directly. Presence of chlorides in the alkali sulfate can also decrease melting point and expand the temperature range that corrosion can occur. Correlations exist for all sulfidation mechanisms under air-fired conditions.

Sulfur in the presence of chlorine can have different roles in corrosion depending on local environment. Under reducing conditions, metal loss through sulfidation may be accelerated by the presence of chlorine. Under reducing conditions alkali chlorides are stable, but under oxidizing conditions the conversion of alkali chlorides to less corrosion alkali sulfates is favored. Thus, the presence of fuel sulfur can provide some protection against chlorine attack under oxidizing conditions, but may enhance sulfidation instead. Chlorine gas forming high temperature gases such as HCl, KCl, and NaCl can cause corrosion through different mechanism from molten sulfate corrosion. Condensed chloride on the tube surface can also affect corrosion. Corrosion can occur by gaseous specie, deposit, or the combination of these corrosive materials.

There are conflicting data in the literature on the significance of gaseous attack by enhanced CO_2 and/or H_2O concentrations. In this case, corrosion may be dominated by other mechanisms. Further study will be conducted to clarify the importance of the changed flue gas environment in oxy-firing mode on corrosion and to identify those correlations able to fundamentally account for changes to corrosion parameters under oxy-combustion conditions.